Università di Roma *"Sapienza"*

DOTTORATO DI RICERCA IN

MECCANICA TEORICA ED APPLICATA

XXIV CICLO

Enhanced SPH modeling of free-surface flows with large deformations

Salvatore Marrone

Docente Guida:	Tutor:
Dr. Andrea Colagrossi	*Prof.* Giorgio Graziani

28 November 2011

ABSTRACT

The subject of the present thesis is the development of a numerical solver to study the violent interaction of marine flows with rigid structures. Among the many numerical models available, the Smoothed Particle Hydrodynamics (SPH) has been chosen as it proved appropriate in dealing with violent free-surface flows. Due to its Lagrangian and meshless character it can naturally handle breaking waves and fragmentation that generally are not easily treated by standard methods. On the other hand, some consolidated features of mesh-based methods, such as the solid boundary treatment, still remain unsolved issues in the SPH context.

In the present work a great part of the research activity has been devoted to tackle some of the bottlenecks of the method. Firstly, an enhanced SPH model, called δ-SPH, has been proposed. In this model, a proper numerical diffusive term has been added in the continuity equation in order to remove the spurious numerical noise in the pressure field which typically affects the weakly-compressible SPH models. Then, particular attention has been paid to the development of suitable techniques for the enforcement of the boundary conditions. As for the free-surface, a specific algorithm has been designed to detect free-surface particles and to define a related level-set function with two main targets: to allow the imposition of peculiar conditions on the free-surface and to analyse and visualize more easily the simulation outcome (especially in 3D cases). Concerning the solid boundary treatment, much effort has been spent to devise new techniques for handling generic body geometries with an adequate accuracy in both 2D and 3D problems. Two different techniques have been described: in the first one the standard ghost fluid method has been extended in order to treat complex solid geometries. Both free-slip and no-slip boundary conditions have been implemented, the latter being a quite complex matter in the SPH context. The proposed boundary treatment proved to be robust and accurate in evaluating local and global loads, though it is not easy to extend to generic 3D surfaces. The second technique has been adopted for these cases. Such a technique has been developed in the context of Riemann-SPH methods and in the present work is reformulated in the context of the standard SPH scheme. The method proved to be robust in treating complex 3D solid surfaces though less accurate than the former.

Finally, an algorithm to correctly initialize the SPH simulation in the case of generic geometries has been described. It forces a resettlement of the fluid particles to achieve a regular and uniform spacing even in complex configurations.

This pre-processing procedure avoids the generation of spurious currents due to local defects in the particle distribution at the beginning of the simulation.

The δ-SPH model has been validated against several problems concerning fluid-structure interactions. Firstly, the capability of the solver in dealing with water impacts has been tested by simulating a jet impinging on a flat plate and a dam-break flow against a vertical wall. In this cases, the accuracy in the prediction of local loads and of the pressure field have been the main focus. Then, the viscous flow around a cylinder, in both steady and unsteady conditions, has been simulated comparing the results with reference solutions. Finally, the generation and propagation of 2D gravity waves has been simulated. Several regimes of propagation have been tested and the results compared against a potential flow solver.

The developed numerical solver has been applied to several cases of free-surface flows striking rigid structures and to the problem of the generation and evolution of ship generated waves. In the former case, the robustness of the solver has been challenged by simulating 2D and 3D water impacts against complex solid surfaces. The numerical outcome have been compared with analytical solutions, experimental data and other numerical results and the limits of the model have been discussed. As for the ship generated waves, the problem has been firstly studied within the $2D + t$ approximation, focusing on the occurrence and features of the breaking bow waves. Then, a dedicated 3D SPH parallel solver has been developed to tackle the simulation of the entire ship in constant forward motion. This simulation is quite demanding in terms of complexities of the boundary geometry and computational resources required. The wave pattern obtained has been compared against experimental data and results from other numerical methods, showing in both the cases a fair and promising agreement.

RINGRAZIAMENTI

Ringrazio Andrea Colagrossi per avermi condotto, sostenuto e sollevato continuamente lungo questo percorso, nei successi e nei momenti più difficili. A lui va la mia più profonda riconoscenza per la pazienza e la fiducia come guida, ma anche e soprattutto per l'onestà ed il supporto come amico.

Ringrazio il prof. Giorgio Graziani per avermi dato l'opportunità di portare avanti questa ricerca, per la disponibilità e le lunghe ed intense discussioni. Ringrazio Claudio Lugni per aver reso possibile la mia attività presso l'istituto CNR-INSEAN e per avermi fatto credere in questa esperienza, trasmettendomi il suo genuino entusiasmo per la ricerca.

Un grazie a tutti i ricercatori ed i collaboratori del CNR-INSEAN che mi hanno aiutato e sostenuto in questi anni, in particolare Matteo, Giuseppina e Marilena sempre disponibili e pazienti nell'aiutarmi ed incitarmi, ognuno con le proprie preziose peculiarità, Benjamin come fondamentale spalla cattiva, Tomaso come necessario e rigoroso personal trainer, Luigi per le quotidiane competizioni (che è ancora convinto che il Mar Adriatico sia più bello del Tirreno) e infine tutta la gloriosa squadra della Dynamo US3 con cui sono stati raggiunti grandi traguardi.

Ancora vorrei ringraziare il prof. David Le Touzé per le stimolanti e piacevoli discussioni e i fondamentali contributi al mio lavoro, i ricercatori dell'Università della Calabria con cui ho avuto il piacere di collaborare, Ivan Federico e Francesco Aristodemo, per il loro impegno continuo e costante ed una lunga serie di cose che vanno ben oltre l'attività scientifica. Grazie ai ricercatori del CASPUR di Roma e in particolare a Giorgio Amati per il supporto ed i suggerimenti durante lo sviluppo dei solutori numerici.

Un ringraziamento al sostegno morale della tribù MaSaVi, a quell'esperienza di convivenza partecipata che è iniziata con il dottorato e mi ha accompagnato durante tutto questo percorso e oltre. Grazie a Matteo, Vincenzo, Camila, Gabriele, Martina, Maurizio, Assunta, Alessia, Mariana, Diana, Silvia, Elena.

Grazie a Federico e Lapo che, ovunque i nostri percorsi ci porteranno, rimarranno sempre indiscutibili punti fermi.

Un grazie ai ragazzi di Ingegneria Senza Frontiere, Nicoletta, Fabrizio, Giovanni, Mauro, Elisa, Giuseppe, Silvio, Toni, Vito, con cui ho condiviso tante esperienze e con i quali sto imparando a de-costruire e confrontarmi su tanti aspetti, dal ruolo che giochiamo nella società, alla opinabile salubrità dei distillati al metanolo del Madagascar.

Infine il ringraziamento più sentito va a Margherita che permea e ispira ogni passo che faccio, e alla mia famiglia per il loro affetto incondizionato e la serenità che mi donano. A loro è dedicato questo lavoro.

CONTENTS

NOMENCLATURE

GENERAL RULES

- Only the most used symbols in the following sections are listed
- Meaning of symbols is given at least when introduced in the thesis
- Sometimes the same symbol is used to indicate different things
- Symbols for vectors and matrices are generally written in boldface
- Symbols between angle brackets (e.g. $\langle f \rangle$) represent the *regularized* values, i.e. obtained through an integral interpolation

SYMBOLS

$\mathbf{r}$	Position vector
$\mathbf{u}$	Velocity vector
ρ_0	Density
p	Pressure
c	Speed of sound
e	Specific internal energy
μ	Dynamic viscosity
ν	Kinematic viscosity
σ	Thermal conductivity
$\mathbf{g}$	Vector of the external volume forces
$\mathbf{q}$	Heat flux
$\mathbb{D}$	Strain rate tensor
$\mathbb{T}$	Stress tensor
$\mathbb{V}$	Viscous component of the stress tensor
$\mathcal{M}$	Global mass of the system
$\mathcal{Q}$	Linear momentum of the system
$\mathcal{L}$	Angular momentum of the system
$\mathcal{E}_{TOT}$	Total energy of the system
$\mathcal{E}_{M}$	Mechanical energy of the system
W	Weight function called *smoothing function* or *kernel*
h	Smoothing length

N_{part}	Total number of particles
$\mathcal{N}_i$	Number of neighbours of the i-th particle
$\mathcal{N}$	Average number of neighbours
Δx	Mean inter-particle distance
Δt	Numerical integration time step
$\boldsymbol{n}$	Unit normal vector
$\boldsymbol{\tau}$	Unit tangent vector
Γ	Integral of the kernel function on its support
α	Artificial viscosity
δ	Numerical coefficient to control the diffusive term in the continuity equation
χ	Numerical coefficient for artificial thermal conductivity
Ξ	Numerical coefficient related to the state equation
C	Convergence rate

Re	Reynolds number (= UL/ν)
St	Strouhal number (= fL/U, where f is a characteristic frequency)
Fr	Froude number (= $U/\sqrt{(gL)}$)
Ma	Mach number (= U/c)

ACRONYMS AND ABBREVIATIONS

B.C.	Boundary Conditions
BEM-MEL	Boundary Element Method Mixed Eulerian-Lagrangian
CFL	Courant–Friedrichs–Lewy condition
ISPH	Incompressible Smoothed Particle Hydrodynamics
MEAF	Morris et al. formulation
MGF	Monaghan & Gingold formulation
MLS	Moving Least Square Interpolation
ODE	Ordinary Differential Equation
PDE	Partial Differential Equation
PVW	Principle of Virtual Work
SPH	Smoothed Particle Hydrodynamics
VOF	Volume Of Fluid
WCSPH	Weakly-Compressible Smoothed Particle Hydrodynamics

1 INTRODUCTION

1.1 MOTIVATIONS AND BACKGROUND

Motivations

The present thesis deals with the violent interaction of free-surface flows with rigid structures. Breaking waves, fragmentation of the liquid phase and air entrapment phenomena are all features of this scenario and they make this research subject particularly complex. Its relevance to maritime and coastal engineering lies on the key role played by the involved phenomena in the design and safety assessment of marine structures, vessels, offshore platforms and littoral structures.

Engineering applications

Examples of practical engineering issues are the violent gravity waves-structure impacts (see e.g. figure 1.1). The importance of this topic is significantly increasing also in connection with the rising demand for marine renewable resources due to the need of greener and long-term available energies in the today's society. In this sense, offshore wind farms represent an important medium for the energy harvesting. The current trend is to build such structures further offshore in order to exploit higher wind velocities and avoid noise and visual conflicts. Such a choice, however, implies higher sea states to cope with and, thus, more demanding safety issues. This applies also to offshore platforms devoted to oil and gas extraction. In this case the growing energy demand has made convenient the exploitation in deep and very-deep water conditions. The fish farms are another kind of offshore industry that is going to move to open-sea areas. In this case, the reason is to access wider spaces and decrease environmental impacts on coastal areas. The multipurpose platforms, that are currently being designed to join together these and other functions, will have to manage the same and even more restrictive safety requirements.

Fast ships represent another instance in which the violent interaction between a free-surface flow and a solid structure play an important role. Some of the more relevant phenomena related to this topic are the occurrence of bottom and flare slamming, and the ship wave pattern and resulting wash. The former is related to the safety of the vessel while the latter is linked with noise, vessel signature, and possible disturbance to other ships and to the coast.

Regarding the coastal environment, the topic of present work has a great variety of applications, ranging from the problems of erosion and scouring around buildings close to the shoreline, to the more recent disasters related to extreme marine events, like tsunami and hurricanes, in highly urbanized

Figure 1.1.: Examples of water impacts on coastal structures under extreme sea states (*Pictures taken from the web*).

regions. In the latter case, the assessment of the flooding scenarios may allow limiting the potential damages by guiding effective strategies of coast protection, land use planning and efficient evacuation rules.

Since all these phenomena are characterized by strong dynamics and large fluid deformations, their analysis is quite challenging: analytical results are generally available for simple geometrical configurations while experimental data are often of difficult interpretation due to the interaction between several physical phenomena. In the latter case the scale effects are sometimes difficult to quantify especially when the water impact involves trapped and entrained air. In this context, the numerical simulation can worthily support the analysis.

Numerical approach

Among the many numerical models available, the Smoothed Particle Hydrodynamics (hereinafter SPH) concept seems to be a promising method in dealing with violent free-surface flows. It relies on a Lagrangian approach, that is, the fluid motion is described as a fluid-particle system and the derivatives of the flow quantities are computed along the trajectory of each particle. This leads to an intrinsic meshless character of the solver. The latter implies that the numerical grid points have no predetermined topological connections as in the case of mesh-based methods. The derivatives of the fluid quantities are evaluated for each particle through an interpolation procedure over its neighbouring particles. Thanks to these features the SPH method can naturally treat breaking waves and fragmentation that generally are not easily handled by standard methods. On the other hand, some consolidated features of mesh-based methods, such as the solid boundary treatment by body-fitted solvers, still remain unsolved issues in the SPH context. Therefore, the large part of the present research activity has been devoted to tackle some of the major open challenges of the method.

Physical assumptions

Targeting the aforementioned problems, the model of a weakly-compressible Newtonian fluid is adopted all over this work. Such a choice allows remarkable simplifications in the numerical scheme provided that the speed of the acoustic waves is sufficiently large respect to the highest flow velocity. Surface tension is not taken into account since its effects can be considered negligible for the length scales involved in the studied problems, though it should be taken into account to accurately describe wave breaking phenomena. Further, in the simulations just the liquid phase is modelled and the air-water interface is treated as a free-surface. This simplification is possible in a multi-phase flow when the density ratio between the different phases is large enough to consider the heavier phase as the one governing the flow evolution. The use of a one-fluid solver allows saving a significant amount of computational resources, provided that suitable conditions are enforced on the free surface boundary. However, when evaluating hydrodynamic loads on structures, the air entrainment can have non-negligible effects due to air compressibility. As a consequence, in the present work the consequences of this approximation on the numerical prediction are discussed whenever air entrapments could occur. Finally, in the majority of the cases the fluid is modelled as inviscid. Indeed, at the first stages of the water impacts the viscous effects are quite small. The fluid viscosity is taken into account only for problems characterized by low Reynolds numbers and therefore no turbulence model is needed. This choice is motivated by the fact that, in the SPH literature, references about implementation of turbulence models are still exiguous.

1.2 STRUCTURE OF THE THESIS

The thesis is formally divided in two parts. In the first one, a comprehensive state-of-the art concerning the SPH method in terms of governing equations and boundary conditions is provided. Then, the basic SPH model of the Navier-Stokes equations for weakly-compressible fluids is derived at continuous level with particular focus on consistency issues related to the presence of the free surface (chapter 3). The discrete equations are presented in chapter 4 along with some numerical aspects related to the SPH solver developed in this work. An enhanced SPH model, called δ-SPH, is proposed in chapter 5. In chapter 6 the problem of best initial-particle distribution in the case of generic solid-boundary geometries is examined and a new algorithm is proposed. Finally, in chapter 7 dedicated techniques to properly enforce the boundary conditions are presented: two alternative strategies for solid boundaries; a model to detect the free-surface configuration and impose special conditions along it, and an algorithm to simulate inflow and ouflow conditions at control surfaces.

In the second part of the work, the developed SPH model is applied in several test cases. In chapter 8 the model is validated through benchmark tests involving interaction of the fluid with rigid structures, starting from classical problems, like the jet impinging a flat plate and the flow past a cylinder, and then moving towards more unusual test cases like the propagation of highly non-linear gravity waves. In chapter 9 dam-break flows are studied in detail for several geometries in order to evaluate the capability of the solver in predicting local loads and the free-surface evolution. A final test case representing a 2D flash-flood impacting a bridge is devised as an example of violent water impact in a free-surface channel flow. Finally in chapter 10 the solver is applied to the case of ship generated waves and related breaking phenomena, first within the 2D+t approximation and then as a fully 3D method. The main conclusions of the work are drawn in chapter 11 and some suggestions for further improvements and developments of the code are given.

1.3 MAJOR FINDINGS

Although the research activity on SPH has been largely increased over the past decade, it still suffers from important drawbacks as the method is relatively new in the context of free-surface hydrodynamics. Therefore the present work has been devoted to develop and validate new numerical techniques specifically conceived to solve free-surface flows interacting with solid structures. In the following the main contributions of the present thesis are summarized:

The δ-SPH model

The occurrence of spurious numerical noise in the pressure field represents a major drawback of the naive SPH method for weakly-compressible fluids. This problem has been tackled through the introduction of diffusive numerical terms in the continuity equation. This term allows the reduction of high frequency acoustic noise in a conservative fashion. Further, this diffusive pro-

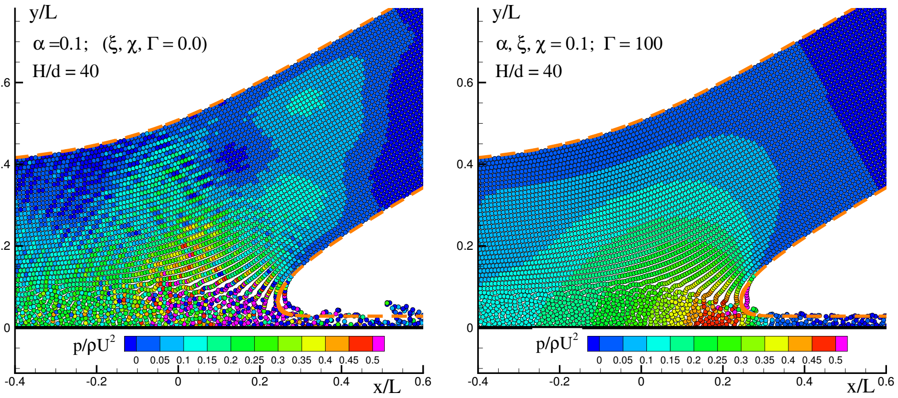

Figure 1.2.: The pressure field as predicted by the standard SPH scheme (left panel) and by the δ-SPH model (right panel) for the case of a jet impinging on a flat plate with $\vartheta = \pi/6$. The dashed lines represent the free surface analytical solution.

cess induces small mass exchanges between particles that make the particle distribution more uniform, with remarkable benefits for the accuracy of the interpolation procedure. This new diffusion term is consistent and convergent all over the fluid domain and preserves the mass. The resulting numerical scheme has been called δ-SPH. Figure 1.2 shows a comparison of the pressure fields obtained through the standard SPH model and δ-SPH for a jet impact.

Solid boundary conditions

In the SPH framework, the definition of proper boundary conditions along solid surfaces is a quite complex matter. In the present work two different techniques are developed: the first is a generalization of the classical ghost particle technique in order to treat complex solid geometries. This boundary treatment has shown to be robust and accurate in evaluating local and global loads (see figure 1.3), though it is not easy to extend to generic 3D surfaces. In the latter case, another technique, developed in the Riemann SPH context and here adapted for the standard SPH model, has been used.

Free-surface boundary conditions

A novel algorithm for the detection of free-surface particles is proposed. This can be useful to enforce peculiar free-surface conditions or to better analyse the numerical outcome, especially when dealing with complex 3D flows. The algorithm has been extensively validated and, further, an appropriate Level-Set function (i.e. a color function representing the signed distance of the particles from the free surface) has been defined in order to interpolate particle data onto a regular grid.

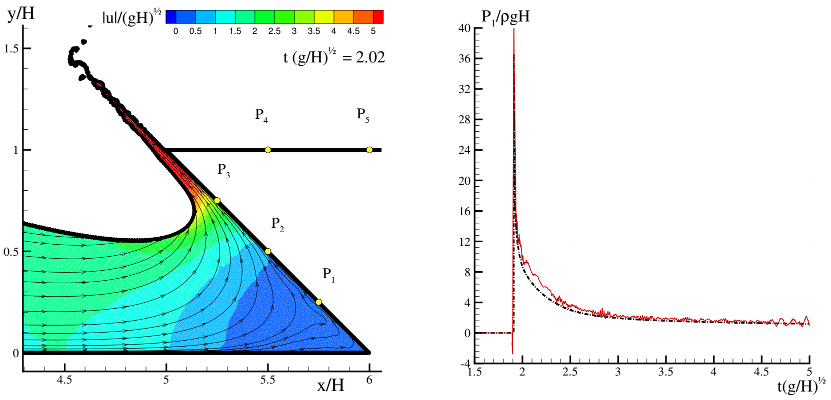

Figure 1.3.: Dam break flow against a sharp-edged obstacle. Left panel: contours of the velocity magnitude and streamlines at $t = 2.02\sqrt{H/g}$. Right panel: Pressure at probe P_1 from the δ-SPH solver (solid lines), and a Navier-Stokes Level-Set solver (dash-dotted lines).

Gravity waves

An extensive validation of the solver on gravity wave generation and propagation into a 2D basin is provided. Ship generated waves have also been studied. Firstly, the analysis has been carried on within the $2D + t$ theory, focusing on the features of the bow breaking wave. Then, a dedicated 3D SPH parallel solver has been developed to tackle the simulation of the entire ship in stationary forward motion. The problem is quite demanding because of the complexities of the solid boundaries and the required computational resources. The obtained wave pattern (see figure 1.4) has been compared against experimental data and results from other numerical methods, showing in both cases a fair and encouraging agreement.

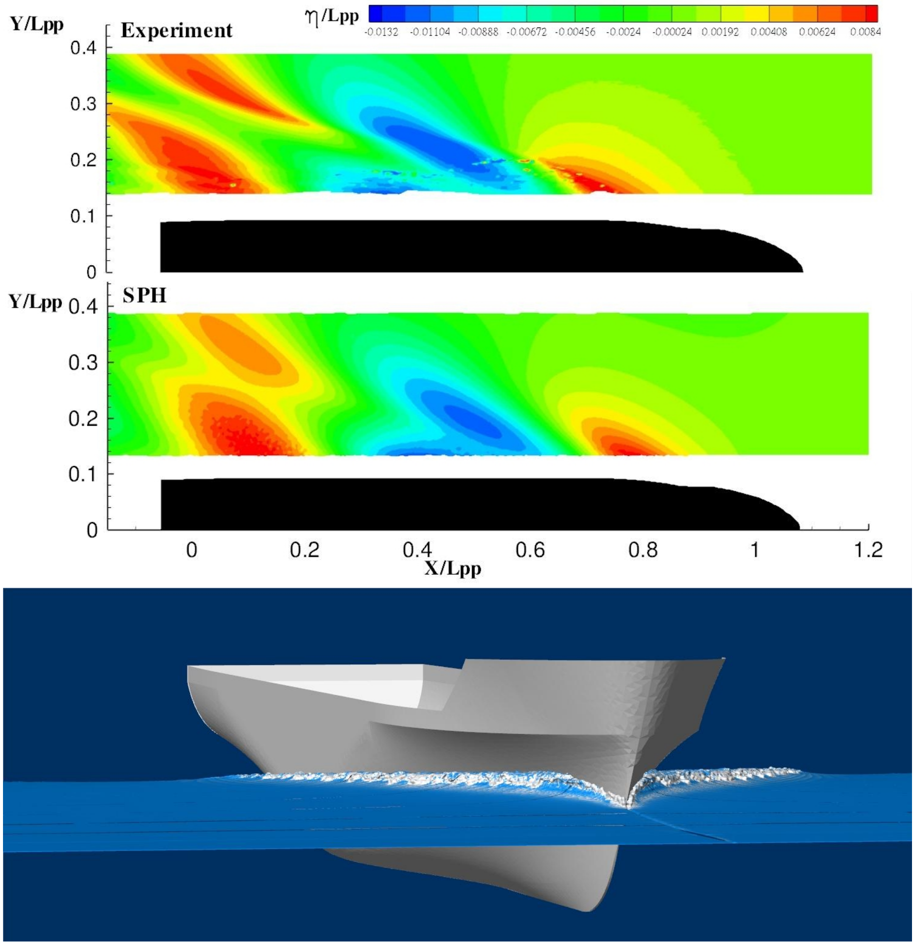

Figure 1.4.: Top and middle panel: contours of the wave elevation for the Alliance ship at $Fr = 0.328$ from experimental results performed at DGA-Hydrodynamics and SPH simulation respectively; bottom plot: 3D view of the breaking bow wave in the SPH simulation .

Part I

NUMERICAL MODEL AND THEORETICAL ASPECTS

2 SPH STATE-OF-THE ART

The Smoothed Particle Hydrodynamics method was introduced about three decades ago in astrophysics by Lucy (1977) and Gingold and Monaghan (1977). It dealt with simulation of interacting boundless fluid masses in vacuum. The SPH basics were inherited from statistical theories and Monte Carlo integrations. For more than ten years it was solely used for astronomical problems. Then, its applications spread to several physics and engineering problems, ranging from solid mechanics to multiphase flows. Monaghan firstly applied it for simulating free-surface inviscid flows. With respect to Eulerian finite difference method, it was found to be more suitable to handle breaking and fragmentation, due to its Lagrangian nature, and furthermore, within this method the free-surface boundary condition is treated in a straightforward fashion. Thanks to this valuable features interest on SPH has been growing very fast in the last decade and several researchers have devoted their activity to improve this method. In the following the most recent and remarkable works in this field are summarized starting from the main theoretical results regarding the method itself, and then describing the most significant improvements in its applications in the fields of fluid dynamics and solid mechanics.

Consistency and convergence of the SPH method

The fundamental theoretical achievements on the SPH method have been obtained considering a compressible inviscid fluid since the astrophysics represents the main context application of the method. The core of the SPH model is represented by the integral interpolation through which spatial derivatives of field functions are evaluated. The integral interpolation acts a convolution between the function values and a smoothing function called *kernel*. The kernel generally is a "bell"-shaped function with a compact support whose measure is given by the so-called smoothing length h. In this way it is possible to rewrite the fluid governing equations by substituting exact differential operators with "smoothed" ones. Hence the SPH governing equations are derived by discretizing the fluid in a finite number, say N_{part}, of "particles" and converting integral interpolations of the smoothed equations in summations over neighbouring points. The difficulties in proving the consistency of the SPH arise from these two consecutive approximation steps and have led to a delay of more than ten years in the achievement of a rigorous theoretical framework for the method.

Firstly, Di Lisio et al. (1997) demonstrated the convergence of the solution of the regularized version (i.e. by means of the SPH smoothing techniques) of Euler equations for a compressible flow to the solution of the genuine system of Euler equations. The same authors one year later (Di Lisio et al. 1998) proved the convergence of the SPH discrete equation to the regularized Euler equation for a generic polytropic fluid for $N_{\text{part}} \to \infty$ provided that $\mathcal{N} \to \infty$ (being $\mathcal{N}$ the number of interacting neighbours of each particle). It is worth noting that a similar result was found about ten years before by Mas-Gallic and Raviart (1987) for linear hyperbolic and parabolic equation systems. The conclusions drawn by Di Lisio et al. have been further confirmed in the work by Rasio (2000) where the convergence properties of SPH are studied using an analysis based on acoustic wave propagation. In particular, it has been pointed out that SPH schemes are convergent for $N_{\text{part}} \to \infty$ but they are consistent (i.e. converge towards the physical solution) only when $\mathcal{N} \to \infty$, with N_{part} increasing faster than $\mathcal{N}$. Bicknell (1991) showed how the equation of motion of particles in SPH may be rigorously derived from the motion equation of a continuous mean. That is, applying SPH integral interpolation the advective terms in the Euler or Navier-Stokes equations can be replaced by the total derivative with respect to time of the (non-smoothed) particle velocity.

Though those works give a sound rigorous basis for SPH, they do not give indications about the behaviour of errors when solving discrete SPH equations. Some authors have tried to give insights in this matter by studying the accuracy performances of the integral interpolation on scattered points. Colagrossi (2005) found that integral interpolation inside the fluid domain converges with second order, as expected by theory, if points are distributed on a regular mesh and $\mathcal{N}$ is constant but large enough. Conversely, when the point spatial configuration is non-uniform the interpolation does not even converge. Later, Quinlan et al. (2006) investigated analytically the truncation error of the gradient estimate using Taylor series expansions in 1D, giving a deeper description of the main factors responsible for interpolation accuracy. They showed that, while increasing the number of points, the second-order convergence is retained only up to a certain threshold refinement. Beyond that, further increase of N_{part} does not reduce the error made in the interpolation procedure. This sort of "saturation" is related to the number of neighbours $\mathcal{N}$ and to kernel shape. Increasing $\mathcal{N}$, this threshold is lowered in accordance with the conclusions drawn by Rasio (2000). When particles are not equi-spaced, second-order convergence is retained only when perturbations on particle position are small respect to h while the interpolation even diverges when they become larger. Moreover Quinlan et al. (2006) showed how renormalization of the kernel (Bonet and Lok 1999) significantly reduces interpolation sensitivity to particle distribution.

Adopting the same procedure devised by Quinlan et al. (2006), Amicarelli et al. (2011*a*,*b*) extended the errors analysis to 3D interpolations of field functions and derivatives. Both interpolations in bounded and unbounded domains have been studied, coming to results similar to those obtained by Quinlan et al. (2006). Recently, Springel (2010) has provided a characterization of the overall accuracy of the standard SPH scheme, testing the SPH model on several simple cases. For the problem of a travelling acoustic wave in a periodic box, he found the second order convergence predicted by analytical results by Rasio (2000). Note that, in contrast with prescriptions given above, in their numerical simulation the convergence is achieved keeping the number of neighbours constant. However, Springel (2010) has proven that, even with this procedure, numerical results converge to a solution that is close to the correct physical solution. Nonetheless, for a canonical problem involving shear flows he found a convergence rate of order less than one and a less favourable behaviour in terms of convergence to the physical solution.

Properties of the kernel renormalization to recover first-order consistency (i.e. exact estimation of a linear function) of the discrete integral interpolation (e.g. Johnson and Beissel 1996; Randles and Libersky 2000) have been studied by Moussa et al. (1999). In their work Riemann solvers are used to stabilize the scheme and convergence in the case of linear symmetric hyperbolic systems is proven under the less restrictive condition that $\mathcal{N}$ is finite and constant. Recently, convergence studies have been extended to the case of scalar non-linear hyperbolic conservation laws in bounded domains and it has been rigorously proven by Moussa (2006) that using Riemann solvers the SPH scheme is L^1 stable and converges to the unique entropy solution of the conservation law.

A fundamental property of the naive SPH scheme is the exact conservation of linear and angular momenta at discrete level. Gingold and Monaghan (1982) firstly proved this feature deriving SPH governing equations from a Lagrangian function for a non-dissipative, isentropic gas. Later, Oelschläger (1991) showed the strong link between SPH and Hamiltonian systems. He considered Hamiltonian systems with many particles interacting through a potential whose range is large respect average inter-particle distance. In this context, he rigorously demonstrated that Euler equations can be derived as a continuum limit of those particle systems.

SPH for simulating liquids

As mentioned above Monaghan (1994) was the first who applied SPH to simulate free-surface flows. He used a stiff equation of state to link density and pressure considering the fluid as weakly compressible (WCSPH). For simulations involving fluids like water, the speed of sound is chosen much smaller then the real one but large enough to ensure negligible density fluctuations. This approach has become quite popular and has been applied and validated in several problems ranging from sloshing flows (Colagrossi 2005; Marsh et al. 2010; Souto-Iglesias et al. 2004) to impact flows (Colagrossi and Landrini

2003; Ferrari et al. 2010; Marrone et al. 2011; Oger et al. 2006; Trivellato et al. 2006) and gravity waves propagation in different regimes (Antuono et al. 2011; Dalrymple and Rogers 2006; Landrini et al. 2007; Monaghan and Kos 1999) [1].

An alternative approach to enforce incompressibility is based on a two-step projection method where a divergence-free velocity field is obtained solving the Poisson pressure equation derived from an approximate projection. This method is similar to the approach adopted in Moving Particle Semi-implicit models (Koshizuka and Oka 1996) and was firstly proposed by Cummins and Rudman (1999) calling it Incompressible SPH (ISPH) . Other methods to strictly enforce incompressibility have been developed by Shao and Edmond (2003) and Ellero et al. (2007). From a numerical point of view the main differences between the weakly-compressible and incompressible approaches is that the former requires small time steps constrained by the speed of sound, while the later needs to solve an algebraic system with a sparse matrix, permitting larger time steps but rather complex for an efficient parallelization.

When dealing with free-surface flows, that is multi-phase flows in which the interface is essentially governed by the heaviest phase, enforcement of suitable boundary conditions is needed. In the context of WCSPH, Bonet and Lok (1999) proposed two alternative formulations for continuity and momentum equations, both suitable for free-surface flows and physically consistent as derived through the minimisation of an energy functional. Both the final systems obtained conserves exactly linear and angular momenta at discrete level.

The two different formulae come from the different ways through which the continuity equation is solved: one is derived from the Monte Carlo density evaluation proposed at the very beginning of the SPH method (Lucy 1977) and mostly used in the astrophysical context; the other is derived from direct discretization of the continuity equation. The latter has been considered by Colagrossi et al. (2009*b*) for an in-depth study regarding enforcement of dynamic and kinematic free-surface boundary conditions. It was rigorously proven that both formulae are implicitly satisfied by the weakly-compressible scheme when the adopted governing equations are those described in Bonet and Lok (1999).

Conversely, incompressible schemes require the explicit detection of the free surface to assign the dynamic boundary condition. Unfortunately, this is not an easy task, especially in three dimensional violent free-surface flows (see e.g. Haque and Dilts 2007; Marrone et al. 2010)[2]. Further, the solution of a Poisson equation (that is needed by all the incompressible schemes) is strongly dependent on the free surface configuration and, consequently, small errors in the free-surface detection can lead to different flow dynamics.

On the other hand, WCSPH schemes can be interpreted as explicit central finite difference scheme and therefore need an artificial viscosity term for sta-

---

[1] see also section 8.3 and chapter 9

[2] see also section 7.2

bility reasons. Nonetheless, they suffer from unphysical high frequency noise in pressure (e.g. Colagrossi and Landrini 2003; Ferrari et al. 2009). Some authors provided corrected models to enhance the pressure evaluation in WC-SPH scheme retaining its advantages. Firstly, in the aforementioned work by Moussa et al. (1999), the Riemann solvers are introduced to avoid the use of artificial viscosity and regularize the pressure field. This approach has become quite popular but, in some problems, it can result too diffusive to compute the particle positions correctly (Ferrari et al. 2009).

In a less radical approach, Colagrossi and Landrini (2003) proposed a periodic density reinitialization through a Moving Least Square (MLS) interpolant to eliminate spurious oscillations in the density (and, consequently, in the pressure field). This technique proved to be effective but it requires some parameters to be tuned and, above all, it does not preserve hydrostatic pressure distribution for long-time simulations. Later, Molteni and Colagrossi (2009) proposed to add conservative diffusive terms in the continuity equation. This proved very good to smooth out the numerical noise inside the pressure field but it introduced spurious contributions inside the density equation for particle close to the free surface.

Ferrari et al. (2009) proposed an alternative model inspired by Riemann-based SPH schemes by introducing the Rusanov flux in the continuity equation. This correction avoids the use of the artificial viscosity and results in an effective regularization of pressure. In Antuono et al. (2010)[3] the idea proposed by Molteni and Colagrossi (2009) has been exploited to add more stable and consistent diffusive terms in the continuity equations. Further an ad-hoc thermal energy is defined aiming to change the sound speed as compressions/deformations occur.

SPH for viscous flows

The first viscous term introduced in the SPH scheme was proposed by Gingold and Monaghan (1982) in order to dampen the oscillations appearing in shock waves. It was a Lax type correction based on a smoothed velocity field but resulted too dissipative if shocks formation is needed to be solved accurately. Therefore, Monaghan and Gingold (1983) devised a pairwise artificial viscosity based on a Neumann-Richtmyer artificial viscosity and on a bulk viscosity. Although this term had been devised to act only in compression in order to treat shocks, they noted that a spurious amount of entropy was created also for pure shear flows and both Balsara (1995) and Colagrossi and Landrini (2003) performed corrections in that viscosity term in order to mitigate that effect.

When Monaghan (1994) carried out the first free-surface simulations, he used the same viscous term developed ten years before to stabilize the scheme. At the same time, Takeda et al. (1994) noticed that the naive estimation of

---

[3] see chapter 5

second derivatives of the velocity field leads to some problems due to the randomness of the particle distribution. Then, they preserved linear momentum in the Navier-Stokes viscous term for compressible flow by anti-symmetrizing those derivatives; combined with appropriate boundary conditions this expression is very accurate for the solution of canonical flows like Poiseuille. Even the drag force on a cylinder in free stream at low Reynolds number is correctly computed. The main drawbacks of that formulation lie in the non-conservative form for angular momentum and in the more expensive computational effort required.

With similar background, Watkins et al. (1996) obtained a formulation that could conserve both linear and angular momenta but that was extremely expensive from a computational point of view because of the need for an extra loop over particles. Morris et al. (1997) were the first to focus on incompressible viscous flows with SPH. They devised a viscosity term based on hybrid expression that combines a standard SPH first derivative with a finite difference approximation of a first derivative. In this way linear momentum is conserved exactly while angular momentum is only approximately conserved. In Cleary and Monaghan (1993) and Cleary (1998) the term developed by Monaghan and Gingold (1983) is slightly modified introducing a real viscosity coefficient and used as a shear viscosity for incompressible flows.

Later, Español and Revenga (2003) provided a general expression valid for the continuous formulation of the second order derivatives within the SPH framework and Hu and Adams (2006*b*) used that expression to show the consistency of viscous term presented by Cleary and Monaghan (1993). Recently, Colagrossi et al. (2010*b*) and Colagrossi et al. (2011) have provided an in-depth study of the behaviour of the same viscous term for incompressible free-surface viscous flows, proving, even in this context, its consistency with the Navier-Stokes' viscous term.

SPH for solid mechanics

Thanks to the suitability of the method in modeling continuous media, SPH has been applied to solve solid mechanics problems in which large deformations and fragmentation occur. Libersky et al. (1993) was the first to consider the SPH technique in this context, that was only used for astrophysical studies up to that time, and they extended it to problems requiring an accurate evaluation of the entire stress tensor. The resulting model was robust with the advantage of naturally handling high strain and void. Unfortunately, Swegle et al. (1995) noticed that serious instabilities in the numerical scheme can develop when tensile stresses occur. Performing a Von Neumann stability analysis on the simplified one-dimensional SPH equations, they found that the instability is triggered depending on the sign of the particle stress and on the second derivative of the kernel function. Morris (1996*a*) drawn similar conclusions in his work. There, the stability analysis is carried out studying the propagation of a linear acoustic wave in both 1D and 2D and rewriting the SPH equations through the Poisson's summation formula. Read et al. (2010) extended this approach, performing a 3D stability analysis.

Several strategies have been proposed to eliminate this problem. The same authors (Morris 1996*a*; Read et al. 2010) proposed adjusted kernel functions that ensure repulsion between particles but they resulted in lower accuracy of the derivatives. Dyka and Ingel (1995) argued that the main problem relies in collocation nature of SPH (for more details see Fries and Matthies 2004). Hence, inspired by other collocation methods like Finite Element Method, they introduced *stress points*, staggered with respect to particle positions, where only the constitutive equation is evaluated. The method proved to be stable in tension and it was further extended for higher-order accuracy schemes by Randles and Libersky (1996) and Randles and Libersky (2000). However its effectiveness was shown only for solid mechanics and was never applied in hydrodynamic problems. Monaghan and Kos (2000) and Gray et al. (2001) proposed an artificial short-range repulsive term to easily avoid particle clumping, even though introducing spurious disturbances in the stress field.

In a more radical approach Dilts (1999) used the Moving-Least-Square (MLS) interpolant instead of the SPH one with a Galerkin approximation similarly to finite element method. In this way he introduced first-order consistency and removed tensile instability. Finally, Bonet and Kulasegaram (2001) proposed a Lagrangian kernel formulation with the analogous purposes pursued by Dyka and Ingel (1995).

Tensile instability when simulating liquids

The tensile instability generally does not represent a critical problem when dealing with hydrodynamic flows in presence of gravity. In this case the fluid is compressed almost everywhere, apart from specific situations (violent pressure waves traveling in the medium, high vorticity regions, etc.), conversely to solid structures that are always subjected both to tension and compression. When gravity can be neglected, if the flow occurs with no free-surface (as in the majority of these cases), it is possible to add a background pressure to avoid negative pressures (see Morris et al. 1997). This is not possible when dealing with free-surface flows in WCSPH schemes, for which the dynamic free-surface boundary condition is intrinsically satisfied only for zero-value of the pressure at the interface (for more details see Colagrossi et al. 2010*b*). Most of the techniques proposed in the context of solid mechanics are not applicable to free-surface flows and, for the above mentioned reasons, there are still few reference works available treating tensile instability in free-surface flows.

Boundary conditions for solid profiles

When SPH started to be applied to fields other than astrophysics, where problems are usually boundless, the problem of enforcing solid boundary condition arose. This is non-trivial in SPH and, recently, it has been elected subject of study by many research groups. A first solution was proposed by Monaghan (1994) using repellent particles along the solid boundaries. The concept behind this method relies on the repulsive forces that exist at microscopic scale. In this way, wall penetration by fluid particles is avoided, even for complex geometries, but the pressure field result noisy near the solid boundaries. This technique has been recently improved in Monaghan and Kajtar (2009) for treating more effectively arbitrary shapes.

An alternative popular method relies on the well known ghost fluid technique. Libersky et al. (1993) was the first to adopt such technique. In problems of solid mechanics he used imaginary particles mirroring the particle physical domain. Then, Takeda et al. (1994) extended this technique to solve laminar viscous flows and enforce no-slip boundary conditions. With a similar approach, Morris et al. (1997) modeled no-slip condition through boundary particles. In this case, the velocity of the fictitious particles is a linear extrapolation of the fluid one, tuned with an empirical parameter. The method was applied to solve incompressible flows at low Reynolds number. Simulations of medium and high Reynolds numbers are still challenging in the SPH context as instabilities may occur in connection with the enforcement of no-slip conditions.

In a rigorous mathematical framework Vila (1999) provided some fundamental prescriptions for the consistent implementation of ghost fluid, repulsive forces and semi-analytic approaches. Finally in Colagrossi and Landrini (2003), a ghost particle method was proposed for exactly enforcing free-slip boundary conditions in inviscid free-surface incompressible flows and, up to now, it is referred to as the "classical" ghost technique. Unfortunately, even if the method is fairly accurate, it can be easily applied only for flat profiles or right angle. In fact, its extension to generic solid shapes is not straightforward nor unique.

For this reason, recently many other techniques have been proposed. Kulasegaram et al. (2004) developed a method based on boundary integrals in order to compute a contact force term to introduce in the momentum equation. Similarly, Feldman and Bonet (2007) and Di Monaco et al. (2009) used an analytic approach to compute the intersection between the kernel support and boundary surface. This procedure results in a more accurate evaluation of the boundary term but it is more expensive from the computational point of view. Hieber and Koumoutsakos (2008) proposed an extension to particle methods of the immersed boundary technique used in finite difference schemes. The method is accurate and flexible but requires particles lying on a regular mesh.

The multi-tangent algorithm is an extension of the classical ghost technique by Yildiz et al. (2009) for generic boundaries: fluid particle are mirrored using different local boundary normals in order to complete the kernel for non-flat profiles. It has been applied by Shadloo et al. (2010) for the problem of the flow past an airfoil but it was never applied in free-surface flows and still remains not easy to implement especially in 3D.

Marongiu et al. (2008) inspired by normal flux technique of finite volume methods developed an effective and straightforward method in the context of Riemann-based SPH. It is based on the calculation of the boundary contribution using the kernel values on the solid profile and the local normals to the boundary. De Leffe et al. (2009) improved this technique through the use of specific upwind flux schemes,they found that this technique is a promising way for enforcing solid boundary conditions, being computationally cheap and fairly robust. Recently, Ferrand et al. (2010) extended the method by introducing a time integration of that boundary term. Finally, another extension of the ghost method for generic profiles has been proposed in Marrone et al. (2011) [4] and has been proven to be robust and fairly accurate though not simple to extend in 3D. As for the enforcement of no-slip boundary conditions, recently new insights have been given by De Leffe et al. (2011) and Macià et al. (2011) allowing the simulation of viscous flows at higher Reynolds numbers [5].

---

[4] see also section 7.1

[5] see section 8.2 for further details

3 THE SPH REGULARIZED NAVIER-STOKES EQUATIONS

In this chapter a detailed analysis of the theoretical structure of the SPH is presented for weakly compressible viscous flows in presence of a free surface. In particular the general continuous formulation of the SPH method is considered postponing to the next chapter the discussion on the SPH discrete equations.

The SPH formulation is based on the use of integral interpolations adopted to approximate the differential operators in the Navier-Stokes equations. The smoothed differential operator are constructed by using a mollification kernel. Once this approximation are introduced in the PDE system a *regularized* version of the flow equations is obtained. Great care is taken to address some inconsistencies occurring when considering free-surface inviscid flows. Incidentally, a discussion on the choice of the weakly compressible model is provided along with a new relation for the equation of state.

3.1 GOVERNING EQUATION

When modelling almost incompressible liquids two different strategies can be adopted. The first one is to consider the liquid as incompressible, so that the mass conservation equation

$$\frac{D\rho}{Dt} + \rho\,\mathrm{div}(\mathbf{u}) = 0$$

reduces to:

$$\mathrm{div}(\mathbf{u}) = 0\,.$$

The introduction of this constraint into the Navier-Stokes equations leads to write a Poisson equation for the pressure field p. In such a truly-incompressible formulation the pressure solution is therefore obtained through the solution of an algebraic system. All the boundaries of the fluid domain have to be explicitely known and in a meshless context, this can be troublesome for the free surface, see e.g. section 7.2.

The second strategy considers the flow as weakly-compressible. This approach consists in modelling a compressible flow in order to simulate a problem under the constraint of negligible compressibility effects. Therefore an equation of state $p = p(\rho, e)$ is introduced, where e is the specific internal energy and ρ is the fluid density. In this way, the energy equation has to be considered along with the continuity and momentum equations. In weakly-compressible formulations a fully-explicit method is used. This approach is classically adopted in SPH formulations. The Navier-Stokes equations for a weakly-compressible barotropic fluid (in Lagrangian formalism) read:

$$\begin{cases} \dfrac{D\rho}{Dt} + \rho \, \mathrm{div}(\mathbf{u}) = 0 \\[2ex] \dfrac{D\mathbf{u}}{Dt} = \mathbf{g} + \dfrac{\nabla \cdot \mathbb{T}}{\rho} \\[2ex] \dfrac{De}{Dt} = \dfrac{\mathbb{T} : \mathbb{D}}{\rho} - \mathrm{div}(\mathbf{q}) \\[2ex] p = p(\rho, e) \end{cases} \tag{3.1}$$

where $\mathbf{g}$ represent the external volume forces, $\mathbf{q}$ the heat flux, and $\mathbb{D}$ the strain rate tensor, *i.e.* $\mathbb{D} = (\nabla\mathbf{u} + \nabla\mathbf{u}^T)/2$.

The flow velocity $\mathbf{u}$ is defined as the material derivative of a fluid element at the position $\mathbf{r}$:

$$\frac{D\mathbf{r}}{Dt} = \mathbf{u}\,. \tag{3.2}$$

$\mathbb{T}$ is the stress tensor of a Newtonian fluid:

$$\mathbb{T} = (-p + \lambda \, \mathrm{tr}\, \mathbb{D}) \, \mathbb{1} + 2\,\mu\,\mathbb{D}\,, \tag{3.3}$$

Finally, μ and λ are respectively the dynamic and the bulk viscosity coefficients. For the present discussion, it is useful to identify the viscous part of the stress tensor:

$$\mathbb{V} = \lambda \, \mathrm{tr}\, \mathbb{D} \, \mathbb{1} + 2\,\mu\,\mathbb{D}\,, \tag{3.4}$$

thus, the divergence of the stress tensor writes:

$$\nabla \cdot \mathbb{T} = -\nabla p + \nabla \cdot \mathbb{V} = -\nabla p + (\lambda + \mu)\,\nabla(\mathrm{div}(\mathbf{u})) + \mu \nabla^2 \mathbf{u}\,. \tag{3.5}$$

Generally liquids can be treated as a barotropic fluid (see e.g. Batchelor 1967), which means that pressure p and internal energy e are both single-valued functions of density ρ. It implies also that the energy equation is decoupled from the other governing equations. The choice of the state of equation in the SPH model is discussed in section 4.

3.1.1 Boundary conditions

The previous field equations apply on a domain Ω that is bounded by $\partial\Omega$. $\partial\Omega$ is composed by solid boundaries, $\partial\Omega_B$, and free surfaces, $\partial\Omega_F$. There are two types of Boundary Conditions (BCs) to be considered on free surfaces: kinematic and dynamic. The kinematic free-surface BC states that an elementary fluid volume belonging to the free surface will remain on it during the flow evolution. This condition is naturally satisfied in the Lagrangian formalism adopted. The dynamic free-surface BC expresses the continuity of stresses across the free surface. Assuming that surface tension is negligible, a "free" surface does not stand either normal stresses or tangential shear stresses. For a Newtonian fluid, by denoting such stress field as $\mathbf{t}$, the dynamic boundary condition reads:

$$\mathbf{t} = \mathbb{T}\mathbf{n} = (-p\,\mathbb{1} + \mathbb{V})\,\mathbf{n} = (-p + \lambda\,\mathrm{tr}\,\mathbb{D})\,\mathbf{n} + 2\mu\,\mathbb{D}\mathbf{n} = 0\,. \tag{3.6}$$

where $\mathbf{n}$ is the free-surface normal unit vector. After normal and tangential projections, considering that $\mathrm{tr}\,\mathbb{D} = \mathrm{div}(\mathbf{u})$ and $\mathbf{n}\cdot\mathbb{D}\mathbf{n} = \mathbf{n}\cdot\partial\,\mathbf{u}/\partial\,\mathbf{n}$, equation (3.6) becomes:

$$p = \lambda\,\mathrm{div}(\mathbf{u}) + 2\mu\,\mathbf{n}\cdot\partial\,\mathbf{u}/\partial\,\mathbf{n}\,, \tag{3.7}$$

$$\boldsymbol{\tau}\cdot\mathbb{D}\mathbf{n} = 0. \tag{3.8}$$

where $\boldsymbol{\tau}$ is a unit vector of the free-surface tangent plane. As a consequence of equation (3.7) the pressure field is generally discontinuous across the free surface.

However, since the viscous coefficients are generally very small for the liquids considered in this thesis, the pressure can be considered continuous across $\partial\Omega_F$, therefore equal to the external pressure p_e

$$p = p_e \qquad \forall\mathbf{r} \in \partial\Omega_F \tag{3.9}$$

If p_e is constant, a trivial change of the reference pressure leads to $p = 0$ on the free surface, which is commonly used by SPH practitioners. Since the pressure is constant on the free surface, the density has also to be constant there (barotropic flow). As a consequence, the following equation is satisfied on the free surface:

$$\mathrm{div}\mathbf{u} = 0 \qquad \forall\mathbf{r} \in \partial\Omega_F \tag{3.10}$$

Note that, since ρ and p are constant along the free surface, e is constant as well and, therefore, the free surface is also an isothermal curve. In the following, we denote such constant values through ρ_0 and e_0.

On $\partial\Omega_B$ the no-penetration condition and the adherence condition have to be enforced, that is:

$$\mathbf{u}\cdot\mathbf{n}_B = \mathbf{V}_B\cdot\mathbf{n}_B \tag{3.11}$$

$$\mathbf{u}\cdot\boldsymbol{\tau}_B = \mathbf{V}_B\cdot\boldsymbol{\tau}_B \tag{3.12}$$

where $\mathbf{n}_B$ and $\boldsymbol{\tau}_B$ are the normal and the tangential unit vectors and $\mathbf{V}_B$ is the boundary velocity. When solving inviscid fluid, the free-slip condition is imposed on the solid surface, that is, only condition (3.12) is required. For more details about enforcement of solid boundary condition in SPH see section 7.1.

3.2 SPH INTEGRAL INTERPOLATION

3.2.1 Interpolation of functions and their gradients

In meshless methods the generic scalar field f is interpolated through a convolution integral over the domain Ω, so that its value in the position $\mathbf{r}$ is given by:

$$\langle f\rangle(\mathbf{r}) = \int_{\Omega} f(\mathbf{r}')\,W(\mathbf{r}-\mathbf{r}';h)\,dV'\,, \tag{3.13}$$

The weight function $W(\mathbf{r}-\mathbf{r}';h)$, called *smoothing function* or *kernel*, is positive, radially centered in $\mathbf{r}$ and decreases monotonously with $s = \|\,\mathbf{r}-\mathbf{r}'\|$ to zero on the border of its support $\partial\Omega$. Practically, the kernel has a compact support $\Omega(\mathbf{r})$ of characteristic length h, often referred to as the "smoothing length", see figure 3.1. Physically, h can be regarded to as a measure of the domain of influence of the point in $\mathbf{r}$. Since the kernel is spherical it depends only on s and h. Hereinafter we adopt the notation $W(\mathbf{r}'-\mathbf{r})$, implicitly assuming the dependence on h. In this thesis h is considered constant in the whole domain Ω. It is possible to derive interpolation formulae with variable h (see e.g. Bonet and Rodriguez-Paz 2005; Hernquist and Katz 1989; Monaghan 2005*b*) however these are not treated in this thesis.

Finally, the kernel is assumed symmetric, i.e. $W(\mathbf{r}-\mathbf{r}') = W(\mathbf{r}'-\mathbf{r})$. Its integral on the domain Ω

$$\Gamma(\mathbf{r}) = \int_{\Omega} W(\mathbf{r}-\mathbf{r}')\,dV' \tag{3.14}$$

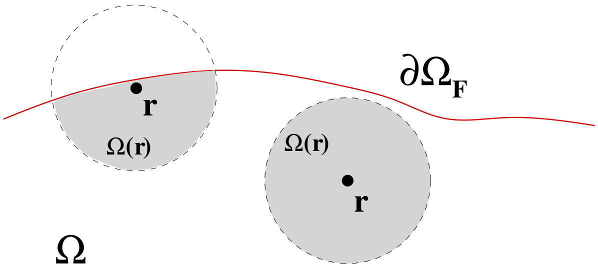

Figure 3.1.: Configurations of the kernel support $\Omega(\mathbf{r})$ deep inside the fluid domain and near the free surface.

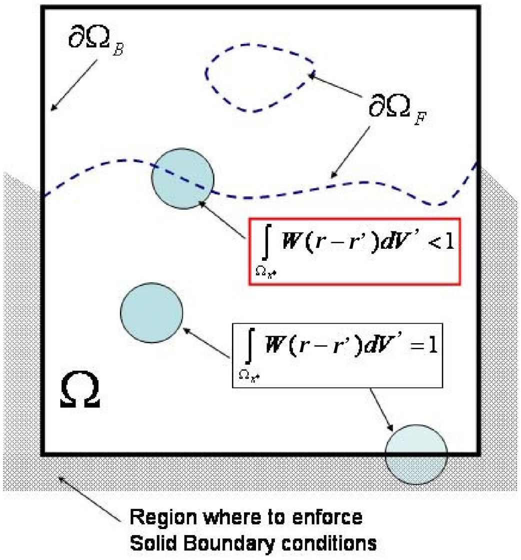

Figure 3.2.: Behaviour of $\Gamma(\mathbf{r})$ inside the fluid domain and near the boundaries.

is unitary. As $h \to 0$, the kernel function W becomes a Dirac delta function, and, $\langle f \rangle$ turns out exactly f. In continuous form, the smoothed representation of $\langle f \rangle$ leads to an error

$$\langle f \rangle = f + \mathcal{O}(h^2) \tag{3.15}$$

inside the domain Ω (see Mas-Gallic and Raviart 1987) [1]. Moreover, it must be noted that the relation (3.15) is not true if $\mathbf{r} \in \partial\Omega_F$. In this case it becomes

$$\langle f \rangle = f \lim_{h \to 0} \Gamma + \mathcal{O}(h) \tag{3.16}$$

and $\lim_{h \to 0} \Gamma < 1$ (see, for example, sketch 3.2). If $\partial\Omega_F$ is a regular curve, $\Gamma \to 1/2$ as h goes to zero and (3.16) becomes

$$\langle f \rangle = f/2 + \mathcal{O}(h) \tag{3.17}$$

However, the convergence is recovered if the field f is null along the free surface.

The same interpolation can be applied to the gradient of a generic function

$$\langle \nabla f \rangle(\mathbf{r}) = \int_{\Omega} \nabla' f(\mathbf{r}')\, W(\mathbf{r} - \mathbf{r}')\, dV' \tag{3.18}$$

where ∇' means that the derivatives are computed on the $\mathbf{r}'$ variable. Integrating by parts, it becomes

$$\langle \nabla f \rangle(\mathbf{r}) = \int_{\Omega} f(\mathbf{r}')\, \nabla W(\mathbf{r} - \mathbf{r}')\, dV' + \int_{\partial\Omega} f(\mathbf{r}')\, W(\mathbf{r} - \mathbf{r}')\, \mathbf{n}'\, dS' \tag{3.19}$$

---

[1] However, after discretization the convergence obtained does not remain as favorable (Quinlan et al. 2006)

where $\mathbf{n}'$ is a unitary vector normal to $\partial\Omega$, pointing outside Ω, and ∇ stands for the gradients with respect to the variable $\mathbf{r}$. In the latter equation, the symmetry property of the kernel $\nabla' W(\mathbf{r}-\mathbf{r}') = -\nabla W(\mathbf{r}-\mathbf{r}')$ has been used. Equation (3.19) shows how the gradient of a generic function is obtained using the knowledge of the function values itself and the gradient of the kernel function. This last aspect is a key feature of SPH methods.

3.2.2 Surface integrals

To further stress the convergence properties of the smoothed gradient, let us consider the following identity

$$\nabla\Gamma \equiv \int_{\Omega} \nabla W(\mathbf{r}-\mathbf{r}')\, dV' = -\int_{\partial\Omega} W(\mathbf{r}-\mathbf{r}')\, \mathbf{n}'\, dS' . \tag{3.20}$$

Inside the fluid domain the contour integral is null since W is identically zero along $\partial\Omega$ and, therefore, $\nabla\Gamma = 0$ as well. Conversely, on the free surface, the contour integral is different from zero and $\nabla\Gamma \neq 0$. For the same reasons, inside the fluid domain the last integral of (3.19) is identically zero and

$$\langle \nabla f \rangle(\mathbf{r}) = \int_{\Omega} f(\mathbf{r}')\, \nabla W(\mathbf{r}-\mathbf{r}')\, dV' \tag{3.21}$$

Such a formula is often used in the SPH solvers to approximate the gradient of functions. However, it provides just a poor approximation close to free surfaces.

3.3 REGULARIZED VERSION OF THE GOVERNING EQUATIONS

This section is dedicated to the approximation of the governing equation introduced in section 3.1 through the integral interpolation described in the previous section. Introducing the smoothed differential operator in the system of equation (3.1) the new set of equation:

$$\begin{cases} \dfrac{D\rho}{Dt} + \rho\, \langle \mathrm{div}(\mathbf{u}) \rangle = 0 , \\[2ex] \dfrac{D\mathbf{u}}{Dt} = \mathbf{g} - \dfrac{\langle \nabla p \rangle}{\rho} + \dfrac{\langle \nabla \cdot \mathbb{V} \rangle}{\rho} , \\[2ex] \dfrac{De}{Dt} = -\dfrac{p}{\rho} \langle \mathrm{div}(\mathbf{u}) \rangle + \langle \mathbb{V} : \mathbb{D} \rangle - \langle \mathrm{div}(\mathbf{q}) \rangle \\[2ex] p = p(\rho, e) \end{cases} \tag{3.22}$$

is obtained. To preserve global conservation properties, this system must be suitably modified because the formulae (3.19) and (3.21) cannot be used to approximate the differential operator. This aspect is described in the following.

3.3.1 Considerations on $\langle \nabla p \rangle$ and $\langle \mathrm{div}\, \mathbf{u} \rangle$ in the presence of a free surface

For gravity flows, the pressure field is generally almost linear close to the free surface. In such conditions, the interpolation (3.18) of ∇p close to the free surface is a rough approximation, as previously discussed in section 3.2.1, and does not converge to the expected value as h goes to zero. Indeed, let us assume p to be exactly a linear field. As a consequence, we get $\nabla p = C_0$ (where C_0 is a constant different from zero). Substituting it inside (3.18), we obtain

$$\langle \nabla p \rangle = C_0 \, \Gamma \tag{3.23}$$

It thus does not converge to the exact value near the free surface (it gives half of the theoretical value on a flat free surface). Since (3.18) converges to a wrong value, (3.19) and (3.21) will do the same.

As for the divergence of the velocity field, the boundary condition (3.10) forces it to be exactly zero along the free surface. Then, $\langle \mathrm{div}(\mathbf{u}) \rangle$ converges to the exact value as h goes to zero. After applying the integration by parts, equation (3.18) becomes:

$$\langle \mathrm{div} \mathbf{u} \rangle (\mathbf{r}) = \int_{\Omega} \mathbf{u}(\mathbf{r}') \cdot \nabla W(\mathbf{r} - \mathbf{r}')\, dV' + \int_{\partial\Omega} \mathbf{u}(\mathbf{r}') \cdot \mathbf{n}' W(\mathbf{r} - \mathbf{r}')\, dS' \tag{3.24}$$

In the latter equation, the surface term generally has the same order of magnitude of the volume term and, therefore, it is not possible to neglect it. Indeed, despite (3.24) converges, the surface and volume integral are both divergent as $\mathcal{O}(1/h)$ (see Colagrossi et al. 2009*b*).

A way to impose the $\mathcal{O}(h)$ convergence of both the integral terms of equation (3.24) is to subtract the following term:

$$\mathbf{u}(\mathbf{r}) \cdot \left[\int_{\Omega} \nabla W(\mathbf{r} - \mathbf{r}') dV' + \left(\int_{\partial\Omega} W(\mathbf{r} - \mathbf{r}') \mathbf{n}' dS' \right) \right] \tag{3.25}$$

where the sum in brackets is null by definition, obtaining:

$$\begin{aligned} \langle \mathrm{div} \mathbf{u} \rangle (\mathbf{r}) = & \int_{\Omega} [\mathbf{u}(\mathbf{r}') - \mathbf{u}(\mathbf{r})] \cdot \nabla W(\mathbf{r} - \mathbf{r}')\, dV' + \\ & + \int_{\partial\Omega} [\mathbf{u}(\mathbf{r}') - \mathbf{u}(\mathbf{r})] \cdot \mathbf{n}' W(\mathbf{r} - \mathbf{r}') dS' \quad . \end{aligned} \tag{3.26}$$

This expression permits to neglect the surface integral without affecting the convergence of the divergence operator but decreasing its accuracy (see Colagrossi et al. 2009*b*):

$$\langle \mathrm{div}\mathbf{u}\rangle^{B}(\mathbf{r}) = \int_{\Omega} [\mathbf{u}(\mathbf{r}') - \mathbf{u}(\mathbf{r})] \cdot \nabla W(\mathbf{r} - \mathbf{r}')\, dV'. \tag{3.27}$$

Usually the surface integral is neglected, assuming that is $\mathcal{O}(h)$. This is helpful because of the great difficulties in the evaluation of surface integral, which requires the explicit identification of the free surface.

The analysis of the smoothed version of the differential operators close to the free surface points out a consistent approximation of the continuity equation, which still holds if the surface term is neglected. As opposite, for the pressure gradient approximation no convergence is obtained on the free surface when using formula (3.19). In the following, a consistent formulation, in integral sense, is derived applying the Principle of Virtual Work.

3.3.2 SPH conservation properties through the Principle of Virtual Work

The present section deals with the conservation properties (energy and momenta) of the SPH fluid equations. At the *continuum*, the Principle of Virtual Work (PVW) is rewritten including the external work part (see Colagrossi et al. 2009*b*, for more details). Using such a formulation, it is possible to discuss about:

- the way in which the dynamic boundary condition is enforced on the free surface in the SPH formulation,
- how it is possible to choose a formulation for $\langle \nabla p\rangle$ starting on the specific form used for $\langle \mathrm{div}\mathbf{u}\rangle$
- the role of the mechanical work associated to the surface terms in (3.26).

The Principle of Virtual Works (PVW) expresses the equality between the work of the internal forces δW_I and the one of the external forces δW_E due to the virtual displacement field $\delta \boldsymbol{w}$. In its general form, it reads (see e.g. Glowinski and Le Tallec 1989; Marsden and Hughes 1994)

$$\underbrace{\int_{\partial\Omega} \mathbb{T}\boldsymbol{n} \cdot \delta\boldsymbol{w}\, dS - \int_{\Omega} \rho\mathbf{F} \cdot \delta\boldsymbol{w}\, dV}_{\delta W_E} = \underbrace{\int_{\Omega} \mathbb{T} : \mathbb{D}(\delta\boldsymbol{w})\, dV}_{\delta W_I} \tag{3.28}$$

where $\mathbb{T}$ is the stress tensor, $\rho\mathbf{F}$ are the volume forces (including the inertial ones). Neglecting the viscous term, which will be discussed in the next paragraph, the PVW can be written as

$$\underbrace{\int_{\partial\Omega}(-p)\mathbf{n}\cdot\delta\boldsymbol{w}\,dS}_{①}-\underbrace{\int_{\Omega}(-\nabla p)\cdot\delta\boldsymbol{w}\,dV}_{②}=\underbrace{\int_{\Omega}-p\,\mathrm{div}(\delta\boldsymbol{w})\,dV}_{③} \tag{3.29}$$

Even though the latter expression is a simple application of the divergence theorem, it expresses the PVW which has an important physical meaning. Indeed, the two terms ① and ② represent the work of the stress tensor respectively on the free surface and in the fluid domain. Their difference equals the variation of the internal energy ③ due to the virtual displacement field. The balance of the three integral terms guarantees the conservation of both the linear and angular momenta (Bonet and Lok 1999).

Considering zero the solid boundaries displacement, as $p = 0$ along $\partial\Omega_F$, the expression (3.29) becomes

$$-\int_{\Omega}(-\nabla p)\cdot\delta\boldsymbol{w}\,dV = \int_{\Omega}-p\,\mathrm{div}(\delta\boldsymbol{w})\,dV \tag{3.30}$$

Such a formula states that the work of the stress tensor inside the fluid domain must be equal to the variation of the internal energy while the work of the stress tensor along the surface is zero.

Thus, to satisfy the dynamic boundary condition in a weak sense, it is sufficient to verify the equality (3.30) using the smoothed operators instead of the ordinary ones. In that case, no other specific condition has to be explicitly enforced onto that surface. This worthwhile feature is commonly used in SPH. However, this does not imply the local consistency of the smoothed operators chosen for the pressure gradient as detailed in the following.

Using the same form of equation (3.27) for $\delta\boldsymbol{w}$:

$$\langle\mathrm{div}(\delta\boldsymbol{w})\rangle^B(\mathbf{r}) = \int_{\Omega}[\delta\boldsymbol{w}(\mathbf{r}')-\delta\boldsymbol{w}(\mathbf{r})]\cdot\nabla W(\mathbf{r}-\mathbf{r}')\,dV' \tag{3.31}$$

Substituting this expression inside (3.30), and manipulating it (see Colagrossi et al. 2009*b*), it is possible to write:

$$-\int_{\Omega}(-\langle\nabla p\rangle^B)\cdot\delta\boldsymbol{w}\,dV = \int_{\Omega}-p\,\langle\mathrm{div}(\delta\boldsymbol{w})\rangle^B\,dV\,, \tag{3.32}$$

where

$$\langle\nabla p\rangle^B(\mathbf{r}) = \int_{\Omega}p(\mathbf{r}')\,\nabla W(\mathbf{r}-\mathbf{r}')\,dV' + p(\mathbf{r})\int_{\Omega}\nabla W(\mathbf{r}-\mathbf{r}')\,dV'\,, \tag{3.33}$$

which is the continuous version of the pressure gradient formulation proposed by Bonet and Lok (1999) using the PVW after discretization. No surface integral appears in (3.32), it is simple to show that $\langle\nabla p\rangle^B$ behaves as $\langle\nabla p\rangle$ for h

going to zero. Indeed, if $\mathbf{r} \notin \partial\Omega_F$, there exists a value of h such that $\Omega(\mathbf{r}') \subset \Omega$ and, therefore $\nabla\Gamma(\mathbf{r}) = 0$ and the second term of the right-hand side of (3.33) is zero. Finally, if $\mathbf{r} \in \partial\Omega_F$, $p(\mathbf{r}) = 0$ and, again, the second term of the right-hand side of (3.33) is identically zero. In this way it is possible to recover:

$$\langle \nabla p \rangle^B = \nabla p \lim_{h \to 0} \Gamma + \mathcal{O}(h) \,. \tag{3.34}$$

3.3.3 Smoothed viscous term

In SPH-related literature several formulations have been proposed to model the smoothed viscous term. In this section we focus on two of the most used formulations, namely: *i)* the one by Monaghan and Gingold (1983), *ii)* the one by Morris et al. (1997).

Assuming that the viscosity coefficients are constant all over the fluid domain, the continuous Monaghan & Gingold formulation (hereinafter MGF) of the viscous term is:

$$\langle \nabla \cdot \mathbb{V} \rangle^{MG}(\mathbf{r}) = \mu K \int_\Omega \frac{\left[\mathbf{u}(\mathbf{r}') - \mathbf{u}(\mathbf{r})\right] \cdot (\mathbf{r}' - \mathbf{r})}{|\mathbf{r}' - \mathbf{r}|^2} \nabla W(\mathbf{r}' - \mathbf{r}) \, dV' \,, \tag{3.35}$$

where K is a parameter depending on the spatial dimension ($K = 6, 8, 10$, respectively in 1D, 2D and 3D). Using the Taylor expansion of the velocity field:

$$\mathbf{u}' - \mathbf{u} = \nabla \mathbf{u}\Big|_{\mathbf{r}} \cdot \mathbf{r}' + \frac{1}{2} \mathbf{r}' \cdot \mathbb{H}\Big|_{\mathbf{r}} \cdot \mathbf{r}' + \mathcal{O}(|\mathbf{r}'|^3) \,, \tag{3.36}$$

in equation (3.35), Español and Revenga (2003) showed that inside the domain this formulation is consistent as:

$$\lim_{h \to 0} \langle \nabla \cdot \mathbb{V} \rangle^{MG} = \mu \nabla^2 \mathbf{u} + 2\mu \nabla(\mathrm{div}(\mathbf{u})) \,. \tag{3.37}$$

Note that expression (3.37) is consistent with the continuous viscous stress definition (3.5) only if $\lambda = \mu$. This means that the MGF does not satisfy the Stokes hypothesis ($\lambda = -2\mu/3$). The consequences of this fact have not received much attention in the literature.

The second classical expression of the viscous term considered in the literature is the formulation by Morris et al. (1997), hereinafter indicated as MEAF. Its continuous expression reads as:

$$\langle \nabla \cdot \mathbb{V} \rangle^{MEA}(\mathbf{r}) = 2\mu \int_\Omega \frac{(\mathbf{r}' - \mathbf{r}) \cdot \nabla W(\mathbf{r}' - \mathbf{r})}{|\mathbf{r}' - \mathbf{r}|^2} \left[\mathbf{u}(\mathbf{r}') - \mathbf{u}(\mathbf{r})\right] dV' \,. \tag{3.38}$$

In the same way as for the MGF, the use of the Taylor expansion (3.36), leads to:

$$\lim_{h \to 0} \langle \nabla \cdot \mathbb{V} \rangle^{MEA} = \mu \nabla^2 \mathbf{u} \,. \tag{3.39}$$

This means that, inside the domain, the MEAF approximates the exact viscous term for incompressible flows while the MGF also takes into account the weak-compressibility effects, but not respecting the Stokes hypothesis.

At this stage it has been established that both MGF and MEAF are consistent inside the domain. Conversely, due to the incompleteness of the kernel support, at the free surface, these formulations are locally not consistent and both diverge linearly with h (see for details Colagrossi et al. 2011).

However, similarly to the smoothed pressure gradient (3.33), this does not mine the global consistency of these formulations. That can be checked evaluating the dissipation introduced by the smoothed viscous terms. It is represented by the following integral:

$$\int_{\Omega} \langle \nabla \cdot \mathbb{V} \rangle \cdot \mathbf{u} \, dV \,. \tag{3.40}$$

From a theoretical point of view, the expression (3.40) can be integrated by parts to give a boundary term which is associated to the power of the surface forces and a bulk term which, for the second principle of thermodynamics, is never negative and, therefore, causes the loss of energy of the fluid body (see equation 3.28). If one considers a free-surface flow with no other boundary the following expressions can be derived (see Colagrossi et al. 2011, for more details):

$$\int_{\Omega} \langle \nabla \cdot \mathbb{V} \rangle^{MG} \cdot \mathbf{u} \, dV \;=\; -\int_{\Omega} \mathbb{V} : \mathbb{D} \, dV + \mathcal{O}(h) \,, \tag{3.41}$$

$$\int_{\Omega} \langle \nabla \cdot \mathbb{V} \rangle^{MEA} \cdot \mathbf{u} \, dV \;=\; -\mu \int_{\Omega} \|\nabla \mathbf{u}\|^2 \, dV + \mathcal{O}(h) \,. \tag{3.42}$$

From this result different interesting conclusions can be drawn. First, both the integrals for the MGF and the MEAF are convergent, despite the local singularity of these formulations at the free surface. Second, as shown by (3.42), the dissipation associated to the MEAF is different from zero even in the case of a pure rigid rotation (that is, $\mathbb{D} \equiv 0$) where there should be no dissipation at all. Last, by choosing $\mathbf{u}$ as virtual displacement field into (3.41), the MGF satisfies the Principle of Virtual Works (3.28) with an error of order $\mathcal{O}(h)$.

Summarizing, despite their local inconsistency at the free surface, MGF is theoretically globally consistent for free-surface flows. Conversely, the MEAF is globally convergent but not to the proper viscous dissipation and is likely to be discarded for free-surface flows.

3.3.4 Smoothed heat conduction term

To complete the equations (3.22) an expression for the term $\langle \mathrm{div}\,\mathbf{q} \rangle$ need to be derived. The divergence of the heat flux can be linked to the laplacian of the internal energy using the Fourier law:

$$\mathbf{q} = -\sigma \nabla e \tag{3.43}$$

where σ is a thermal conductivity coefficient. Therefore

$$\mathrm{div}\,\mathbf{q} = -\sigma \nabla^2 e$$

since spatial variation of σ are neglected for the problems of interest in this thesis. The smoothed approximation of a laplacian can be derived rewriting equation (3.38) for a scalar field:

$$\langle \mathrm{div}\,\mathbf{q} \rangle^{MEA} = -2\,\sigma \int_\Omega \frac{(\mathbf{r}'-\mathbf{r})\cdot\nabla W(\mathbf{r}'-\mathbf{r})}{|\mathbf{r}'-\mathbf{r}|^2}\left[e(\mathbf{r}')-e(\mathbf{r})\right] dV' \,. \tag{3.44}$$

3.3.5 SPH Regularized version of the governing equation

Finally, after the discussion provided in previous sections, we can rewrite the SPH regularized Navier-Stokes equations (3.22) as:

$$\begin{cases} \dfrac{D\rho}{Dt} & = & -\rho \displaystyle\int_\Omega [\mathbf{u}(\mathbf{r}')-\mathbf{u}(\mathbf{r})]\cdot\nabla W\, dV' \\[2ex] \dfrac{D\mathbf{u}}{Dt} & = & \mathbf{g} - \dfrac{1}{\rho}\displaystyle\int_\Omega \left[p(\mathbf{r}')+p(\mathbf{r})\right]\nabla W\, dV' + K\dfrac{\mu}{\rho}\displaystyle\int_\Omega \pi(\mathbf{r}',\mathbf{r})\,\nabla W\, dV' \\[2ex] \dfrac{De}{Dt} & = & -\dfrac{p}{\rho}\displaystyle\int_\Omega [\mathbf{u}(\mathbf{r}')-\mathbf{u}(\mathbf{r})]\cdot\nabla W\, dV' + \dfrac{\sigma}{\rho}\displaystyle\int_\Omega \boldsymbol{\phi}(\mathbf{r}',\mathbf{r})\cdot\nabla W\, dV' + \\[2ex] & & +\dfrac{1}{2}K\dfrac{\mu}{\rho}\displaystyle\int_\Omega \pi(\mathbf{r}',\mathbf{r})\,\nabla W\cdot[\mathbf{u}(\mathbf{r}')-\mathbf{u}(\mathbf{r})]dV' + \\[2ex] p & = & p(\rho, e) \end{cases} \tag{3.45}$$

where the two fields $\pi(\mathbf{r}',\mathbf{r})$ and $\boldsymbol{\phi}(\mathbf{r}',\mathbf{r})$ are respectively equal to:

$$\pi(\mathbf{r}',\mathbf{r}) = \frac{\left[\mathbf{u}(\mathbf{r}')-\mathbf{u}(\mathbf{r})\right]\cdot(\mathbf{r}'-\mathbf{r})}{|\mathbf{r}'-\mathbf{r}|^2}\,, \qquad \boldsymbol{\phi}(\mathbf{r}',\mathbf{r}) = 2\left[e(\mathbf{r}')-e(\mathbf{r})\right]\frac{(\mathbf{r}'-\mathbf{r})}{|\mathbf{r}'-\mathbf{r}|^2}$$

and the integral interpolation formulae $\langle \mathrm{div}(\mathbf{u}) \rangle^B$ (3.27), $\langle \nabla p \rangle^B$ (3.33), $\langle \nabla\cdot\mathbb{V} \rangle^{MG}$ (3.35) and $\langle \mathrm{div}\,\mathbf{q} \rangle^{MEA}$ (3.44) have been used. Inside the fluid domain Ω, these regularized PDEs are consistent for $h \to 0$ to the original governing equations

(3.1). However, the demonstration that the solution of the regularized PDEs (3.45) converges to the solution of the governing equation (3.1) is not trivial. An in-depth analysis regarding convergence of regularized equations has been given by Di Lisio et al. (1997) for inviscid compressible flows in unbounded domain.

Even if the momentum equation is affected by local singularities close to the free surface, this local inconsistency does not prejudge the global consistency. Indeed, using equations (3.32) and (3.41) the approximation of the mechanical energy of the system can be written as:

$$\begin{aligned} \langle \frac{D\mathcal{E}_M}{Dt} \rangle &= \int_\Omega \big(-\langle \nabla p \rangle^B + \langle \nabla \cdot \mathbb{V} \rangle^{MG} \big) \cdot \mathbf{u} \, dV = \\ &= \int_\Omega p \, \langle \mathrm{div}(\mathbf{u}) \rangle^B \, dV + \int_\Omega \langle \nabla \cdot \mathbb{V} \rangle^{MG} \cdot \mathbf{u} \, dV \end{aligned} \tag{3.46}$$

that is consistent in the limit $h \to 0$:

$$\langle \frac{D\mathcal{E}_M}{Dt} \rangle = -\int_\Omega \mathbb{T} : \mathbb{D} \, dV + \mu \, \mathcal{O}(h) \tag{3.47}$$

Further, the previous results implies also that:

$$\int_{\partial\Omega} (-p \, \mathbf{n} + \mathbb{V}\mathbf{n}) \cdot \mathbf{u} \, dS = \mu \, \mathcal{O}(h) \tag{3.48}$$

and therefore for liquid like water this surface integral is practically zero even with finite value of h. If $\partial\Omega$ is a free surface the latter result implies that the dynamic boundary condition (3.6) is satisfied in an integral sense.

3.4 CHOICE OF THE STATE EQUATION IN THE WEAKLY COMPRESSIBLE MODEL

In this paragraph the choice of the state equation for liquid phase in the SPH model is discussed. As already explained in section 3.1 the liquids are modelled as weakly compressible media, and generally the Tait equation (see Monaghan 1994) is used :

$$p = B \left[\left(\frac{\rho}{\rho_0} \right)^\gamma - 1 \right]. \tag{3.49}$$

ρ_0 is the density at the free surface where $p = 0$ as requested by the pressure condition (3.9). B is linked to the speed of sound of the media (further details are given in the following) and γ is a constant set equal to 7. In (3.49) the pressure is not influenced by the specific entropy S but only by the density fluctuations. It is well known that S has a large influence on the pressure field for gaseous phases while it is generally negligible for liquids (at least for pressure regime less than 1 GPa) (Fey and Jeltsch 1999).

The speed of sound is defined as:

$$c^2 = \left.\frac{\partial p}{\partial \rho}\right|_{S=cost}, \tag{3.50}$$

It follows from the Tait equation that the variations of the speed of sound are given by:

$$c^2 = c_0^2 \left(\frac{\rho}{\rho_0}\right)^{\gamma-1}; \qquad c_0^2 = \frac{B\gamma}{\rho_0} \tag{3.51}$$

Therefore c is subjected to a polytropic law.

In the SPH simulations the speed of sound at rest c_0 (i.e. for $\rho = \rho_0$) is fixed at the beginning of the simulations under the constrain:

$$c_0 \geqslant 10 \max_t(\|\mathbf{u}\|), \qquad Ma := \max_t(\|\mathbf{u}\|)/c_0 \leqslant 0.1 \tag{3.52}$$

where $\max_t(\|u\|)$ is the maximum intensity of the velocity expected in the flow time evolution, and Ma is the Mach number defined with such a velocity. Under this constrain it is possible to consider the media as weakly compressible since the condition (3.52) implies a variation of the density field $\Delta\rho/\rho_0 \sim 1\%$, being the density fluctuations proportional to Ma^2 (see Monaghan 1994). For the problems treated in this thesis, c_0 is generally chosen two order of magnitude less than the real one (e.g. for water $c_0 \simeq 1500$ m/s). This is mainly due to numerical reason since large values of c_0 imply very small integration time steps (see section 4.2).

Note that in the presence of gravity waves the wave celerity can be larger than the flow velocity and may represent a more restrictive constrain for the choice of the speed of sound (see, for example Madsen and Shäffer 2006). The wave celerity is defined as $c_w^2 = g\tanh(kH)/k$ where H is the still water depth, k is the wave number and g the gravity acceleration. For kH going to zero, the shallow water regime is approached and the relation above becomes $c_w^2 = gH$. Since the latter expression is an upper bound for the wave celerity, a conservative choice is $c_0 = 10\sqrt{gH}$. Then, the condition (3.52) finally takes the form:

$$c_0 \geqslant 10\,\mathrm{Max}(\sqrt{gH}, \max_t(\|\mathbf{u}\|)). \tag{3.53}$$

Another form of the state equation can be derived linearising the Tait equation by neglecting the higher order terms in $\Delta\rho/\rho_0$:

$$\begin{aligned} p = B\left[\left(\frac{\rho_0 + \Delta\rho}{\rho_0}\right)^{\gamma} - 1\right] = B\left\{1 + \gamma\frac{\Delta\rho}{\rho_0} + \mathcal{O}\left[\left(\frac{\Delta\rho}{\rho_0}\right)^2\right] - 1\right\} \simeq \\ \simeq B\gamma\frac{\Delta\rho}{\rho_0} = c_0^2(\rho - \rho_0) \end{aligned} \tag{3.54}$$

Similarly, linearising (3.51) for the speed of sound c one gets:

$$c^2 = c_0^2\left(\frac{\rho}{\rho_0}\right)^{\gamma-1} = c_0^2\left(\frac{\rho_0+\Delta\rho}{\rho_0}\right)^{\gamma-1} = c_0^2\left[1+(\gamma-1)\frac{\Delta\rho}{\rho_0}+\mathcal{O}\left[\left(\frac{\Delta\rho}{\rho_0}\right)^2\right]\right];$$

$$c \simeq c_0 + \frac{(\gamma-1)}{2}\frac{\Delta\rho}{\rho_0} \tag{3.55}$$

One can observe that the parameter γ does not affect the pressure field while induces small perturbation on the speed of sound through fluctuations of the density field. Therefore, under the weakly compressible assumption, the equation (3.54) can be adopted instead of (3.49) and the speed of sound can be considered constant, $c = c_0$, since the small variation given by (3.55) are in practice negligible. These two choices for the evolution of the pressure and the speed of sound give remarkable benefits in term of reduction of the CPU time costs.

Regarding the internal energy e, it can be derived from the first law of thermodynamics under the isentropic hypothesis:

$$\frac{d\,e}{d\,\rho} = \frac{p}{\rho^2} \tag{3.56}$$

substituting the Tait equation and integrating (3.56) the internal energy e is:

$$e(\rho) = \frac{c^2}{\gamma(\gamma-1)} + \frac{B}{\rho} + \text{const} \qquad \forall\gamma \neq 1 \tag{3.57}$$

Introducing (3.57) in (3.51) and (3.49) the pressure field can be linked to the internal energy as:

$$p = \rho(\gamma-1)e(\rho) - B\gamma \tag{3.58}$$

If one reintroduces the dependency on the entropy S, the relation known in literature as *Stiffned equation of state* is obtained:

$$p = \rho(\gamma-1)e(\rho, S) - B\gamma. \tag{3.59}$$

This equation is adopted in the literature also for modelling liquids (Fey and Jeltsch 1999).

The two state equations (3.49),(3.59) in practice give very similar results even tough in the second equation the internal energy e is evaluated through the energy equation and contributes to the evaluation of p (energy and momentum equations are not decoupled as in the case for barotropic fluid). This means that the viscous effects in e (i.e. the effects of the entropy S) does not influence significantly the pressure field even if the speed of sound c_0 chosen for the SPH simulations is quite low respect to the real one.

When simulating problems with violent fluid motion it is possible to record large decay of the mechanical energy which are linked to large increases of e due to the small value of the speed of sound. In order to obtain a more stable and accurate numerical scheme it can be useful to artificially link the variation of internal energy e to the speed of sound. In this way during impact stage the speed of sound grows according to the increase of e leading to a reduction of the time steps to solve this critical regime with an higher time resolution.

Considering a general state equation $p = F(\rho, e)$ and using a Taylor expansion in the neighborhood of the reference state $Q_0 = (\rho_0, e_0)$, we get:

$$\begin{aligned} p \;=\; & F(\rho_0, e_0) + \left.\frac{\partial p}{\partial \rho}\right|_{Q_0} (\rho - \rho_0) + \left.\frac{\partial p}{\partial e}\right|_{Q_0} (e - e_0) + \frac{1}{2}\left.\frac{\partial^2 p}{\partial \rho^2}\right|_{Q_0} (\rho - \rho_0)^2 + \\ & + \left.\frac{\partial^2 p}{\partial \rho \partial e}\right|_{Q_0} (\rho - \rho_0)(e - e_0) + \frac{1}{2}\left.\frac{\partial^2 p}{\partial e^2}\right|_{Q_0} (e - e_0)^2 + \dots \, . \end{aligned} \tag{3.60}$$

The expression (3.60) provides a general formula which takes into account the main contributions coming from the variation of both the density and the specific internal energy. The values of the derivatives depend on the structure of $F(\rho, e)$. In the specific, if we consider the following state equation:

$$p = c^2(e)\,(\rho - \rho_0) \qquad \text{where} \quad c^2(e) = \left.\frac{\partial p}{\partial \rho}\right|_{\rho_0}, \tag{3.61}$$

the second-order Taylor expansion gives:

$$p \;=\; \left[c_0^2 + \left.\frac{\partial^2 p}{\partial \rho \partial e}\right|_{Q_0} (e - e_0) + \dots \right] (\rho - \rho_0) \quad \text{where} \quad c_0 = c(e_0)\,. \tag{3.62}$$

Finally denoting by $c_0^2\,\Xi / e_0$ the second order derivative, we get:

$$p = c_0^2 \left[1 + \Xi \left(\frac{e}{e_0} - 1 \right) \right] (\rho - \rho_0)\,. \tag{3.63}$$

Note that in this case, the influence of the specific internal energy variation is limited at the second order. The sound velocity is:

$$c(e) \;=\; \sqrt{\left.\frac{\partial p}{\partial \rho}\right|_{\rho_0}} \;=\; c_0 \sqrt{1 + \Xi \left(\frac{e}{e_0} - 1 \right)}, \tag{3.64}$$

and clearly depends on both the density and the internal energy. Finally, choosing $\Xi > 0$, the sound velocity increases when the thermal energy increases. The parameter Ξ is order of $\mathcal{O}(10^2)$ and for its tuning the reader is referred to Antuono et al. (2010).

4 SPH EQUATIONS FOR SOLVING FREE-SURFACE FLOWS

4.1 SPH EQUATIONS FOR VISCOUS FLOWS

In this chapter the regularized Navier Stokes equations (3.45) derived in chapter 3 are used to write the SPH equations. Discretizing the convolution integrals of (3.45), i.e. substituting integrals by summations, the ODEs for the particle time evolution are expressed as:

$$\begin{cases} \dfrac{D\rho_i}{Dt} = -\rho_i \sum_j (\mathbf{u}_j - \mathbf{u}_i) \cdot \nabla_i W_{ij}\, V_j \\[2ex] \dfrac{D\mathbf{u}_i}{Dt} = \mathbf{g} - \dfrac{1}{\rho_i} \sum_j (p_j + p_i)\, \nabla_i W_{ij}\, V_j \; + K \dfrac{\mu}{\rho_i} \sum_j \pi_{ij} \nabla_i W_{ij}\, V_j \\[2ex] \dfrac{De_i}{Dt} = -\dfrac{p_i}{\rho_i} \sum_j (\mathbf{u}_j - \mathbf{u}_i) \cdot \nabla_i W_{ij}\, V_j + \dfrac{\sigma}{\rho_i} \sum_j \boldsymbol{\phi}_{ij} \cdot \nabla_i W_{ij}\, V_j \\[1ex] \qquad\quad + \dfrac{K}{2} \dfrac{\mu}{\rho_i} \sum_j \pi_{ij}\, \nabla_i W_{ij} \cdot (\mathbf{u}_j - \mathbf{u}_i)\, V_j \\[2ex] \dfrac{D\mathbf{r}_i}{Dt} = \mathbf{u}_i\,; \qquad p_i = p(\rho_i\,, e_i) \end{cases} \tag{4.1}$$

where the term π_{ij} and $\boldsymbol{\phi}_{ij}$ are respectively:

$$\pi_{ij} = \frac{(\mathbf{u}_j - \mathbf{u}_i) \cdot (\mathbf{r}_j - \mathbf{r}_i)}{|\mathbf{r}_j - \mathbf{r}_i|^2}\,, \qquad \boldsymbol{\phi}_{ij} = 2\,(e_j - e_i)\, \frac{(\mathbf{r}_j - \mathbf{r}_i)}{|\mathbf{r}_j - \mathbf{r}_i|^2}. \tag{4.2}$$

$K = 2(d+2)$ is a parameter depending on the spatial dimension d. V_i represents the volume associated with the i-th particle and, similarly, it is possible to define a mass m_i associated with the generic particle through the product $m_i = \rho_i V_i$. Different SPH equations can be derived if a different link between ρ, V and m is used, as discussed in section 4.4. It is important to remind that in this thesis only formulations with a constant smoothing length are considered. The system of equations (4.1) governs the dynamics of the whole system of particles and is characterized by some valuable properties (which are easy to prove, see e.g. Bonet and Lok 1999, Colagrossi 2005):

I) the equations are invariant for Galilean transformation.

II) If the mass of the particles, m_i, at the beginning of the simulation are set equal to $m_i = V_i \rho_i$ and the volumes $V_i(t)$ are evaluated during the time evolution through the ratio

$$V_i(t) = m_i / \rho_i(t) \tag{4.3}$$

the global mass of the system $\mathcal{M} = \sum_i m_i$ is exactly conserved in time.

III) the linear momentum

$$\mathcal{Q} = \sum_i m_i \mathbf{u}_i \tag{4.4}$$

and the angular momentum

$$\mathcal{L} = \sum_i \mathbf{r}_i \times m_i \mathbf{u}_i \tag{4.5}$$

of the particles system are conserved in time when no external forces are present.

IV) The total energy of the system defined as

$$\mathcal{E}_{TOT} = \sum_i m_i e_i + \frac{1}{2} \sum_i m_i \mathbf{u}_i^2 + \sum_i \mathcal{V}_i , \tag{4.6}$$

(where $\mathcal{V}_i$ is the potential of the body forces evaluated on the i-th particle) is also exactly conserved in time when heat fluxes on boundaries do not occur.

V) If neither external forces or viscous forces are present, the mechanical energy of the system

$$\mathcal{E}_M = \frac{1}{2} \sum_i m_i \mathbf{u}_i^2 + \sum_i \mathcal{V}_i \tag{4.7}$$

is preserved in time. This means that, if the domain boundary is a free surface, the boundary conditions (3.8) are implicitly enforced in a weak sense by the system (4.1).

All these conservation properties are a direct consequence of the smoothed differential operators derived in chapter 3. They characterize the SPH method respect to others numerical methods for which mass, momenta, and energy are only approximatively conserved.

However, the main drawback of the ODEs system (4.1) is that it is not even zero-th order consistent because of the pressure term. Indeed, even with a constant pressure field the formula:

$$\langle \nabla p \rangle_i^B = \sum_j (p_j + p_i) \nabla_i W_{ij} V_j \tag{4.8}$$

is not able to give a zero pressure gradient for an irregular particle configuration. Therefore the particles are subjected to a non-physical force field, the intensity of such field being linked to the gradient of the kernel:

$$\nabla \Gamma_i = \sum_j \nabla_i W_{ij} V_j \tag{4.9}$$

Nevertheless, if the particles lay on an almost regular lattice, that is, the mean inter-particle distance is almost constant, $\nabla \Gamma_i$ is very small and so is the error made in the evaluation of differential operators. Therefore, the position of the particles at the beginning of the simulation is an important aspect for the SPH scheme. Indeed, the particle positions should minimize the quantity $\nabla \Gamma_i$. In chapter 6 it is shown that, with a proper initialization of the particle positions, the SPH equations are able to maintain the hydrostatic solution in a tank of arbitrary geometry restoring first order consistency.

4.1.1 Simulating inviscid flows

In problems characterized by high values of the Reynolds number it can be convenient to solve Euler equations instead of the Navier-Stokes system. Neglecting the viscous terms in system (4.1) and using the state equation (3.63) a SPH version for solving the Euler equations is obtained:

$$\left\{\begin{aligned}
\frac{D\rho_i}{Dt} &= -\rho_i \sum_j (\mathbf{u}_j - \mathbf{u}_i) \cdot \nabla_i W_{ij} V_j \\
\frac{D\mathbf{u}_i}{Dt} &= \mathbf{g} - \frac{1}{\rho_i} \sum_j (p_j + p_i) \nabla_i W_{ij} V_j \\
\frac{De_i}{Dt} &= -\frac{p_i}{\rho_i} \sum_j (\mathbf{u}_j - \mathbf{u}_i) \cdot \nabla_i W_{ij} V_j + \frac{\sigma}{\rho_i} \sum_j \boldsymbol{\phi}_{ij} \cdot \nabla_i W_{ij} V_j \\
\frac{D\mathbf{r}_i}{Dt} &= \mathbf{u}_i\,; \qquad p = c_0^2 \left[1 + \Xi \left(\frac{e}{e_0} - 1\right)\right] (\rho - \rho_0)\,.
\end{aligned}\right. \tag{4.10}$$

The scheme 4.10 is centred in space due to the use of radial function for *W* and is solved in time using an explicit integration. Like Finite Difference Methods, these kinds of scheme are unstable and a common way to ensure the stability is to add a numerical viscosity (see e.g. Hirsch 1990). For this reason, in the SPH framework, an artificial viscosity term is generally added in the momentum equation. This term needs to be proportional to the smoothing length h, so that, when the spatial resolution increases (that is, h decreases), the action of the artificial viscosity becomes smaller and smaller and the consistency with the Euler equations is recovered.

In the SPH literature, different artificial viscous terms exist. In the present work, the artificial viscosity term, A_ν, is expressed through the formula derived by Monaghan and Gingold (1983):

$$A_\nu = \alpha\, h\, c_0 \sum_j \pi_{ij}\, \nabla_i W_{ij}\, V_j. \tag{4.11}$$

This formula is essentially equal to the discrete form of equation (3.35) used to solve viscous flow, the only change being the substitution of the real viscosity with an artificial one:

$$\mu = \rho_0 \frac{\alpha\, h\, c_0}{K} \tag{4.12}$$

The viscosity coefficient in (4.12) decreases linearly with the smoothing length h, allowing the SPH equations to be consistent with the Euler equations. Heuristically, for the problems treated in this thesis it is found that $\alpha > 0.01$ should be satisfied, otherwise strong numerical instabilities may occur (see e.g. Colagrossi and Landrini 2003). As a consequence, in most of the simulations studied, α is set equal to 0.02 when an inviscid fluid has been involved. The parameter α can be related to a small scales Reynolds number:

$$Re_h = \frac{\rho_0\, U\, h}{\mu} = K \frac{Ma}{\alpha} \simeq \frac{1}{\alpha} \tag{4.13}$$

where the last term is obtained using 4.12 and considering that the Mach number is $\mathcal{O}\,(10^{-1})$ while $K = \mathcal{O}(10)$.

Therefore the lower limit on α can be re-read in terms of Re_h:

$$\alpha > 0.01 \qquad \Rightarrow \qquad Re_h < 100 \tag{4.14}$$

In a similar way it is possible also to treat the thermal conductivity term as an artificial term useful only for numerical purposes (see chapter 5). Molteni et al. (2007) proposed $\sigma = \chi\, h\, c_0$, where the parameter χ is $\mathcal{O}(10^{-1})$. The artificial thermal conductivity goes to zero with h as the artificial viscosity. It is important to note that the artificial thermal conductivity term plays a minor role with respect to the other terms and it is just used to smooth the distribution of the speed of sound c_i and to smooth the internal energy field permitting it to reach the steady state e_0 when the fluid is still.

4.1.2 Numerical procedures to recover the SPH zero-th order consistency

Due to the inconsistency of SPH equations (4.1) the magnitude of the quantity $\max_i \nabla \Gamma_i$ has to be monitored during the simulation. This quantity strongly depends on the specific kernel adopted (see section 4.2). In fact, if the flow field leads to a disordered particle distribution the error on the pressure gradient can be quite large, compromising the convergence of the numerical scheme or inducing strong numerical instabilities. Generally this could happen in regions where high velocity gradients occur or when the so-called *Tensile instability* (see Swegle et al. 1995) is excited.

To overcome this problem, one possibility is to re-set periodically the particle positions on a regular lattice (see e.g. Børve et al. 2005; Chaniotis et al. 2002; Koumoutsakos 2005). This ”re-meshing” procedure is quite effective for problems that do not involve a free surface or interfaces between different media. Indeed, for the latter cases the periodic re-meshing can alter and diffuse those interfaces.

Conversely, Monaghan (2000) proposed to introduce a ”repulsive” force field in the momentum equation that forbid the particle clumping. However this kind of corrections can be too intense and induce non-physical pressure noise on the solution.

Introducing diffusive terms in the SPH equations can also alleviate the problems connected to particle disorder. In particular, some authors (see e.g. Ferrari et al. 2009; Moussa 2006) couple solutions of Riemann problems with the SPH smoothing operator in order to handle density, velocity, pressure and internal energy discontinuities between particles. The main mechanism in such SPH variants is related to the exchange of mass between particles that permits to reduce the intensity of the velocity gradients. In the present thesis an original SPH variant, called δ-SPH, is derived in section 5 and largely validated in the following sections. In particular, numerical diffusive terms are introduced into the governing equations in order to improve the evaluation of the pressure field and to obtain a more regular particle distribution.

Following the idea to move particle with ”smoothed” velocity gradients, the so called XSPH correction was derived by Monaghan (1988). It consist in substituting the motion equation with:

$$\frac{D\mathbf{r}_i}{Dt} = \hat{\mathbf{u}}_i = \mathbf{u}_i + \Delta\mathbf{u}_i \tag{4.15}$$

where the term $\Delta\mathbf{u}_i$ takes into account the neighbour velocities through a mean velocity:

$$\frac{D\mathbf{r}_i}{Dt} = \mathbf{u}_i + \epsilon_X \sum_j (\mathbf{u}_j - \mathbf{u}_i)\, W_{ij}\, V_j \tag{4.16}$$

where ϵ_X is a coefficient that controls the intensity of the smoothing. Moving the particles with the new velocity does not change the total linear or angular momentum. However, if the particles are moving with the smoothed velocity, energy is not conserved.

Recently in Monaghan (2009) and Monaghan (2005*b*) the XSPH correction is linked to turbulence model and to preserve also energy a new version of the equation is presented:

$$\hat{\mathbf{u}}_i = \mathbf{u}_i + \epsilon_X \sum_j (\hat{\mathbf{u}}_j - \hat{\mathbf{u}}_i)\, W_{ij}\, V_j . \tag{4.17}$$

This new version is implicit in the corrected velocity $\hat{u}_i$ and therefore is not straightforward to implement.

In gas dynamic context the XSPH correction become quite relevant to proper solve strong shock wave and in particular to prevent particles inter-penetration Monaghan (1989). In any case, when simulating liquids this correction has a limited role and is neglected in the framework of this thesis.

4.1.3 Higher order pressure formulae

Following the works by Libersky, Belytshko and Dilts (see e.g Belytschko et al. 1998; Dilts 1999; Randles and Libersky 1996) different formulae for the pressure gradient have been proposed to achieve the higher order consistency. For example using the formula:

$$\langle \nabla p \rangle_i^D = \sum_j (p_j - p_i) \nabla_i W_{ij} V_j \tag{4.18}$$

when a constant pressure field is considered it gives exactly zero pressure gradient. Using the formula:

$$\langle \nabla p \rangle_i^L = \sum_j (p_j - p_i) \mathbf{B}_i \nabla_i W_{ij} V_j \tag{4.19}$$

$$\mathbf{B}_i = \left[\sum_j \nabla_i W_{ij} \otimes (\mathbf{r}_j - \mathbf{r}_i) V_j \right]^{-1} \tag{4.20}$$

the gradient of a linear pressure field is evaluated exactly for an arbitrary particle distribution. Here, the only constrain is linked to the inversion of the matrix $\mathbf{B}_i^{-1}$ which could be ill-conditioned for some particle configurations.

However, using the formulae (4.18) (4.19) or other consistent formulae (see e.g. Colagrossi 2005) the conservative properties on linear/angular momentum and energy are lost. When dealing with violent free-surface flow, the numerical schemes obtained with higher order integral interpolations may give worst results than using system (4.1). Indeed, for such problems the conservation properties are quite relevant to guarantee the robustness of the numerical scheme. Furthermore, when simulating violent fluid/fluid impacts or fluid/structure impacts the configuration of the free surface can be complex due to high fragmentation and the matrices $\mathbf{B}_i^{-1}$ in equation (4.19) can be ill-conditioned. In such conditions the consistent formulations need to be reduced to the standard one (4.1). In this sense, hybrid formulations are possible as shown in Colagrossi et al. (2010*a*). For the aforementioned reasons, in the present work this corrections are not used even if the corrected gradient evaluation of equation 4.19 is applied in some algorithm here described (see sections 5.1, 7.1.1 and 7.2).

Incidentally, it is important to underline that, when using formulae (4.18) (4.19), the implicit enforcement of the dynamic free-surface boundary condition (see section 3.3.1) is lost and therefore it is necessary to detect the particles belonging to the free surface (see section 7.2) to explicitly enforce such a condition.

4.2 CHOICE OF THE KERNEL AND TIME INTEGRATION OF THE SPH EQUATIONS

To integrate in time the ODEs system (4.1) it is necessary to select a proper kernel function and a scheme for the time integration. In practical SPH computations, the choice of the kernel function affects both the CPU requirements and the stability properties of the algorithm. In this work a renormalized Gaussian kernel has been adopted:

$$W_{ij} = W(r) = \begin{cases} \dfrac{e^{-(r/h)^2} - C_0}{2\pi C_1} & \text{if } r \leqslant \epsilon_h \\ 0 \qquad \text{otherwise} \end{cases} \tag{4.21}$$

$$C_0 = e^{-(\epsilon_h/h)^2}; \qquad C_1 = \int_0^{\epsilon_h} r \left[(e^{-(r/h)^2} - e^{-(\epsilon_h/h)^2} \right] dr$$

where $r = \|\mathbf{r}_j - \mathbf{r}_i\|$ is the Euclidean distance between the two particles. To make its support compact a cut-off radius ϵ_h is introduced and typically set equal to $3h$ as for the classical fifth-order B-spline support (Monaghan 1992). This choice of kernel has been motivated by the fact that from a numerical point of view the behaviour of the renormalized Gaussian kernel is almost identical to the classical Gaussian kernel (the difference between the two kernels is less than 0.04% respect to the maximum of the function). For what concerns the latter the following properties are well established: (i) among ten tested kernel shapes, the Gaussian kernel appears to give the best numerical accuracy in the stable field (Hongbin and Xin 2005); (ii) the comparison of the Gaussian kernel to classically used spline kernels showed that the former leads to better stability properties (Morris 1996*b*); (iii) it presents also a lower computational cost with respect to evolved forms of spline kernels (Colagrossi 2005) its gradient being straightforwardly obtained from the evaluation of W itself.

In SPH the time step Δt adopted to integrate system (4.1) is linked to the *Courant* number (here indicated with CFL) through the relation (see Monaghan and Kos 1999):

$$\Delta t = \text{CFL} \min_i \left(\frac{h}{c_i + |u_i| + h \max_j |\pi_{ij}|} \right); \tag{4.22}$$

where the minimum is over all particles and the maximum is over the particle neighbours of the generic i-particle. The CFL factor depends on the time scheme adopted and in the present work different time integrators have been studied. The relation (4.22) does not apply when simulating viscous flows where Re number is very small (i.e less than 1). In such a case the choice of Δt is governed by the viscosity term and not by the speed of sound (see e.g. Morris et al. 1997). In any case for the applications of interest for this thesis the law (4.22) is always valid.

To describe how the SPH equations (4.1) can be integrated in time the simple *modified Euler* scheme is depicted below. It consists in a predictor and a corrector step that uses an average of the rates of change between the two time instants (see e.g. Monaghan et al. 2003). Re-writing the evolution particle equations as:

$$\left[\frac{D\rho}{Dt}\right]_i = E_i\,; \qquad \left[\frac{D\mathbf{u}}{Dt}\right]_i = \mathbf{F}_i\,; \qquad \left[\frac{De}{Dt}\right]_i = G_i\,; \qquad \left[\frac{D\mathbf{r}}{Dt}\right]_i = \mathbf{u}_i \tag{4.23}$$

with the *modified Euler* these equations evolve in time following the scheme:

$$\begin{cases} \rho_i^{n+1,*} = \rho_i^n + \Delta t\, E_i^n \\ \mathbf{u}_i^{n+1,*} = \mathbf{u}_i^n + \Delta t\, \mathbf{F}_i^n \\ e_i^{n+1,*} = e_i^n + \Delta t\, G_i^n \\ \mathbf{r}_i^{n+1,*} = \mathbf{r}_i^n + \Delta t\, \mathbf{u}_i^n + \dfrac{\Delta t^2}{2}\,\mathbf{F}_i^n \end{cases} \Rightarrow \begin{cases} \rho_i^{n+1} = \rho_i^n + \Delta t\, \dfrac{(E_i^n + E_i^{n+1,*})}{2} \\ \mathbf{u}_i^{n+1} = \mathbf{u}_i^n + \Delta t\, \dfrac{(\mathbf{F}_i^n + \mathbf{F}_i^{n+1,*})}{2} \\ e_i^{n+1} = e_i^n + \Delta t\, \dfrac{(G_i^n + G_i^{n+1,*})}{2} \\ \mathbf{r}_i^{n+1} = \mathbf{r}_i^{n+1,*} \end{cases} \tag{4.24}$$

where the superscript n,$(n+1,*)$ and $(n+1)$ indicate respectively the current time instant, the predicted one and corrected time instant. Following the scheme proposed by Monaghan et al. (2003) the positions of the particles are not corrected. Using a CFL value equal to 0.3 this scheme is stable.

It is possible to obtain greater CFL values using different time integrators. In particular it has been heuristically found that using a 4th order Runge-Kutta scheme a CFL equal to 2.5 can be adopted. Four evaluations of the derivatives (4.23) are requested in the sub time steps respect to the Modified Euler scheme. However a gain of factor 2 is achieved using the 4th Runge-Kutta instead the Modified Euler one. For this reason large part of the simulations discussed in this thesis are obtained with the 4th order Runge-Kutta.

4.3 REMARKS ON THE SMOOTHING LENGTH AND THE INTER-PARTICLE DISTANCE

Since the SPH scheme requires that the particles distribution is close to a regular lattice, it is also possible to define a mean inter-particle distance Δx which is equivalent to the mesh-size used in mesh based solvers. The volumes of the particles are therefore close to Δx^3. The ratio $h/\Delta x$ controls the number of particles $\mathcal{N}_i$ which are in the kernel support $\Omega(\mathbf{r}_i)$ of the generic i-th particle. In other words, $\mathcal{N}_i$ is the number of neighbouring particles interacting with the i-th particle. Excluding the particles which are close to the fluid domain boundary $\partial\Omega$ the distribution of $\mathcal{N}_i$ generally is quite regular and it is possible to refer to the average value $\mathcal{N}$.

The ratio $h/\Delta x$ and $\mathcal{N}$ depend on the adopted kernel function W, however in most of the cases $\mathcal{N}$ is close to 50 in 2D and 250 in 3D simulation (see e.g. Colagrossi 2005). In order to check the convergence of the scheme for a given problem, it is common practice to keep this number constant while increasing the spatial resolution. It is important to underline that from a theoretical point of view the SPH scheme converges only when Δx is going to zero faster than h (see e.g. Di Lisio et al. 1998). However, as commented in Quinlan et al. (2006) and Colagrossi (2005), if the number of interacting neighbours $\mathcal{N}$ is high enough and the particle distribution remains sufficiently regular (*i.e* small values of $|\nabla\Gamma_i|$), the errors made by the discrete operators used in (4.1) are small. In particular for the simulations performed in this thesis the convergence rate of the SPH scheme has been checked and a value between 1 and 2 is usually obtained for the most significant quantities. Some quantities could not locally converge, and this occur for example when the free surface is characterized by complex configurations. In these cases, when increasing the spatial resolution, smaller and smaller jets, drops and cavities are generated thus leading to a turbulence-like behaviour.

A final comment concerns the use of a different smoothing length h_i for each i-th particle, that is, the multi-resolution SPH scheme. In this case, the distribution of h_i is linked to the arbitrary particle size distribution Δx_i, the number of neighbours $\mathcal{N}$ being constant. These models allows for a more efficient use of computational resources. However, such schemes present several complexities and problems which are still not completely addressed in the literature (see e.g Marsh et al. 2011). For this reason these schemes are not used in the present thesis and only constant h schemes are considered. In the specific in chapter 10 multi resolution is achieved by slightly varying the spatial discretization keeping constant h as done by Landrini et al. (2007). Only small size ratio between the low and high resolution are allowed with this technique because for larger particles the number of neighbours decreases and so the accuracy of interpolation.

4.4 CONNECTIONS BETWEEN MASS, DENSITY AND PARTICLE SPATIAL POSITION

In the very first formulation of the SPH the density field was directly linked with the particle masses and positions through the relation:

$$\langle \rho \rangle_i^A = \sum_j m_j W_{ij} \tag{4.25}$$

This relation is still largely used in astrophysics and in gas-dynamic context but it cannot be used in the context of multiphase flow since it is not able to represent correctly density discontinuity between the phases. To overcome this problem recently Hu and Adams (2006*a*) proposed a new density equation:

$$\langle \rho \rangle_i^C = m_i \sum_j W_{ij} \tag{4.26}$$

This formula permits to reproduce density discontinuities inside the computational domain. Indeed, the density of the generic i-th particle is not influenced by the masses of its neighbours m_j , even though the particle i receives the geometric contribution W_{ij} from the particle j. In this way, in the region close to the interface, particles belonging to a different fluid can be taken into account for the evaluation of density without introducing unphysical effects due to differences of mass. Further, using relation (4.3) in (4.26) the volume of the i-th particle can be simply expressed through the kernel summation:

$$n_i = \sum_j W_{ij} \qquad V_i = 1/n_i \tag{4.27}$$

The two relations (4.25) and (4.26) can be related to a divergence velocity operator and used to derive the consistent pressure gradient using the PVW as in section 3.3.2 (see Grenier et al. 2009). To this purpose the following equation has to be proven:

$$\frac{DW_{ij}}{Dt} = (\mathbf{u}_i - \mathbf{u}_j) \cdot \nabla_i W_{ij} \, . \tag{4.28}$$

Since $W_{ij} = W(r_{ij}, h)$ where $r_{ij} = \|\mathbf{r}_j - \mathbf{r}_i\|$, we get:

$$\frac{DW_{ij}}{Dt} = \frac{\partial W}{\partial r_{ij}} \frac{Dr_{ij}}{Dt} = \frac{\partial W}{\partial r_{ij}} \frac{(\mathbf{u}_j - \mathbf{u}_i) \cdot (\mathbf{r}_j - \mathbf{r}_i)}{r_{ij}} \, , \tag{4.29}$$

and the last equality has been obtained using $D\mathbf{r}_i/Dt = \mathbf{u}_i$. Then, the equality in (4.28) is obtained by using the following identity:

$$\nabla_i W_{ij} = - \frac{(\mathbf{r}_j - \mathbf{r}_i)}{r_{ij}} \frac{\partial W}{\partial r_{ij}} \, . \tag{4.30}$$

Deriving in time (4.25) and using (4.28) in the continuity equation of (3.1) one obtains that equation (4.25) is linked to the velocity divergence with the following relation:

$$\langle \mathrm{div}\mathbf{u} \rangle^A = \frac{1}{\rho_i} \sum_j (\mathbf{u}_j - \mathbf{u}_i) \cdot \nabla_i W_{ij}\, m_j \,. \tag{4.31}$$

while the (4.26) leads to:

$$\langle \mathrm{div}\mathbf{u} \rangle^C = \frac{1}{n_i} \sum_j (\mathbf{u}_j - \mathbf{u}_i) \cdot \nabla_i W_{ij} \,. \tag{4.32}$$

The corresponding pressure gradient obtained through the PVW as in section 3.3.2 are:

$$\langle \nabla p \rangle^A = \rho_i \sum_j \left(\frac{p_j}{\rho_j^2} + \frac{p_i}{\rho_i^2} \right) \nabla_i W_{ij}\, m_j \,, \tag{4.33}$$

$$\langle \nabla p \rangle^C = n_i \sum_j \left(\frac{p_j}{n_i^2} + \frac{p_i}{n_j^2} \right) \nabla_i W_{ij} \,. \tag{4.34}$$

Equation (4.33) is the first SPH formulation derived in literature in the astrophysical context (Gingold and Monaghan 1982)), while the second one has been presented by Hu and Adams (2006*a*) in the context of multiphase flows.

It is important to underline that both relations (4.25) and (4.26) cannot be used when a free surface is present, since close to the interface the kernel truncation leads to an unphysical decreasing of the density. At the same time it is not possible to link the formula $\langle \mathrm{div}\mathbf{u} \rangle^B$ (see section 3.3.1)to a direct relation $\rho_i = f(W_{ij})$ like (4.25) and (4.26). As a consequence, for the object of this thesis only the SPH formulation (4.1) will be considered.

5

SPH WITH NUMERICAL DIFFUSIVE TERMS: THE δ -SPH

5.1 SPH SCHEME WITH NUMERICAL DIFFUSIVE TERMS

This chapter is dedicated to a novel SPH system of equations derived from the standard one (4.10) in which numerical diffusive terms are added in both continuity and energy equations. The diffusive term inside the continuity equation allows reducing the high frequency numerical acoustic noise in the pressure field in a conservative fashion. Further, this diffusive process induces small mass exchanges between particles that make the particle distribution more uniform, with remarkable benefits for the accuracy of the interpolation procedure.

The state equation 3.63 is used to associate the internal energy variation to the pressure field and to increase the speed of sound when strong deformations/compressions of the fluid occur, allowing a better time discretization during both breaking waves and impact events. For inviscid fluids this system reads as:

$$\begin{cases} \dfrac{D\rho_i}{Dt} = -\rho_i \sum_j (\mathbf{u}_j - \mathbf{u}_i) \cdot \nabla_i W_{ij}\, V_j + \delta\, c_0\, h \sum_j \boldsymbol{\psi}_{ij} \cdot \nabla_i W_{ij}\, V_j \\[2ex] \dfrac{D\mathbf{u}_i}{Dt} = \mathbf{g} - \dfrac{1}{\rho_i} \sum_j (p_j + p_i)\, \nabla_i W_{ij}\, V_j + \alpha\, c_0\, h\, \dfrac{\rho_0}{\rho_i} \sum_j \pi_{ij}\, \nabla_i W_{ij}\, V_j \\[2ex] \dfrac{De_i}{Dt} = -\dfrac{p_i}{\rho_i} \sum_j (\mathbf{u}_j - \mathbf{u}_i) \cdot \nabla_i W_{ij}\, V_j + \chi\, c_0\, h\, \dfrac{\rho_0}{\rho_i} \sum_j \boldsymbol{\phi}_{ij} \cdot \nabla_i W_{ij}\, V_j \\[2ex] \qquad\qquad + \dfrac{1}{2}\, \alpha\, c_0\, h\, \dfrac{\rho_0}{\rho_i} \sum_j \pi_{ij}\, \nabla_i W_{ij} \cdot (\mathbf{u}_j - \mathbf{u}_i)\, V_j \\[2ex] \dfrac{D\mathbf{r}_i}{Dt} = \mathbf{u}_i\,; \qquad p = c_0^2 \left[1 + \Xi \left(\dfrac{e}{e_0} - 1 \right) \right] (\rho - \rho_0)\,. \end{cases} \tag{5.1}$$

where the term π_{ij}, $\boldsymbol{\phi}_{ij}$ are defined in equation (4.2) and the new term $\boldsymbol{\psi}_{ij}$ is:

$$\boldsymbol{\psi}_{ij} = 2\, (\rho_j - \rho_i)\, \frac{\mathbf{r}_{ji}}{|\mathbf{r}_{ij}|^2} - \left[\langle \nabla \rho \rangle_i^L + \langle \nabla \rho \rangle_j^L \right] \tag{5.2}$$

The blue coloured terms indicate the artificial numerical terms that are proportional to the smoothing length h, so that in the limit $h \to 0$ the consistency with Euler equations is recovered. The gradient $\langle \nabla \rangle^L$ has been defined in (4.19) while $\mathbf{r}_{ij} = -\mathbf{r}_{ji} = \mathbf{r}_i - \mathbf{r}_j$. The coefficients δ and χ control the order of magnitude of the diffusive terms, α the order of magnitude of the viscous terms and Ξ the influence of the internal energy variation inside the state equation. All the coefficients above but δ are have to be properly tuned as discussed in section 4.1.1. Regarding δ, Antuono et al. (2010) provided a linear stability analysis to set its range of variability in $0 < \delta < 0.2$. In any case, in all the simulation of the present work the value of δ is fixed and set equal to 0.1 (with the exception of gas dynamic test cases in section 5.3). The diffusive term $\boldsymbol{\psi}_{ij}$ in the continuity equation is more effective for improving the SPH scheme with respect to the term related to the coupling of the internal energy with pressure through the state equation, the latter requiring the integration of the energy equation. Therefore, for some applications presented in this thesis the parameter Ξ is set to zero to simplify the numerical scheme. When solving viscous flows, the artificial viscosity term in the system (5.1) is replaced by the real one as expressed in equation 4.12. The system thus reads:

$$\left\{\begin{aligned}
\frac{D\rho_i}{Dt} &= -\rho_i \sum_j (\mathbf{u}_j - \mathbf{u}_i) \cdot \nabla_i W_{ij}\, V_j \;+\; \delta\, c_0\, h \sum_j \boldsymbol{\psi}_{ij} \cdot \nabla_i W_{ij}\, V_j \\
\frac{D\mathbf{u}_i}{Dt} &= \mathbf{g} - \frac{1}{\rho_i} \sum_j (p_j + p_i)\, \nabla_i W_{ij}\, V_j \;+\; K\, \frac{\mu}{\rho_i} \sum_j \pi_{ij} \nabla_i W_{ij}\, V_j \\
\frac{De_i}{Dt} &= -\frac{p_i}{\rho_i} \sum_j (\mathbf{u}_j - \mathbf{u}_i) \cdot \nabla_i W_{ij}\, V_j \;+\; \chi\, c_0\, h\, \frac{\rho_0}{\rho_i} \sum_j \boldsymbol{\phi}_{ij} \cdot \nabla_i W_{ij}\, V_j \\
&\qquad + \frac{1}{2}\, \alpha\, c_0\, h\, \frac{\rho_0}{\rho_i} \sum_j \pi_{ij}\, \nabla_i W_{ij} \cdot (\mathbf{u}_j - \mathbf{u}_i)\, V_j \\
\frac{D\mathbf{r}_i}{Dt} &= \mathbf{u}_i\,; \qquad p = c_0^2 \left[1 + \Xi \left(\frac{e}{e_0} - 1\right)\right] (\rho - \rho_0)\,.
\end{aligned}\right. \tag{5.3}$$

$K = 2(d+2)$ is a parameter depending on the spatial dimension d.

The additional terms of systems (5.1) and (5.3) are motivated by the fact that the standard weakly-compressible SPH scheme is generally affected by some drawbacks. The main problems are the correct evaluation of the pressure values for strong impacts and the flickering of pressure profiles that may occur also in not particularly violent flows. The former was addressed by Molteni et al. (2007). In that work, the sound speed was proposed to vary *locally*, that is, only for the particles involved in strong collisions. This corresponds to make the fluid more incompressible where and when it is hitting against some obstacle. Since this procedure requires the use of the energy equation, an *ad hoc* thermal energy is defined aiming to change the sound speed as compressions/deformations occur. Note that, notwithstanding the use of a thermal energy equation is a quite standard matter for compressible fluids, it is generally not used when the weakly-compressible assumption is considered to model liquids. Here, the energy equation is used merely for numerical purposes and, therefore, such an energy does not necessarily correspond to the real physical temperature of the fluid.

Regarding the pressure field, it is well known in literature that standard SPH schemes suffers from high-frequency numerical noise on pressure profiles (see e.g. Colagrossi and Landrini 2003). The term ψ_{ij} of system (5.1) thus represents the main improvement of the present scheme since it strongly contributes to eliminate this spurious noise. This term is inspired by the work of Molteni and Colagrossi (2009) who added a numerical diffusion term in the density equation as well. That term ψ_{ij} was:

$$\psi_{ij} = 2\left(\rho_j - \rho_i\right)\frac{\mathbf{r}_{ji}}{|\mathbf{r}_{ij}|^2} \tag{5.4}$$

that is a standard formula to approximate diffusion (see e.g. section 3.3.4). In the SPH scheme (Brookshaw 1985, see for example), this formula is conservative and, therefore, it preserves the total amount of the diffused quantities (that is, the mass). This proved to smooth out the numerical noise inside the pressure field but, unfortunately, did not preserve the hydrostatic solution as well. As a consequence, an ad-hoc switch had to be introduced to turn off the diffusive term when the pressure gradient was smaller than the hydrostatic gradient. The reason of such a behaviour was not clearly understood. This aspect has been discussed in the next section. Indeed, in Antuono et al. (2010) it is proven that the standard SPH formula used to model the diffusive terms (5.4) diverges near the free surface and, therefore, introduces spurious contributions inside the density equation. To avoid such a problem, in the work by Antuono et al. (2010) the improved formula (5.2) is derived. This new diffusion term is consistent and convergent all over the fluid domain and, further, it preserves the mass conservation.

Finally, some analogies with the present scheme can be found with the SPH formulations by Vila (1999) and Moussa et al. (1999). In fact, these works are based on Riemann solvers to evaluate a numerical flux between each couple of interacting fluid particles. This leads to the generation of intrinsic numerical diffusion into all the equations of evolution. The strong point of the SPH Riemann solvers is that it does not need any parameter to tune to control diffusion. Anyway, as pointed out by Ferrari et al. (2009), this is also a drawback since they are often too much diffusive/dissipative and, therefore, are not suitable to study problems with strong free-surface deformation. Further, those schemes are more difficult to implement and more CPU time-consuming than the SPH scheme here proposed. The numerical scheme proposed by Ferrari et al. (2009) is the nearest to that defined in Molteni and Colagrossi (2009) as the former intrinsically accounts for diffusion only inside the density equation and, further, does not present any tuning coefficient. Consequently, it is less diffusive/dissipative than the schemes proposed by Vila (1999) and Moussa et al. (1999) and can be effectively applied to free-surface problems.

5.2 DERIVATION OF A CONSERVATIVE EXPRESSION FOR THE DIFFUSIVE TERM

The diffusive terms ϕ_{ij} in equation (4.2) and ψ_{ij} in equation (5.4) approximate the Laplacian of the density and of the internal energy respectively. Generally, within the SPH scheme, the Laplacian is represented through the Morris formula which, for a generic scalar function f, reads:

$$\langle \nabla^2 f \rangle = 2 \sum_j (f_j - f_i) \frac{\mathbf{r}_{ji} \cdot \nabla_i W_{ij}}{\mathbf{r}_{ij}^2} V_j \tag{5.5}$$

Antuono et al. (2010) proved that this formula is singular near the free-surface. Considering a Gaussian kernel (see section 4.2) for which the kernel gradient can be expressed by:

$$\nabla_i W_{ij} = \frac{2}{h^2} \mathbf{r}_{ji} W_{ij} \tag{5.6}$$

the expression in (5.5) becomes:

$$\langle \nabla^2 f \rangle = \frac{4}{h^2} \sum_j (f_j - f_i) W_{ij} V_j \tag{5.7}$$

Through a Taylor expansion it is possible to prove that equation (5.7) can be expressed as (see Antuono et al. 2010):

$$\begin{aligned} \langle \nabla^2 f \rangle\Big|_i &= \frac{4}{h^2} \sum_j (f_j - f_i) W_{ij} V_j - 2 \nabla f\Big|_i \cdot \nabla \Gamma\Big|_i + \\ &+ \mathcal{O}\big((1 - \Gamma\big|_i)\big) + \mathcal{O}(h^2) . \end{aligned} \tag{5.8}$$

This means that the Morris formula converges to the Laplacian of f if $\nabla \Gamma = 0$ and $\Gamma = 1$. As proved in Colagrossi et al. (2009*b*), this is true inside the fluid but not near the free surface where $\nabla \Gamma$ diverges like h^{-1}. As a consequence, the Morris formula diverges near the free surface as well. A conservative expression for the diffusive term can be derived using again a Taylor expansion (for details see Antuono et al. 2010):

$$\langle D(f) \rangle\Big|_i = \frac{4}{h^2} \sum_j \left\{ f_j - f_i - \frac{1}{2} \left(\nabla f\Big|_j + \nabla f\Big|_i \right) \cdot \mathbf{r}_{ji} \right\} W_{ij} V_j + \mathcal{O}(h) . \tag{5.9}$$

in which the dependency on $\nabla\Gamma$ is removed. Within the SPH scheme, the previous expression can be approximated through:

$$\langle D(f)\rangle\Big|_i = \frac{4}{h^2}\sum_j \left\{ f_j - f_i - \frac{1}{2}\left(\langle\nabla f\rangle\Big|_j + \langle\nabla f\rangle\Big|_i\right)\cdot \mathbf{r}_{ji} \right\} W_{ij}\, V_j + \mathcal{O}(h)\,. \tag{5.10}$$

Since we need $\langle\nabla f\rangle$ to converge to ∇f all over the fluid domain, we use the first order integral interpolation (4.19) (for details see e.g. Randles and Libersky 1996) to evaluate the gradients inside the expression (5.10). Moreover, it is simple to show that, using (5.10), it follows:

$$\sum_i \langle D(f)\rangle\Big|_i V_i = 0\,, \tag{5.11}$$

recovering the integral conservation of the continuity equation.

It is important to underline that the results here obtained hold for a generic kernel with the following structure:

$$W = W\left(-\frac{|\mathbf{r}_{ij}|^2}{h^2}\right) \qquad \Rightarrow \qquad \nabla_i W\left(-\frac{|\mathbf{r}_{ij}|^2}{h^2}\right) = \frac{2}{h^2}\,\mathbf{r}_{ji}\,\frac{\partial W}{\partial r}\left(-\frac{|\mathbf{r}_{ij}|^2}{h^2}\right) \tag{5.12}$$

5.3 1-D TEST CASES

To preliminary check the effectiveness of the diffusive term inside the continuity equation, two one-dimensional problems are considered: the propagation of sound waves and the Riemann Problem. To this purpose the continuity and momentum equations are decoupled from the thermal energy equation (that is, we set $\Xi = 0$). Only for these problems a fine tuning of the parameter δ has been done since the acoustic problems are more sensitive to this parameter.

Traveling acoustic waves

In order to study the propagation of sound waves, the solution of the wave equation is adopted as initial data:

$$u(0,x) = U_0 \sin(n\lambda x)\,, \qquad p(0,x) = \rho_0\, c_0\, U_0 \sin(n\lambda x)\,, \tag{5.13}$$

where $n \in \mathbb{N}$ and λ is the wave length and implemented periodic boundary conditions. As a consequence of this specific choice, the sound waves tend to propagate with an unaltered shape towards the increasing values of the spatial coordinate. Anyway, because of the non-linear effects, they deform and steepen during the evolution and, incidentally, some spurious numerical noise is generated. In figure 5.1 the comparison between the numerical solution of system (5.1) is shown with $\alpha = 0.01$, $\delta = 0$ (solid lines) and $\alpha = 0.01$, $\delta = 0.01$

(dashed lines) after nine periods of the evolution (in both the cases $\Xi = 0$, $\chi = 0$). The former case is equivalent to the standard SPH scheme described in section 4.1.1. The values of the wave parameters are $U_0 = 0.2, c_0 = 20$ and $n = 2$. In the case with $\delta \neq 0$ the numerical high-frequency noise is completely damped by the diffusive term. It is worth noting that the action of the viscosity term is fundamental for the stability of the numerical solution. Indeed, in all the cases in which $\alpha = 0$ is chosen, the wave signals were completely destroyed by the numerical noise, notwithstanding the use of the diffusion inside the continuity equation. This also means that the diffusive terms have to be regarded as an improvement of the standard SPH scheme with artificial viscosity but cannot be used instead of the artificial viscosity itself.

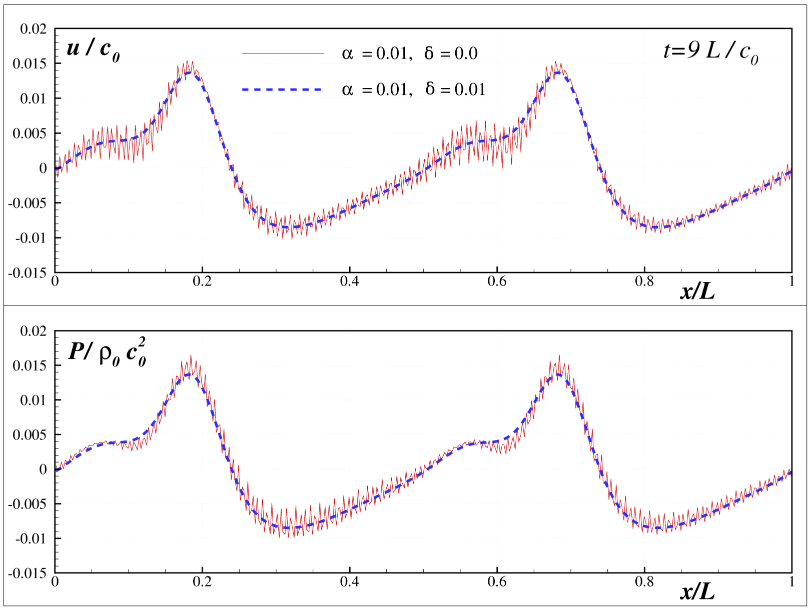

Figure 5.1.: Traveling acoustic waves. Comparison between the standard SPH scheme with $\alpha = 0.01$ (solid lines) and numerical solution of system (5.1) with $\alpha = 0.01$, $\delta = 0.01$, $\chi = 0$ and $\Xi = 0$ (solid lines) after nine periods of the evolution ($U_0 = 0.2, c_0 = 20$, $n = 2$).

The Riemann Problem

The Riemann Problem is represented by a sharp discontinuity separating two constant states, that is:

$$\begin{cases} \rho \equiv \rho_L\,, & u \equiv u_L \qquad \text{for} \quad x < 0 \\ \rho \equiv \rho_R\,, & u \equiv u_R \qquad \text{for} \quad x > 0\,. \end{cases} \tag{5.14}$$

Following Marongiu (2007), the values $\rho_L/\rho_0 = 1.1$, $u_L/c_0 = 0.1362$, $\rho_R/\rho_0 = 1.0$, $u_R/c_0 = 0$ are chosen. Differently from the nonlinear propagation of acoustic waves, the Riemann Problem admits an analytical solution and, therefore, allows us to check the accuracy of the present SPH scheme. Figure (5.2) shows the comparison between the analytical solution (solid lines), the standard SPH scheme with $\alpha = 0.01$ (cross points) and the numerical solution of system (5.1) with $\alpha = 0.01$ and $\delta = 0.2$ (circles) for two different spatial resolutions. Similarly to the 1D propagation of acoustic waves, some spurious high-frequency oscillations develop near the shock discontinuities. Anyway, at the coarser resolution the present SPH model shows oscillations which are smaller than those predicted by the standard SPH ones. Further, the numerical noise is almost-completely damped down at the finer discretization.

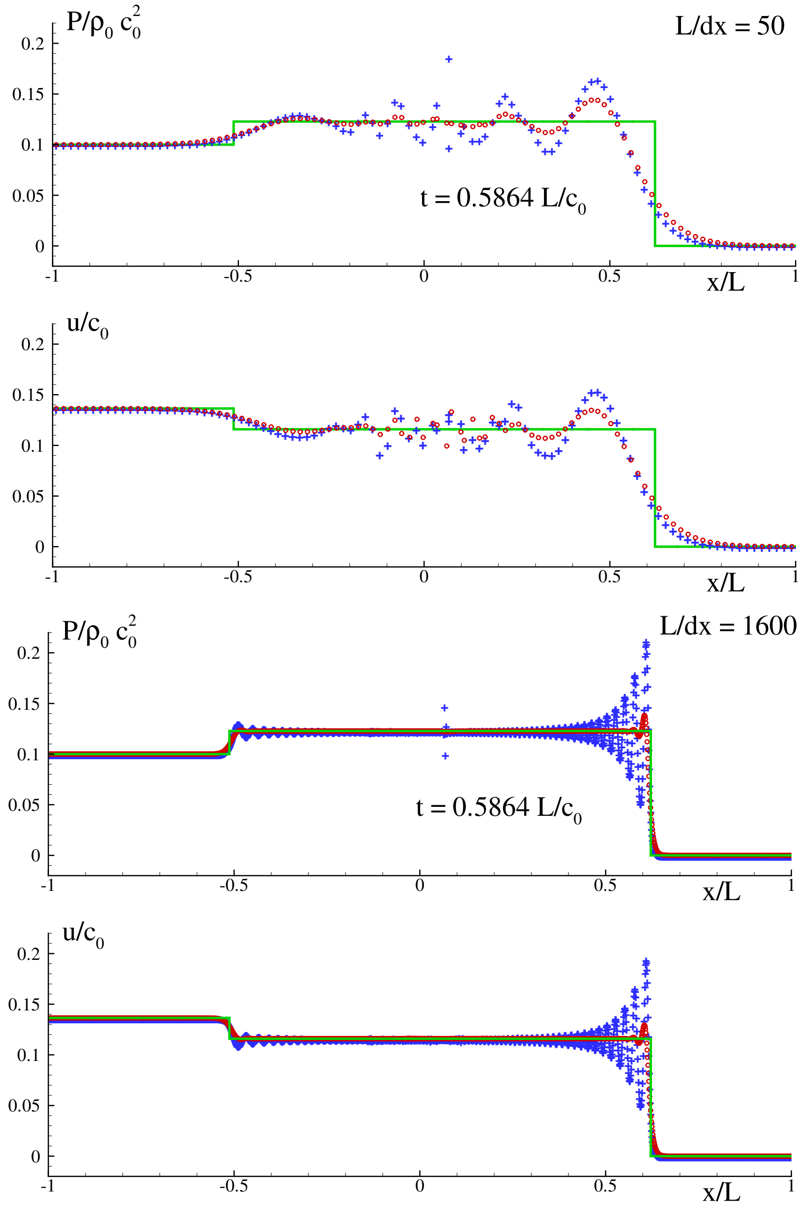

Figure 5.2.: The Riemann Problem. Comparison between the analytical solution (solid lines), the standard SPH scheme with $\alpha = 0.01$ (cross points) and the numerical solution of system (5.1) with $\alpha = 0.01$, $\delta = 0.2$, $\chi = 0$ and $\Xi = 0$ (circles).

6 INITIAL CONDITIONS SETTING

In SPH the matter of how initialize the particle positions plays a relevant role. If particles are not initially set in "equilibrium" positions, they may resettle giving rise to spurious motions which can strongly affect the fluid evolution. One refers to an equilibrium configuration as the set of particle positions which, under static conditions, does not lead to particle resettlement. This resettlement is due to the lack of zero-th order consistency of the momentum equation (i.e. the ability in maintaining exactly a constant pressure field) when particles are arbitrary distributed. In other words, finding an equilibrium configuration means achieve a set of particle positions that allows recovering zero-th and even first order consistency of SPH equations as already shown in chapter 4.

A part from few cases characterized by simple geometries, the equilibrium configuration is not known "a priori". Further, the generation of spurious currents/vorticity may be particularly strong in presence of complex solid boundary profiles (i.e. corners, bended bodies, etc.). A possible solution is to start numerical simulations with a high numerical damping and leave a long enough time to make particle self-resettle in equilibrium positions (see, for example Monaghan 1994)). Unfortunately, the attainment of a stable configuration can require a very long evolution, this leading to a large increase of computational costs. Moreover, the high damping used for particle initialization does not exclude that a further resettlement occurs when the actual simulation is started with smaller values of the viscosity.

In the SPH framework, the first attempt to define a proper algorithm for particle initialization is due to Oger et al. (2009) who adapted the Bubble method described by Shimada (1993) to SPH solvers. This algorithm is based on the use of Van der Waals-like forces to place particles throughout the fluid domain. This method proves to be quite fast, applies to general geometries and provides a regular particle distribution. One of the weak points is that the particle positions obtained through the Bubble algorithm may be not perfectly compatible with the SPH static solution leading to a further resettlement.

To this purpose in the following a packing algorithm is described that takes advantage of some intrinsic features of the SPH schemes. Thanks to this, the method allows the attainment of a regular particle distribution compatible with the static solution. Further, it can be easily derived starting from whatever SPH solvers and applies to weakly-compressible or incompressible SPH schemes as well.

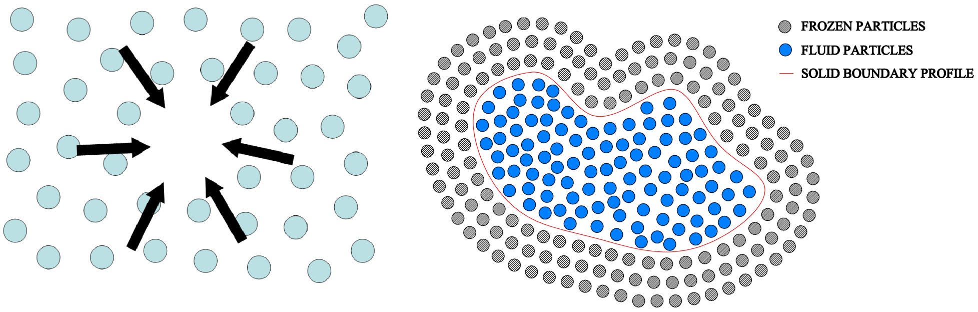

Figure 6.1.: Left panel: sketch of the vector $\boldsymbol{w} = -\nabla\Gamma$ in the neighbourhood of a spatial anisotropy. Right panel: sketch of the solid and fluid particles in the packing algorithm framework.

6.1 THE PARTICLE PACKING ALGORITHM: DESCRIPTION OF THE METHOD

The Particle Packing Algorithm is built on a simple idea: to use the SPH characteristics to initialize the particle distribution and minimize $\|\nabla\Gamma\|$ (see section 4.1.2 for a discussion). This is made by observing that the vector $\boldsymbol{w} = -\nabla\Gamma$ always points in the direction of the maximum lack of "mass" and maximum anisotropy (see figure 6.1). Now, let assume to use it to move particles during the initialization. If the fluid domain is bounded and particles are not allowed to escape form the boundaries, $\boldsymbol{w}$ tends to fill all the asymmetries in the particle distribution and, at the same time, it reduces as a consequence of the more regular distribution of particles themselves. Then, the final distribution would be the most regular possible and $\|\boldsymbol{w}\|$ (that is, $\|\nabla\Gamma\|$) would be minimized as requested.

The first step to build the Particle Packing Algorithm is to close the domain boundaries. As a consequence, this implies that the free surface has to be treated as a solid boundary. The domain boundary has to be modelled through fixed solid particles, that is, particles with zero velocity and fixed positions. A sketch of this procedure is displayed in the right panel of figure 6.1. Note that particles do not need any specific rule to be positioned inside the fluid domain nor inside the solid bodies. The second step consists in assuming the density, the pressure and the volumes constant all over the fluid domain. They are indicated through the symbols ρ_0, p_0 and V_0 respectively. Since volumes are constant and the packing algorithm has to converge towards a static solution, we neglect the continuity equation. Conversely, the momentum equation of system (4.10) becomes:

$$\begin{cases} \dfrac{D\mathbf{u}_i}{Dt} = -\beta\,\nabla\Gamma_i + \mathbf{T}_i^{(\zeta)} \\[2ex] \dfrac{D\mathbf{r}_i}{Dt} = \mathbf{u}_i \end{cases} \tag{6.1}$$

where $\beta = 2\,p_0/\rho_0$ and $\Gamma_i = \sum_j W_{ij}\,V_0$. The viscous force can be chosen independently from the adopted SPH scheme since $\mathbf{T}_i^{(\zeta)}$ is just used to ensure the convergence of the Particle Packing Algorithm. In the specific, a simple linear damping is chosen:

$$\mathbf{T}_i^{(\zeta)} = -\zeta\,\mathbf{u}_i \qquad \text{with} \qquad \zeta = \alpha_\zeta\,\frac{\sqrt{\beta}}{V_0^{1/d}} \tag{6.2}$$

where d is the spatial dimension and α_ζ is a free dimensionless parameter. By numerical simulations it has been found that a good choice for α ranges between $1\cdot 10^{-3}$ and $5\cdot 10^{-3}$. Then, the Particle Packing system becomes:

$$\begin{cases} \dfrac{D\mathbf{u}_i}{Dt} = -\beta\,\nabla\Gamma_i - \zeta\,\mathbf{u}_i \\[2ex] \dfrac{D\mathbf{r}_i}{Dt} = \mathbf{u}_i\,. \end{cases} \tag{6.3}$$

The initial conditions for the Particle Packing Algorithm are obtained by setting all the particle velocities to zero and $V_0 = V_{tot}/N_{part}$ where V_{tot} is the total fluid volume and N_{part} is the total number of particles. The time-step adopted for the present algorithm is:

$$\Delta t = \mathrm{CFL}\,\frac{V_0^{1/d}}{\sqrt{\beta}}\,, \tag{6.4}$$

where $\mathrm{CFL} = 1$.

The system (6.3) tends to converge as much as possible towards a steady state characterized by $\mathbf{u}_i = 0$ and $\nabla\Gamma_i = 0$. When the fluid system is sufficiently close to this state, the particle positions are used to initialize the SPH simulations. Since the spatial distribution is very regular, the particle volumes can be assumed to be identical. Then, the volume used for the initialization of the SPH is $V^* = V_0$. The initial particle pressure, p_i^*, is assigned by using the analytical expression for the hydrostatic pressure and the particle positions. Then, inverting the state equation, the initial density ρ_i^* is computed and, finally, the particle mass is obtained through $m_i^* = \rho_i^*/V^*$. During the SPH simulations, the particle masses are kept constant while the densities and the volumes are updated using the continuity equation and the relation $V_i = m_i/\rho_i$.

6.2 APPLICATION ON HYDROSTATIC PROBLEMS

As an example of the algorithm effectiveness, a trapezoidal tank like that drawn in figure 6.2 (H is the filling height) is considered in order to study the influence of the particle initialization on the capability of the SPH of simulating the hydrostatic solution. As stated in Section 6.1, the first step is to "close" the fluid domain. This means that the free surface has to be substituted by a solid boundary and modelled accordingly. This procedure is displayed in figure 6.3 where the fluid domain has been initialized through a Cartesian grid (left panel) and using the packing algorithm (right panel).

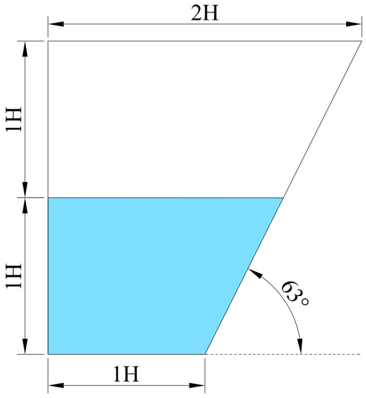

Figure 6.2.: sketch of the trapezoidal tank.

In the former case, the use of a Cartesian grid leads to the generation of large spatial anisotropies along the inclined plane. Here, $\|\nabla\Gamma\| = \mathcal{O}(1)$ and, therefore, an intense particle resettlement is expected during the early stages of the fluid evolution. Conversely, the particle packing algorithm eliminates the spatial anisotropies and drastically reduces the magnitude of $\|\nabla\Gamma\|$ (whose order of magnitude is about $10^{-13}H$).

It is also interesting to give a brief insight on the computational costs of the proposed algorithm and on its dependence on the spatial resolution. In figure 6.4 the specific Kinetic energy of the packing scheme defined as

$$\mathcal{T} = \sum_i \frac{\|\mathbf{u}_i\|^2}{2}$$

is displayed for three different spatial resolutions versus the number of iterations. This heuristically shows that after $2,500$ iterations, the particle are practically motionless (the order of magnitude of the specific kinetic energy is about $10^{-8}\beta$). This means that the equilibrium configuration has been attained and that the packing algorithm can be stopped. Obviously, the number of iterations required for the attainment of equilibria may vary according to the specific problem at hand, to the choice of the kernel function (i.e., Gaussian,

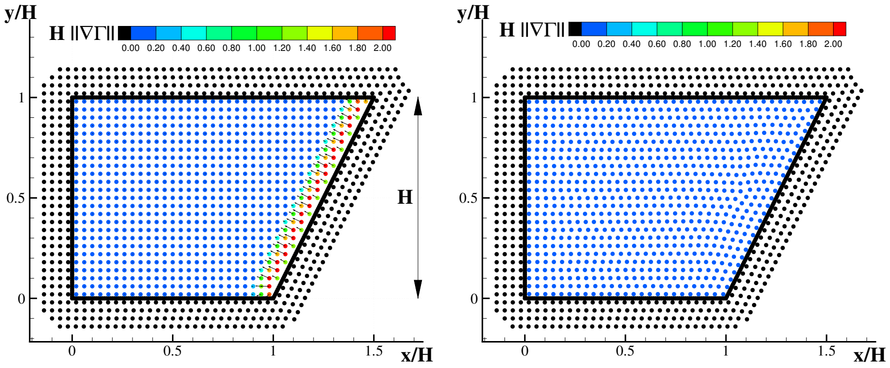

Figure 6.3.: trapezoidal tank ($H/dx = 25$). Initialization using a Cartesian grid (left) and through the particle packing algorithm (right).

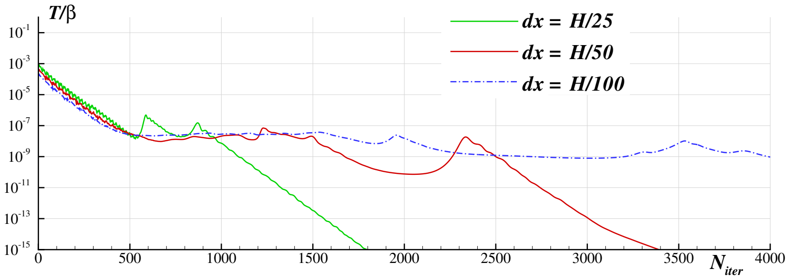

Figure 6.4.: trapezoidal tank. Evolution of the specific kinetic energy during the initialization through the particle packing algorithm.

cubic spline, quintic spline etc.) and to the adopted damping but generally range between $2,000 - 2,500$ iterations.

When the particle initialization is complete, the hydrostatic solution is assigned to the fluid domain (that is, hydrostatic pressure field and zero initial velocity) and the simulation is started through the standard SPH scheme (Monaghan 2005*a*).

As shown in the left panel of figure 6.5, the initialization through the Cartesian grid, because of the high values of $\|\nabla\Gamma\|$ near the sloping plane, leads to the generation of high spurious currents which, on the contrary, are completely absent when the simulations is initialized through the particle packing algorithm (right panel of the same figure).

A global measure of the particle resettlement phenomenon is easily obtained by inspecting the kinetic energy evolution during the simulation of the hydrostatic solution. As shown in figure 6.6, the kinetic energy of the SPH simulation after the use of packing algorithm is at least two orders of magnitude smaller than the simulation started on the Cartesian grid. In the former case the dimensionless kinetic energy is of order $10^{-7} - 10^{-8}$ proving that the fluid particles are practically motionless. On the contrary, the simulation started on a Cartesian grid shows a particle motion which still persists at $t = 100\sqrt{H/g}$.

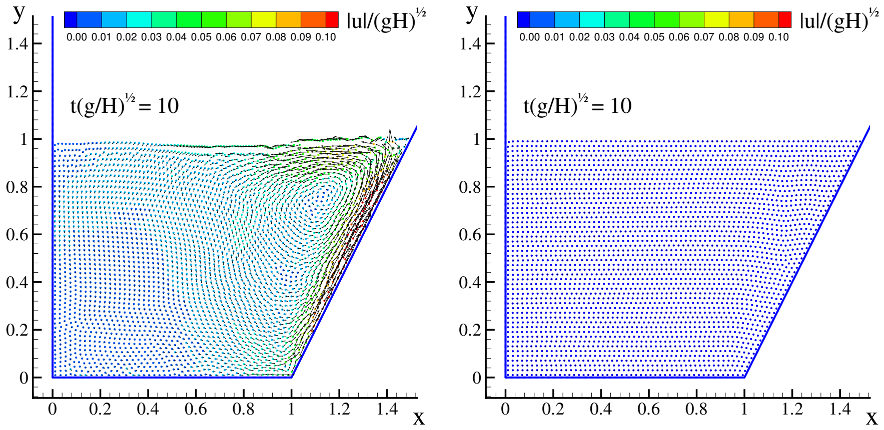

Figure 6.5.: hydrostatic solution for the trapezoidal tank ($H/dx = 50$). Evolution using a Cartesian grid (left) and after the initialization through the particle packing algorithm (right).

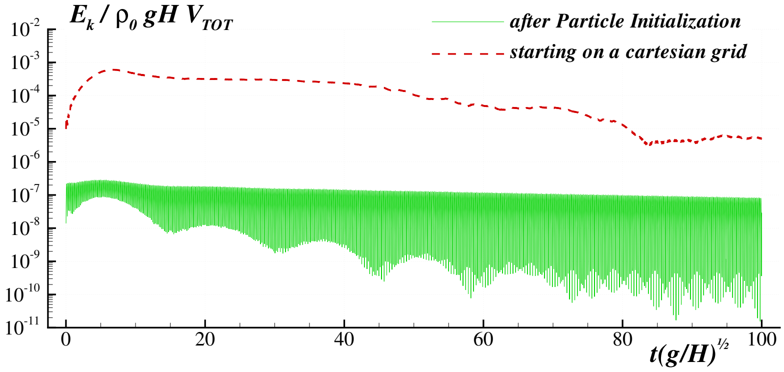

Figure 6.6.: hydorstatic solution for the trapezoidal tank ($H/dx = 50$). Time history of the kinetic energy.

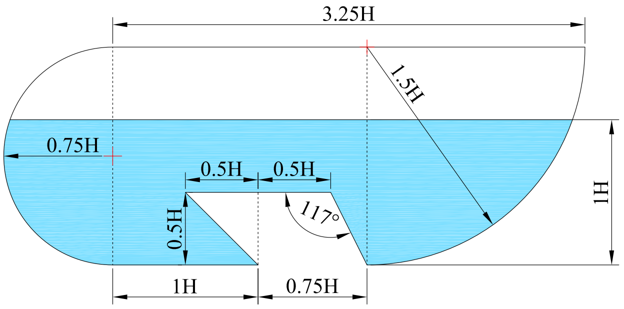

Figure 6.7.: sketch of the complex tank geometry.

As a second example, a complex geometry characterized by bended profiles with different curvatures and by acute and obtuse solid angles is considered (see figure 6.7). Because of these features, the particle initialization of such a geometry represents a very difficult problem. The top panel of figure 6.8

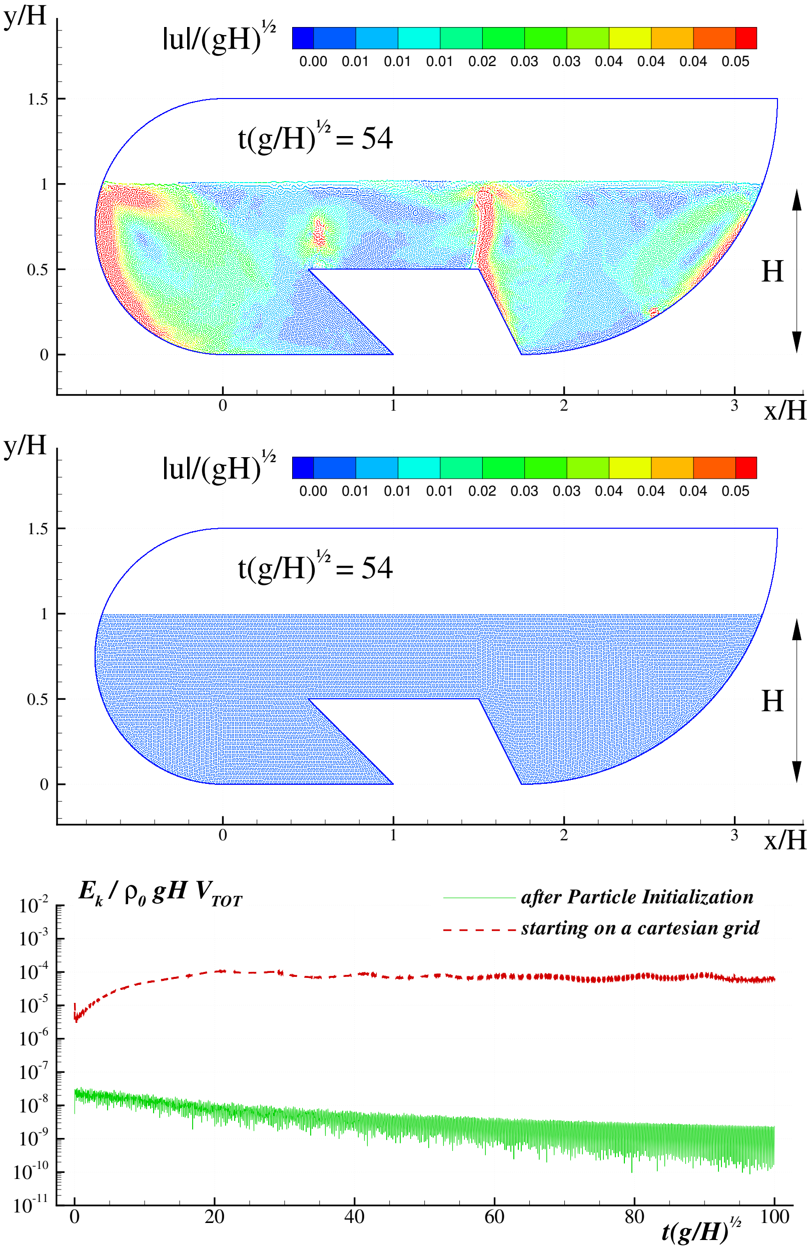

Figure 6.8.: Hydrostatic solution for a complex tank geometry. Top: evolution after initialization on a Cartesian grid. Middle: evolution after initialization through packing algorithm. Bottom: time history of the kinetic energy.

displays the fluid evolution under hydrostatic conditions after the initialization on a Cartesian grid. In this case, the generation of spurious currents and vorticity near corners and bended profiles is very strong and persists for long times. On the contrary, the use of the particle packing algorithm eliminates such an undesirable behaviour and gives a uniform particle distribution which keeps stable for long times (middle panel of figure 6.8) . The evolution of the kinetic energy confirms the findings above proving that, after the use of the proposed algorithm, particles are almost motionless (bottom panel of figure 6.8).

7 BOUNDARY CONDITION ENFORCEMENT

In engineering applications the fluid domain can be limited by several kind of boundaries (see figure 7.1): solid boundaries, free surface, inflow and outflow. The presence of those boundaries causes the truncation of the kernel support and the lack of interpolation points leads to large inaccuracies in the SPH operators. They must be accounted for and properly handled when studying these problems.

In WCSPH schemes, the free-surface boundary is easily taken into account (see section 3.3) while solid boundaries still represent a bottleneck for the method. In the following sections insights on this subject are provided. Two different approaches are proposed to take into account solid boundaries, as well as a new algorithm to detect the free surface in order to enforce special conditions and to simplify the analysis of such flows. Moreover an algorithm for simulating inflow and outflow condition is provided in order to treat continuous free-surface currents.

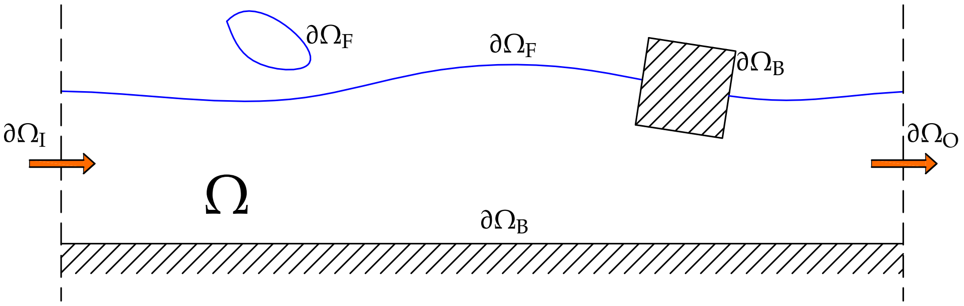

Figure 7.1.: Sketch of the fluid domain with solid boundaries, free surface, inflow and outflow.

7.1 SOLID B.C.

In the SPH framework, the definition of proper boundary conditions along solid surfaces is a quite complex matter. Indeed, near solid bodies the support of the kernel function is cut by the body profile and the interpolation accuracy rapidly decreases. For this reason, different techniques have been proposed to make up for the loss of mass and, at the same time, to impose the correct boundary conditions. Two approaches are generally used in the SPH literature: ghost particle and repulsive-type particles (see section 2 for a summary of the main techniques available in literature). In any case, both the cited methods have significant drawbacks that do not allow a general as well accurate modelling of solid boundaries. Indeed, in the standard ghost method, *ad hoc* tuning for curves and angles are needed to avoid local excess (or lack) of ghost mass (see e.g. Oger et al. 2006; Yildiz et al. 2009). On the other hand, the use of repulsive particles produces an unphysical numerical noise into the pressure field.

In the following two new different techniques are developed and applied in sections 8, 9 and 10. The first one provides a simple and accurate procedure for the description of generic solid profiles through *fixed ghost particles*(fixed in the frame of reference of the solid body) and can be regarded as a generalization of the classical *ghost-particle* method widely used in the SPH literature (see section 2).

The method is successfully applied in several 2D cases (see chapters 8, 9 and section 10.1) as well as in problems involving 3D simple geometries (see sections 8.4, 9.1 and 9.2). However, it has not been generalized for 3D generic curved surface. For this cases, in the specific the modelling of a ship hull (see section sec:dalida), another technique has been used, adapting the *normal flux* method by De Leffe et al. (2009); Marongiu et al. (2008) to the δ-SPH model.

7.1.1 Fixed ghost particle method

Here an enhanced treatment of solid boundaries is proposed by using *fixed ghost particles*. In the standard ghost particle technique at each time step any particle nearby the solid boundary is mirrored into a ghost with respect to that boundary. Conversely, in the proposed technique the ghost particles are fixed in the frame of reference of the body and the values attributed to those particles are calculated in their mirror point inside the fluid (see Figure 7.2). Then, the interpolated quantities are evaluated through a Moving-Least Square (MLS) interpolation (see e.g. Fries and Matthies 2004) of the fluid particle values. This approach allows enforcing both Dirichlet and Neumann conditions.

The algorithm to generate the fixed ghost particles is detailed in the following:

a) the solid profile is approximated by regular equispaced body nodes with a prescribed distance ds;

b) the normal and the tangent unit vectors are computed, assuming the normal vectors to point outwards from the fluid domain;

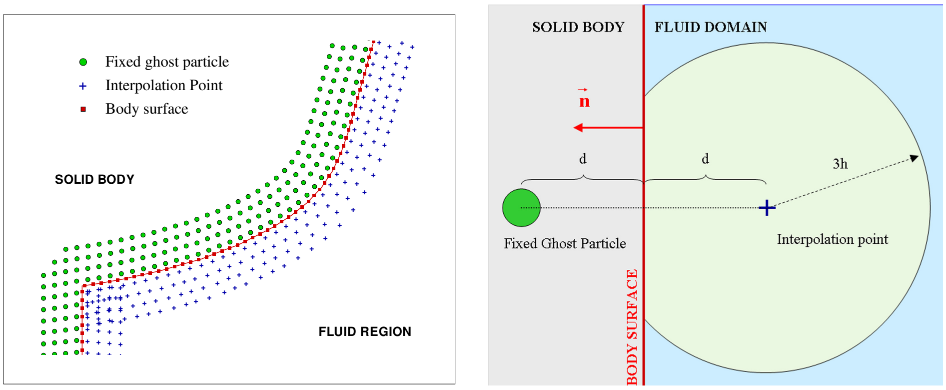

Figure 7.2.: Left: position of fixed ghost particles, body nodes and interpolation points for a generic boundary surface. Right: sketch of the interpolation procedure.

c) using the normal vector, the body nodes are moved outwards from the fluid at a distance $ds/2$ from the body profile;

d) a new profile is generated along which equispaced nodes with distance ds are set.

Such a profile represents an expansion of the body profile and the nodes along it are the fixed ghost particles. In the same way but using a vector opposite to the normal, each fixed ghost particle is associated with an interpolation point inside the fluid. This procedure is repeated to cover a body area of width equal to the kernel support radius, see Figure 7.2.

In case of singular points along the body profile, the algorithm described above is applied starting on both sides of the singularity. For rigid motions of the body the fixed ghost particles are generated once for all and then translated according to the body time evolution while if deformations occur (see e.g. 10.1) the generation of the fixed ghost particles is repeated at each time step according to the evolving body surface.

The main advantage of using the fixed ghost particles instead of the standard ghost ones is that their distribution is always uniform and does not depend on the fluid particle positions. This allows for a simple modelling of complex 2D geometries. For 3D geometries this procedure is straightforwardly extended in the case of plane walls and right angles, while it is more complex for generic curved profiles and solid narrow angles. For these cases two main difficulties arise: *i)* tessellation of complex solid volumes is not as easy as in 2D with splines; *ii)* positioning of interpolation nodes may be cumbersome for a generic solid angle. Hence, in those cases another technique is adopted.

Regarding the physical conditions to impose on fixed ghost particles, both free-slip and no-slip conditions can be implemented. In the former case the

the velocity imposed to the fixed ghost particle has to guarantee the boundary condition:

$$\mathbf{u} \cdot \mathbf{n} = \mathbf{u}_B \cdot \mathbf{n} \tag{7.1}$$

where $\mathbf{u_B}$ is the velocity of the solid boundary and $\mathbf{n}$ is the normal unit vector to the solid boundary. So the ghost velocity is given by:

$$u_{nG} = 2u_{nB} + u_{ni}, \qquad u_{\tau G} = u_{\tau i} \tag{7.2}$$

where u_{nG} and $u_{\tau G}$ are respectively the local normal and tangential component of the velocity associated with the fixed ghost particle, u_{nB} is the local normal component of the displacement velocity associated with the solid body, and u_{ni} and $u_{\tau i}$ are the local normal and tangential component of the velocity evaluated on the corresponding interpolation point. Regarding the enforcement of no-slip condition, the discussion is postponed to section 7.1.3. For what concerns the assignment of the pressure field along the solid boundaries, the Neumann boundary condition is enforced. Differentiating eq. 7.1:

$$\frac{d\mathbf{u}}{dt} \cdot \mathbf{n} + \mathbf{u} \cdot \frac{d\mathbf{n}}{dt} = \frac{d\mathbf{u}_B}{dt} \cdot \mathbf{n} + \mathbf{u}_B \cdot \frac{d\mathbf{n}}{dt} \tag{7.3}$$

then, using the momentum equation one obtains:

$$\frac{\partial p}{\partial n} = -\rho \left[\frac{d\mathbf{u}_b}{dt} \cdot \mathbf{n} + (\mathbf{u}_B - \mathbf{u}) \cdot \frac{d\mathbf{n}}{dt} - \mathbf{g} \cdot \mathbf{n} \right], \tag{7.4}$$

that is the correct Neumann condition for the pressure for a rigid moving boundary. Note that alog a body in pure translation motion the term $d\mathbf{n}/dt$ vanishes.

The use of an MLS interpolant (see Colagrossi 2005, for details) ensures an accurate mirroring of the flow quantities. For example, considering the right sketch of figure 7.2, the pressure of a generic ghost particle for a still body subjected to the gravity force is evaluated as follows:

$$p_G = \sum_{j \in \text{Fluid}} p_j \, W^{MLS}(\mathbf{r}_j) \, dV_j + 2d \, \rho \, \mathbf{g} \cdot \mathbf{n} \tag{7.5}$$

and the Moving Least-Squares kernel W^{MLS} is given by:

$$\begin{cases} W^{MLS}(\mathbf{r_j}) = \mathbf{M}_i^{-1} \, \mathbf{e}_1 \cdot \mathbf{b}_{ij} \, W(\mathbf{r}_j) \\ \mathbf{b}_{ij}^T = [1, (x_j - x_i), (y_j - y_i), (z_j - z_i)]; \qquad \mathbf{e}_1^T = [1, 0, 0, 0] \\ \mathbf{M}_i = \sum_j \mathbf{b}_{ij} \otimes \mathbf{b}_{ij} \, , W(\mathbf{r}_j) \, dV_j \end{cases} \tag{7.6}$$

Particular care has to be paid to the geometrical singularities, since a naive mirroring procedure would result in incorrect placement of the interpolation point. Measuring the angles on the fluid side, the simplest example is that given by the angle $\theta = \pi/2$ represented in Figure 7.3 where the fixed ghost particles are represented by circles and the interpolation points inside the fluid by crosses. The left panel shows how interpolation points are defined from fixed ghost particles located along one side of the angle. In this case we simply use the normal to the solid boundary to define interpolation points from the fixed ghost particles. Considering the fixed ghost particles located within the angle region, a central symmetry is used, see right panel of Figure 7.3. Thanks to this procedure, adjacent fixed ghost particles are always associated to interpolation points themselves adjacent. This feature is very important to get a regular behaviour of the fluid particles. The same procedure is applied for angles from $\theta = \pi/2$ to $\theta = \pi$.

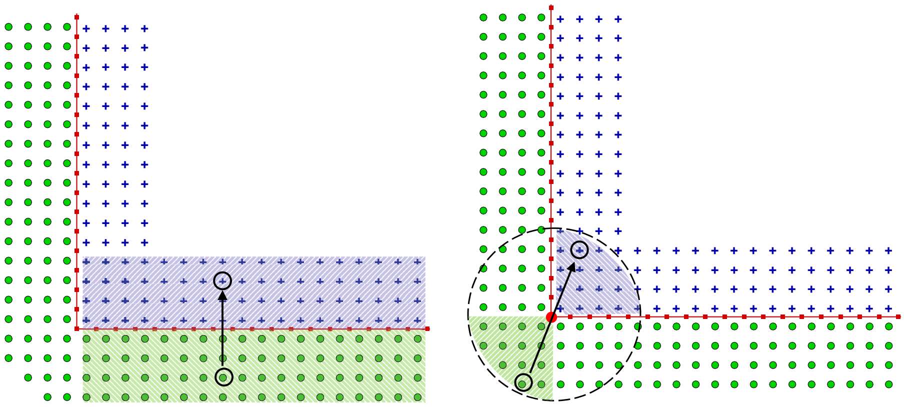

Figure 7.3.: Interpolation points definition for $\theta = 3\pi/2$. The dashed circle in the right panel represents the kernel support radius.

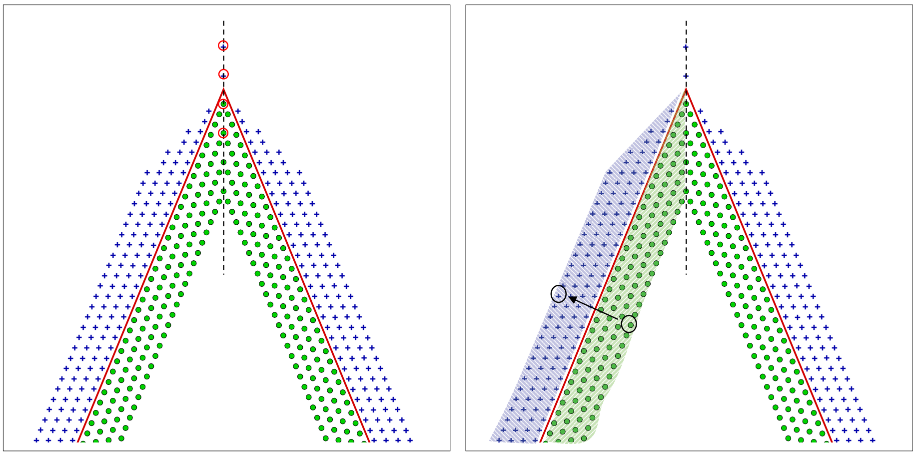

Figure 7.4.: Interpolation points definition for $\theta = \pi/4$.

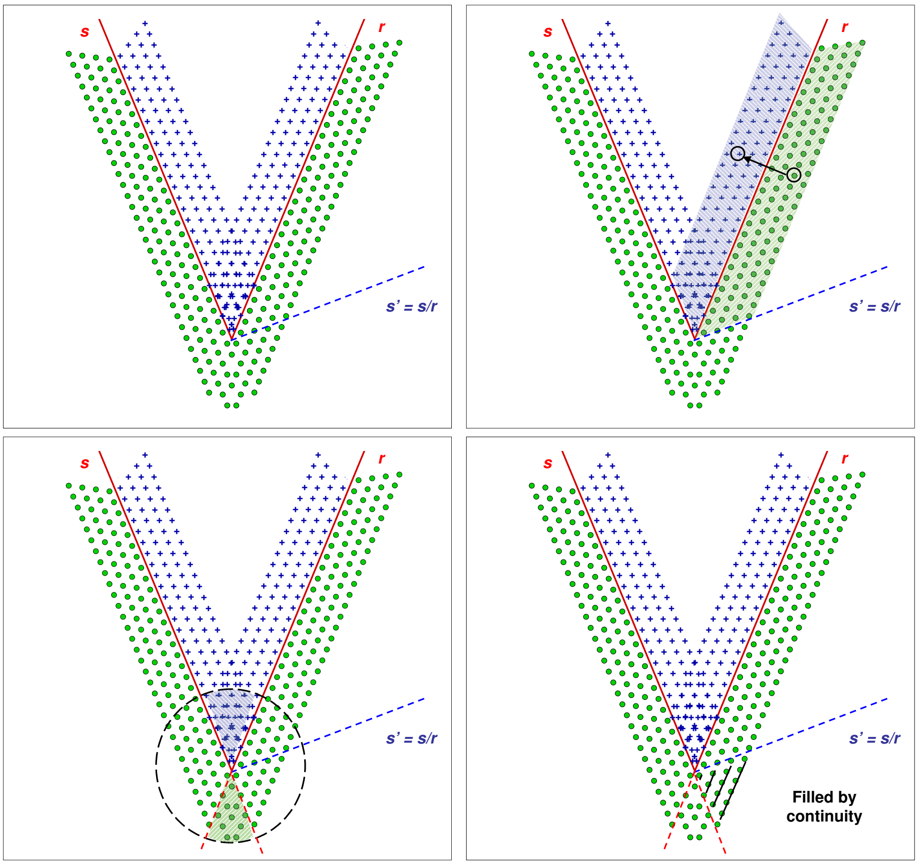

Figure 7.5.: Interpolation points definition for $\theta = 7\pi/4$. The dashed circle in the left bottom panel represents the kernel support radius.

The case with $\theta > \pi$ is slightly more difficult. As an example, in Figure 7.4 we consider an angle $\theta = 7\pi/4$. In this case, some ghost particles are placed along the bisector line of the angle and interpolation points are defined by mirroring them with respect to the vertex. Interpolation points further than one kernel support from the vertex are avoided. Their corresponding ghost particles take the physical properties from the nearest ghost particle along the bisector line. Applying this strategy in the case illustrated in figure 7.4, the two higher fixed ghost particles on the bisector line (surrounded in red in left panel) will be associated with interpolation points (also surrounded in red), whereas the two lower ones will use the value from the highest interpolation point among the previous ones. These interpolation points on the bisector line are important for avoiding any fluid particle travelling towards the body vertex to penetrate into the body. Finally, the definition of interpolation points along each wall constitutive of the angle is made through the same procedure as in the previous case, see right panel of Figure 7.4. Note that for angles close to 2π this technique is not consistent and close to the body vertex one should use two sets of fixed ghost particles with a visibility criterion to switch from one to the other.

Other difficulties arise for angles smaller than $\pi/2$. Figure 7.5 shows the example of $\theta = \pi/4$. For the sake of simplicity, let us denote by $\mathbf{s}$ and $\mathbf{r}$ the straight lines forming the angle θ, and by $\mathbf{s'}$ the mirroring of $\mathbf{s}$ with respect to $\mathbf{r}$, noted $\mathbf{s'} = \mathbf{s}/\mathbf{r}$ (see top left panel). Ghost particles between $\mathbf{r}$ and $\mathbf{s'}$ are mirrored with respect to $\mathbf{r}$ (top right panel). The fixed ghost particles located in the angle between $\mathbf{s}$ and $\mathbf{r}$ are mirrored by a central symmetry as previously (see bottom left panel).

Finally, the ghost particles in the region between $\mathbf{s'}$ and the extension of $\mathbf{s}$ are split in rows parallel to $\mathbf{r}$ (see right bottom panel). This region is covered by continuity with respect to the adjacent solid regions. In other words, we assign to all the particles of each row of this region the interpolation points associated to the particle at the intersection between that row and the $\mathbf{s'}$ line (which indeed coincides with that of the particle at the intersection between the row and the extension of $\mathbf{s}$). It is simple to prove that, thanks to this procedure, the quantities associated to adjacent interpolation nodes are again mirrored on adjacent boundary particles.

Evaluation of hydrodynamic loads using ghost fluid

In SPH the forces on solid bodies are generally evaluated integrating the surface stresses along the body surface. However, the use of ghost particles permits to estimate loads on solid bodies through another technique that relies on a volume integral over the ghost fluid domain (see e.g. Doring 2005). In the following an alternative formulation of this approach is given showing the equivalence, at continuous level, with the direct estimate of surface integrals.

The fluid and solid domains are denoted by Ω and Ω_B respectively. Denoting by $\mathbb{T}$ the stress tensor, the global force on the body is:

$$\mathbf{F}_{surf} = \int_{\partial\Omega_B} \mathbb{T} \cdot \mathbf{n} \, dS \,, \tag{7.7}$$

where $\mathbf{n}$ is the unit outward normal to the solid profile. In the SPH framework, $\mathbb{T}$ is generally replaced by its smoothed approximation $\langle\mathbb{T}\rangle$, that is:

$$\mathbf{F}_{surf} = \int_{\partial\Omega_B} \langle\mathbb{T}\rangle \cdot \mathbf{n} \, dS \,. \tag{7.8}$$

Assuming the flow field to be mirrored on the solid body through proper techniques (e.g., ghost particles, boundary particles etc.), we can write:

$$\langle\mathbb{T}\rangle(\mathbf{r}) = \int_{\Omega} \mathbb{T}' \, W(\mathbf{r}' - \mathbf{r}) \, dV' + \int_{\Omega_B} \mathbb{T}^* \, W(\mathbf{r}^* - \mathbf{r}) \, dV^* \,, \tag{7.9}$$

where the starred variables indicate quantities mirrored over the solid domain Ω_B. Substituting (7.9) into (7.8) and using the divergence theorem and the symmetry properties of the kernel function, it is possible to prove that the following equality holds:

$$\mathbf{F}_{\text{surf}} = \int_{\Omega_B} dV \int_{\Omega} (\mathbb{T}^* + \mathbb{T}) \cdot \nabla W(\mathbf{r}^* - \mathbf{r})\, dV^* + \mathcal{O}(h)\,, \tag{7.10}$$

where h is the smoothing length and ∇ indicates the differentiation with respect to the position $\mathbf{r}$. When equations (7.8) is discretized, we get:

$$\mathbf{F}_{\text{surf}} = \sum_k \langle \mathbb{T} \rangle_k \cdot \mathbf{n}_k\, S_k \tag{7.11}$$

where k indicates quantities associated with nodes along the solid profile and $\langle \mathbb{T} \rangle_k$ is obtained by interpolation over the fluid domain. Conversely, equation (7.10) gives:

$$\mathbf{F}_{\text{surf}} = \sum_j \sum_i (\mathbb{T}_j + \mathbb{T}_i) \cdot \nabla_i W_{ij}\, V_i\, V_j \tag{7.12}$$

where i and j denote quantities associated with the fluid particles and the ghost particles respectively. Note that equations (7.11) and (7.12) are only partially equivalent since the divergence theorem at the discrete level is approximately valid. However, differently from (7.11), equation (7.12) does not require a further smoothing procedure as quantities already computed in the momentum equation can be exploited. For these reasons it is simpler and faster in practical applications and, in the following, is preferred to equation (7.11).

Since the inner summation of (7.12) (or equivalently, the inner integral of equation 7.10) approximates the divergence of the stress tensor, at coding level it is sufficient to substitute the corresponding operator of the SPH scheme. In the present case, this leads to the following substitution:

$$\sum_j (\mathbb{T}_j + \mathbb{T}_i) \cdot \nabla_i W_{ij}\, V_j \longrightarrow \sum_j \left[-\,(p_j + p_i) + \rho_0\, \nu\, \pi_{ij} \right] \nabla_i W_{ij}\, V_j\,, \tag{7.13}$$

in which the first term on the right-hand side represents the pressure component and the second acts as the viscous component of the stress tensor.

7.1.2 Normal flux method

The fixed ghost particle method is fairly robust and accurate but, unfortunately, this technique is difficult to manage in 3D framework when solid surfaces are characterized by complex geometries. To this purpose, the technique recently presented by De Leffe et al. (2009) has been adopted. Such a technique has been developed in the context of Riemann-SPH methods and in the present work is reformulated in the context of the standard SPH scheme. The advantage is that the kernel truncation due to the boundary is evaluated through a surface integral over the intersection between the solid surface and the kernel support. In this way only an accurate discretization of solid surface is needed, avoiding any tessellation of solid volume. On the other hand, because of the approximation underlying, the accuracy of the present method is in principle lower respect to fixed ghost particles as shown in the following. Further, it is not possible to enforce no-slip conditions with the present formulation. The method has been applied and validated for the problem of a ship in stationary forward motion (see section 10.2. Starting from relation 3.19 for the gradient estimate of a generic function, it is possible to rewrite the SPH discrete differential operators near the solid boundaries as follows:

$$\begin{cases} \langle \nabla \cdot \mathbf{u} \rangle_i = \sum_j \left(\mathbf{u}_j - \mathbf{u}_i\right) \cdot \nabla W_{ij} \, V_j + \sum_k \left(\mathbf{u}_k - \mathbf{u}_i\right) \cdot \mathbf{n}_k \, W_{ij} \, S_k \\ \\ \langle \nabla p \rangle_i = \sum_j (p_j + p_i) \nabla W_{ij} \, V_j + \sum_k (p_k + p_i) \, \mathbf{n}_k \, W_{ij} \, S_k \end{cases} \tag{7.14}$$

The summations on j are performed on the fluid particles in the neighbourhood of the particle i while the summations on k are made on the nodes of the discretized boundary $\partial\Omega$ (see sketch in figure 7.6). As mentioned at the beginning of this chapter, it is not necessary to evaluate the boundary terms on the free surface and, consequently, they have to be considered only on the solid surface and are used to enforce the solid boundary conditions. It is important to underline that De Leffe et al. (2009) correct these expressions through a Shepard normalization (i.e. diving by Γ) since the kernel truncation leads to inaccuracies in the gradient estimation of equation 3.19. Nonetheless, in the present thesis this correction is not taken into account because of the difficulties occurring when the free-surface pierces the solid body. Further, it would require a switch for the particles far from the solid bodies for which this normalization is not required. In any case, in equations 7.14 the boundary terms are zero inside the fluid and, therefore, the expressions for $\mathrm{sphdiv}\mathbf{u}^B$ and $\langle \nabla p \rangle^B$, described in chapter 3, are recovered.

In the first equation of (7.14) the value $\mathbf{u}_k$ is replaced by the velocity of the solid surfaces at the position $\mathbf{r}_k$. Conversely in the second equation of (7.14) the pressure p_k on the solid surfaces is not known a priori. Then, a Taylor expansion around the particle i is used:

$$p_k = p_i + \nabla p_i \cdot (\mathbf{r}_k - \mathbf{r}_i) + \mathcal{O}\left(\|\mathbf{r}_k - \mathbf{r}_i\|^2\right) . \tag{7.15}$$

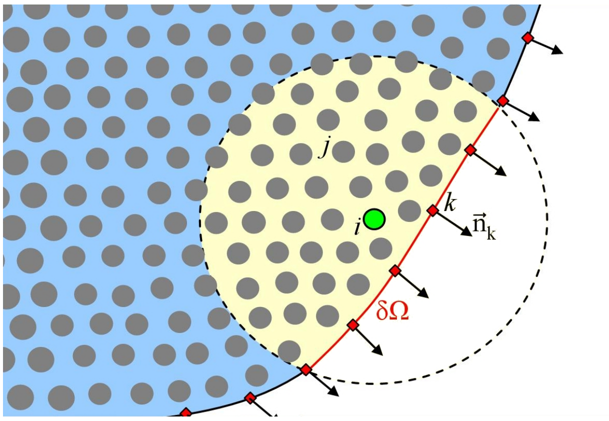

Figure 7.6.: Sketch of the solid boundary treatment.

that is:

$$\begin{aligned} p_k &= p_i + \frac{\partial p_i}{\partial n_j}(\mathbf{r}_k - \mathbf{r}_i)\cdot \mathbf{n}_k + \frac{\partial p_i}{\partial \tau_k}(\mathbf{r}_k - \mathbf{r}_i)\cdot \boldsymbol{\tau}_k + \\ &+ \frac{\partial p_i}{\partial b_k}(\mathbf{r}_k - \mathbf{r}_i)\cdot \mathbf{b}_k + \mathcal{O}\left(\|\mathbf{r}_k - \mathbf{r}_i\|^2\right) , \end{aligned} \tag{7.16}$$

where $\boldsymbol{\tau}_k$ and $\mathbf{b}_k$ are the unit vectors tangent to the solid profile at $\mathbf{r}_k$, and $(\mathbf{n}_k, \boldsymbol{\tau}_k, \mathbf{b}_k)$ is an orthogonal triad. The subsequent step is to approximate the partial derivatives of the pressure field along the normal and tangential directions. In the latter case, one simply assumes that the body forces are predominant with respect to the inertial forces and write:

$$\frac{\partial p_i}{\partial \tau_k} = \rho\,\mathbf{g}\cdot\boldsymbol{\tau}_k + \mathcal{O}(h), \qquad \frac{\partial p_i}{\partial b_k} = \rho\,\mathbf{g}\cdot\mathbf{b}_k + \mathcal{O}(h). \tag{7.17}$$

Conversely, the normal pressure gradient in (7.16) can be derived by the projection of momentum equation in the $\mathbf{n}_k$ direction:

$$\frac{\partial p_i}{\partial n_k} = \rho\,(\,\mathbf{g}\cdot\mathbf{n}_k - \mathbf{a}_i\cdot\mathbf{n}_k\,) \tag{7.18}$$

where $\mathbf{a}_i$ is the acceleration of the i-th particle. A simple approximation of $\mathbf{a}_i$ is derived in the following. At time t, the particle i close to the solid body is characterized by a normal velocity $\mathbf{u}_i\cdot\mathbf{n}_k$. Due to the impermeability of the solid surface, a wave signal, travelling at the speed of sound c_0, is reflected by the wall and comes back to the particle i after a time interval equal to $(\mathbf{r}_k - \mathbf{r}_i)\cdot\mathbf{n}_k/c_0$ nullifying the normal velocity $\mathbf{u}_i\cdot\mathbf{n}_k$. Therefore the acceleration $\mathbf{a}_i\cdot\mathbf{n}_k$ can be expressed as follows:

$$\mathbf{a}_i\cdot\mathbf{n}_k = -\frac{c_0\,(\mathbf{u}_i\cdot\mathbf{n}_k)}{(\mathbf{r}_k - \mathbf{r}_i)\cdot\mathbf{n}_k}\,. \tag{7.19}$$

Then, substituting (7.18) and (7.17) in (7.16), we, finally, get:

$$p_k = p_i + c_0 (\mathbf{u}_i \cdot \mathbf{n}_k) + \mathbf{g} \cdot (\mathbf{r}_k - \mathbf{r}_i) . \tag{7.20}$$

This expression is used to evaluate the boundary term of the pressure gradient given in (7.14). Equation (7.20) is the same derived by De Leffe et al. (2009) in the framework of Finite Volume with Characteristic Flux scheme (for more details see Ghidaglia and Pascal 2005).

7.1.3 No-slip B.C. on solid surfaces

Ghost fluid methods give very good results when free-slip conditions are imposed on solid boundaries. Conversely, when dealing with no-slip conditions several difficulties arise, a more complex mirroring technique being necessary to accurately model the viscous stress at the wall. In particular, it is common practice to introduce constraints on the tangential velocity component of the ghost particles $u_{\tau G}$ in order to enforce such a condition. The most representative mirroring techniques in SPH literature impose ghost-particle tangential velocity by:

- Explicitly imposing boundary velocity, that is $u_{\tau G} = u_{\tau B}$, where $u_{\tau B}$ is the tangential velocity component of the solid body.
- Anti-symmetric mirroring, that is $u_{\tau G} = 2u_{\tau B} - u_{\tau i}$ where $u_{\tau i}$ is the tangential component of the velocity evaluated on the ghost interpolation point (or of the matching fluid particle for the classical ghost method)
- The method by Takeda et al. (1994): each fluid particle is associated with its own set of ghost particles whose tangential velocity depends on the distance of the fluid particle from the wall, that is:

  $$u_{\tau G} = (u_{\tau B} - u_{\tau i}) \frac{d_i^B}{d_G^B} + u_{\tau B}$$

  where d_i^B and d_G^B are respectively the distance of the fluid particle and ghost particle from the solid boundary.

An in-depth description of the properties and convergence of the differential operators using these techniques has been given by Macià et al. (2011). In that work it is shown that Takeda's method, among the others, results in the most accurate approximation of the viscous tensor $\mathbb{V}$ close to the boundary.

Another issue well documented in literature regards numerical instabilities that occur in simulations of viscous flows in laminar regime at Reynolds number $\mathcal{O}(100)$ (see e.g. Basa et al. 2008; Federico 2010; Watkins et al. 1996). It is observed that, in those case, the particles close to the walls rapidly loose uniform distribution, leading to clumping and substantial failure of the simulation. Recently, De Leffe et al. (2011) has proved that this behaviour is due to the velocity divergence operator evaluation close to the boundaries. Indeed, the alteration of the tangential component of the ghost particles produces large errors in the continuity equation. With a simple but fundamental intuition, they suggested to use to different velocities for ghost particles: one corresponding to free-slip condition to be used for the velocity divergence estimation, and another one with the adopted mirroring scheme for no-slip condition to be used in the momentum equation.

7.2 FREE-SURFACE B.C.

If an interface between a liquid and a gaseous phase occur, such that the latter does not influence the evolution of the former, this interface can be considered as a free surface. Free-surface flows can be solved by modelling only the liquid phase, provided that suitable boundary condition are enforced on it. Denoting by $\partial\Omega_F$ the free-surface boundary (see 7.1), a kinematic and a dynamic conditions have to be imposed on $\partial\Omega_F$. The first one implies that the fluid particles initially on $\partial\Omega_F$ will remain on the boundary. This condition is intrinsically satisfied by the Lagrangian nature of the SPH method. Differently, the dynamic boundary condition states that, in absence of surface tension, the neither normal or tangential stresses stand at the interface $\partial\Omega_F$. In section 3.1.1 is has been shown that this condition is implicitly satisfied in weakly compressible SPH schemes provided that the external pressure is null and the momentum equation is consistently derived from the chosen continuity equation (see Bonet and Lok 1999, for more details).

This feature is retained in the $\delta-\mathrm{SPH}$ model and, thanks to this, it is not necessary to detect at each time step the particles belonging to the free surface to explicitly enforce the dynamic boundary condition as in incompressible schemes. This is a worthy advantage especially for 3D flows where the free surface configuration/evolution may be very complex.

In any case, in order to analyse simulations for which the free-surface pattern is not trivial (fragmentations, air entrapment, etc.) and to face a larger range of problems it is useful to know which particles belong to the free surface. This detection, indeed, can be required for the enforcement of suitable boundary conditions along the free surface (surface tension, isothermal condition, etc) in order to deal with different physical phenomena and flow behaviours. For example in this thesis the isothermal condition on the free surface is required to correctly solve internal energy equation of system (5.1).

Dilts (2000) developed an algorithm for the free-surface tracking that can detect free-surface particles in a robust and reliable way and that is applicable to any meshless method. However it is quite difficult to implement, especially in its extension to three-dimensional simulations proposed by Haque and Dilts (2007). Here a new method is proposed whose accuracy is comparable to that of the method proposed by Dilts. It is possible, indeed, to catch small cavities of diameter as small as $2h$ (h being the smoothing length) and fluid elements with dimension smaller than h (like jets and drops). Thanks to these valuable features, the proposed algorithm can be used at each time-step of the simulations, without an appreciable increase of the CPU-time.

Moreover, free-surface detection permits strong improvement of the post-processing phase, particularly in three-dimensional simulations with complex flow features. In fact, if one uses merely a SPH output, flow analysis is problematic since data are known on scattered points, and it is difficult to obtain contour plots, slices and iso-surfaces. Such an analysis can be performed in a straightforward way using standard tools if data are interpolated on a regular grid. In this context it is useful to define a level-set function among the grid nodes. This function permits to distinguish between nodes inside and outside of the fluid domain. To define the level-set function the detection of the free-surface particles is required as a first step. Besides its utility for flow analysis the definition of this function may be useful to extend remeshing techniques (see e.g. Chaniotis et al. 2002) to free-surface flow problems.

7.2.1 Tracking free-surface particles: 2D algorithm

The algorithm is composed of two steps: in the first one the properties of the renormalization matrix, defined by Randles and Libersky (1996), are used to find particles next to the free surface. This first step strongly decreases the number of particles that will be processed in the second step. In the second step the algorithm, by means of geometric properties, detects particles that actually belong to the free surface and evaluates their local normals.

In order to validate it the algorithm has been applied to simple geometries as well as to a dam break problem (see section 8.4) which sketch and initial conditions are displayed in figure 8.27. The complex free surface behaviour of the flow after the impact is displayed in figure 7.7. In this figure the plotted rectangles delimit the zones which are enlarged in figure 7.8 to highlight the flow complexity there, and which are the most challenging for the detection algorithm.

The method used to perform the first step of the algorithm was proposed by Doring (2005); it exploits eigenvalues of the renormalization matrix (Randles and Libersky 1996) defined as:

$$\mathbf{B}(\mathbf{r}_i) = \left[\sum_j \nabla W_{ij} \otimes (\mathbf{r}_j - \mathbf{r}_i)\, V_j \right]^{-1} \tag{7.21}$$

where V_j is the volume of the j-th particle and W_{ij} is the interpolating kernel centred on particle j and evaluated in the position $\mathbf{r}_i$. The spatial derivatives of W_{ij} are referred with respect to the position $\mathbf{r}_i$.

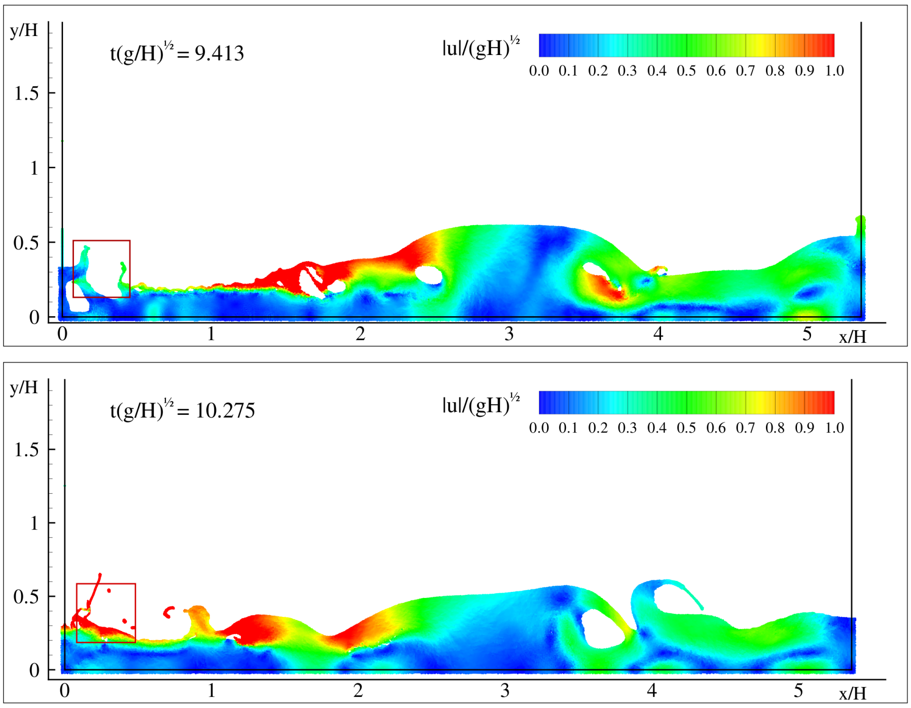

Figure 7.7.: Different time instants of the impact flow after the dam-break. The rectangles delimit the zones enlarged in figure 7.8.

Doring showed that the value of the minimum eigenvalue, λ, of the matrix $\mathbf{B}^{-1}$ depends on the spatial organization of the particles j in the neighbourhood of the considered calculation point i. When going away from the fluid domain this eigenvalue λ tends theoretically to 0 while inside this domain λ tends theoretically to 1. This allows to determine regions of the fluid domain where the free surface can lie or not. Let us define $\mathbb{N}$ as the set of all the fluid particles and $\mathbb{F} \subset \mathbb{N}$ as the subset of particles belonging to the free surface. Then, computing λ for each particle, it is possible to further define three complementary subsets: $\mathbb{E}$ composed by particles belonging to thin jets and drops, characterized by low values of λ; $\mathbb{I}$ composed by interior particles far from the free surface, characterized by high values of λ; and $\mathbb{B}$ composed by particles which are close to the free surface or are in regions of the domain where particles are not uniformly spread. Particles belonging to the last subset are characterized by intermediate values of λ. We have that $\mathbb{N} = \mathbb{E} \cup \mathbb{I} \cup \mathbb{B}$. The free-surface particles subset $\mathbb{F}$ is thus composed of all the particles of subset $\mathbb{E}$ and a part of the elements of subset $\mathbb{B}$.

To identify these subsets it is possible to define threshold values of λ which depend on the considered kernel. Here a renormalized Gaussian kernel shape is used (see Colagrossi and Landrini 2003), with a support radius equal to $3h$, where h is the smoothing length and is equal to $1.33\,dx$. dx is the average

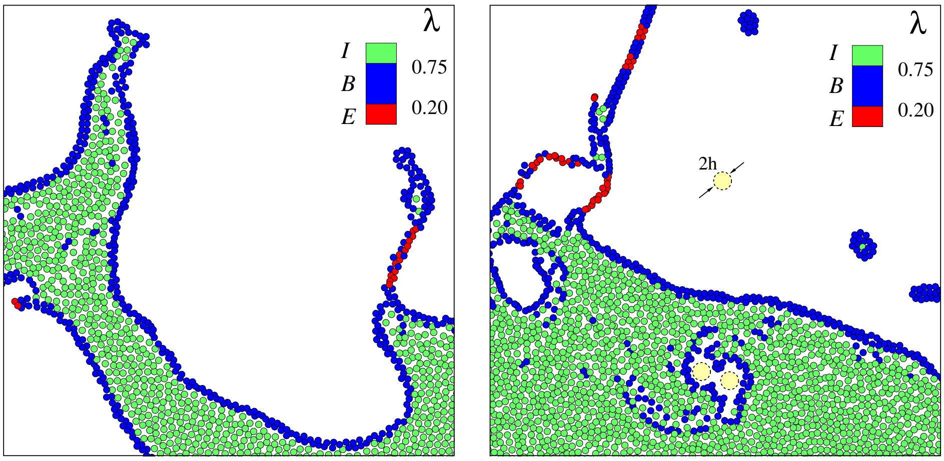

Figure 7.8.: Values of the minimum eigenvalue λ of the matrix $\mathbf{B}^{-1}$. Red particles belong to subset $\mathbb{E}$; green particles belong to subset $\mathbb{I}$; blue particles belong to subset $\mathbb{B}$.

particle spacing which means that in two dimensions a particle has $\simeq dx^2$ for volume and an average number of neighbours equal to 50. All the results and the conclusions presented in this work have to be considered valid only for the aforementioned h/dx ratio. Several tests have been performed to set the proper thresholds for λ. Being i the particle under examination, the values found are the following:

$$\begin{cases} i \in \mathbb{E} & \Longleftrightarrow & & \lambda \leqslant & 0.20 \\ i \in \mathbb{B} & \Longleftrightarrow & 0.20 & < \lambda \leqslant & 0.75 \\ i \in \mathbb{I} & \Longleftrightarrow & 0.75 & < \lambda & \end{cases} \tag{7.22}$$

In this way the first step of the algorithm computes the minimum eigenvalue for each particle and gives a first rough detection of the free surface. This operation has a low computational cost especially if the renormalization matrix is already computed for solving the SPH governing equations, as *e.g.* in the SPH scheme proposed in Randles and Libersky 1996. In figures 7.8 one can observe the result of this first detection. Particles next to the free surface and near cavities are correctly detected but this also happens for some particles within internal fluid regions characterized by non-uniform distribution. Conversely, particles which belong to drops and thin jets are easily captured by the lower threshold and directly identified as free-surface particles (red coloured).

In the second step of the algorithm, a more precise and reliable control is performed on particles belonging to $\mathbb{B}$ in order to complete the free surface detection. The proposed method is based on the fact that, inside the fluid domain, the sum of the kernel gradient over neighbours is very close to zero. When a particle, instead, is near the free surface, such sum is a good approximation of the local normal $\mathbf{n}$ to the free surface (see Randles and Libersky

1996). Since the accuracy of the evaluation of this vector depends on the particle disorder, it is possible to get a more accurate evaluation by using again the renormalization matrix:

$$\mathbf{n}(\mathbf{r}_i) = \frac{\xi(\mathbf{r}_i)}{|\xi(\mathbf{r}_i)|}; \quad \xi(\mathbf{r}_i) = -\mathbf{B}(\mathbf{r}_i) \sum_j \nabla W_{ij} V_j \tag{7.23}$$

This is a standard way to improve accuracy of the SPH interpolation within the fluid domain, (see e.g. Randles and Libersky 1996). Here it is used the same principle to improve the accuracy of the evaluation of the local normal. Once this vector **n** is known, it is possible to define a region of the domain like the one sketched in figure 7.9. The algorithm then checks whether or not at least one neighbour particle lies in this region, hereinafter referred to as *scan region*. If no neighbour is found inside it, the candidate particle belongs to the free surface. It must be noted that inside the fluid domain this region cannot be void since $h = 1.33\,dx$.

This control is carried out by the algorithm in the following way. Let us denote by $i \in \mathbb{B}$ the particle that is under examination and by $j \in \mathbb{N}$ the neighbour of i which is included in a $3h$ radius distance. Let us define also the point T at distance h from i in the normal direction and the unit vector $\boldsymbol{\tau}$ perpendicular to $\mathbf{n}$. The conditions to assess whether particle i belongs or not to the free surface are therefore:

$$\begin{cases} \forall j \in \mathbb{N} \left[|\mathbf{r}_{ji}| \geqslant \sqrt{2}h, |\mathbf{r}_{jT}| < h \right] & \Rightarrow \quad i \notin \mathbb{F} \\ \forall j \in \mathbb{N} \left[|\mathbf{r}_{ji}| < \sqrt{2}h, |\mathbf{n} \cdot \mathbf{r}_{jT}| + |\boldsymbol{\tau} \cdot \mathbf{r}_{jT}| < h \right] & \Rightarrow \quad i \notin \mathbb{F} \\ \text{otherwise} & \quad\quad\; i \in \mathbb{F} \end{cases} \tag{7.24}$$

where notation $A_{ij} = A_i - A_j$ has been used. If the first condition is true it means that the neighbour under examination is in the dark grey region (S1) in

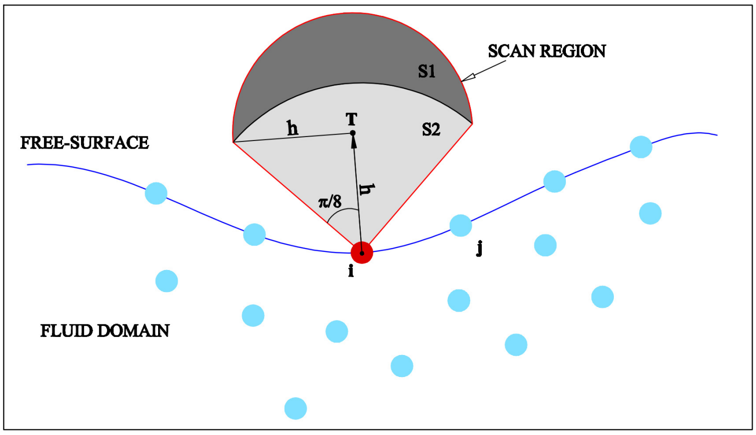

Figure 7.9.: Sketch of the regions used in the algorithm.

figure 7.9 while, if the second condition is true, it means that the neighbour is in the pearl grey region (S2). The two regions together form the *scan region*.

If any neighbour is located in the *scan region* it means that there is no cavity in the normal direction, or that this cavity has a diameter less than $2h$, so that particles inside it are deeply interacting and it is not a true cavity. Therefore through this process the free surface of cavities of diameter larger than $2h$ are tracked.

The choice of the shape of the *scan region*, composed by a half circle and a half square rather than by a simple circle for instance, is explained in the following. In top sketch of figure 7.10 a uniform distribution of particles is considered. In such a configuration only the first row of particles should be detected as free surface. In the left part of the sketch the *scan region* is reported for a particle belonging to the second row. Two particles are present in the *scan region* which means that the second row is not detected as free surface. On the right part of the same sketch circles with diameter equal to h have been reported in order to show that also the *arc-method* proposed by Dilts (2000) gives the same result. In the bottom sketch of figure 7.10 a divergence-free stretching is applied to the previous particle distribution. Due to this

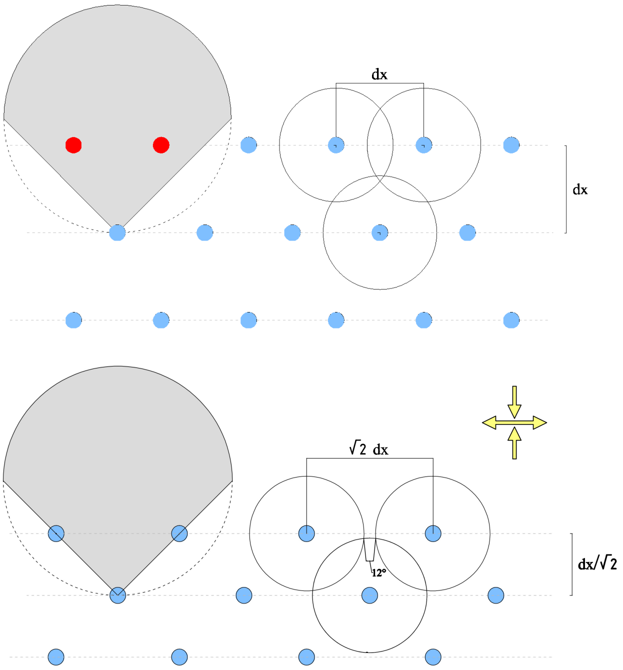

Figure 7.10.: Sketch of the *scan region* applied on uniform distribution (top panel) and on free-divergence stretched distribution (bottom panel). On the right a comparison with the *arc method*, (see Dilts 2000).

stretching, the horizontal distances between the particles are equal to $\sqrt{2}dx$ while the vertical ones are equal to $dx/\sqrt{2}$. There is hence a ratio 2 between these two distances. It can be considered as a limiting case: for a ratio 2 or higher, the considered particle of the "second row" belongs to the free surface, for a lower ratio it does not belong to it. Using the procedure described in Dilts (2000) an arc of 12° is not covered by other neighbour circles; hence the particles of the second row are considered as free-surface particles. This occurs also using the proposed algorithm since the *scan region* is now empty. If a fully circular shape was used as *scan region*, the particles of the second row would not be detected as free-surface particles.

Other shapes could be adopted as *scan region*. Anyway, in order to correctly detect the free surface, two requirements have to be satisfied: a) the detection of circular cavities of diameter equal to $2h$, b) in the example discussed above the second row of particles in bottom plot of figure 7.10 has to be detected as free-surface.

It can be noticed that for some particle distributions, e.g. for thin jets, the sum of the kernel gradient can go to zero, giving wrong values for vector $\mathbf{n}$. However, in this circumstance the eigenvalue λ will be very low and the particle will hence have already been detected as a free-surface particle in the first step of the algorithm. This first step has thus two functions: it is an efficient selection allowing to quickly perform the second step, and a tool to detect particles belonging to jets and drops which could hardly be detected by the second step of the algorithm.

In the left part of figure 7.11 the algorithm is validated for an elliptic fluid domain, with 0.661 eccentricity. Since the evaluation of the free-surface normals is critical for the algorithm effectiveness, the ones calculated by the algorithm are compared to the analytical values. In this comparison a uniform distribution of particles had to be used inside the fluid domain in order to assign exact volumes to the particles. Results are reported in table 7.2.1 in terms of average relative angle error. The convergence is close to quadratic.

$h/a \times 10^{-2}$	7.52	3.76	1.88	0.94	0.63	0.38
ε	2.16	1.23	0.68	0.34	0.23	0.13

Table 7.1.: Average relative angle error between the analytically computed normals and the one evaluated by equation 7.23. h/a denotes the ratio between the smoothing length and the semi-major axis.

In the right part of figure 7.11 an elliptic cavity with minor axis equal to $2h$ was introduced in the ellipse. This cavity has thus the minimum dimension which the algorithm is able to detect. After this simple test, the algorithm is further assessed on the complex flow situations presented in figure 7.8. The free-surface particles detected by the algorithm are plotted in pink in figure 7.12. Despite the geometrical complexity of these configurations, the proposed

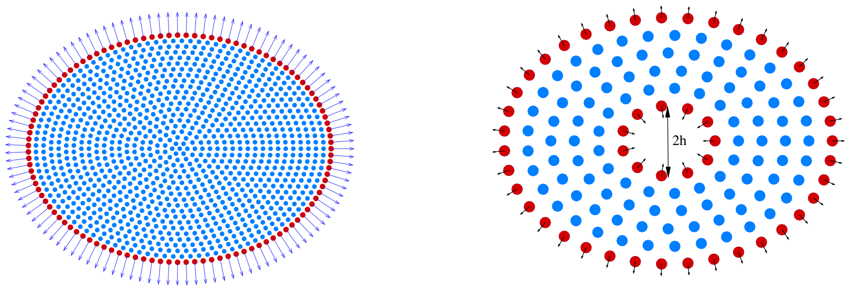

Figure 7.11.: Left: free-surface detection of an elliptic fluid domain. Right: free-surface detection in an elliptic cavity of minor axis equal to $2h$. Red particles are those detected by the proposed free-surface algorithm.

method is able to provide a very good qualitative estimation of the particles which form the boundary. In particular one can observe that approximately circular cavities of diameter just larger than $2h$ are well detected.

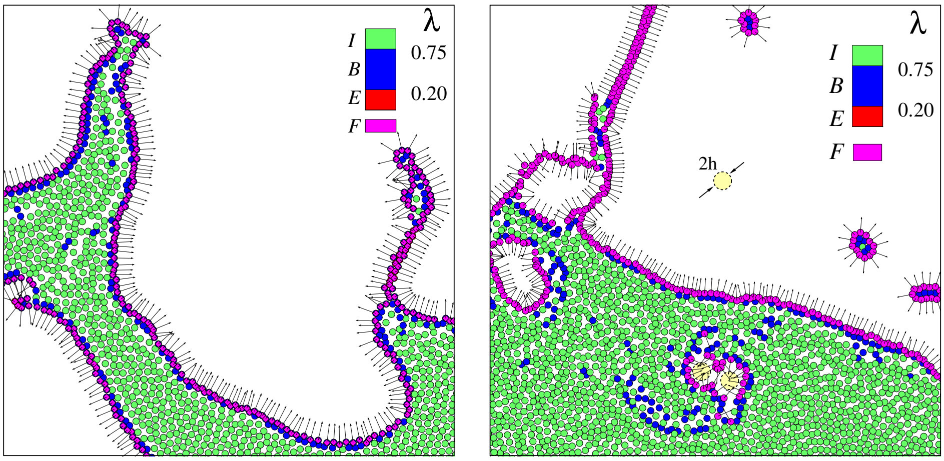

Figure 7.12.: Results after the application of free-surface detection algorithm: free-surface particles are displayed in pink with their normals; in the bottom part small cavities of $2h$ diameter are shown. A circle with dimension $2h$ is reported for comparison.

Even though the algorithm requires a cycle on the neighbours for each particle involved in the second step, it has still a very low computational cost. Actually, all but a few percent of the particles are filtered out in the first step. The CPU time cost of the algorithm is lower than 5% of the total cost of a standard SPH calculation, where the latter includes the calculation of the neighbour list and the summations for the continuity and momentum equation. Generally, it is the computation of the renormalization matrix which takes the most part of the CPU time required by the algorithm (about 90%). Hence, if the renormalization matrix is already evaluated in the numerical scheme, (see e.g. Bonet and Lok 1999; Randles and Libersky 1996), the increase of CPU time due to free-surface detection is absolutely negligible. Moreover, if the algorithm is used only for visualization or analysis purposes, it has to be applied only periodically (typically every 100 time steps), and its cost becomes again negligible.

7.2.2 Tracking free-surface particles: 3D algorithm

The extension of the algorithm to the third dimension is rather straightforward and easy to implement. The algorithm has still the same structure as the two-dimensional one: it is composed of a first step where particles far from the free surface are filtered out, and of a second step to refine the detection only to the particles belonging to the free surface. In the first step the minimum eigenvalue λ of the renormalization matrix is again needed for each particle. Again, two thresholds are used which are the same as in two dimensions. These thresholds are valid for the renormalized Gaussian kernel with support radius equal to $3h$ and $h/dx = 1.33$ (this means an average number of neighbours equal to 266).

While the first step is formally unchanged in the extension to three dimensions, the second step is slightly modified. The vector $\mathbf{n}$ is still evaluated through equation 7.23 but the conditions which define the region to scan become:

$$\begin{cases} \forall j \in \mathbb{N} \quad \left[|\mathbf{r}_{ji}| \geqslant \sqrt{2}h, |\mathbf{r}_{jT}| < h \right] & \Rightarrow \quad i \notin \mathbb{F} \\ \forall j \in \mathbb{N} \quad \left[|\mathbf{r}_{ji}| < \sqrt{2}h, \arccos\left(\frac{\mathbf{n} \cdot \mathbf{r}_{ji}}{|\mathbf{r}_{ji}|} \right) < \frac{\pi}{4} \right] & \Rightarrow \quad i \notin \mathbb{F} \\ \text{otherwise} & \qquad i \in \mathbb{F} \end{cases} \tag{7.25}$$

Therefore, in an intuitive way, the triangular region in figure 7.9 becomes a cone in three dimensions, while the semicircle becomes a hemisphere.

In the three-dimensional case it is more complex to test the algorithm and assess its accuracy. Indeed, unlike in 2D cases, in 3D problems even a qualitative evaluation of the particles belonging to the free surface could be quite difficult. In particular cavities and jets are generally blurred since particles are spread in the space in a disordered way.

In order to overcome this problem the algorithm was tested on a particle distribution with a free surface which is known *a priori*. According to this strategy two tests were performed. In the first one particles are arranged to form a sphere with a spherical cavity inside, as sketched in left panel of figure 7.13. In order to have a regular distribution, particles are placed on concentric spheres with radius increasing by dx, where dx is cubic root of the particle volume. On each sphere, particles are equispaced with a distance approximatively equal to dx. The cavity inside the sphere has a diameter equal to $4dx \simeq 3h$. This quantity is actually slightly larger than $2h$ which is the limit size for detecting a cavity. However, choosing a smaller cavity radius was not possible in practice. Indeed, this would have resulted in having too few particles distributed on the cavity surface, resulting in a bad approximation of their volumes, and consequently providing an inappropriate test of the algorithm. The particle distribution is shown in the right panel of figure 7.13. In such a view it is not possible to detect the cavity inside the sphere.

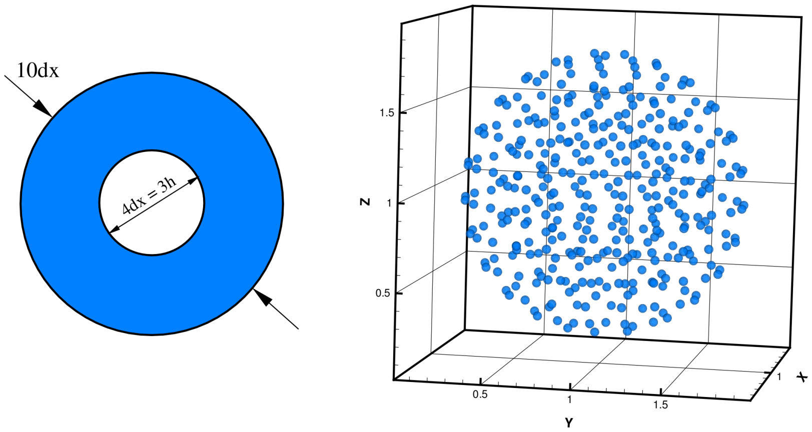

Figure 7.13.: Left panel: sketch of the tested geometry. Right panel: corresponding set of particles.

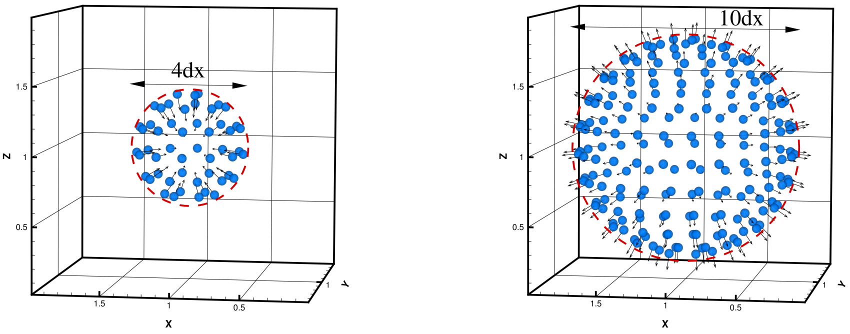

Figure 7.14.: Left: detected free-surface particles and normals on the spherical cavity boundary. Right: detected free-surface particles and normals on the outer sphere.

The result given by the algorithm is presented in figure 7.14. The two detected free surfaces (the ones from the inner and outer spheres) are shown sep-

$h/r \times 10^{-2}$	15.0	7.52	3.76	1.88
$\varepsilon \times 10^{-2}$	14.0	4.42	1.84	0.77

Table 7.2.: Average relative angle error between the analytically computed normals and the one evaluated by equation 7.23 for a spherical fluid domain. h/r denotes the ratio between the smoothing length and the radius of the sphere.

arately to better evidence the normals. The free-surface particles and normals are correctly evaluated both in the cavity and along the external surface. Similarly to the 2D case, in table 7.2.2 calculated free-surface normals are compared to analytical values in terms of average relative angle error for a spherical fluid domain. Again, the convergence rate is close to quadratic.

In order to assess the capability of the algorithm to capture cavities of dimension equal to $2h$, a more complex test was performed. As displayed in the left panel of figure 7.15, a toroidal cavity was created inside the sphere. The width of the torus is $2h$ and the torus ring diameter is $14dx$. Again, when showing the whole particle set, it is not possible to distinguish the toroidal cavity inside the sphere (see right panel of 7.15). The free-surface particles detected by the algorithm are shown in figure 7.16. Also in this case free-surface particles and normals are correctly evaluated.

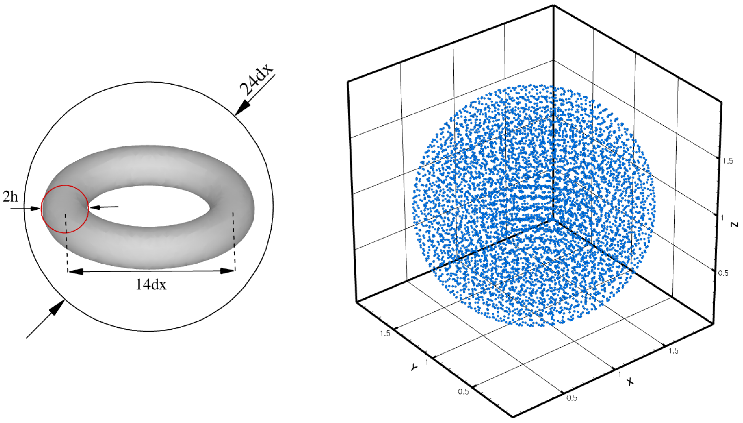

Figure 7.15.: Left panel: sketch of the second tested geometry. Right panel: corresponding set of particles.

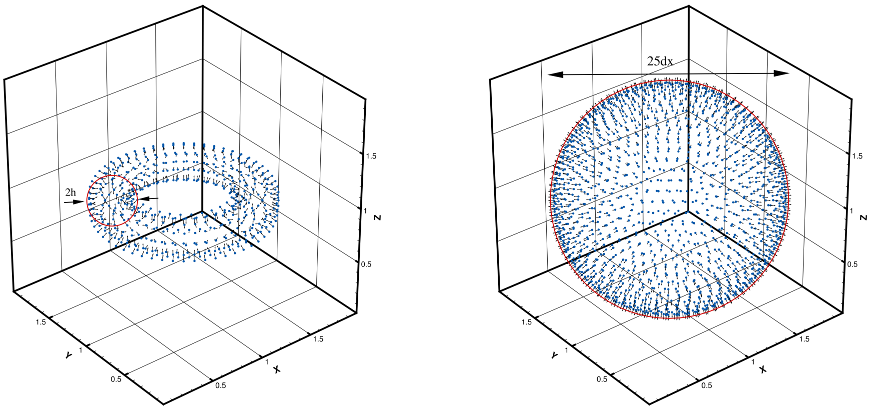

Figure 7.16.: Left: detected free-surface particles and normals on the toroidal cavity boundary. Right: detected free-surface particles and normals on the outer sphere.

7.3 INFLOW AND OUTFLOW B.C.

In free-surface continuous flows, such as open channel flows can occur, a general boundary treatment has to be used to impose suitable in/out-flow boundary conditions. In the present work the algorithm proposed by Federico (2010) is adopted. The modelling permits to investigate a wide range of flow phenomena in water streams through the initial imposition of flow characteristics such as surface elevation, velocity and pressure at in/out-flow boundaries. It allows also the enforcement of different conditions between upstream and downstream.

In order to assign different upstream and downstream flow conditions two new sets of boundary particles are defined. In all, four sets of particles are used: fluid (f), fixed ghost (s), inflow (i) and outflow (o) particles. Similarly to the fixed ghost particles, the in/out-flow particles affect the fluid particles but not vice versa. The region covered by these particles is at least as wide as the kernel radius.

Fig. 7.17 shows the initial sketch of the computational domain: different colours are associated to different sets of particles. The flow extends along the x-axis and is limited by an *inlet* and an *outlet* boundary. An *inflow* and an *outflow* threshold are defined, the particles that cross these thresholds change the set they belongs to.

The use of in/out-flow particles allows the imposition of different velocity and pressure fields both upstream and downstream in the computational domain. A constant or time variation of the water level can be assigned at upstream boundary, while the downstream condition is determined by the flow evolution. Note that the use of in/out-flow particles avoids the generation

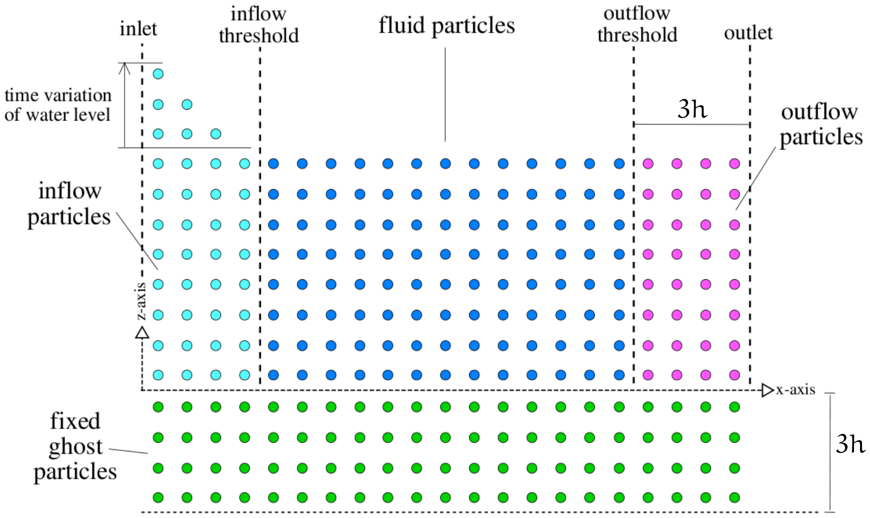

Figure 7.17.: Initial sketch of the computational domain: different colours are associated to different sets of particles.

of unphysical pressure shock waves of weakly-compressible due to the direct creation/deletion of fluid particles.

Part II

VALIDATIONS AND PHYSICAL INVESTIGATIONS

8 VALIDATION CASES

In this chapter the δ-SPH solver discussed in chapter 5 is validated on several test cases comparing the outcomes with reference analytical solutions, experimental data and results from other numerical solvers. Here the capabilities of the present solver are investigated mainly focusing on the prediction of pressure fields and loads on structures as well as the free-surface evolution. Further, in most of the benchmarks here presented, at least three different resolutions are adopted and convergence rates are provided. Four problems are discussed:

I) the steady flow of a jet impinging with a narrow angle on a flat plate

II) the viscous flow past a cylinder both in confined fluid domain and in continuous current

III) the propagation of regular and transient gravity waves generated by a wavemaker in several propagation regimes

IV) the dam-break flow against a vertical wall in both 2D and 3D

For all the cases the Euler equations for weakly-compressible flows, system (5.1), are solved but for the case *II*) for which Navier-Stokes equations, system (5.3), are adopted.

8.1 JET IMPINGING ON A FLAT PLATE

The jet on plate problem is a steady state problem, for which an analytical solution for the pressure is available. A two dimensional water jet impinges on a rigid plate without any physical viscosity. The wall defines the x axis. The plate may be inclined or orthogonal to the impinging flow. This problem has been solved analytically by Michell (1890) in a very complex way. Taylor (1966) gives an implicit expression for the speed and the pressure at the wall and here is reported the specific function in the case of a jet impinging with an angle ϑ:

$$\frac{x}{H} = \frac{[(1+\cos\vartheta)\,\ln(1+q) - (1-\cos\vartheta)\,\ln(1-q)]}{2\pi} + \frac{\sin\vartheta}{\pi}\arcsin q + \text{const} \qquad (8.1)$$

where:

$$u = \frac{-1 + q\cos\vartheta + \sqrt{(1-q^2)}\sin\vartheta}{q - \cos\vartheta}. \qquad (8.2)$$

while q is an auxiliary variable and x is the horizontal distance. The physical reference length is the width of the impinging jet which has been indicated with H (see left plot in figure 8.1), u is the dimensionless speed, the reference speed is the inflow velocity of the jet U. From the field velocity u obtained by eq. (8.1) and (8.2) the pressure is evaluated through the Bernoulli theorem.

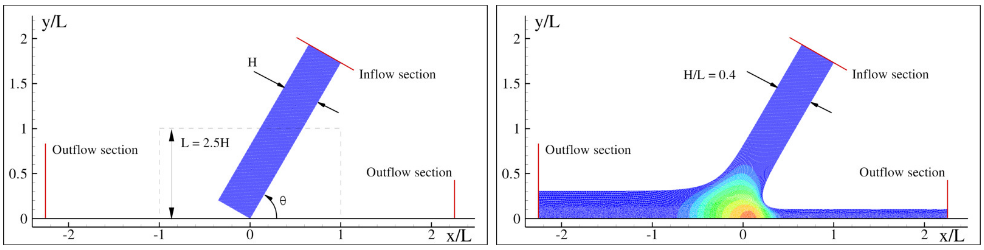

Figure 8.1.: Sketches of the jet impinging on a flat plate.

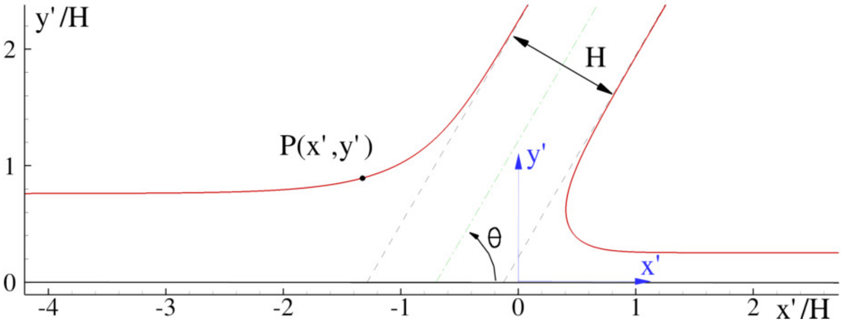

Figure 8.2.: The free surface solution for the jet impinging on a flat plate.

The solution for the free surface has been derived by Milne-Thomson (1968). Let us consider a polar frame of reference with the origin like in figure 8.2 and denote by β the angle of a generic point of the free surface. For $0 < \beta < \vartheta$ the point describes the right branch of the free surface and its coordinates are given by:

$$\frac{x'}{H} = \frac{1}{\pi}\left\{(\vartheta - \pi)\sin\vartheta + \ln\left[\tan\left(\frac{\beta}{2}\right)\right]\right.$$
$$\left. + \cos\vartheta\left[\ln\left(\frac{\sin\beta}{2}\right) - \ln\left(\sin\left(\frac{\vartheta+\beta}{2}\right)\sin\left(\frac{\vartheta-\beta}{2}\right)\right)\right]\right\}$$

$$\frac{y'}{H} = \frac{1}{\pi}\left\{\frac{\pi}{2}(1+\cos\vartheta) + \sin\vartheta \ln\left[\sin\left(\frac{\vartheta+\beta}{2}\right)\right] - \sin\vartheta \ln\left[\sin\left(\frac{\vartheta-\beta}{2}\right)\right]\right\}.$$

The left branch of the free surface is described by the following expressions valid for $\vartheta < \beta < \pi$:

$$\begin{aligned}\frac{x'}{H} &= \frac{1}{\pi}\left\{\vartheta \sin\vartheta + \ln\left[\tan\left(\frac{\beta}{2}\right)\right]\right.\\ &\qquad\left. + \cos\vartheta\left[\ln\left(\frac{\sin\beta}{2}\right) - \ln\left(\sin\left(\frac{\vartheta+\beta}{2}\right)\sin\left(\frac{\beta-\vartheta}{2}\right)\right)\right]\right\}\\ \frac{y'}{H} &= \frac{1}{\pi}\left\{\frac{\pi}{2}(1-\cos\vartheta) + \sin\vartheta \ln\left[\sin\left(\frac{\vartheta+\beta}{2}\right)\right] - \sin\vartheta \ln\left[\sin\left(\frac{\beta-\vartheta}{2}\right)\right]\right\}.\end{aligned}$$

The case for $\vartheta = \pi/2$ has been studied in Molteni and Colagrossi (2009) proving the diffusive term inside the continuity equation to act as a damping for the high frequency numerical noise affecting the pressure field. The comparison with the analytical solution clearly showed the showed the accuracy of the diffusive scheme with respect to the classical SPH scheme. Here the δ-SPH scheme is proven to be effective as well being tested on a jet characterized by $\vartheta = \pi/6$. This represents a very demanding test for the SPH schemes.

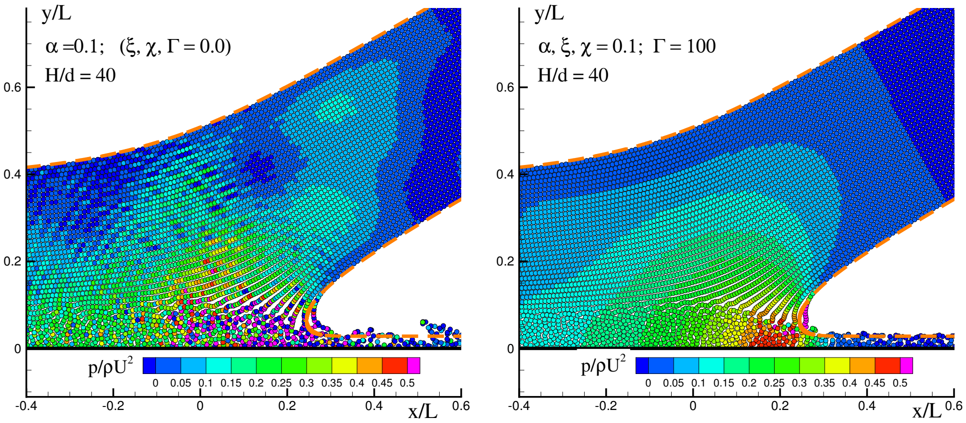

Figure 8.3.: The pressure field as predicted by the standard SPH scheme ($\alpha = 0.1$, $\delta, \chi, \Xi = 0$, left panel) and by the present scheme ($\alpha, \delta, \chi = 0.1$, $\Xi = 100$, right panel) for the case of a jet impinging on a flat plate with $\vartheta = \pi/6$. The spacial resolution is $H/d = 40$ where d is the mean particle distance. The dashed lines represent the free surface analytical solution.

In figures 8.3 and 8.4 the comparison between the pressure field as predicted by the classical SPH scheme (left panels) and the present solver (right panels) are shown for two different spatial resolutions. Both the models capture the

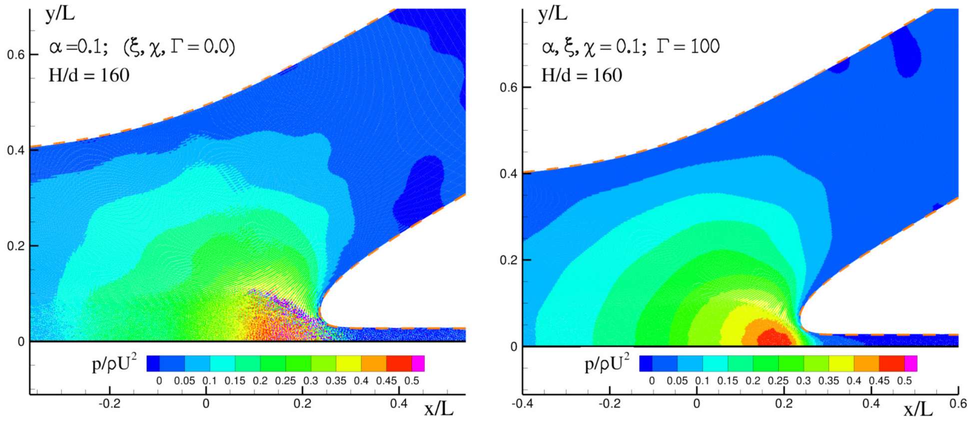

Figure 8.4.: The pressure field as predicted by the standard SPH scheme ($\alpha = 0.1, \delta, \chi, \Xi = 0$, left panel) and by the present model scheme ($\alpha, \delta, \chi = 0.1$, $\Xi = 100$, right panel) for the case of a jet impinging on a flat plate with $\vartheta = \pi/6$. The spacial resolution is $H/d = 160$ where d is the mean particle distance. The dashed lines represent the free surface analytical solution.

free surface solution in a satisfactory way even if for the coarser resolution the standard SPH scheme shows some numerical instabilities along the free surface for the right outgoing flow. Conversely, the δ-SPH scheme always shows a good match with the analytical free surface solution and, moreover, gives a pressure field which is less noisy and more accurate than the classic SPH. Finally, a more regular distribution of the particles is observed (see for example figure 8.3). This means that the particles are subjected to a slightly different force field with respect to the standard SPH scheme. The accuracy of the present model in the evaluation of the pressure field is underlined by the figure 8.5 where the numerical pressure field at the impact point (that is, on the plate at $x/L = 0.2$) is compared with the analytical solution by Taylor. In this case, a convergence analysis is provided in figure 8.6 clearly showing that the convergence rate for the present model is almost linear.

The figure 8.7 shows a snapshot of the internal energy evolution highlighting how the internal energy field grows in the fluid regions which are subjected to high compressions/deformations.

Finally, the time step history as obtained through the standard and the present SPH scheme is drawn in figure 8.8. Thanks to the less noisy solution, the present model shows a more regular time step history and, therefore, allows a faster integration. Moreover, the time step is generally larger than the one predicted by the standard SPH. The smoother fields and the more regular particle distribution lead to smaller values of $h \max_j |\pi_{ij}|$ and, therefore, allow using a larger time step.

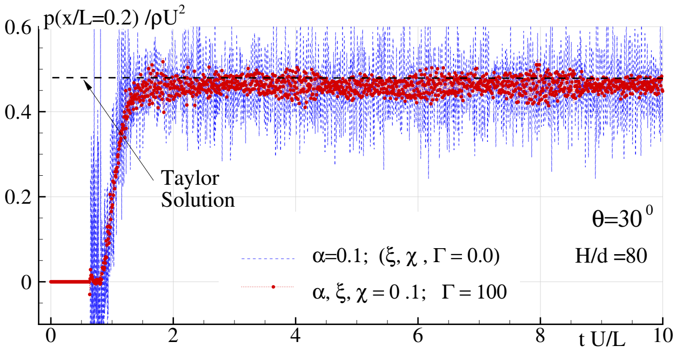

Figure 8.5.: Comparison between the pressure evaluated at $x/L = 0.2$, $y/L = 0$ as obtained through the standard SPH scheme ($\alpha = 0.1$, $\delta, \chi, \Xi = 0$) and through the present model scheme ($\alpha, \delta, \chi = 0.1$, $\Xi = 100$) for the case of a jet impinging on a flat plate with $\vartheta = \pi/6$. The spatial resolution is $H/d = 80$ where d is the mean particle distance.

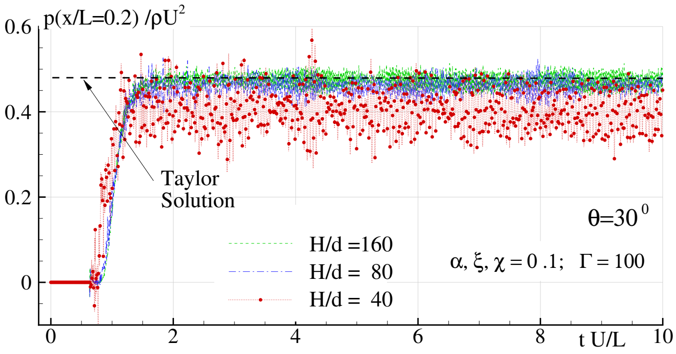

Figure 8.6.: Convergence test for the pressure evaluated at $x/L = 0.2$, $y/L = 0$ as obtained through the present model scheme ($\alpha, \delta, \chi = 0.1$, $\Xi = 100$) for the case of a jet impinging on a flat plate with $\vartheta = \pi/6$.

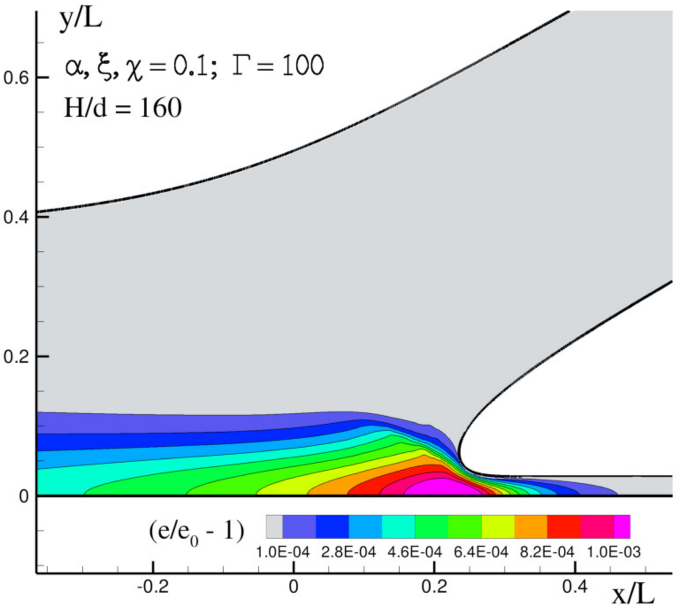

Figure 8.7.: The internal energy field as predicted by the present model scheme ($\alpha, \delta, \chi = 0.1$, $\Xi = 100$) for the case of a jet impinging on a flat plate with $\vartheta = \pi/6$. The spatial resolution is $H/d = 160$ where d is the mean particle distance.

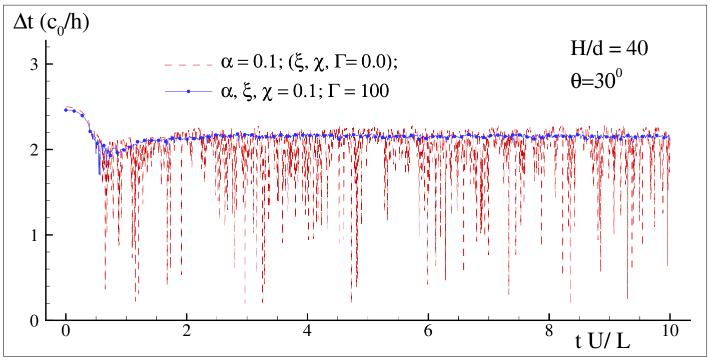

Figure 8.8.: Comparison between time step history as obtained through the standard SPH scheme ($\alpha = 0.1$, $\delta, \chi, \Xi = 0$) and through the present model scheme ($\alpha, \delta, \chi = 0.1$, $\Xi = 100$) for the case of a jet impinging on a flat plate with $\vartheta = \pi/6$. The spatial resolution is $H/d = 40$ where d is the mean particle distance.

8.2 VISCOUS FLOW PAST A CIRCULAR CYLINDER

In this section the capability of the δ-SPH solver in dealing with viscous flows at moderate Reynolds numbers is investigated. Specifically, simulations on two test cases have been performed. In the former case a cylinder is completely immersed in a fluid confined by a rectangular box and it is moved with a prescribed time law. In the second test case the classical problem of a cylinder in a steady current is studied for two different Reynolds numbers. In the Particle Method context the first problem is more simple to treat since no inflow/outflow conditions are needed. Indeed, in the latter case the definition of a proper algorithm using sets of inflow and outflow particles is required (see 7.3). Conversely, for classical mesh based solvers problems involving moving bodies are generally more challenging since they require the reconstruction of the grid around the body at each time step.

For all the test cases of this section the δ-SPH form of the Navier-Stokes equations for weakly-compressible fluids, that is system 5.3, is adopted and no-slip conditions on solid boundaries are achieved through the Takeda mirroring technique (see 7.1.3). It is important to highlight that the implementation of such a technique require a modification in the fixed ghost particle algorithm. In fact, two different sets of ghost velocities are needed, in order to correctly evaluate velocity divergence and viscous stresses (see 7.1.3). For the first one the free-slip conditions are adopted and the ghost velocities are obtained through interpolation points (see 7.1). For the second term a linear extrapolation of the fluid particle tangential velocity, as prescribed by Takeda et al. (1994), is performed in order to enforce no slip. As a consequence, for the calculation of the viscous stresses each fluid particle owns its set of ghost velocities. For what concern the remaining quantities (pressure, densities, etc.) they are gathered through interpolation points as usual.

8.2.1 2D flow around a moving circular cylinder inside a rectangular box

In this section the problem the flow around a moving circular cylinder inside a rectangular box is studied. A smooth acceleration along the x-axis is applied

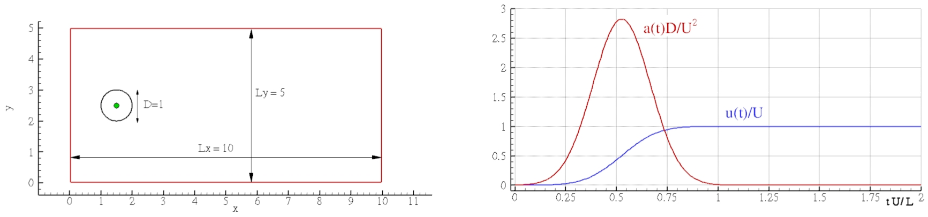

Figure 8.9.: Geometry of the problem and time law of the body motion.

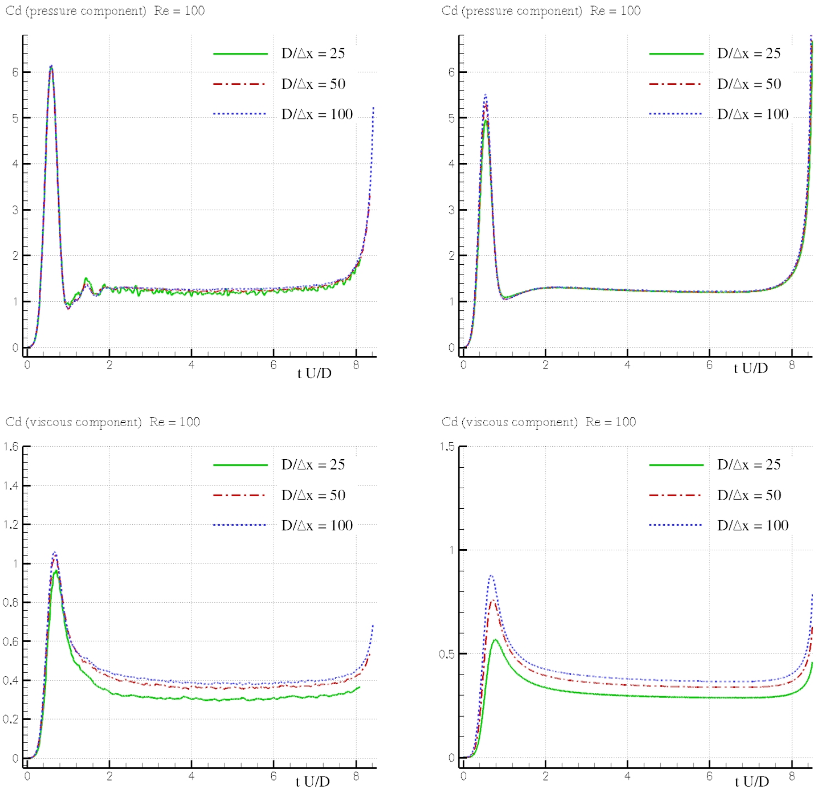

Figure 8.10.: Convergence for viscous component of drag coefficient (top plots) and pressure component (bottom plots) (Δx is the initial particle distance). Left plots: δ-SPH scheme. Right plots: Navier-Stokes Level-Set solver.

to the cylinder until it reaches the velocity U. In figure 8.9 a sketch of the geometry and the time law of the cylinder motion are plotted.

Results obtained through the Navier-Stokes solver by Colicchio et al. (2006) have been used as a reference solution. This solver employs a second-order finite-difference scheme on a Cartesian fixed staggered grid. This is combined with a Projection method to solve the governing equations while time integration is performed by a second-order predictor-corrector algorithm.

To avoid mesh-reconstruction algorithms, the presence of a solid boundary is handled by introducing a Level-Set function ψ defined on the grid points as the distance with sign from the body surface. ψ is positive on the points outside the body and negative otherwise. A relaxed no-slip condition is enforced applying a smoothing between the fluid Navier-Stokes equations and the body equations of motion within a layer across the body. Consistently, the velocity varies smoothly from the fluid to the body values, and vice versa (for details see Colicchio et al. 2006).

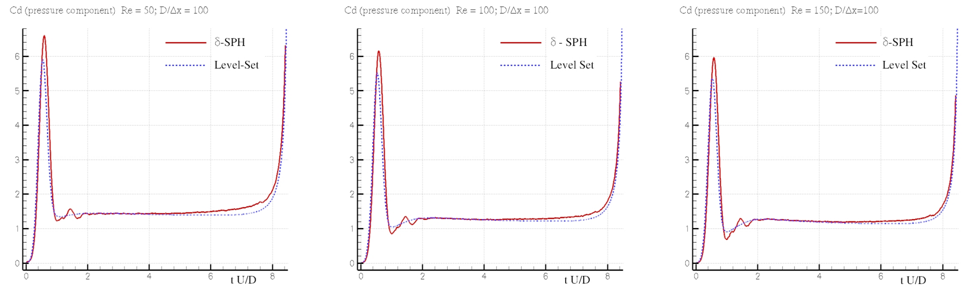

Figure 8.11.: Comparison for the pressure component of C_D for $Re = 50$, $Re = 100$, $Re = 150$.

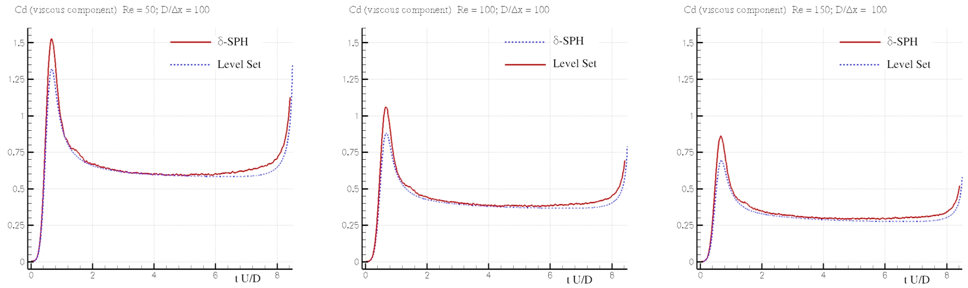

Figure 8.12.: Comparison for the viscous component of C_D for $Re = 50$, $Re = 100$, $Re = 150$.

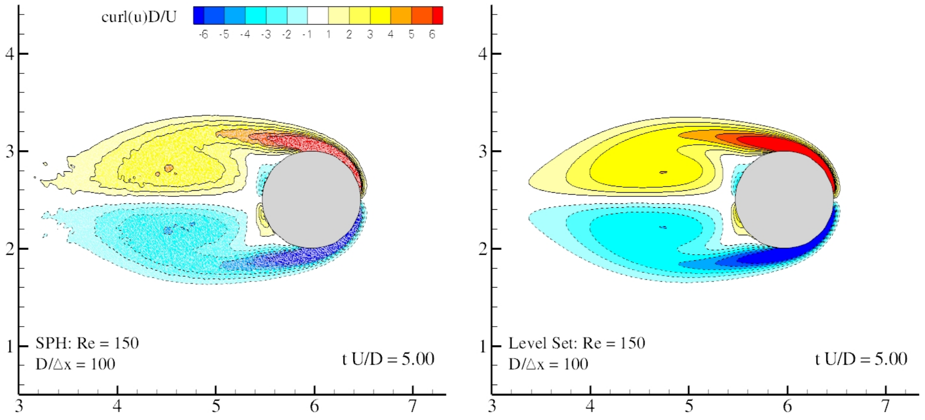

Figure 8.13.: Comparison of the contour plot of the vorticity for $Re = 150$ ($D/\Delta x = 100$). Left panel: δ-SPH scheme. Right panel: Navier-Stokes Level-Set solver.

Hereinafter the Reynolds number is defined as $Re = UD/\nu$ where D is the cylinder diameter, U is the maximum cylinder velocity and ν is the kinematic viscosity. It is useful to define also the drag coefficient,

$$C_D = \frac{2F_D}{\rho U^2 \pi R}$$

where F_D is the drag force and R is the cylinder radius, and the lift coefficient,

$$C_L = \frac{2F_L}{\rho U^2 \pi R}$$

where F_L is the lift force.

Figure 8.10 shows the convergence of pressure and viscous components of the drag coefficient (top and bottom plots respectively) as predicted by using the δ-SPH scheme (left plots) and the Navier-Stokes Level-Set solver (right plots) for $Re = 100$. The convergence rate for the SPH (evaluated using the L_2-norm, see C) is 0.75 for the pressure component and 1.50 for the viscous one while the corresponding convergence rates of the Level-Set solver are 0.87 and 0.77 respectively.

Figure 8.11 displays the comparison between the δ-SPH and the Level-Set solver for the pressure component of drag coefficient for $Re = 50, 100, 150$. The global agreement is good even if the SPH scheme predicts a larger force peak during the acceleration stage. Further in the SPH time histories small oscillations appear after $tU/D = 1$, these are due to the assumption of weak-compressibility of the fluid. Indeed, acoustic wave are released during the acceleration stage and they are reflected by the right wall coming back to the body (the speed of sound used in the simulation is $10U$). However, the Drag force evaluated by the two solvers during the steady regime is practically coincident. Note that, after $tU/D = 6$ the presence of the right wall starts to influence the flow around the cylinder, giving rise to the peak at the end of the simulation.

Figure 8.12 shows the comparison between the δ-SPH and the Level-Set solver for the viscous component of drag coefficient for the three Reynolds. The overestimation of the δ-SPH with respect to the Level-Set solver still occurs for the force peak. In any case, the agreement is good and, consistently with the increase of the Reynolds number, the mean value of the viscous component decreases.

As a final comparison, figure 8.13 shows the contour plot of the vorticity past the cylinder as predicted by the SPH solver (left panel) and by the Level-Set solver (right panel) for $Re = 150$ at $tU/D = 5$. The spatial resolution for this cases is $D/\Delta x = 100$ for both the solvers. Apart from the noisy signals due to the Lagrangian nature of the SPH scheme, the global distribution of the vorticity field is in good agreement with the Level Set solution.

8.2.2 2D flow past a circular cylinder in a steady current

Here the classical evolution of the flow past a circular cylinder is analysed and the obtained results are compared with reference solutions available in literature. Two Reynolds number have been investigated $Re = 100$, $Re = 200$. In such regimes an unsteady wake develops through the continuous shedding

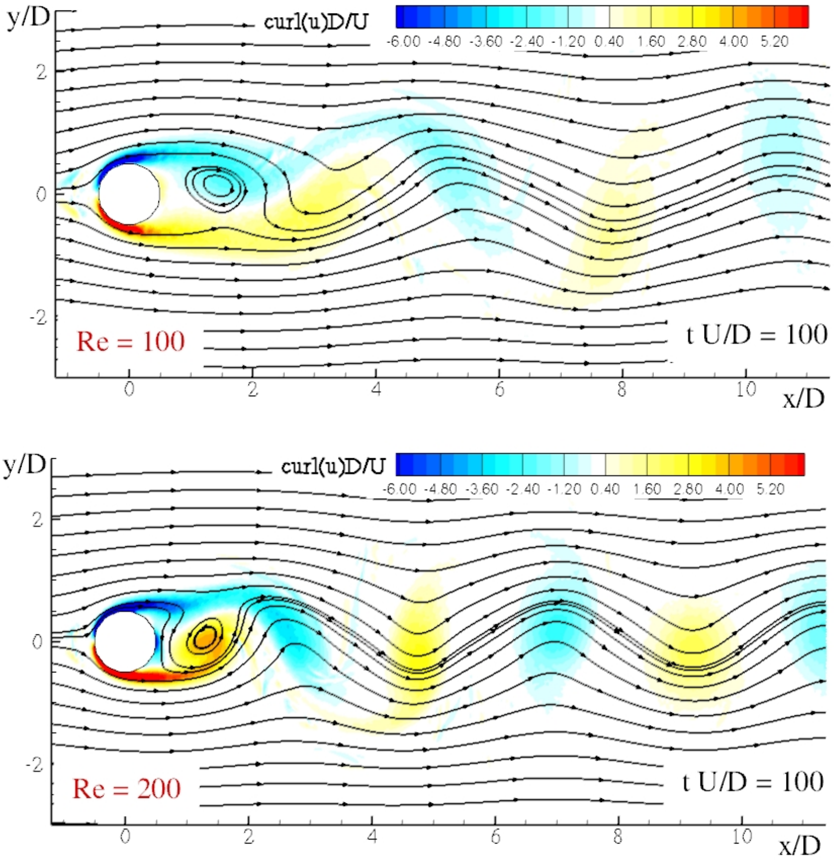

Figure 8.14.: Streamlines and contour plot of the vorticity of the flow past a circular cylinder for $Re = 100$ (top) and $Re = 200$ (bottom)

of opposite sign vortices leading to an oscillatory behaviour of the drag and lift forces acting on the cylinder. Plots of figure 8.14 show two snapshot of the wake at $Re = 100$ and $Re = 200$. In particular the contour plots refer to the vorticity field and the streamlines are superposed.

Table 8.1 provides the drag and lift coefficients (C_D and C_L respectively) compared against some reference data available in the literature. The SPH results are referred to the simulations with discretization $D/dx = 80$ that for these cases is almost converged. The values obtained with the present solver are in fair agreement with reference data. Note that for the case at $Re = 100$ it is difficult to estimate the values of the oscillations in the drag force since they are quite small. Further, this simulations at moderate Reynolds numbers are rather challenging in the SPH context as high velocity gradients occur and, therefore, the non-uniform particle distribution generates numerical noise.

In figures 8.15 and 8.16 the time evolution of the drag and lift coefficients is plotted while table 8.2 provides the Strouhal number St obtained for the two Reynolds numbers studied and defined as:

$$St = \frac{fR}{U}$$

where f is the frequency of vortex shedding. Also in this case, the results are in agreement with literature references.

	C_D		C_L	
	Re = 100	Re = 200	Re = 100	Re = 200
Lecointe and Piquet (1984)	–	1.46 ± 0.04	–	± 0.70
Braza et al. (1986)	1.364 ± 0.015	1.40 ± 0.05	± 0.25	± 0.75
Calhoun (2002)	1.330 ± 0.014	1.172 ± 0.058	± 0.298	± 0.668
Ng et al. (2009)	1.368 ± 0.016	1.373 ± 0.05	± 0.360	± 0.724
δ-SPH	1.36 ± 0.01	1.48 ± 0.05	± 0.24	± 0.69

Table 8.1.: Flow past a circular cylinder: values of the drag and lift coefficients obtained with the present SPH formulation and results available in literature for Re = 100 and 200. The discretization adopted in the SPH simulation is D/dx = 80.

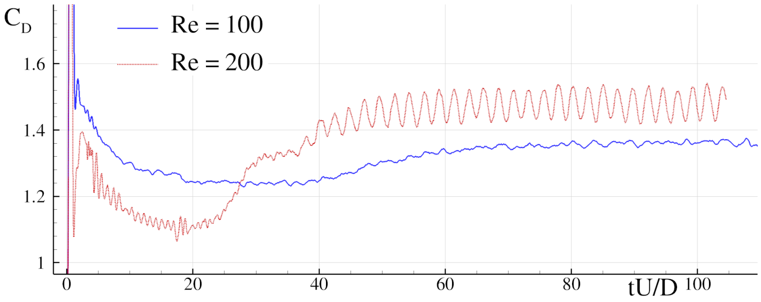

Figure 8.15.: Flow past a circular cylinder: time evolution of the drag coefficient for Re = 100 and 200.

8.3 GRAVITY WAVE PROPAGATION

In this section the δ-SPH solver for Euler equation is validated in the problem of propagation of 2D gravity waves generated by a wavemaker. In the SPH literature a few works dealing with the modelling of propagation of gravity waves are present (see e.g. Guilcher 2008) whilst several papers treats the evolution of breaking waves and bore propagation. Here, both regular and transient wave systems are considered. In the former, a several simulations

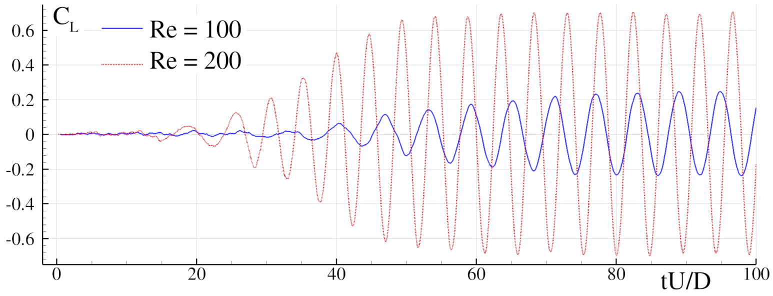

Figure 8.16.: Flow past a circular cylinder: time evolution of the lift coefficient for Re = 100 and 200.

	St	
	Re = 100	Re = 200
Braza et al. (1986)	0.16	0.20
Williamson (1996)	0.164	0.197
δ-SPH	0.168	0.210

Table 8.2.: Flow past a circular cylinder: values of the Strouhal number obtained with the present SPH formulation for Re = 100 and 200. The discretization adopted in the SPH simulation is D/dx = 80.

are performed for different wave steepness and height-to-depth ratio and the results are compared with the BEM Mixed-Eulerian-Lagrangian solver (here denoted BEM-MEL solver) developed by Lugni (1999).

In the latter, the propagation of wave packets is studied. A wave packet is given by the interaction of several wave components whose amplitudes are chosen in a prescribed frequency spectrum. The corresponding wave phases are calculated to realize their focusing in a prescribed position of the wave basin (i.e. the focusing point) and at a fixed time instant. Because of its nature, the wave packet is a good candidate to check the non-linear propagation of a multicomponent wave train. Following Dommermuth et al. (1988), the wave packet is used to get a breaking wave at the focusing point and the numerical results are then compared with the experimental data provided in Dommermuth et al. (1988) and with outcomes from BEM-MEL solver.

In all the SPH simulations a uniform spatial resolution is used. This is not an optimal choice because the use of a finer spatial resolution near the free surface and a coarser one as the depth increases strongly reduces the CPU cost. Anyway, since the present section is meant to be a validation of the δ-SPH solver, it has been preferred to limit the numerical variables/parameters. For the same reason, no beach or damping technique has been adopted to reduce wave reflection at the end walls of the tank. As a consequence, the tank length, L, is set to simulate about 12 wave periods without any reflection at the right end wall. This time of simulation is generally too short to reach a steady-state solution and, therefore, only the transient evolution is considered. A longer time interval would require an extension of the tank and a large increase of the particle number and of the computational cost. In any case, the comparison between different numerical solvers is generally more demanding during the transient evolution than during the steady-state.

The wavemaker is modelled through fixed ghost particles (see section 7.1.1). Both piston and flap wavemaker have been simulated depending on the wave length to generate. In figure 8.17 a sketch of the fixed ghost particle configuration is plotted for the flap wavemaker. In this case the fixed ghost particles are re-generated at each time step to correctly cover the solid region close to the hinge, avoiding lack/excess of mass.

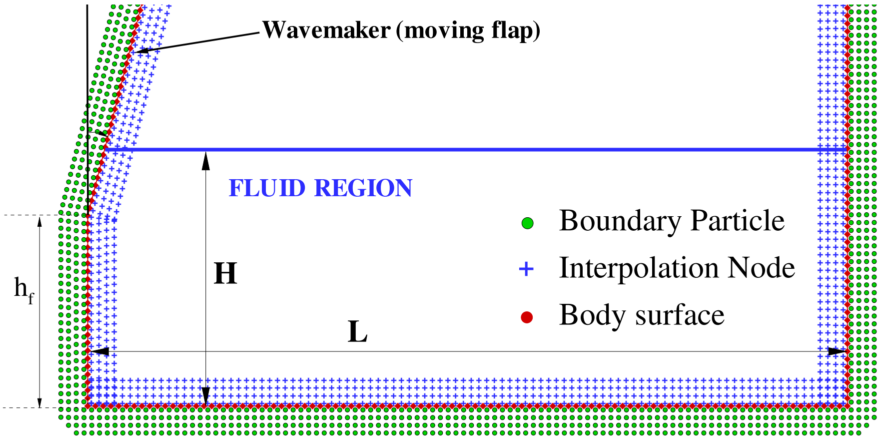

Figure 8.17.: Sketch of the fixed ghost particles for the wavemaker and the basin geometry. The symbol h_f indicates the distance of the flap hinge from the tank bottom.

Regarding the numerical parameters adopted for this kind of simulation, it is worth noting that in the case of gravity waves the flow velocity is generally small and one could be led to choose very low speed of sound in weakly compressible schemes. However, the most important quantity associated with the wave propagation is the wave celerity, that is, $c_w^2 = g/k \tanh(kH)$ where H is the still water depth, k is the wave number and g the gravity acceleration (see, for example, Madsen and Shäffer 2006)). For kH going to zero, the shallow water regime is approached and the relation above becomes $c_w^2 = gH$. Since the latter expression is an upper bound for the wave celerity (that is $g/k \tanh(kH) \leqslant gH$), here $c_0 = 10\sqrt{gH}$ is chosen.

8.3.1 Regular waves

Regular waves have been modelled in several regimes of propagation. Tables 8.3,8.4 and 8.5 represents the main parameters of the test cases considered. Specifically, λ is the wave length, $\mu_w = 2\pi H/\lambda$ is the parameter accounting for the dispersive effects, $\epsilon = 2A/H$ is the non-linearity parameter (A is the wave amplitude) and kA is the wave steepness. To allow a comparison with the BEM-MEL solver, test cases are split in Deep-water ($\mu_w > 3$, see table 8.3), Intermediate-water ($0.3 < \mu_w \leqslant 3$, see table 8.4) and Shallow-water ($\mu_w \leqslant 0.3$, see table 8.5) regime. The parameters ϵ and kA are chosen to avoid the occurrence wave breaking, but for the case DW_04 where the leading crest is breaking. The wave maker is a piston for $\lambda/H \geqslant 12$ while a flap has been adopted for the remaining cases (see figure 8.17). The flap paddle is hinged at the tank bottom. In all the cases a sinusoidal time law has been imposed to the paddle. Further, a ramp has been used in some test cases during the initial stage of the evolution to avoid impulsive transitory. The time law of the piston is given by:

$$x_m(t) = \frac{\Delta x}{2} \sin(\omega t) , \tag{8.3}$$

where x_m is the x-coordinate of the wave maker and $\Delta x/2$ is its maximum displacement from the position of rest. For the flap it is:

$$x_m(t, z) = \frac{\Delta x}{2} \left[1 - \frac{z}{H - h_f} \sin(\omega t) \right] , \tag{8.4}$$

where h_f is the position of the hinge from the tank bottom. In some test cases, a ramp is used to avoid impulsive transitory. This is given by a function $R(t)$ which multiplies $x_m(t)$. This function is given below:

$$R(t) = \frac{1}{2} \left[1 - \cos\left(\pi \frac{t}{\tau} \right) \right] , \tag{8.5}$$

where τ is a fixed time interval which corresponds to the ramp duration. All the details on the wave maker and on the ramp are summarized in Table 8.6.

	Deep water							
	λ/H	μ	ϵ	kA	Np	H/dx	λ/dx	A/dx
DW_01	2.00	3.14	0.03	0.05	404K	130	260	1.95
DW_02	2.00	3.14	0.07	0.11	404K	130	260	4.55
DW_03	2.00	3.14	0.13	0.20	404K	130	260	8.45
DW_04	2.00	3.14	0.23	0.36	468K	150	260	17.3

Table 8.3.: Test case matrix for regular waves in deep water regime

	Intermediate water							
	λ/H	μ	ϵ	kA	Np	H/dx	λ/dx	A/dx
IW_01	12.0	0.52	0.22	0.06	223K	40	480	4.40
IW_02	12.0	0.52	0.34	0.09	223K	40	480	6.80
IW_03	7.40	0.85	0.04	0.04	265K	60	444	1.20
IW_04	7.40	0.85	0.23	0.20	265K	60	444	6.90

Table 8.4.: Test case matrix for regular waves in intermediate water regime

	Shallow water							
	λ/H	μ	ϵ	kA	Np	H/dx	λ/dx	A/dx
SW_01	30.0	0.21	0.12	0.01	400K	40	1200	2.40
SW_02	30.0	0.21	0.39	0.08	400K	40	1200	7.80
SW_03	25.0	0.25	0.13	0.02	400K	40	1000	2.60
SW_02	25.0	0.25	0.44	0.11	400K	40	1000	8.80

Table 8.5.: Test case matrix for regular waves in shallow water regime

	WM	$\Delta x/H$	h_f/H	$\tau\sqrt{g/H}$
DW_01	F	0.025	0.0	5.00
DW_02	F	0.050	0.0	5.00
DW_03	F	0.100	0.0	5.00
DW_04	F	0.200	0.0	5.00
IW_01	P	0.400	/	6.00
IW_02	P	0.600	/	6.00
IW_03	P	0.052	/	2.13
IW_04	P	0.264	/	2.13
SW_01	P	0.50	/	/
SW_02	P	1.00	/	/
SW_03	P	1.30	/	15.00
SW_04	P	0.40	/	/

Table 8.6.: Parameters of the wavemaker for regular wave tests. Letters 'P' and 'F' indicate that respectively a piston or a flap is used.

In the three tables 8.3,8.4,8.5 are also reported the parameters related to the spatial resolutions used in the SPH simulations: the total number of particles N_p, the number of particles along the depth (i.e H/dx) and the ratios λ/dx, A/dx, i.e. the number of particle for wavelength and wave amplitude, respectively.

A wave amplitude A greater than dx has been chosen for all simulations of regular wave. This choice ensures a small dissipation due to spurious numerical effects of the SPH solver. Further, to get an accurate enough representation of the wave propagation phenomenon, a spatial discretization $\lambda/dx > 100$ is chosen. In the BEM-MEL solver, a spatial discretization $\lambda/dx = 90$ is used while no limits exist for wave amplitude.

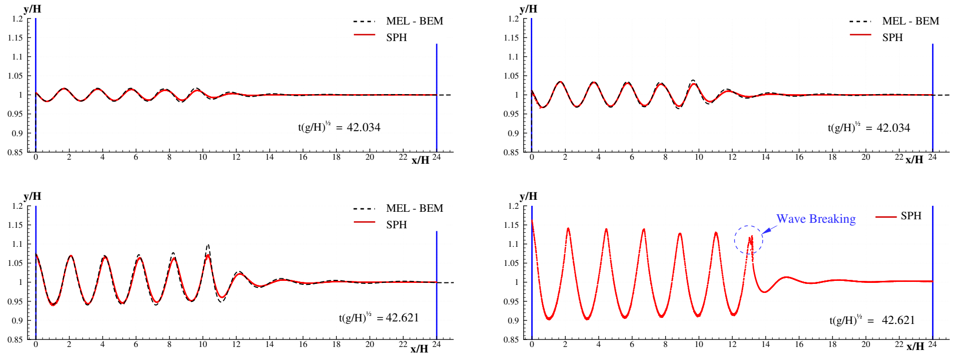

Figure 8.18.: free-surface evolution as predicted by the SPH solver (solid lines) and the BEM solver (dashed lines). Top panels: DW_01, DW_02. Bottom panels: DW_03, DW_04. The wave length of these cases is $\lambda/H = 2$ while the steepness increases from $kA = 0.05$ up to $kA = 0.36$.

In figure 8.18 (from left to right and from top to bottom), we show the comparison of the free surface evolution as predicted by the δ-SPH solver (solid lines) and the BEM solver (dashed lines) for the deep-water cases DW_01, DW_02, DW_03, DW_04 (reported in table 8.3). These cases are characterized by a wave length $\lambda/H = 2$ while the amplitude increases from $\epsilon = 0.03$ up to $\epsilon = 0.23$. Therefore in these four cases we move from an almost linear wave (DW_01) to a highly non-linear wave (DW_04). In the latter case, the steepness is quite large (i.e. $kA = 0.36$) leading to the breaking of the first crest at a distance of about $13H$ away from the wave maker (see bottom-right plot of figure 8.18). The BEM-MEL solver is not able to simulate such a quite steep wave while for the first three cases the match between SPH and BEM-MEL is generally very good: both wave shape and wave celerity are fairly well reproduced and only small damping is observed in the SPH simulations at the wave front. The relative errors for these cases are $\varepsilon_R = 0.27, 0.19, 0.17$ respectively (see appendix C) for more details).

Figures 8.19 and 8.20 show the intermediate- and shallow-water test cases. The overall agreement between the δ-SPH and BEM results is fairly good. The cases IW_02 and SW_04 having the largest ratios λ/dx and A/dx show a good agreement with the BEM-MEL solution. Incidentally, it is important to underline that for the propagation of shallow water waves it is generally important to account for the action of boundary layer at the tank bottom. Anyway, the

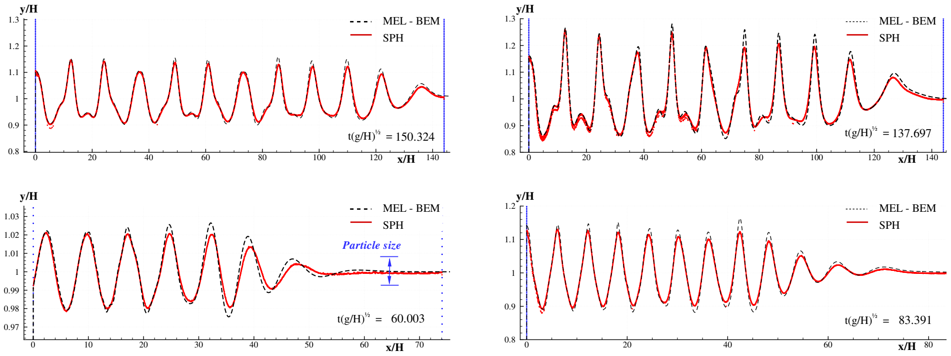

Figure 8.19.: free-surface evolution as predicted by the SPH solver (solid lines) and the BEM solver (dashed lines). Top panels: IW_01, IW_02. Bottom panels: IW_03, IW_04.

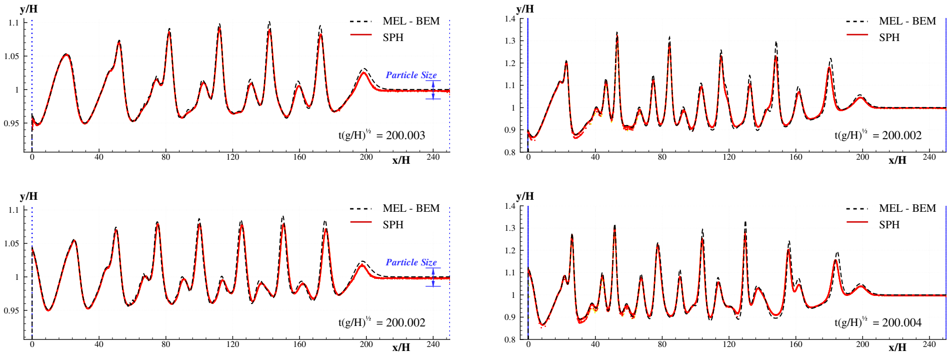

Figure 8.20.: free-surface evolution as predicted by the SPH solver (solid lines) and the BEM solver (dashed lines). Top panels: SW_01, SW_02. Bottom panels: SW_03, SW_04. Arrows indicate the particle diameter (the length is referred to the y-axis).

BEM solver cannot implement a no-slip condition along the solid boundary because it is based on the potential theory. Consequently, the influence of the boundary layer at the tank bottom has been neglected and a free-slip condition has been implemented in the SPH solver as well.

Plots in figure 8.21 show the same test case (that is, SW_01) using two different spatial resolutions ($H/dx = 20$, $A/dx = 1.2$, top; $H/dx = 40$, $A/dx = 2.4$, bottom). For the smallest spatial resolution small oscillations associated with the weakly compressibility appear. This effect disappears when a larges resolution (i.e. $H/dx = 40$) is used. In figures 8.19,8.20 and 8.21 arrows indicate the particle diameter (the length is referred to the y-axis) and proves that the spurious dissipative effects become smaller for the cases with the largest ratio A/dx.

In figure 8.22 the convergence analysis of the wave elevation is displayed. The test case is the IW_04 and the wave elevation has been recorded at $x/H = 18$

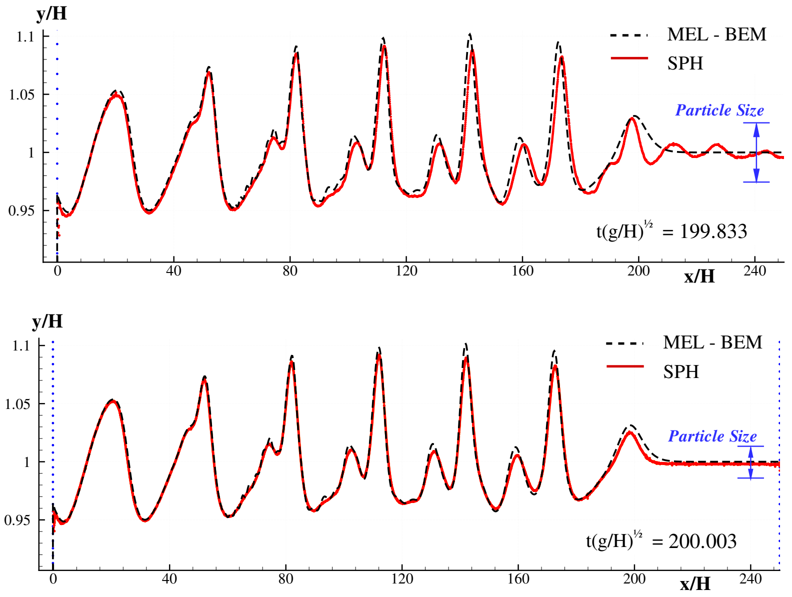

Figure 8.21.: Test case SW_01. Comparison between two different spatial resolutions: top panel $H/dx = 20$, bottom panel $H/dx = 40$.

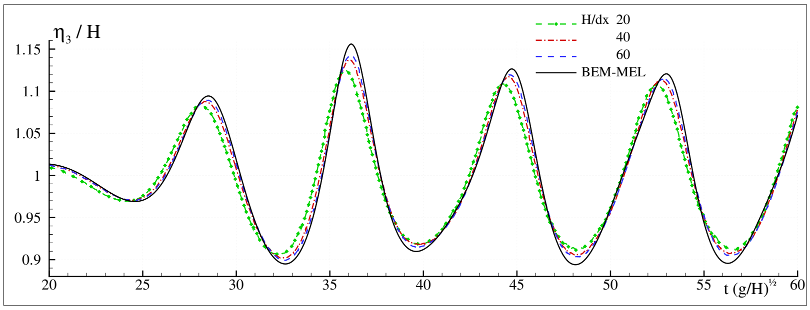

Figure 8.22.: convergence analysis for the time history of the wave elevation recorded at $x/H = 18$. Test case IW_04.

using three different spatial discretizations. The convergence rate of the SPH is about $C = 1.5$ (see the appendix C for more details) and the SPH solution tends to the convergent solution of the BEM-MEL signal.

8.3.2 Wave Packet

Having shown the capability of the SPH solver to reproduce the evolution of the regular wave system, in the following the wave packets evolution is used to stress further the ability of the algorithm to deal with the wave propagation problem. The wave packet proposed by Dommermuth et al. (1988) is used to get a plunging breaking wave. In figure 8.23 a sketch of the basin used for their experiments is depicted. The wave packet is generated by a linear superposition of wave frequency components with suitable amplitude and phase to get their superposition at a prescribed distance from the wave maker. The point where the several components focus is called focusing point. The left plot of figure 8.24 shows the time history of the piston motion. As shown in the right panel of the same figure, this signal contains several harmonic components in the dimensionless frequency range $(0.15 : 0.30)$. To proper capture the highest one, a fine enough spatial discretization is required to avoid spurious dissipative effects.

Along the basin there are nine probes which measure the wave elevation (see figure 8.23). Specifically, probes P_8 and P_9 are placed near the breaking point. The comparison with the experimental measurements in figure 8.25 shows an overall good agreement except for a small disturbance observed in the SPH signals at probes P_8 and P_9. In the low right panel of the same figure, the convergence analysis for the SPH free surface is displayed for a detail of the signal at probe P_8. The convergence rate obtained using the resolutions $H/dx = 25, 50, 100$ is $C = 1.3$ while for $H/dx = 50, 100, 200$ a rate of $C = 1.1$ is achieved. Note that the time signals have been considered up to $t = 51\sqrt{H/g}$ since for longer times wave breaking occurs. Finally, this analysis is repeated

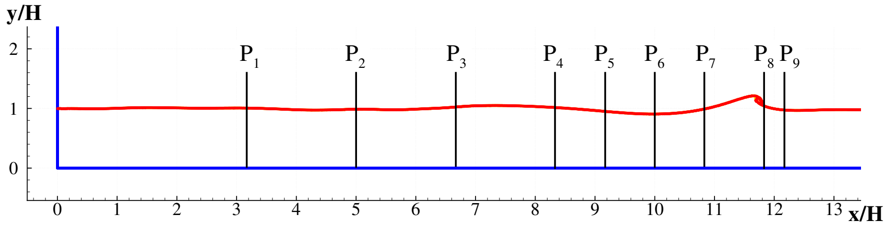

Figure 8.23.: The basin used in the work by Dommermuth et al. (1988). Probe positions are: $x/H = 3.16, 5.00, 6.66, 8.33, 9.16, 10, 10.83, 11.83, 12.16$.

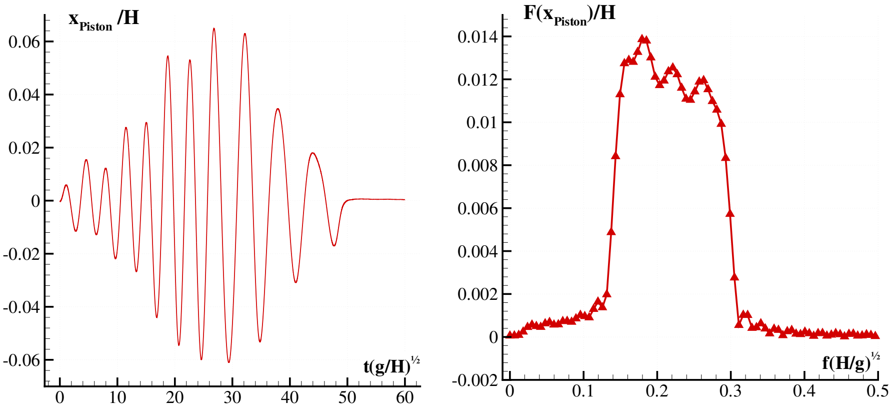

Figure 8.24.: Left panel: time law of the piston motion used in the work by Dommermuth et al. (1988). Right panel: modulus of the Fourier series coefficients of the wave maker motion.

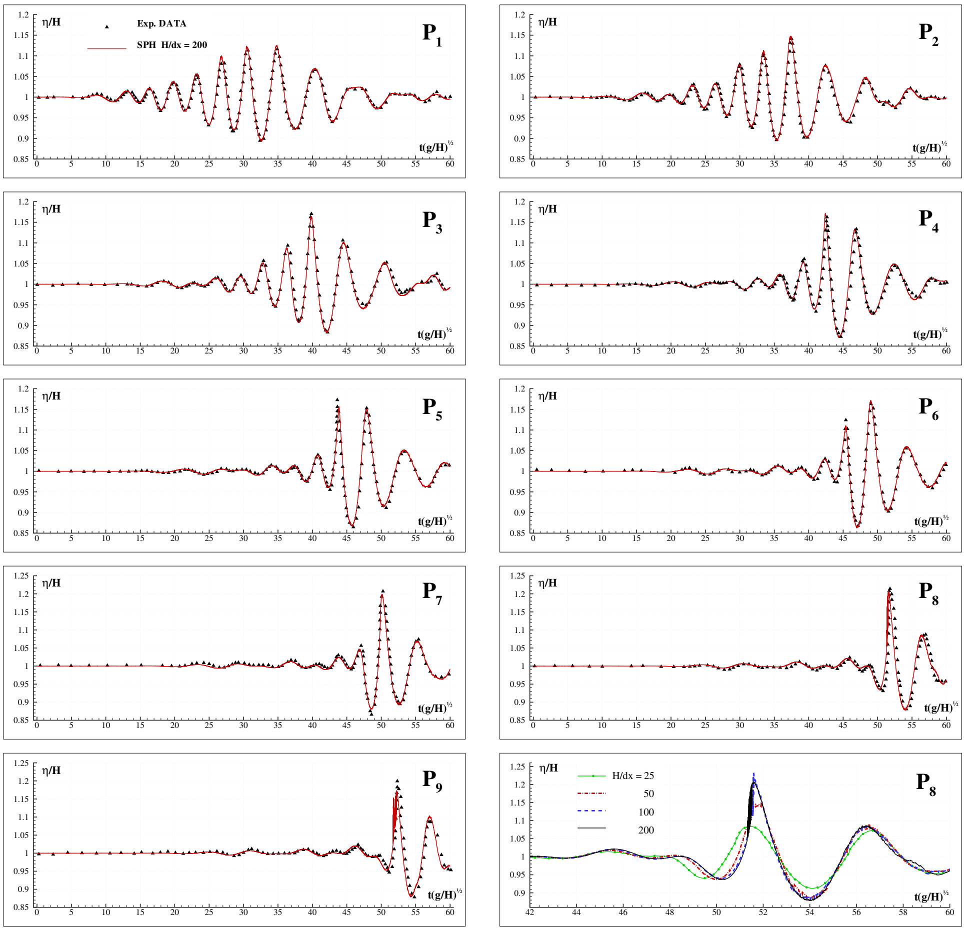

Figure 8.25.: Free-surface elevation at probes P_1 to P_9. Comparison between the experimental data and the solution predicted by the δ-SPH model. The bottom right panel shows the convergence analysis at probe P_8 (H is the still water depth and dx is the mean particle distance).

for a snapshot of the free surface evolution near the focusing point (see figure 8.26). The SPH solutions at different spatial resolutions are compared with the BEM solution. The relative errors with respect to the BEM-MEL solver are $\varepsilon_R = 0.41, 0.24, 0.15, 0.13$ respectively.

The overall agreement of the proposed test cases proves the capability of the δ-SPH solver and of the fixed ghost particles in dealing with gravity wave propagation. In particular the results clearly show that a fine enough resolution is needed to avoid the underestimation of the wave height being the ratios A/dx and λ/dx the most restrictive parameters in this context. The convergence rates obtained for these problems are all greater than 1, confirming the basic insights given by theory (see chapter 4). It is important to underline

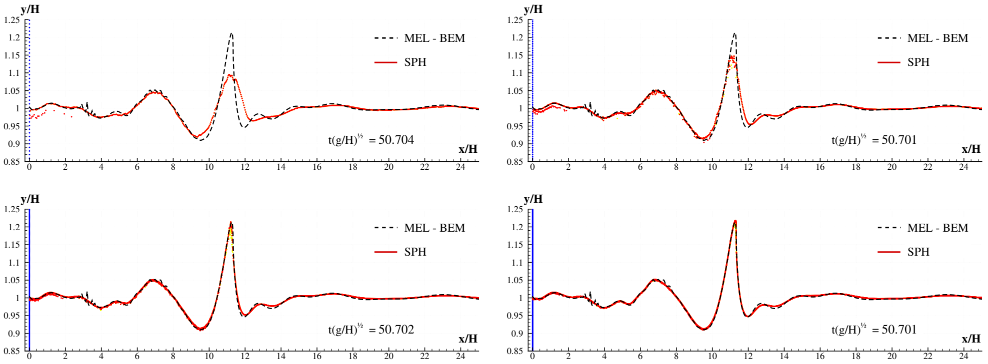

Figure 8.26.: Convergence analysis for the free-surface elevation as predicted by the δ-SPH model. Top left panel: $H/dx = 25$; top right panel: $H/dx = 50$; low left panel: $H/dx = 100$; low right panel: $H/dx = 200$ (H is the still water depth and dx is the mean particle distance).

that for these problems particles generally remain uniformly distributed, even if high stretch occur.

8.4 DAM-BREAK FLOW IN A RECTANGULAR TANK

In this test case the δ-SPH solver is validated through a quite popular benchmark: a dam-break flow impacting a vertical wall (see e.g. Colagrossi and Landrini 2003). This test is useful in order to investigate the capability of the solver in predicting local impact loads. Moreover, insight on how the model preserves mechanical energy is provided. The present analysis represents also a preliminary validation for the study of the next chapter where the solver is applied and further validated in problems regarding violent flows striking different structures.

The sketch of the problem is depicted in Figure 8.27 where the points P_1, P_2, P_3 indicate the pressure probes. Their positions are chosen accordingly to the experiment made by Buchner (2002). The problem is first studied numerically in 2D. A 3D analysis is then performed in order to assess the importance of 3D effects. Figure 8.28 displays snapshots of the flow evolution up to the plunging wave closure (which occurs at about $t\sqrt{g/H} = 6.0$) and the subsequent generation of a cavity. Here, the pressure probes are drawn according to their actual size, that is $\phi = 90mm$.

The left panel of Figure 8.29 shows an enlarged view of the fluid tongue just before its impact against the wall. This tongue has a triangular shape and the free surface makes an angle β of about 10 degrees with the bottom. This angle being small, an asymptotic solution based on potential theory (see Greco 2001) can be used to provide a comparison. Since the velocity of the front is about $U_{MAX} = 1.95\sqrt{gH}$, the maximum pressure peak predicted by this theory is $2.3\,\rho\,g\,H$ at the corner of the tank. To compare this value with the SPH result a further pressure probe P_0 was added at the bottom of the right wall. The pressure signal obtained with the δ-SPH model is displayed in the right panel of Figure 8.29. The maximum pressure recorded in SPH is quite close to the one by the asymptotic solution. In order to check the influence of the weak-compressibility assumption on the pressure field, the same impact is simulated by using two different values of the speed of sound, namely $c_0 = 20\sqrt{gH}$ and $c_0 = 40\sqrt{gH}$. These values approximately correspond to Mach numbers $Ma = U_{MAX}/c_0 = 0.1$ and 0.05. One can observe in the right panel of Figure 8.29 that the compressibility effects are actually very limited.

Comparison with the experiments by Buchner (2002) is provided in Figure 8.30. The SPH pressure signals reported are integrated on the actual probe areas (for comments see Greco 2001). In the top panel of Figure 8.30 this comparison is shown at probe P_1. The match is very good up to $t\sqrt{g/H} = 5.7$. After this time, the plunging wave is closing a cavity which is filled with air in the experiments. The experimental pressure probe thus starts recording the influence of the air-cushioning before the actual closure of the cavity (see Colagrossi and Landrini 2003). Conversely, in the present mono-fluid simulation the pressure increase is predicted with a small delay, occurring only when the

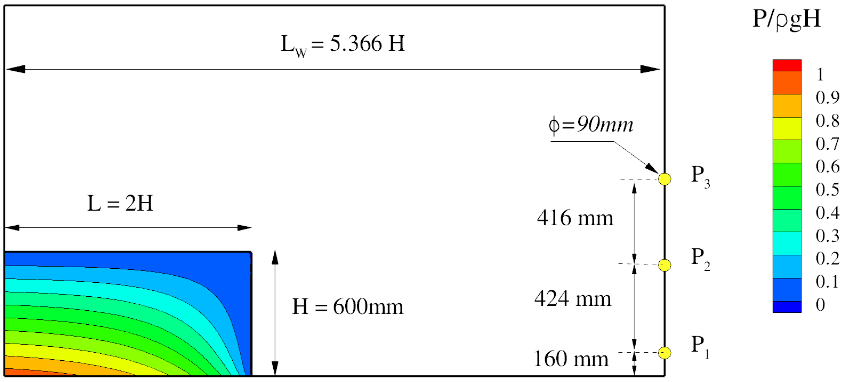

Figure 8.27.: Sketch of the dam-break flow against a vertical wall. P_1, P_2 and P_3 denote the pressure probes.

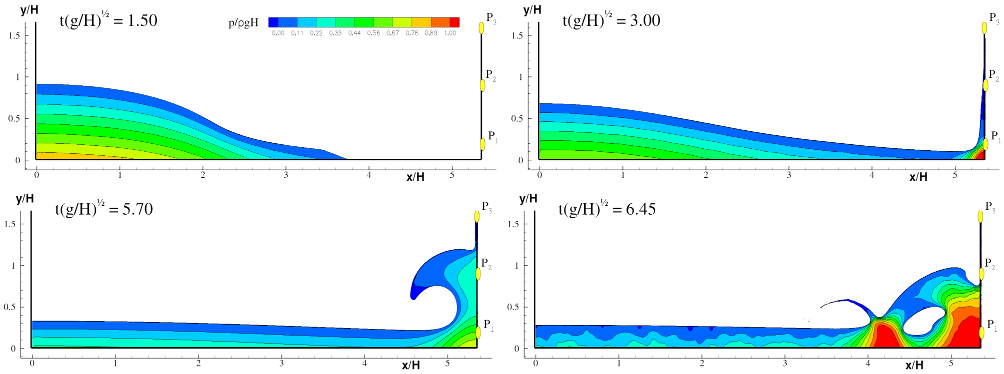

Figure 8.28.: Snapshots of the evolution of the dam-break flow against a vertical wall.

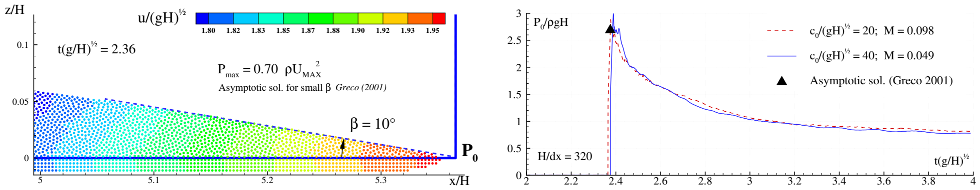

Figure 8.29.: Left: enlarged view of the fluid tongue just before its impact against the vertical wall. Particle colors are representative of the horizontal velocity magnitude. Right: time history of SPH pressure signals evaluated at the point P_0 using two different values of the speed of sound c_0.

plunging wave actually closes the cavity at $t\sqrt{g/H} = 6.0$. Regarding probe P_2 evolution plotted in the bottom panel of Figure 8.30, an experimental pressure increase is observed at about $t\sqrt{g/H} = 4.5$ and reaches its maximum at $t\sqrt{g/H} = 5.5$, that is earlier than at probe P_1. The SPH result plotted at $t\sqrt{g/H} = 5.7$ in Figure 8.31 explains this behavior: near the pressure probe P_2, a stagnation point forms causing this pressure increase. After $t\sqrt{g/H} = 5.7$

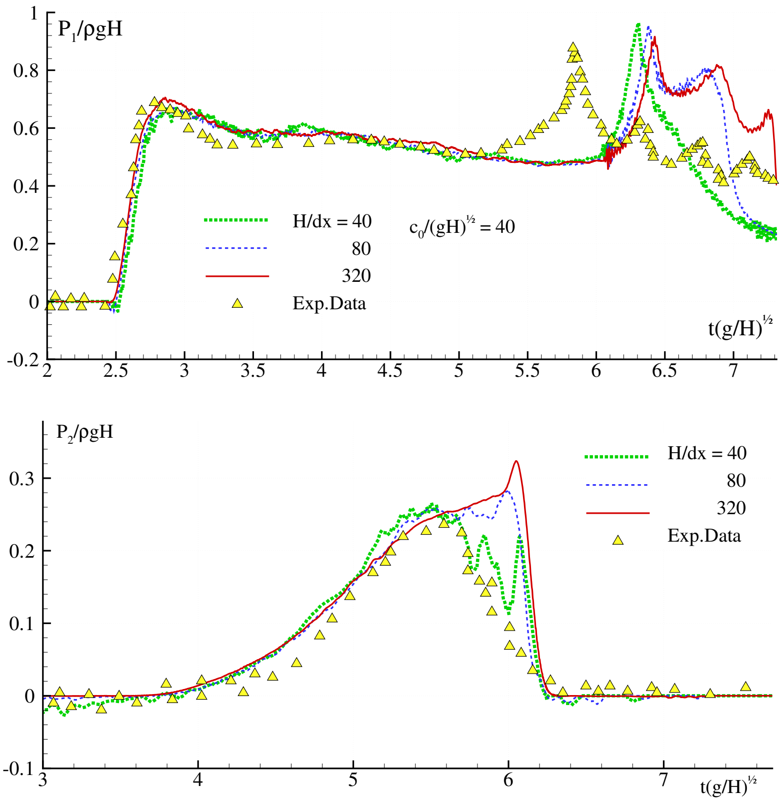

Figure 8.30.: Dam-break flow against a vertical wall. Comparison between the pressure loads measured experimentally and predicted by the numerical model at probes P_1 (top panel) and P_2 (bottom panel). Results are shown for three different space resolutions.

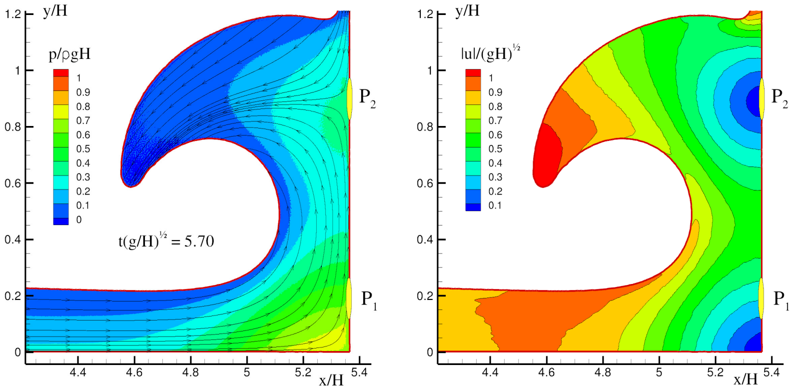

Figure 8.31.: Impact of the dam-break flow against a vertical wall: pressure (left) and magnitude of the velocity field (right) at time $t\sqrt{g/H} = 5.7$.

the numerical and experimental results are different, for the same reason as for the probe P_1. To monitor the flow evolution, it can also be interesting to look at the mechanical energy E_{mech} of the flow. During the flow evolution,

E_{mech} evolves between two levels. Initially, the fluid is at rest and E_{mech} is only the potential energy $E_{pot}^{(1)}$. Finally, the flow reaches a new state of rest by filling

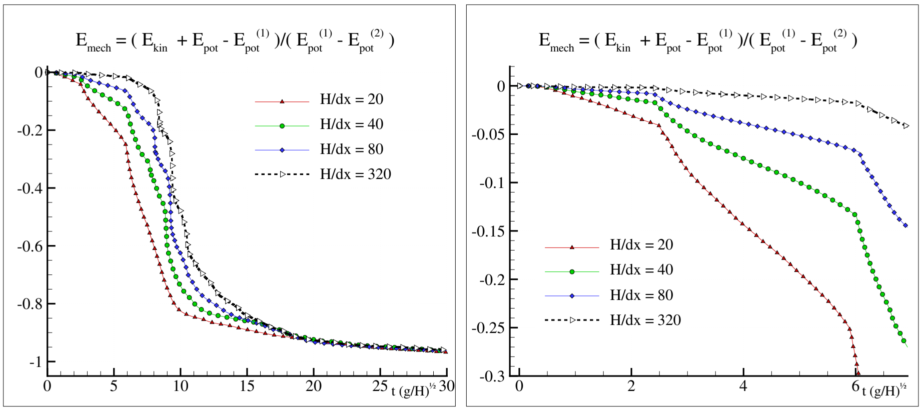

Figure 8.32.: Dam-break flow against a vertical wall. Mechanical energy evolution for different space resolutions. The mechanical energy is made non-dimensional by the potential-energy imbalance $E_{pot}^{(1)} - E_{pot}^{(2)}$ between initial and final situations. Left: global evolution. Right: zoom on the initial evolution.

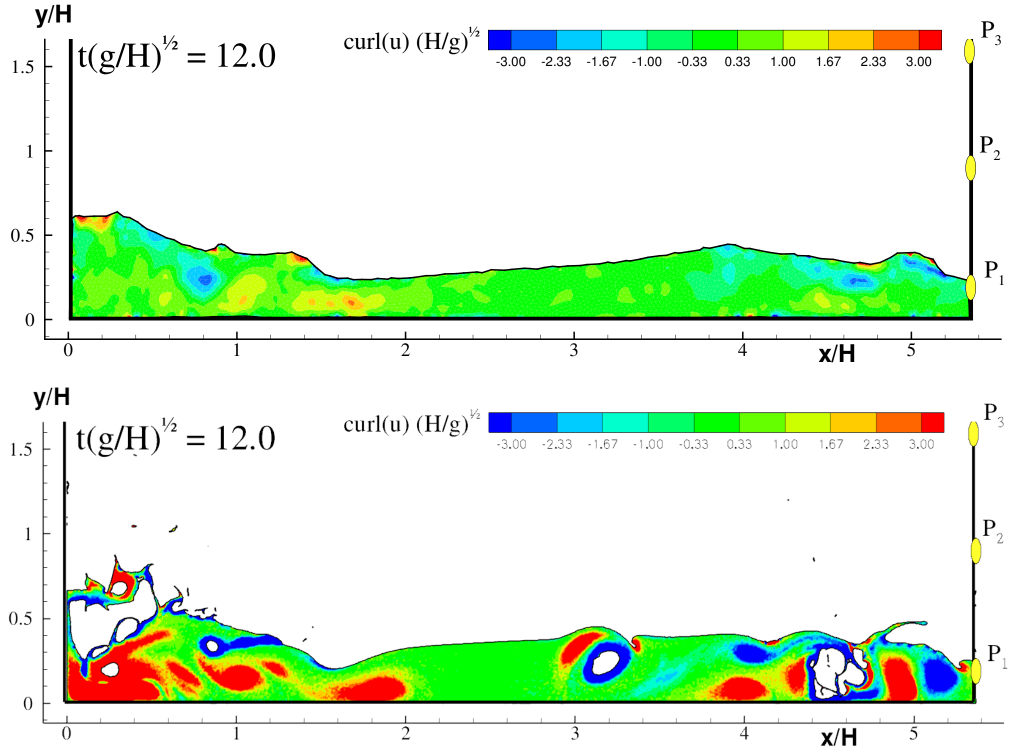

Figure 8.33.: Dam-break flow against a vertical wall. Vorticity field for two different values of the space resolution.

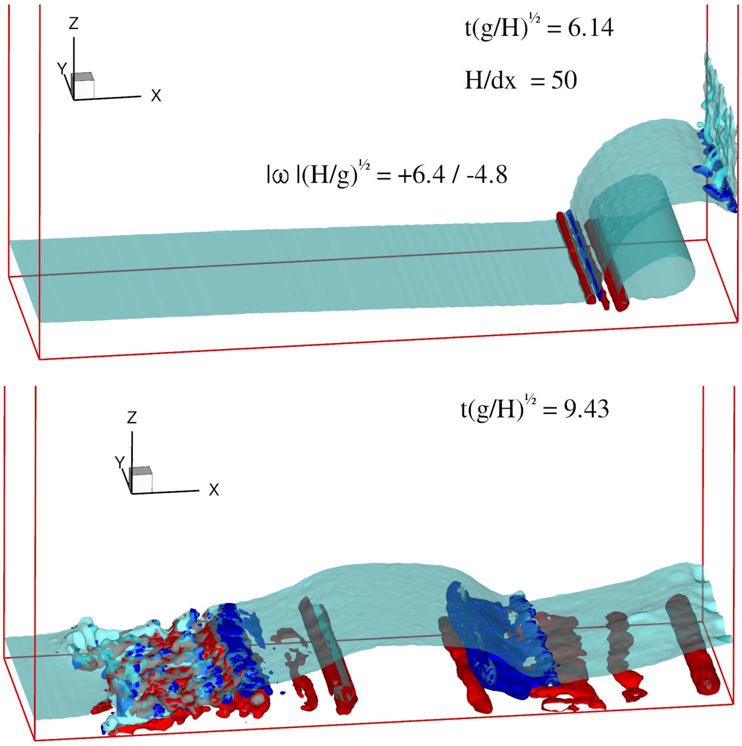

Figure 8.34.: Dam-break flow against a vertical wall in 3D. The fluid structures represent the y-component of the vorticity for two different time values. Red and dark-blue structures represent vorticity of different signs.

the tank width, and E_{mech} is then equal to $E^{(2)}_{\text{pot}}$. In between, potential energy is transformed into kinetic energy which will be slowly dissipated by viscosity (either artificial in SPH, or real in the experiment). Experimentally, it was observed Buchner (2002) that the flow was globally at rest after $t\sqrt{g/H} \simeq 20$, i.e. the free surface was almost still at this time. In the present numerical result plotted in the left panel of Figure 8.32, one observes the same trend and a level close to $E^{(2)}_{\text{pot}}$ is reached at about the same time. However, the evolution between the two levels $E^{(1)}_{\text{pot}}$ and $E^{(2)}_{\text{pot}}$ presents some differences depending on the space resolution used. Before the first splash-up, as illustrated in the right panel of Figure 8.32, the dissipation due to artificial viscosity is lower and lower when increasing the space resolution; a convergence of order 1 is found. Later on, the situation is a bit different. Actually, as shown in Figure 8.33, the finer is the space resolution, the higher is the vorticity embedded within the flow. For a fine space resolution, the vortical structures created due to the multiple wave breakings and splash-ups are diffused into smaller and smaller vortical structures, up to scales getting close to dx where they are dissipated. This explains why the mechanical energy is conserved for a longer duration, as it can be observed in the left panel of Figure 8.32. Conversely, for a coarse space resolution, the scale of the vortical structures created is directly close to dx and these structures are thus dissipated faster.

Finally, 3D effects in the solution are investigated in Figure 8.34. The top panel shows a snapshot of the evolution right after the cavity creation. The vortex tubes created are clearly two-dimensional. Conversely, from the second splash-up and after, a complex three-dimensional vortical pattern is created, proving that the hypothesis of bi-dimensional flow up to the cavity closure is well posed. The free-surface patterns and the vorticity iso-contours shown in this figure have been obtained using the Level-Set function defined in B.

9 VIOLENT IMPACT FLOWS

In violent water/structure interactions, the evaluation of global and local loads is of fundamental importance, their prediction being required for the design of marine structures and their safety in operation. It is indeed a key issue for ocean or coastal structures submitted to extreme sea conditions (see e.g. Mei 1983; Peregrine 2003)). These situations involve different kinds of impact flows: e.g. slamming, sloshing, flooding, and water on deck flows. In the example of the latter flow a large amount of water is shipped on the structure deck, representing a danger both for the structure stability and for the deck superstructures and equipments, (see Greco 2001; Greco et al. 2007). There, the most frequent water shipping events are described in the form of a dam-break flow.

To this purpose, a set of three test cases where impact flows result from dam break situations are investigated with the δ-SPH model. Moreover, the simulation of the complex interaction between a flash flood generated by an unsteady inflow condition and a bridge in a 2D channel is shown as example of engineering application of violent impact flows in continuous current. Within this chapter, specific attention is paid to the evaluation of both pressures and forces on the structures.

Since the Reynolds numbers for the impact problems considered in the following are generally very high, free-slip boundary condition is assumed. This assumption is justified by the fact that the boundary layer has a limited influence on the global flow evolution and on the pressure loads. In the third test case an investigation of the influence of viscosity is provided. In that case no-slip boundary condition is imposed through a simple anti-symmetry mirroring procedure (see 7.1.3). Incidentally, the analysis carried out in this chapter have been obtained using the free-surface tracking and Level-Set function defined in 7.2 and B.

9.1 DAM BREAK FLOW AGAINST A TALL STRUCTURE

The first test case is made of a dam-break flow impacting a tall vertical square column whose width is much smaller than the tank width. For this reason, the flow evolution is expected to show strong three-dimensional effects.

The geometry of the problem is described in Figure 9.1. Numerical results are compared with the experimental measurements by Yeh and Petroff at the University of Washington, while numerical simulations have been performed

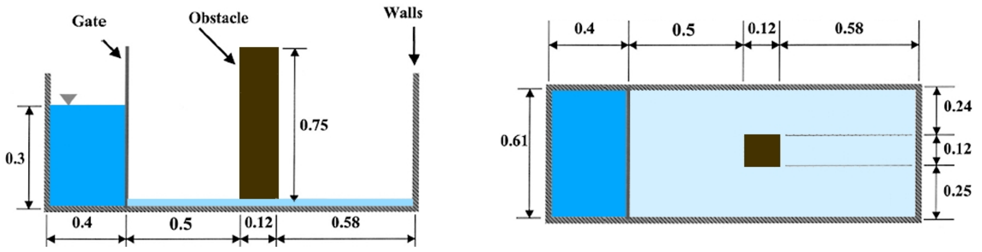

Figure 9.1.: Sketch of the dam break flow against a tall structure.

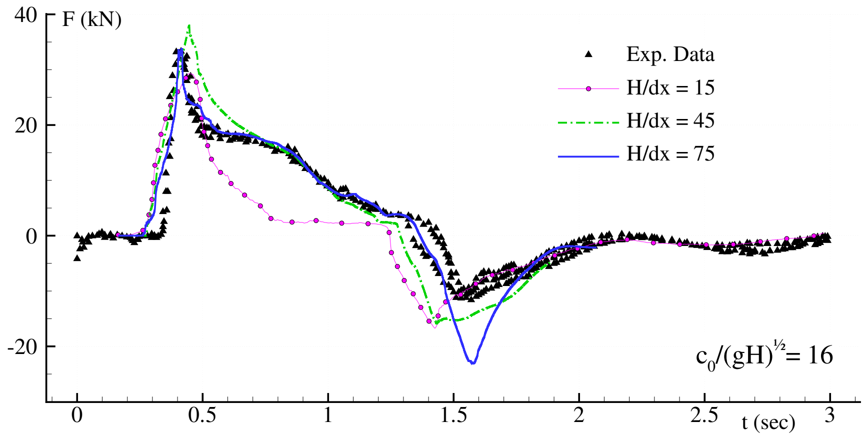

Figure 9.2.: Dam break flow against a tall structure. Comparison of the x-force measured experimentally on the tall structure to the one predicted by the δ-SPH model. H is the initial water depth behind the dam, $H = 0.3$m.

by Dalrymple and Rogers (2006). Experimental measures concerned the time histories of the force on the column and of the velocity at a probe located in front of it. Force was measured with a load cell while velocity was detected through a laser Doppler velocimetry (LDV) system. The velocity measurement was taken 14.6 cm upstream of the center of the column and 2.6 cm off the floor of the tank. In this experiment, a layer of water (approximately 1 cm deep) was present initially on the bottom of the tank. Figures 9.2 and 9.3 show the comparison between experiments and SPH results for different spatial resolutions. For what concerns the x-force on the vertical column plotted in Figure 9.2, a good agreement is obtained. As done by Dalrymple and Rogers (2006), the result is shifted by 0.16s to compensate an offset in the experimental measurement. The amplitude of the first peak is well predicted, the SPH data are convergent to the experimental one, the finest space resolution result being superimposed to the experimental result up to $t = 1.45$s. However, the SPH model overestimates the negative force peak at 1.6s. At that time, the flow has already hit the right wall of the tank and, consequently, has generated several complex fluid structures with air entrapment, see Figure 9.4. Since air is not

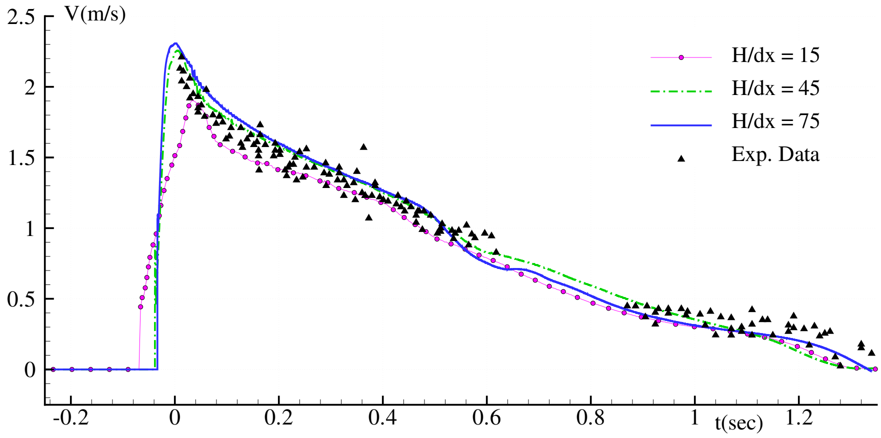

Figure 9.3.: Dam break flow against a tall structure. Comparison of the flow velocity experimentally measured by the LDV probe and the one predicted by the δ-SPH model.

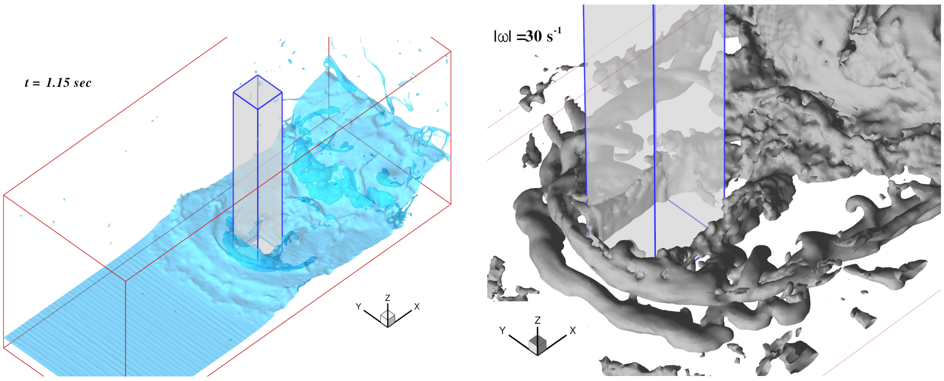

Figure 9.4.: Dam break flow against a tall structure. Left: free-surface snapshot at $t = 1.15$s. Right: iso-contour of the vorticity at same time.

modelled here this further evolution is different, which explains this difference in the negative force peak registered.

Comparison to the velocity recorded by the LDV probe is shown in Figure 9.3. The match with the experiments is excellent and highlights a good convergence. Note that the LDV probes started to measure only once it was wetted by the flow. In the experimental measurements lacks of data can be observed, probably in connection with a bubbly flow generated during the impact on the column.

Finally, a snapshot of the free surface at $t = 1.15$s is displayed in the left part of Figure 9.4, while an iso-contour of the vorticity at same time is shown in the right part. The reader is referred to appendix B for a detailed description of the algorithm used to carry out these figures. An horse shoe pattern vortical tube is visible around the front side of the vertical column whereas a complex,

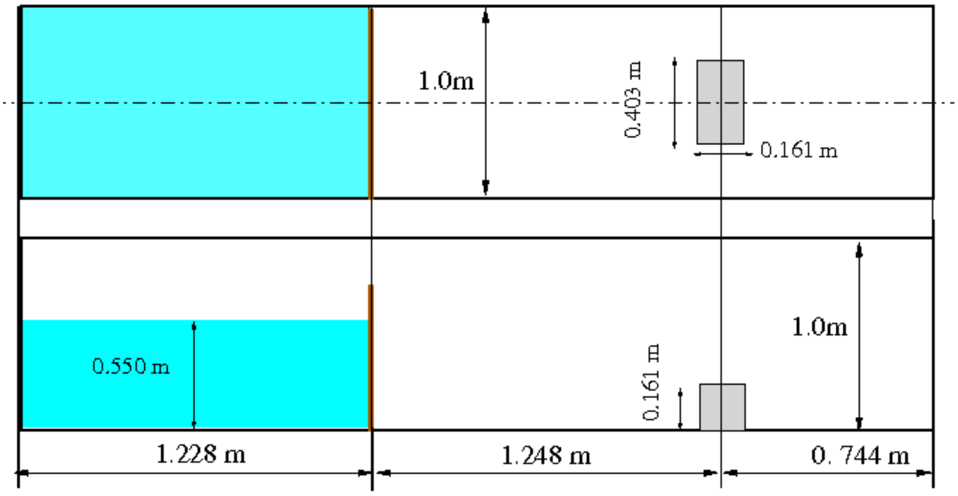

Figure 9.5.: Sketch of the dam break flow against a rectangular step. Top: top view. Bottom: side view along the centerline.

disordered evolution is displayed downstream. The latter is due to the interaction of the upstream flow separating around the column with the downstream flow which comes back after having hit the right wall.

9.2 DAM BREAK FLOW AGAINST A RECTANGULAR STEP

I consider now a dam-break flow with 3D effects where accurate experimental pressure measurements are available. This problem involves a rectangular step whose geometry is depicted in Figure 9.5. Three space resolutions are used in the following; note that the simulation with the finest resolution, $H/dx = 128$, requires 8.5 million particles, while the coarsest one, $H/dx = 32$, involves 133000 particles.

The present dam-break problem has already been studied both experimentally and numerically by Kleefsman et al. (2005) using a Volume Of Fluid (VOF) method. In Figure 9.6 one can observe that, after the impact on the step, water circulates around this obstacle in the horizontal direction and later impacts the right vertical wall. There, two jets are generated which both travel towards the center of this wall, and eventually merge into a backward jet. Simultaneously, the fluid jumps over the step and meets with the backward jet later on.

In the experiments, eight pressure probes were placed along the section of the step corresponding to $y = 0.471$ m. These probes are shown in Figure 9.7 along with an interpolation of the flow pressure in a vertical slice right after the water impact against the step. In Figure 9.8 the pressure signals predicted by the δ-SPH model are displayed for different space resolutions, and compared with the experimental measurements. Probes P_1 and P_3 show a very good

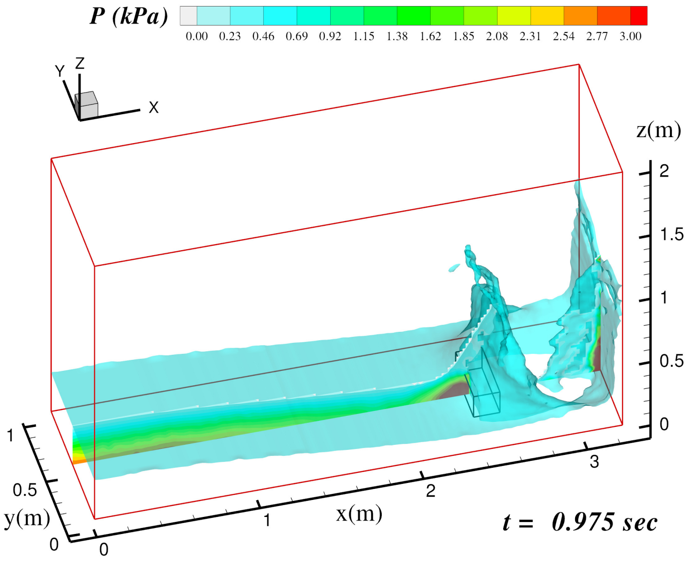

Figure 9.6.: Dam break flow against a rectangular step. Free surface snapshot at $t = 0.975\mathrm{s}$. The central slice shows the pressure contour within the flow.

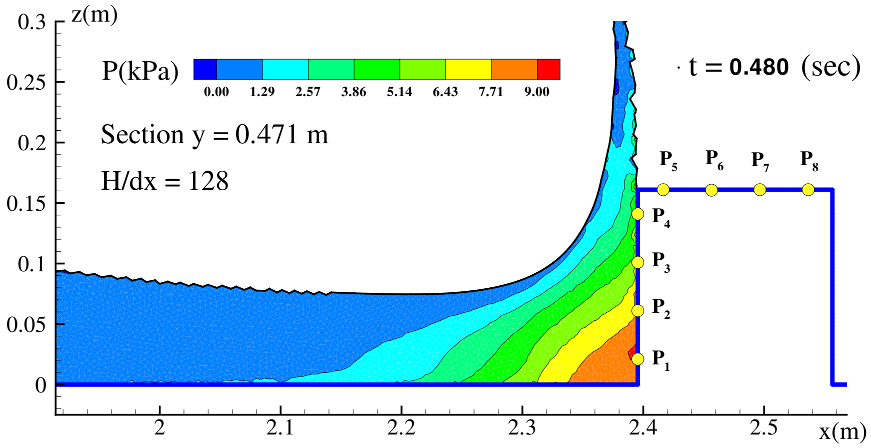

Figure 9.7.: Dam break flow against a rectangular step. Interpolation of the flow pressure in a vertical slice at $y = 0.471\mathrm{m}$. Symbols P_1 to P_8 represent the pressure probe positions.

agreement, even if the maximum peak value is different for P1. It must be noted that experimentally accurately recording such a sharp peak is difficult. Other discrepancies occur between 1s and 3s where spikes are visible in the numerical result. These spikes are due to the collapse of cavities formed on top of the step. A similar behaviour can be observed in the results by Kleefsman et al. (2005) where a single-phase VOF model was used. The comparison between experimental and numerical results becomes worse at probe P_6, mainly because the accurate description of the flow on this probe, which results from

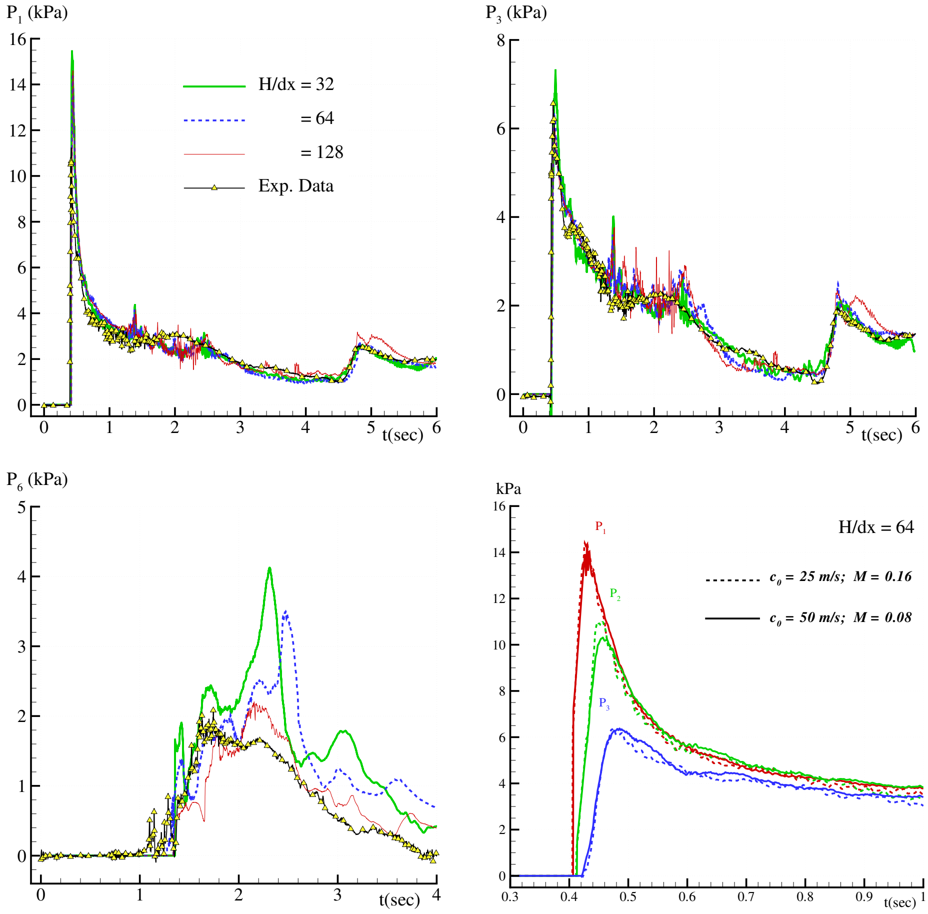

Figure 9.8.: Dam break flow against a rectangular step. Comparison of the pressure signals predicted at probes P_1 (top left), P_3 (top right) and P_6 (bottom left) for different space resolution with the ones recorded experimentally. Bottom right: SPH pressure peaks at probes P_1, P_2 and P_3 for two different sound speeds.

the complex interaction between upstream and downstream parts of the flow, is much more difficult to obtain. Nonetheless, with the finest space resolution used a fair agreement is obtained, especially as air is not considered in the simulation.

In the lower right panel of the same figure the pressure peaks obtained at probes P_1, P_2 and P_3 are displayed for two different choices of the sound velocity c_0, namely $c_0 = 25$ and $50\,\mathrm{m/s}$. This confirms that the influence of the weak-compressibility assumption on the numerical results is very limited.

In Greco (2001) the gravity-less similarity solution by Zhang et al. (1996) was proved to be suitable for studying impact problems similar to those described in the present work. This analytical solution describes the impact of a semi-infinite wedge of fluid against a solid wall. Under the zero-gravity assumption,

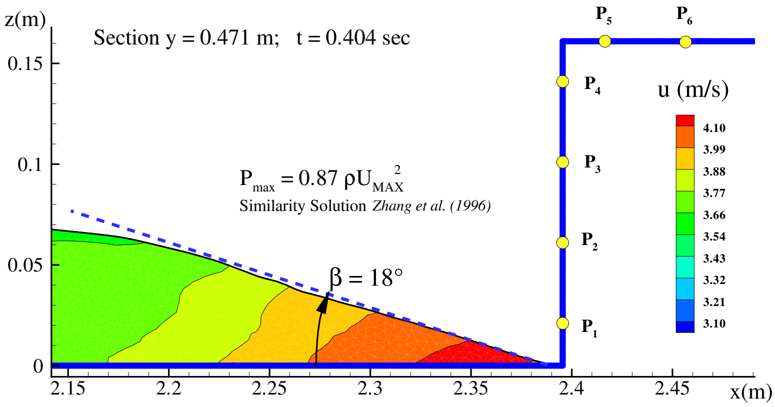

Figure 9.9.: Dam break flow against a rectangular step. Contours of the horizontal component of the velocity field at first impact time, with β the angle of the fluid tongue.

the problem is completely specified by the velocity U of the fluid wedge and by its angle β with respect to the horizontal plane. In the dam-break flow considered here the water front velocity is equal to 4.12 m/s while the front angle is $\beta \simeq 18$ degrees, see Figure 9.9. With these data the analytical solution predicts a maximum pressure of about 14.7 kPa. This value is very close to the one obtained by the SPH solver at probe P_1 which is very close to the corner, see bottom-right plot of Figure 9.8.

9.3 DAM BREAK FLOW AGAINST A SHARP-EDGED OBSTACLE: REMARKS ON VISCOUS EFFECTS

In this test case the influence of viscosity on a dam break flow impacting a sharp-edged obstacle is studied. Note that no experimental data is available for this test case; comparison is thus made with a single-phase Level-Set Finite-Difference solver by Colicchio (2004). This solver is based on a second-order Finite-Difference method and an approximate projection method for the solution of the Poisson equation. The free surface is modelled through a Level-Set function that delimits the water field of the solution.

9.3.1 Inviscid case

First the viscosity influence through the boundary layer is neglected by using a free-slip condition on solid walls. The problem is depicted in Figure 9.10. The solid boundary is characterized by curvilinear parts and convex/concave angles, merging together the need for a proper modelling of complex solid-boundary geometries and the necessity of an accurate description of the free-surface flow. Nine pressure probes are placed on the computational domain boundary, six along the obstacle and three on the tank wall in a curved part. In

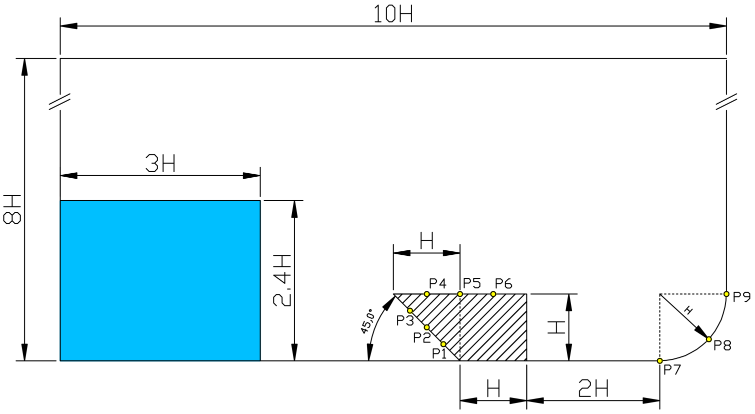

Figure 9.10.: Sketch of the dam break flow against a sharp-edged obstacle. Symbols P_1 to P_9 denote the pressure probes.

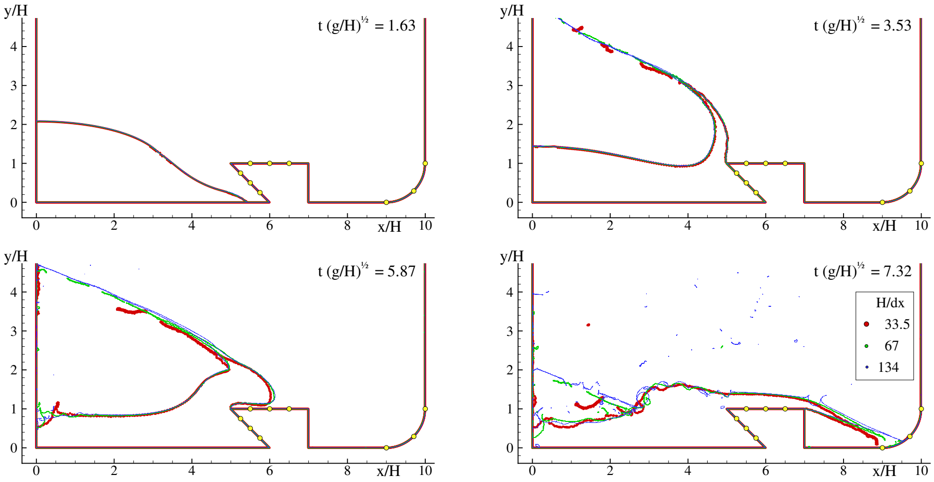

Figure 9.11.: Dam break flow against a sharp-edged obstacle. Evolution of the flow for three different space resolutions.

Figure 9.11 are displayed different snapshots of the dam break flow evolution using three different space resolutions, $H/dx = 33.5$, $H/dx = 67$, and $H/dx = 234$. The fluid motion is first characterized by a violent fluid ejection caused by the sharp edge (top panels) and by a subsequent impact on the obstacle roof (bottom panels). Apart from the last instant ($t = 7.32\,\sqrt{H/g}$) where the flow is largely fragmented, the solution is almost converged from the coarsest resolution. This convergence is further confirmed in the left panel of Figure 9.12 where the pressure at probe P_1 is shown for the three space resolutions. On the right panel of the same figure one can check again that the weak-

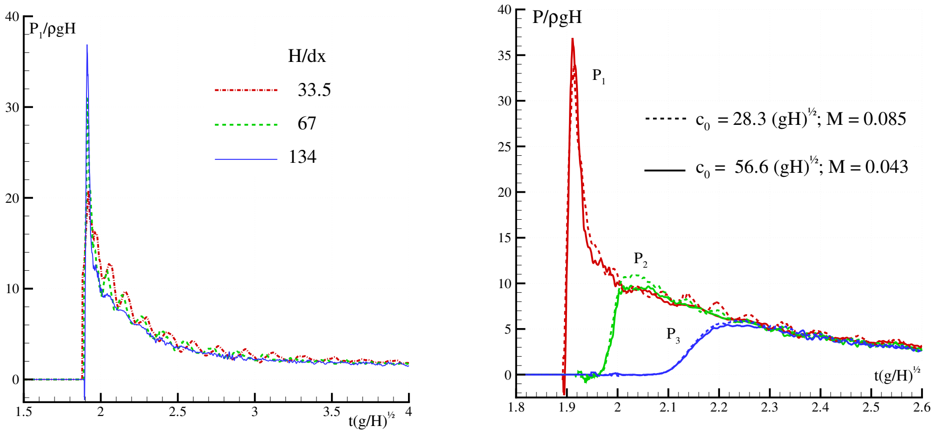

Figure 9.12.: Dam break flow against a sharp-edged obstacle. Left panel: convergence of the pressure solution at probe P_1. Right panel: pressure peaks recorded at probes P_1, P_2, and P_3 for two different values of the sound speed, $c_0/\sqrt{gH}$ =28.3 and 56.6 ($H/dx = 134$).

compressibility assumption is valid since the sound speed has a very limited influence on the predicted pressures.

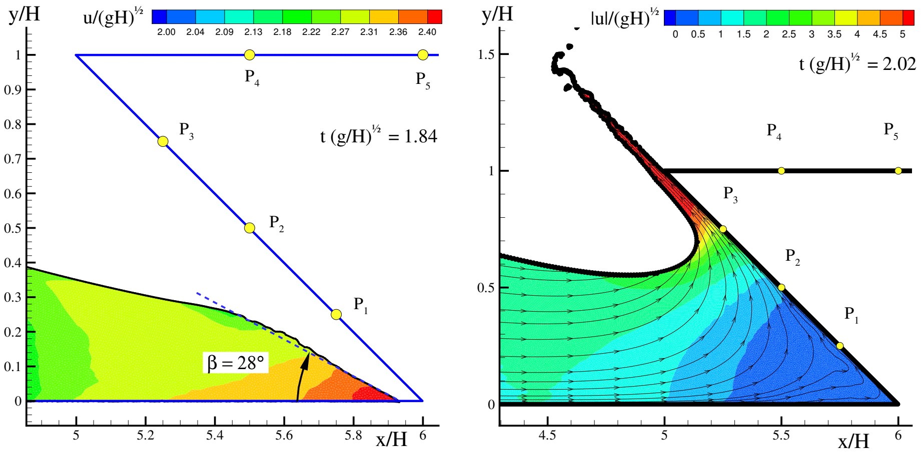

Figure 9.13.: Dam break flow against a sharp-edged obstacle. Left panel: contours of the horizontal component of the velocity right before first impact. Right panel: contours of the velocity magnitude and streamlines at $t = 2.02\sqrt{H/g}$.

In Figure 9.13 a detail of the velocity field near the sharp-edge is shown right before, and after, the first impact. Note that this impact is rather violent since the angle between the free surface and the solid wall at impact is only 13 degrees, and the normal impact velocity is about $1.71\sqrt{gH}$. The pressure peak provided by the Wagner method (Wagner 1932), $P_{MAX} \simeq 36.7\,\rho\,g\,H$, is very close to that predicted by the SPH solver which is displayed in Figure 9.12. Note that the SPH result in not fully converged yet and that the configuration of the impact is not exactly similar to a wedge impact as studied by Wagner.

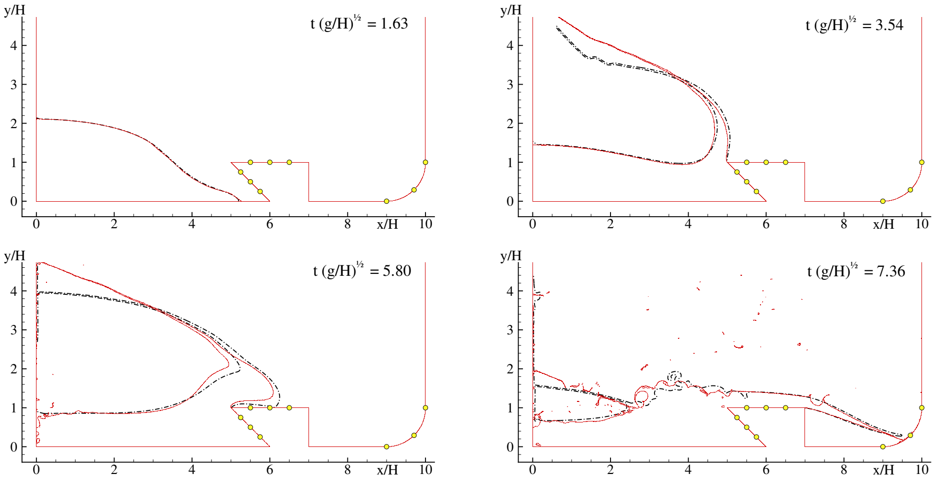

Figure 9.14.: Dam break flow against a sharp-edged obstacle. Comparison between the numerical solutions obtained by the δ-SPH solver with $H/dx = 134$ (solid lines), and the Level-Set solver with $H/dx = 120$ (dash-dotted lines).

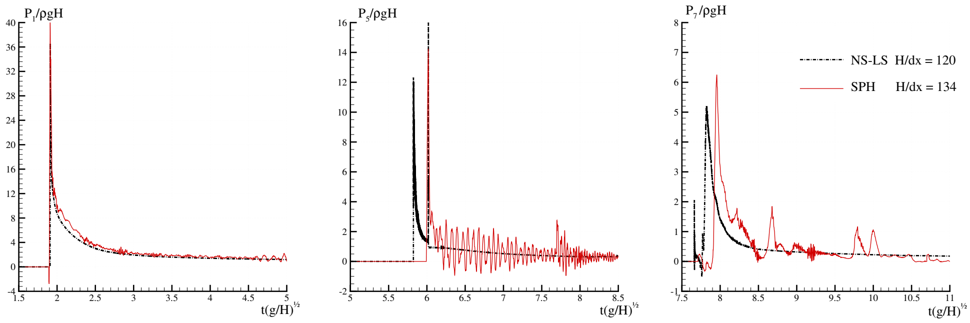

Figure 9.15.: Dam break flow against a sharp-edged obstacle. Pressure at probes P_1, P_5 and P_7 from the δ-SPH solver with $H/dx = 134$ (solid lines), and the Level-Set solver with $H/dx = 120$ (dash-dotted lines).

To check the accuracy of the present model, the SPH solution is then compared to the one obtained through the single-phase Level-Set solver introduced above. Here, free-slip boundary condition is also imposed in that solver. In Figure 9.14 the flow evolution is compared at different times. A good agreement is observed all along the simulation. In Figure 9.15, the pressure given by the two solvers is compared on three probes, P_1, P_5, and P_7. For what concerns probe P_1 the numerical solutions are in close agreement. On probes P_5 and P_7, respectively located on the obstacle top and the on the tank bottom-right wall, the comparison is more qualitative. This is mainly due to a small time

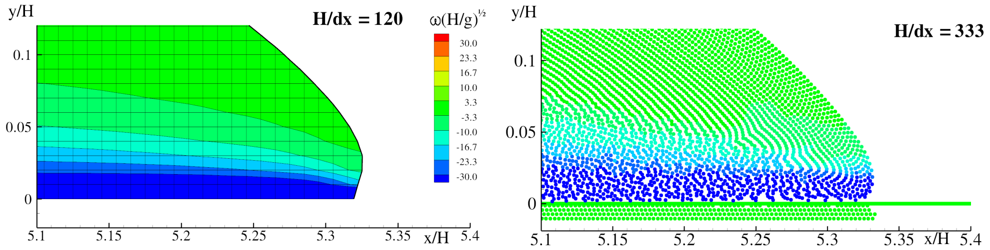

Figure 9.16.: Dam break flow against a sharp-edged obstacle. Detail of the vorticity inside the boundary layer as predicted by the Level-Set (left) and δ-SPH (right) solvers for Re=1000.

shift between the two solutions, as visible in the central panel on P5. On this probe, in the SPH solution the peak is followed by acoustic oscillations related to the weak-compressibility assumption and generated by a cavity closure on the roof of the obstacle. This event appears as a narrow and sharp peak in the tail of the pressure signal of the Level-Set solver for which such a cavity closure is singular. The same time shift is recorded later on probe P7. On this probe the SPH signal exhibits some secondary peaks due to the fact that the fluid jet behind the obstacle is disturbed by several drop impacts.

9.3.2 Viscous case

As final investigation the same comparison between the δ-SPH and Level-Set solvers is performed, this time accounting for the fluid viscosity, i.e. solving system (5.3). A no-slip condition is also enforced in both solvers. In SPH this condition is imposed using the anti-symmetric mirroring (see 7.1.3). In the Level-Set solver this condition is modelled through a second Level-Set function (see 8.2.1 and Colicchio et al. 2006). Two Reynolds number values are considered, $\mathrm{Re} = 1000$ and $\mathrm{Re} = 10000$, where the Reynolds number is defined as $\mathrm{Re} = \sqrt{gH}H/\nu$. Both SPH and Level-Set solvers do not model the turbulence subscale.

Since the chosen Reynolds numbers are quite high, the viscosity influence on the global evolution of the flow is very limited and the numerical solutions for the free surface evolutions are practically identical to those presented in the previous section, at least for $t\sqrt{g/H} \leqslant 5.0$. The main difference with the inviscid case is the generation of the boundary layer along the solid wall. In figure 9.16 we show a detail of the vorticity inside the boundary layer during the early stages of the dam break, for $\mathrm{Re} = 1000$ and for the two solvers. Note that the spatial resolution of the SPH solver is almost three times finer than that of the Level-Set solver because in the Level-Set solver a wall function is used. The thickness of the boundary layer predicted by SPH is in good agreement with the one of the Level-Set solver. Nonetheless, due to the high vorticity

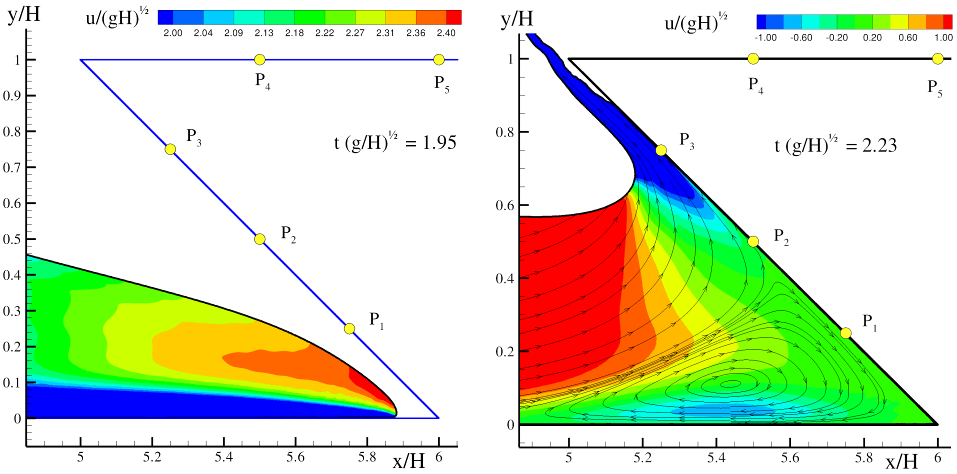

Figure 9.17.: Dam break flow against a sharp-edged obstacle. Contours of the SPH horizontal velocity right before the first impact (left), and after (right) for Re $= 1000$.

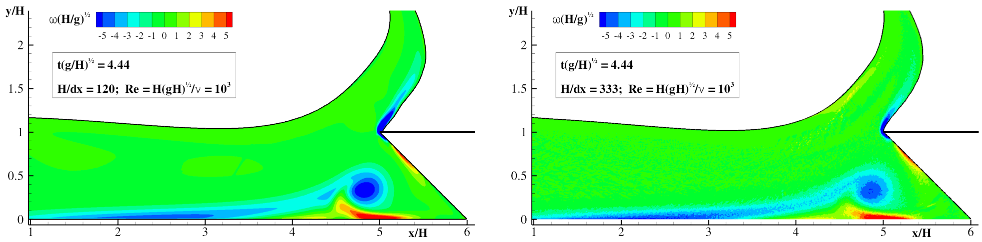

Figure 9.18.: Dam break flow against a sharp-edged obstacle. Vorticity evolution predicted by the Level-Set (left) and δ-SPH (right) solvers for Re=1000.

generated near the bottom wall, the particle position in the SPH boundary layer is noisy and this affects the accuracy of the solution.

When the flow impacts against the sharp obstacle it splits into two fluxes: the first one goes up along the obstacle while the second one goes down to the corner, and then comes back along the bottom wall, see the streamlines in the right part of Figure 9.17. This second flux thus counteracts the action of the incoming flow and detaches the previously formed boundary layer. Later, the interaction between the incoming flow and the new backward flow causes the rolling up of the vorticity, see figure 9.18. This sequence is predicted by both solvers resulting in much comparable vorticity in the flow, as shown in that figure, even though the vorticity is slightly more dissipated by SPH.

Analogous behaviour is found for higher Reynolds numbers. One can observe this by comparing Figures 9.16 and 9.18 for Re $=$ 1000to similar Figures 9.19 and 9.20 for Re $= 10000$. At Re $= 10000$ more differences are visible between SPH and Level-Set than for Re $= 1000$, in the position of the water tongue, and later, in the intensity and shape of the vortical structures. In

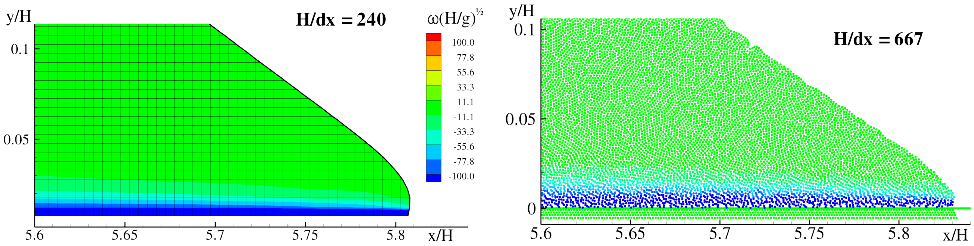

Figure 9.19.: Dam break flow against a sharp-edged obstacle. Detail of the vorticity inside the boundary layer as predicted by the Level-Set (left) and δ-SPH (right) solvers for Re = 10000.

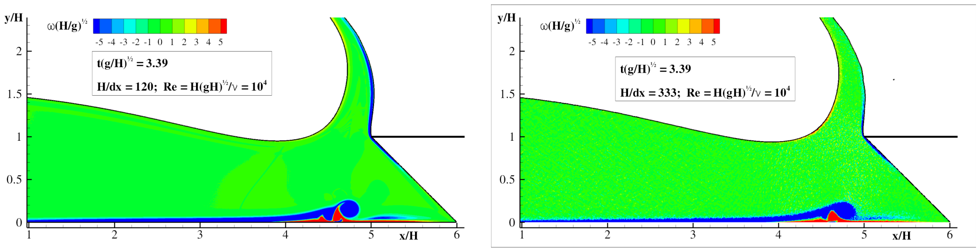

Figure 9.20.: Dam break flow against a sharp-edged obstacle. Vorticity evolution predicted by the Level-Set (left) and δ-SPH (right) solvers for Re = 10000.

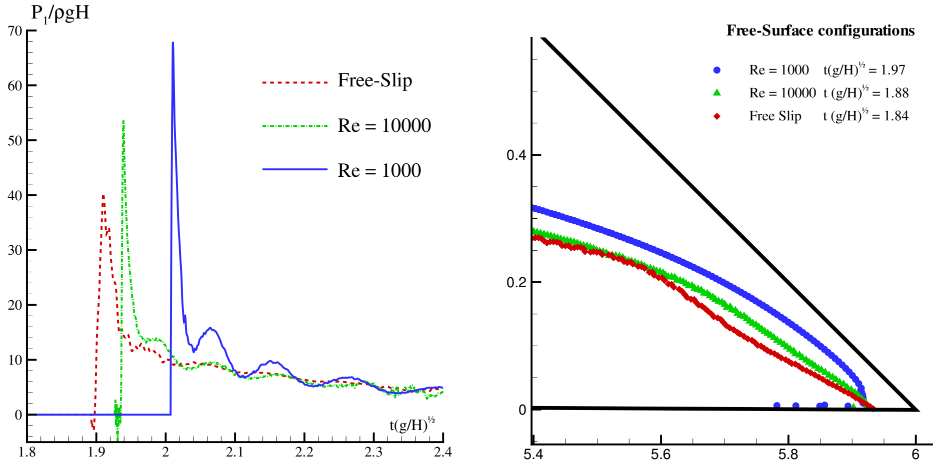

Figure 9.21.: Dam break flow against a sharp-edged obstacle. Influence of the viscosity on the pressure peak at P_1 (left), and on the shape of the fluid front before the first impact (right).

particular, a more intense rolling-up of the boundary layer is present in the Level-Set simulation. Those discrepancies are probably linked to the noisy spatial distribution of the SPH particles in the high vorticity region.

Finally, in the left panel of Figure 9.21 the pressure signal recorded at the probe P_1 is displayed for Re = 1000, Re = 10000, and when using free-slip boundary condition. Surprisingly, the SPH results show that the pressure peak increases with the viscosity. This behaviour is likely to be related to the shape of the fluid front at the first impact which is modified by the no-slip condition. In fact, apart from a delay in the impact time, the viscosity has for effect to bend the fluid front leading to an increase of the free surface angle at the impact point, see right panel of Figure 9.21. This leads to a higher-pressure impact against the obstacle. Anyway, a more careful and exhaustive analysis of the viscosity influence during impacts is postponed to future works.

9.4 FLASH-FLOOD IMPACTING ON A BRIDGE

As an example of a possible application in continuous current a special test case has been devised. The initial set of the simulation is sketched in figure 9.22. A 2D section of a channel and the rectangular section of a bridge crossing over the river are modelled. The bridge section is fixed in space and global forces acting on it are computed integrating the pressures along its boundaries. The flow velocity U is uniform and equal to $\sqrt{2gH}$, where H is the initial channel water level.

At $t_0 = 0$ the inflow water level starts to raise up to $z(t_f) = 2H$ in a time interval equal to $t_f - t_0 = 2\sqrt{2H/g}$. The rapid raising of the water level causes the generation of a gravity wave system propagating forward ahead the main flow and eventually hitting the bridge in the left-bottom corner (top two plots of figure 9.24). The subsequent flow evolution is shown in the three bottom plots of figure 9.24 where the free-surface configuration and the vorticity field are plotted. In figure 9.23 the time history of global loads acting on the body are plotted respectively for the component along the x-axis (D), along the z-axis (L) and for the torque (T) counter-clockwise positive. The first wave impact occurs at approximately $t = 5\sqrt{2H/g}$ where a small peak is registered in the vertical force and in the torque, while the horizontal force increases for a time interval of about $4\sqrt{2H/g}$ due to the incoming flow.

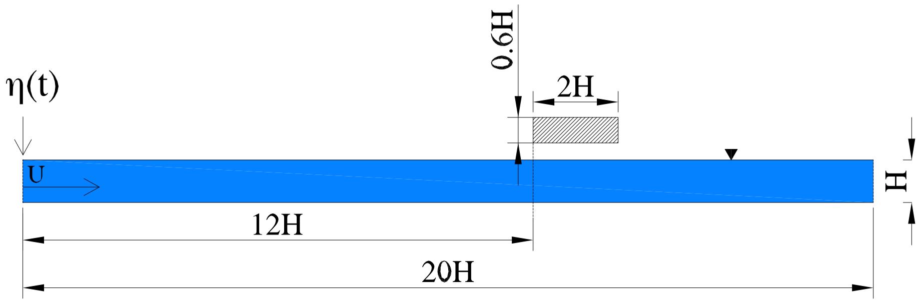

Figure 9.22.: Sketch of the geometry used as initial set for the problem of a flash-flood hitting a bridge

After the first impact a rising jet is generated, fed by the upcoming flow and eventually impinging both the bridge section and the flow upstream (middle plot of figure 9.24) that corresponds to a negative vertical force in middle plot of figure 9.23 at $t = 7.9\sqrt{2H/g}$. This is followed by a complex transient stage where intermittent over-toppings occur until approximately $t = 20\sqrt{2H/g}$. In particular, at $t = 15.7\sqrt{2H/g}$ a force peak is registered in all the three plots of figure 9.23. This is due to the closure of the cavity generated by the plunging jet over-topping the body as clearly visible in the second plot from the bottom of figure 9.24. After that, a more stable regime is established where the flow overpasses the bridge with a stream contraction under the obstacle and an undular bore propagating upstream (bottom plot of figure 9.24). After this instant, the forces are almost stationary even if the flow downstream the body is still intermittent due to cavity closures. The latter phenomenon causes fluctuations in the vorticity field that mostly affect the pitching moment. These vortical structures exit through the outlet without releasing any spurious numerical effect in the velocity field.

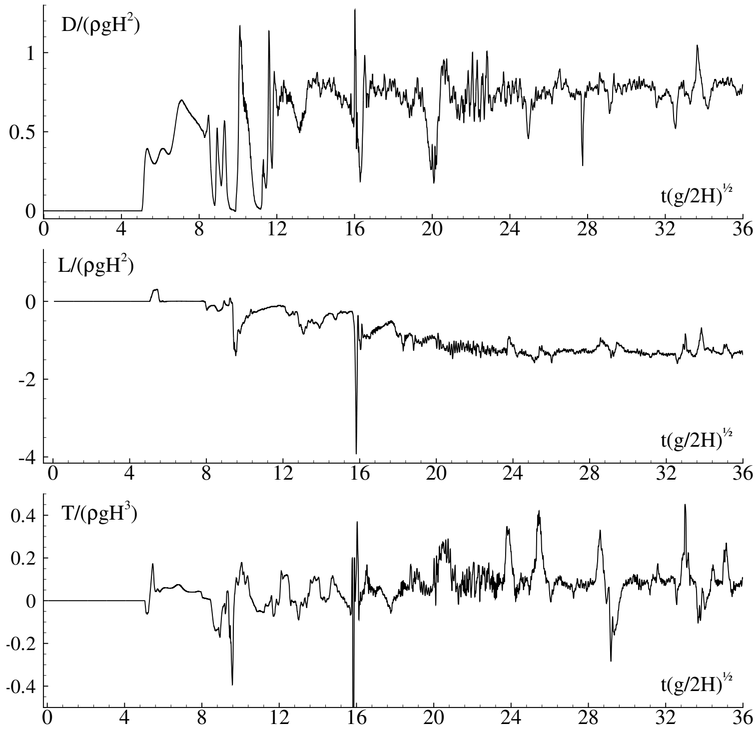

Figure 9.23.: Flash-flood hitting a bridge: time history of the global loads acting on the rectangular body: horizontal forces D (top), vertical forces L (middle), torque T (bottom) counter-clockwise positive.

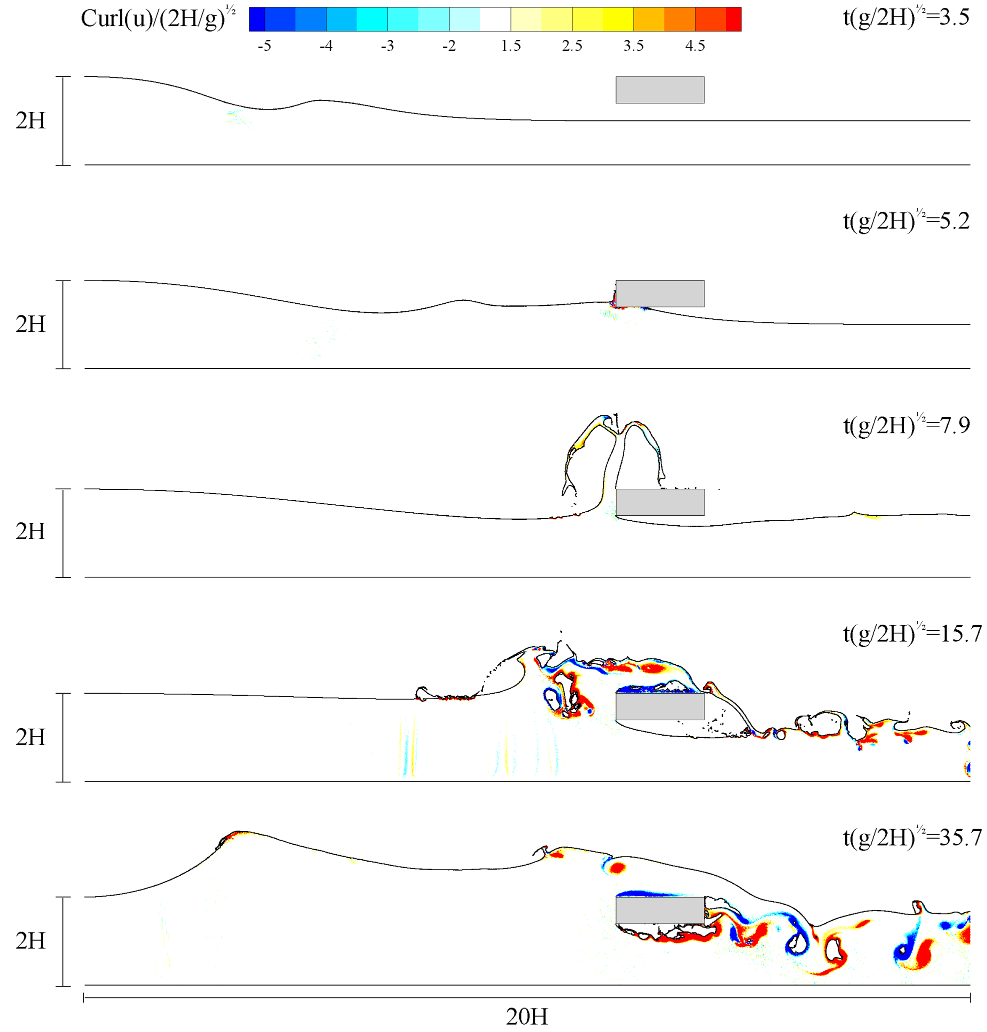

Figure 9.24.: Flash-flood hitting a bridge: plot of the free surface and vorticity field at $t = 3.5\sqrt{2H/g}$, $t = 5.2\sqrt{2H/g}$, $t = 7.9\sqrt{2H/g}$, $t = 15.7\sqrt{2H/g}$ and $t = 35.7\sqrt{2H/g}$.

10 SHIP GENERATED WAVES

In this section the complex fluid-structure interaction problem associated with the ship-wave generation is studied through the developed SPH model. Specifically, a ship in steady forward motion is modelled and the occurrence and features of breaking-bow waves are examined.

From the physical point of view, it has been crucial for long time to understand how the bow wave breaking process develops and how it modifies the flow field. Ship-generated waves have always fascinated scientists and played a key role in surface-ship hydrodynamics contributing to hull resistance (Baba 1969; Inui 1981), generating noise (Oguz and Prosperetti 1991) and radiating very long narrow wakes that are remotely visible (Reed and Milgram 2002). Some of these phenomena originate abeam the ship in the form of extensive breaking of diverging bow and stern waves, eventually developing in wakes. The progress given by the numerical and experimental studies dedicated to the breaking phenomena have has helped in the comprehension of the physical mechanisms connected with ship-wake generation and at present, some numerical models for free-surface flows, in particular RANS with level-set algorithm, are able to simulate 3D breaking phenomena of bow waves (see for example Carrica et al. 2005; Di Mascio et al. 2007).

Two different approaches are here adopted for this problem. Firstly a simplified model is used to study the 3D steady flow around the ship through an equivalent 2D unsteady problem ($2D + t$ approximation). This simplification permits to avoid expensive 3D computations in order to reach high resolution for the modelling of bow breaking waves. An in-depth analysis of the breaking evolution is provided focusing on the different features of the plunging jet as function of the ship forward velocity and qualitatively comparing the results of the parametric analysis to experimental data. After that, a 3D SPH parallel solver, specifically conceived, is used to study the entire wave field and to capture the bow breaking wave phenomenon. For this problem the results of the $2D + t$ model are exploited to obtain basic insights on the resolution needed to solve breaking inception at the bow and features along the ship. This task is remarkably more demanding than previous one since in the full 3D simulation the bottom influence on the solution are more important since in the $2D + t$ approximation the transverse waves, characterized by large wave length for considered velocity range, are neglected (see appendix D for more details). Therefore, preliminary tests are performed to evaluate the capability of the solver in dealing with 3D breaking flows and to identify the smallest computational domain acceptable to simulate a ship advancing in open and deep waters, i.e. with limited effects of the lateral and bottom boundaries on the numerical solution.

Two different hulls are considered: the "Athena" research vessel of the US Navy and the NATO "Alliance" research vessel. The first one is enforced along the vessel to study the different characteristics of the bow flow in a wide range of Froude numbers. Indeed, for this hull several experimental pictures of the bow breaking wave are available. The Alliance ship is instead adopted for the 3D computations since both experimental and numerical data are attainable for the global wave field at Froude number $Fr = U \ \sqrt{gL} \simeq 0.33$, with L and U the ship length and forward velocity, respectively, and g the gravity acceleration.

In all the simulations free-slip conditions are adopted to avoid the complexities related to the evaluation of boundary layers along the ship hull. This simplification is well-posed since the viscous effects are limited on the wave pattern generated by the ship.

10.1 $2D + t$ SPH MODEL TO STUDY BREAKING BOW WAVES

Here the analysis is limited to high speed slender ships with a sharp stem. In this framework basic insights can be achieved by an approximate quasi three-dimensional model based on the idea that longitudinal gradients of relevant flow quantities are small compared with vertical and transverse gradients and the problem equations can be simplified. On this ground, the inviscid three-dimensional problem, steady in the ship reference frame, can be solved in an Earth-fixed transverse plane crossed in time by the ship cross-sections (from the bow to the stern) during the vessel forward motion. The resulting equations are mathematically equivalent to those governing the unsteady two-dimensional free-surface flow generated by a 2D body in the vertical plane transverse to the ship. This body coincides with the instantaneous ship cross section in that plane and so it deforms as the ship moves forward (see sketch in figure 10.1). Consistently, this approximation is here called $2D + t$ model. Within the $2D + t$ framework, the non-linearities induced by hull and free-surface deformations are fully retained.

A historical recollection of slender-body theory for ship hydrodynamics is given in Maruo (1989), Tulin and Wu (1996) and Fontaine and Tulin (1998). This approach results to be quite successful for studying steady and unsteady flows around high-speed vessels (see e.g. Faltinsen and Zhao 1991)). In the context of severe wave-ship interactions, the use of $2D + t$ has been exploited in Maruo and Song (1994) and Wu et al. (2003). In Maxeiner et al. (2008) and Shakeri et al. (2006) an experimental $2D + t$ approach is used to study breaking bow waves through the use of a deformable wavemaker. A previous study of bow wave using SPH method has been provided in the work of Colagrossi

(2005) where the characteristics of the plunging jet are analysed and compared against a Boundary Element Method.

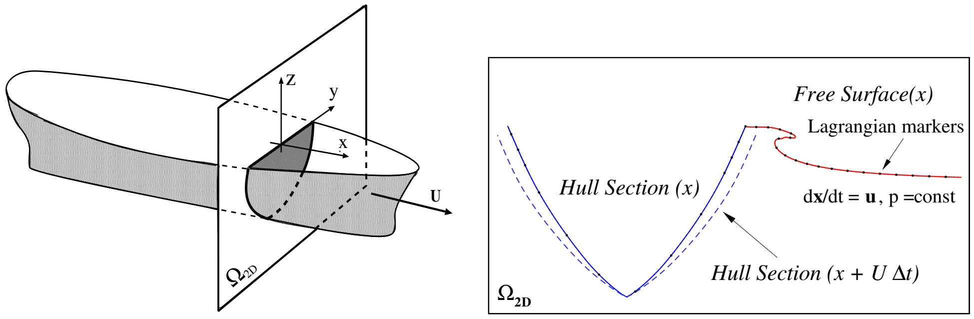

Figure 10.1.: Qualitative sketch of the $2D + t$ approximation for the steady three-dimensional flow around a ship with constant forward speed U. Left: 3D ship problem. Right: equivalent unsteady 2D problem ($2D + t$).

10.1.1 Mathematical model

The mathematical formulation of the $2D + t$ problem has been given in Maruo and Song (1994) and Wu et al. (2003). Here, the study is limited to the prediction of the (inviscid) flow in the immediate neighbourhood of the bow of a ship with constant forward speed and fixed trim and sinkage.

Let us consider the free-surface steady flow generated by a ship moving with constant velocity U into an inviscid fluid. We assume the beam-to-draft ratio $B/D \sim \mathcal{O}(1)$ with B and D individually much smaller than the ship length L, i.e. $\varepsilon = B/L, D/L \ll 1$. We also assume $Fr = \mathcal{O}(1/\sqrt{(\varepsilon)})$ (Fontaine et al. 2000).

Within the $2D + t$ theory, the advancing motion of the hull is modelled through a two-dimensional flux generated by a solid body expansion/contraction (see figure 10.1). Then, we need to evaluate at each time the intersection between the hull and the control Earth-fixed plane ($\partial\Omega_{2D}$ in the left sketch

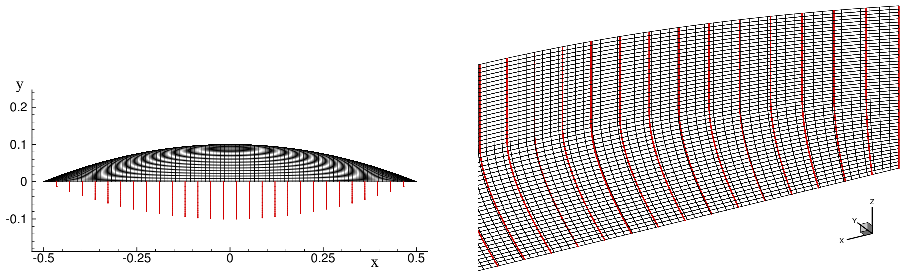

Figure 10.2.: The Wigley hull ($L/B = 5$, $L/D = 10$). The black mesh has been obtained by using a *spline* interpolator algorithm starting on the red sections.

of figure 10.1) where the 2D problem is solved in time. The implemented solution procedure is as follows: first the ship is split in a finite number, say N_{sec} of cross-sections; then the deformation (expansion/contraction) velocity associated to each of them when crossing the control plane is estimated; finally a spline interpolator is used to reconstruct intermediate cross-sections and related deformation velocities from the N_{sec} cross-sections. The last step is necessary to be able to study 2D evolutions with arbitrary time steps, i.e. as required by accuracy and stability issues of the SPH solver (see equation 4.22). The correctness and accuracy of the interpolation algorithm have been checked on a *Wigley* hull (see figure 10.2) since its shape can be easily expressed through an analytical formula.

At each time the intersection between the hull and the control plane is described as follows

$$\begin{cases} y = y(\xi, t), \\ z = z(\xi, t), \end{cases} \tag{10.1}$$

where ξ is the curvilinear abscissa and the time t is related to the velocity U of the ship. Let x_0 be the abscissa of the ship cross-section at the initial time instant. Then,

$$x = Ut + x_0 \tag{10.2}$$

represents the abscissa within a ship-fixed frame of reference. This means that the longitudinal-derivative term $U\partial/\partial x$ in the ship-reference frame becomes the time derivative $\partial/\partial t$ in the Earth-fixed reference frame The unit vector normal to the cross section (10.1) is

$$\mathbf{N}_{2D} = \frac{1}{\sqrt{y_\xi^2 + z_\xi^2}} \begin{pmatrix} z_\xi \\ -y_\xi \end{pmatrix}, \tag{10.3}$$

while the expansion/contraction velocity is:

$$w_n = (y_t, z_t) \cdot \mathbf{N}_{2D} = U(y_x, z_x) \cdot \mathbf{N}_{2D} = U \frac{y_x z_\xi - z_x y_\xi}{\sqrt{y_\xi^2 + z_\xi^2}}. \tag{10.4}$$

Once w_n is known, it is possible to impose the impermeability condition along the hull section. In the three-dimensional case the hull surface can be represented through

$$\mathbf{X} = \begin{cases} x = x, \\ y = y(x, \xi), \\ z = z(x, \xi), \end{cases} \tag{10.5}$$

and the normal unit vector is

$$\begin{aligned}\mathbf{N}_{3D} &= \frac{\mathbf{X}_\xi \times \mathbf{X}_x}{|\mathbf{X}_\xi \times \mathbf{X}_x|} = \\ &= \frac{1}{|\mathbf{X}_\xi \times \mathbf{X}_x|}\begin{pmatrix} y_\xi z_x - y_x z_\xi \\ \\ z_\xi \\ \\ -y_\xi \end{pmatrix},\end{aligned} \tag{10.6}$$

where $|\mathbf{X}_\xi \times \mathbf{X}_x| = \sqrt{y_\xi^2 + z_\xi^2 + y_x^2 z_\xi^2 + z_x^2 y_\xi^2 - 2 y_x y_\xi z_x z_\xi}$. Under the assumption $B/L \ll 1$, it is

$$|y_x z_\xi - y_\xi z_x| \ll |(z_\xi - y_\xi)|, \tag{10.7}$$

and, therefore, $\mathbf{N}_{3D}$ is almost coincident with $\mathbf{N}_{2D}$. In the present implementation, also the evaluation of w_n has been made through a *spline* interpolator.

10.1.2 Description of the problem

Let us consider the fluid domain displayed in figure 10.3 where D is the draft of the ship, B the beam, W is the width of the computational domain and Z is the water depth (that is, the distance between the free surface and the bottom). Assuming a board-starboard symmetry of the ship, the problem is symmetric with respect to the longitudinal central plane of the vessel. So numerically only half part of the vessel can be simulated by using the symmetry property. Therefore, the left side of the computational region is closed by a solid wall going from the keel to the bottom along the symmetry axis of the ship. The horizontal length of the computational region has been chosen in order to avoid spurious reflections from the right solid boundary during the simulation. In the specific, we chose $W = 4\,B$. For what concerns the water depth, $Z = 2\,D$ is used since such a choice ensures a weak influence of the bottom on the breaking wave evolution (see for further details appendix D).

Two different spatial resolutions have been used in all the numerical tests: in the upper part of the fluid domain (that is within a distance $0.2\,D$ down from the free surface) a finer resolution is used to properly handle the breaking phenomena and a coarser one, half of the finer one, in the lower part of the fluid region (that is within a distance D up from the bottom). Between them, a transitional region smoothly goes from one resolution to the other (see figure 10.4). The small size ratio between the two different discretizations is due to the fact that a fixed smoothing length h is used (see section 4.3 for more details).

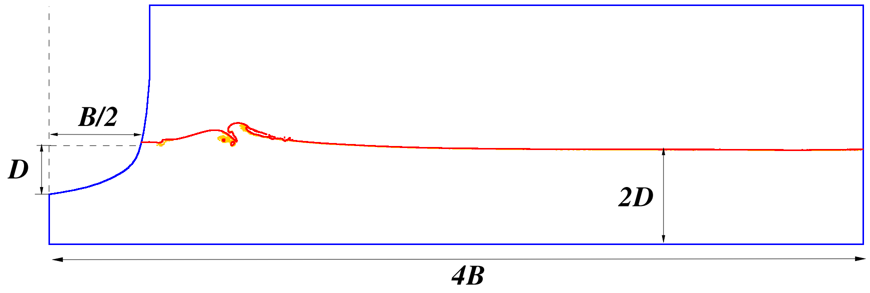

Figure 10.3.: Sketch of the fluid domain.

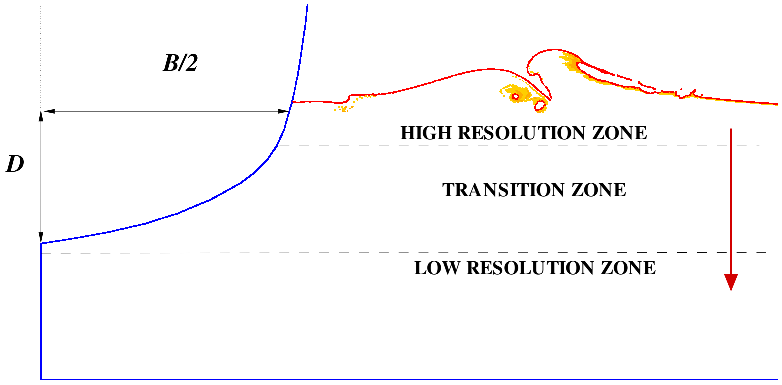

Figure 10.4.: Sketch of the zones with finer and coarser spatial resolutions.

10.1.3 Discussion of the results for the Athena ship

Description of the flow evolution

The analysis is focused on the breaking-bow wave pattern generated by the Athena research vessel, which is a 47 m long multi-purpose boat of the US Navy. Such a vessel has been investigated with a 8.25 scale-ratio at the David Taylor Model Basin (DTMB 5365) and an experimental campaign has been performed at the Italian Ship Model Basin (CNR-INSEAN).

In figure 10.5 the body plan is shown together with the stem and the stern profiles while in figure 10.6 we drew the cross sections for the case with $Fr = 0.5$. Note that the water free surface is tracked using the algorithm proposed in section 7.2.

Within the 2D+t strategy, at the initial time instant, the ship cross section is out of the fluid region (see section S_0 in left plot of figure 10.7). Then, during the first stages of the evolution, the hull section moves toward the free

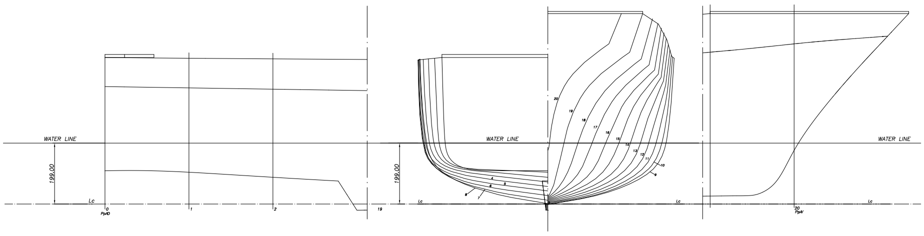

Figure 10.5.: The Athena research vessel DTMB 5365.

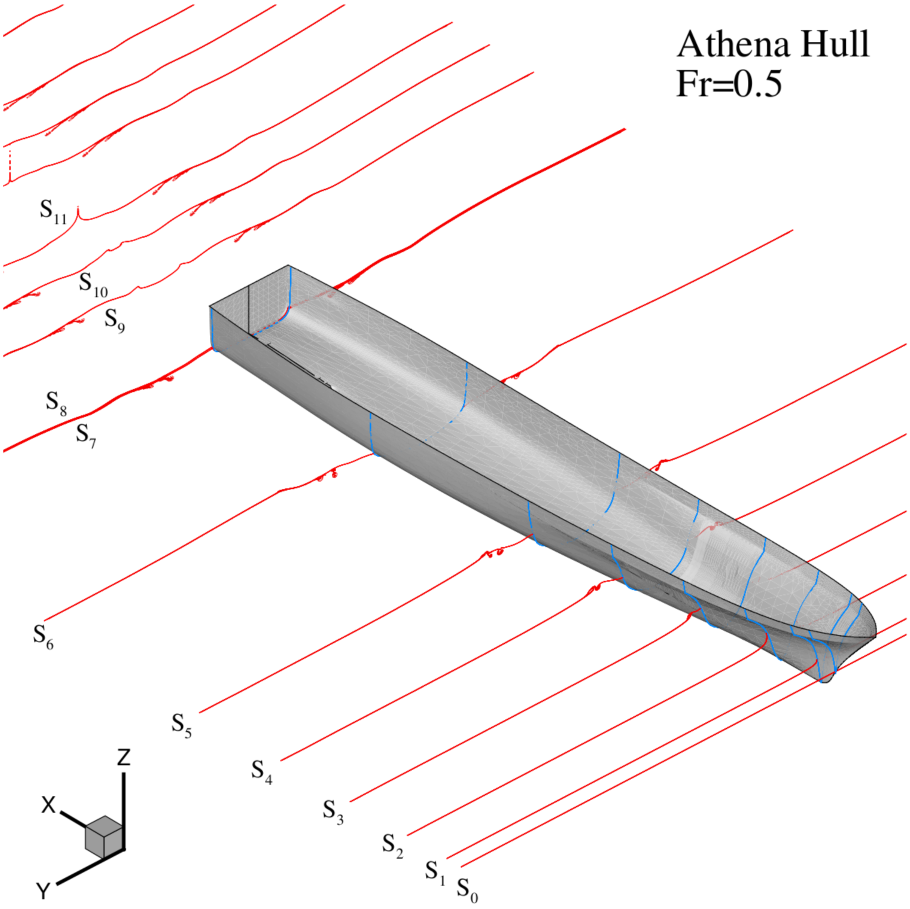

Figure 10.6.: Sketch of the cross sections along the Athena vessel.

surface similarly to a water-entry phenomenon (section S_1). Consequently, a violent water displacement occurs generating a water run-up along the ship bow (section S_2). Such a motion is fed by the expansion of the ship cross section leading to a bow breaking wave (section S_3). The breaking occurs quite close to the ship hull and initiates a cyclic process of splash-up (section S_4). At this stages, multiple vortex structures are generated (see right plot of figure 10.7) and, then, move far from the ship hull. Such a phenomenon is deeply discussed in Tulin and Landrini (2000), Landrini et al. (2003) and Colagrossi and Landrini (2003). The plunging jets and the induced vortical structures are highlighted using the fluid particles which, at the initial stage, lie on the first and second horizontal rows near the free surface. It is worth noting that in real 3D wave breaking the air can escape through the lateral openings of the wave tube while in the 2D + t model this effect can not be taken into account. Therefore, in the present work the air phase is not modelled. However, in problems involving violent fluid-structure interaction the air entrainment can play an important role (see e.g. Colicchio et al. 2010).

In right plot of figure 10.7, section S_5 shows the deepest point of the ship keel. After it, a water exit phenomenon starts. Section S_6 shows the maximum horizontal width of the ship and section S_7 the transom stern, that is, the last cross section of the ship. After it, the water exit is completely realized and a rooster tail, surrounded by steep breaking diverging waves is generated (see left plot of figure 10.8). The analysis of the flow field shows that the rooster tail is caused by i) the inward motion of the fluid in proximity of the ship associated with the contraction of the hull section and eventually colliding after the end of the ship, and ii) the gravity rebound of the free surface (Landrini et al. 2001).

The 2D + t theory can only describe a dry transom stern condition since it cannot model the fluid adherence to the transom. However, according to the experimental results shown in Lugni et al. (2004), the choice $\mathrm{Fr} \geqslant 0.3$ ensures a dry transom stern for the geometry at hand and, therefore, confirms the applicability of the 2D + t to the description of the flow motion after the water-exit phenomenon.

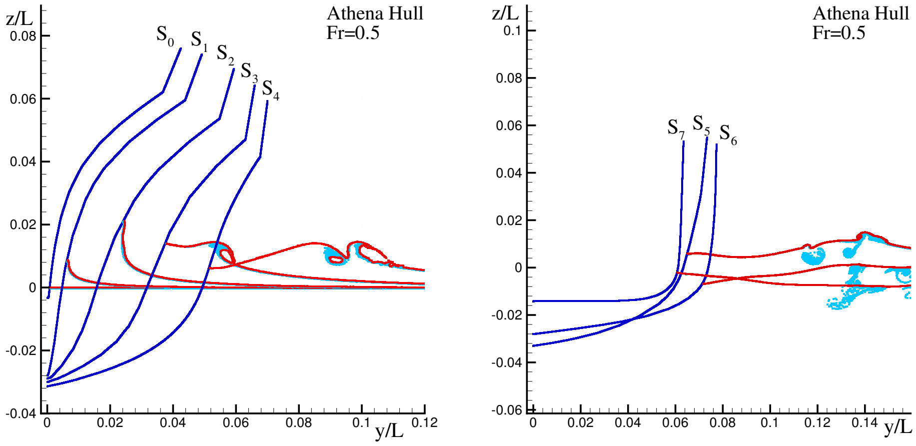

Figure 10.7.: Snapshots of the 2D flow evolution within the 2D+t theory: sections S_0 $(x/L = 0)$, S_1 $(x/L = 0.024)$, S_2 $(x/L = 0.092)$, S_3 $(x/L = 0.189)$, S_4 $(x/L = 0.307)$ (left plot) S_5 $(x/L = 0.446)$, S_6 $(x/L = 0.711)$, S_7 $(x/L = 1.0)$ (right plot).

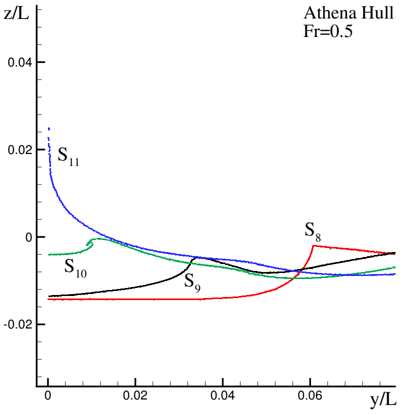

Figure 10.8.: Snapshots of the evolution for sections $S_8(x/L = 1.01), S_9(x/L = 1.152), S_{10}(x/L = 1.228), S_{11}(x/L = 1.290)$.

Note that, in principle, the $2D + t$ theory is well-posed only for Froude numbers of order $\mathcal{O}(1/\sqrt{(\varepsilon)})$ (Fontaine et al. 2000). However, for slower ships, Fontaine and co-authors assessed that asymptotic equations are still valid within a distance L from the bow, given by

$$L \leqslant \mathcal{O}(DFr_D),$$

with Fr_D indicating the Froude number referred to the draught. Since this relation just gives an order of magnitude, Faltinsen (2000) defined a local Froude number, used also in Lugni et al. (2004): $Fr_x = U/\sqrt{g\,(x - x_{BOW})}$ where x_{BOW} is the abscissa of the bow. This is justified by the fact that $2D + t$ is a parabolic theory (i.e. the flow at a generic cross section is influenced only by the flow upstream). In this framework, Fr_x is a useful number to assess the local validity of the $2D + t$ theory, typically for value larger than 0.4. Therefore, in the following, the Fr_x is used as auxiliary abscissa, to assess the consistency of the calculation for studying the local flow.

Analysis of the plunging jets for different forward ship speeds

The strength of the initial plunging jet which develops at the crest of the overturning bow wave is crucial in determining the severity of subsequent splashing and submerged vortical structures. The results of systematic SPH computations of the breaking bow wave are shown in Figure 10.9 for seven ship length-based Froude numbers between 0.3 and 0.64 ($Fr = U/\sqrt{gL}$). In table 10.1 a summary of all the simulations performed is shown: the resolution adopted (dx/L), the coordinates of the plunge point and the height of the bow wave (H_w/D) are indicated for each Froude number. One must underline that a finer spatial resolution is requested for lower Froude numbers in order to correctly catch the plunging jet and its subsequent evolution. The reason

Fr	$dx/L \times 10^4$	x_{plunge}/L	y_{plunge}/L	H_{pj}/D
0.30	0.63	0.103	0.040	0.26
0.35	0.90	0.122	0.045	0.30
0.40	1.20	0.140	0.049	0.34
0.45	1.54	0.163	0.055	0.38
0.50	1.90	0.191	0.063	0.42
0.55	2.17	0.215	0.067	0.47
0.60	2.40	0.237	0.072	0.50
0.64	2.80	0.265	0.078	0.56

Table 10.1.: Summary of the simulated ship Froude numbers, the resolution needed and the main features of the plunging jet.

is that the energy associated with the formed jet, and so the jet dimension, reduces as Fr decreases. At an aft position increasing with Fr, a divergent wave initiates and moves away from the hull forming a jet. The wave crest is in this example higher for higher Fr, but it is reached at about the same transversal distance from the hull, $d \simeq 0.04L$. At this point the jet begins to fall over, extending, until it interacts the free surface from above, as in Figure 10.9, reaching a point further aft and further abaft the hull as Fr increases; this is the onset of splashing.

The shape of the underside of the wave, when turning over, is significantly parabolic like just as in the case of large breaking ocean waves. At impact there is a net circulation around this formed closed cavity, $\Gamma := \oint_{\text{Cavity}} \mathbf{u} \cdot d\mathbf{l}$, positive clockwise. Moving downstream the cavity submerges and collapses, and the connected circulation and entrapped air (not modelled here) give rise to vortical flows forming aerated tunnels, i.e. the ship wake. The non-dimensional circulation, Γ/UD, evaluated in this way is shown in right plot of Figure 10.10, increasing almost linearly with Fr up to 0.5. Beyond that Froude number a collapse of the non-dimensional circulation starts linked to the geometrical properties of the plunging jet as discussed in the following. The shape of the jet and free surface at jet impact are very similar for the first four lower Froude numbers, see Figure 10.9, the scale length increasing almost linearly.

For values of the Froude number higher than 0.5 a non-linear behaviour is observed. This is highlighted in right plot of Figure 10.10 and in left and center plots of Figure 10.11 where the non-dimensional length, L_{JET}/D, and area, $S_{JET}/(DB)$ of the jets are evaluated. In the right plot of Figure 10.11 the non-dimensional moment of inertia around the center-of-mass, I_{OG}/S_{JET}^2, is displayed as function of Fr. Increasing Fr the value of I_{OG}/S_{JET}^2 rapidly decreases, the plunging jet becoming thicker and thicker (see Figure 10.9). This behaviour is coupled with an increase of the jet tip inclination that changes

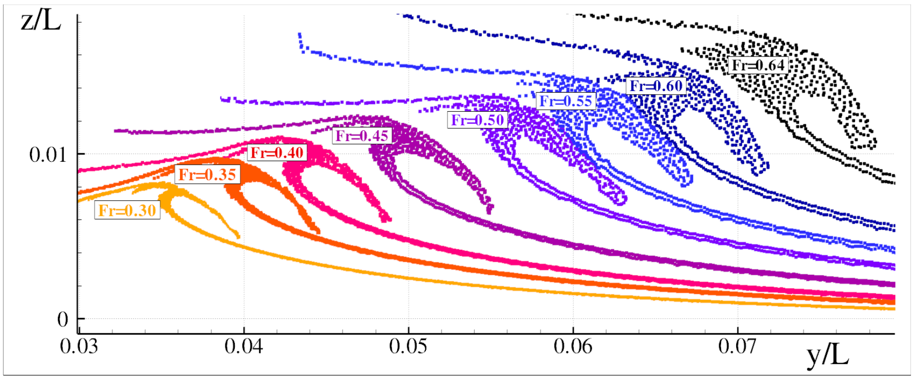

Figure 10.9.: Snapshot of bow breaking wave at the plunge point for all the considered Froude numbers.

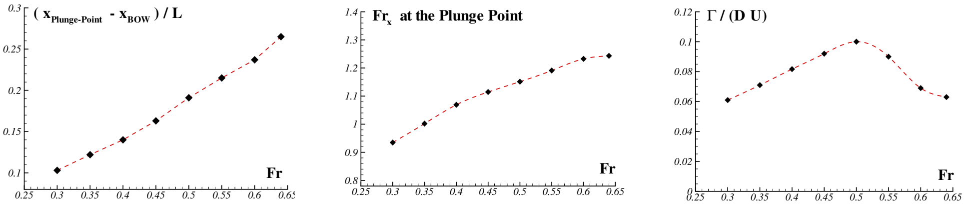

Figure 10.10.: Left: longitudinal location of the plunge point. Middle: local Froude number at the plunge point. Right: circulation around the nascent cavity at the plunge point.

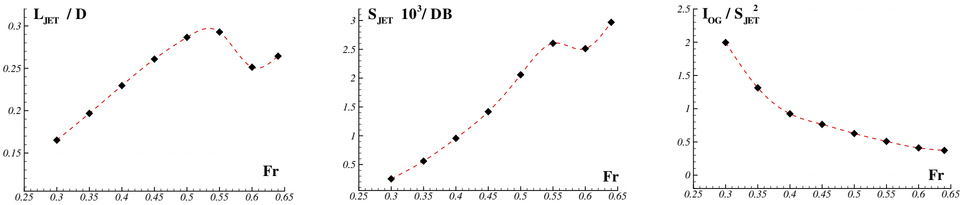

Figure 10.11.: Geometric parameters of the jet at the plunge point. Left: jet length. Middle: area of the plunging jet. Right: moment of inertia around the center-of-mass

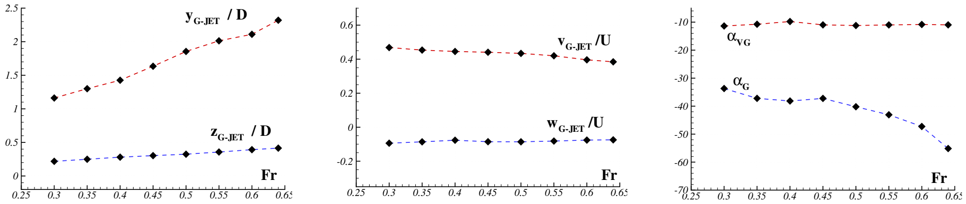

Figure 10.12.: Analysis of the jet at the plunge point. Left: center-of-mass coordinates in the transverse plane yz. Middle: components of the center-of-mass velocity. Right: angles of impact α_G indicates the geometrical inclination of the plunging jet while α_{VG} is the inclination of the velocity vector of the plunging jet center of mass. Angles are given in degrees.

from 40° to approximately 55° with respect to the horizontal plane (see right plot of Figure 10.12). Other kinetic characteristics of the jets at the plunge point are further summarized in Figures 10.11-10.12 for which a more uniform behaviour is observed.

Global wave field and comparison with experimental results

By collecting all sections related to different time instants, it is possible to reconstruct the stationary flow generated by the ship motion. It is drawn in figures 10.13 and 10.14 for Froude numbers equal to 0.4, 0.5, 0.6 and 0.64. As already shown in the previous subsection, the involved dynamics is stronger as the Froude number increases.

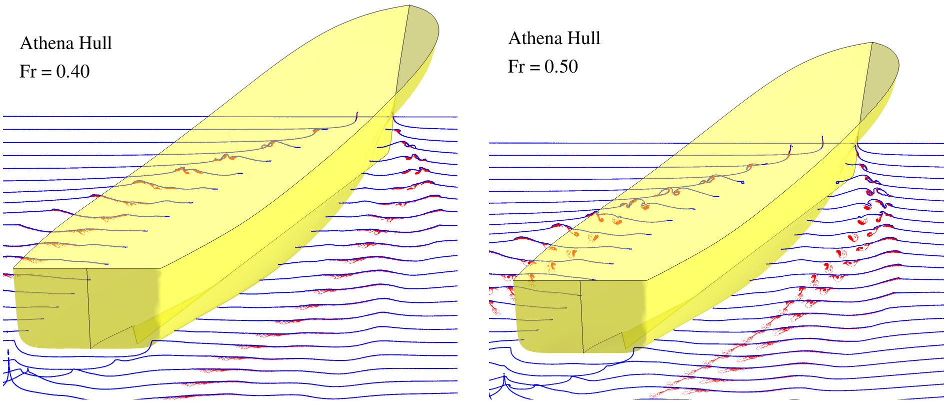

Figure 10.13.: The global wave pattern generated by the Athena vessel motion for Froude numbers equal to 0.4 and 0.5.

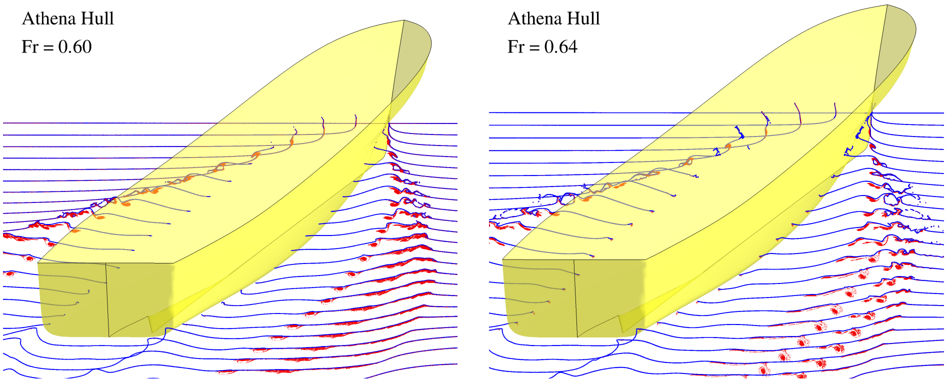

Figure 10.14.: The global wave pattern generated by the Athena vessel motion for Froude numbers 0.6 and 0.64.

In figures 10.15, 10.16 and 10.17 a comparison between numerical results and experiments performed at CNR-INSEAN is provided. Because of the high speed motion, the measurements of the flow quantities around the ship hull are quite difficult and, therefore, only a qualitative comparison is given. From this point of view the main features of the breaking bow wave are well predicted by the numerical solver in terms of elevation of the diverging wave as well as intensity of the splash-up phenomena. At $\mathrm{Fr} = 0.4$ only very small vortical structures due to plunging are predicted by the numerical solver (left picture of figure 10.15) while in the experiment (right picture of figure 10.15) no scars are observed. However, the plunging jet of the divergent wave is quite small and, consequently, in the experiment the effect of the surface tension (that is not taken into account in the simulation) causes the wave to evolve in a spilling breaker. This stands also for $\mathrm{Fr} = 0.5$: a small scar is visible near the hull in the experiment (right picture of figure 10.16) while two vortical structures are present in the numerical results in the left plot of figure 10.16. For $\mathrm{Fr} = 0.64$ a better agreement between experiment and numerical simulation is obtained. In the specific, the stronger splash-up jet is well reproduced by the numerical solver, as well as the first scar close to the hull. Two main reasons combine to give this fair comparison: the first one is related to the higher ship velocity that makes the $2D+t$ model more appropriate; the second one concerns the size of the plunging jet that in this case is quite large and, therefore, is not inhibited by the surface tension which matters for length scales < 5 cm (see Faltinsen 2006, for more details).

In figure 10.18 the free-surface elevation is shown together with the local Froude numbers evaluated at different cross sections of the ship hull. Similarly to the bow divergent wave, it is possible to define a local Froude number for the divergent wave system generated by the ship transom. This helps estimating the width of the fluid region behind the transom which is still well described by the $2D+t$ theory. The main features of the transom divergent wave system are displayed in figure 10.19 where a 3D reconstruction of the free surface for $\mathrm{Fr} = 0.64$ is depicted.

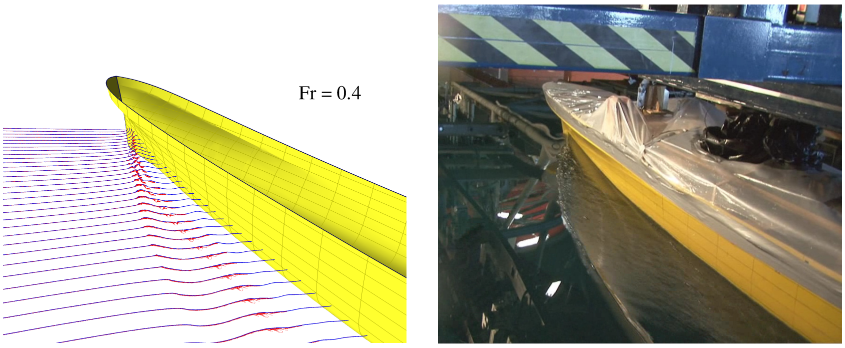

Figure 10.15.: Comparison of the evolution of the breaking bow wave between numerical result and experiments performed at CNR-INSEAN for $\mathrm{Fr} = 0.4$

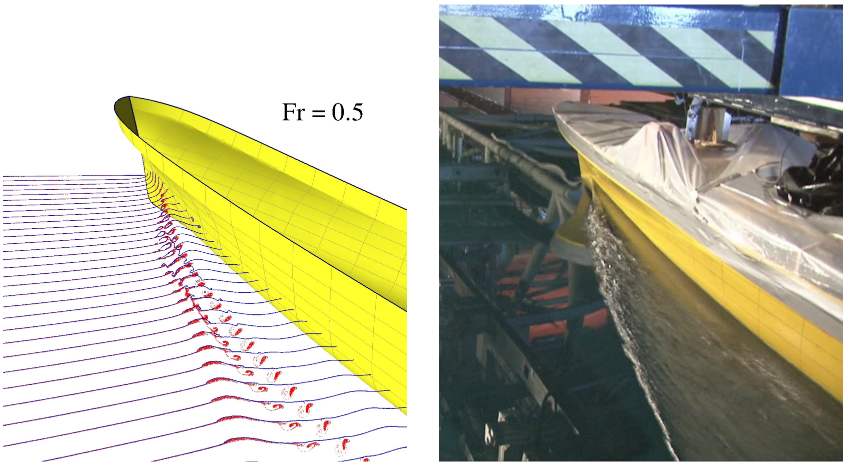

Figure 10.16.: Comparison of the evolution of the breaking bow wave between numerical result and experiments performed at CNR-INSEAN for $\mathrm{Fr} = 0.5$

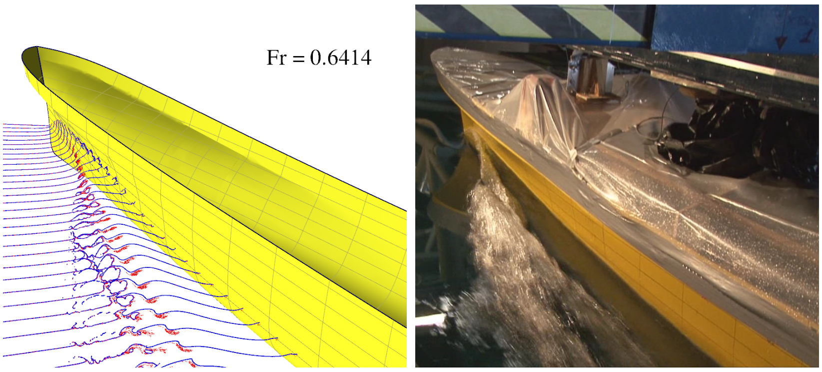

Figure 10.17.: Comparison of the evolution of the breaking bow wave between numerical result and experiments performed at CNR-INSEAN for $\mathrm{Fr} = 0.64$

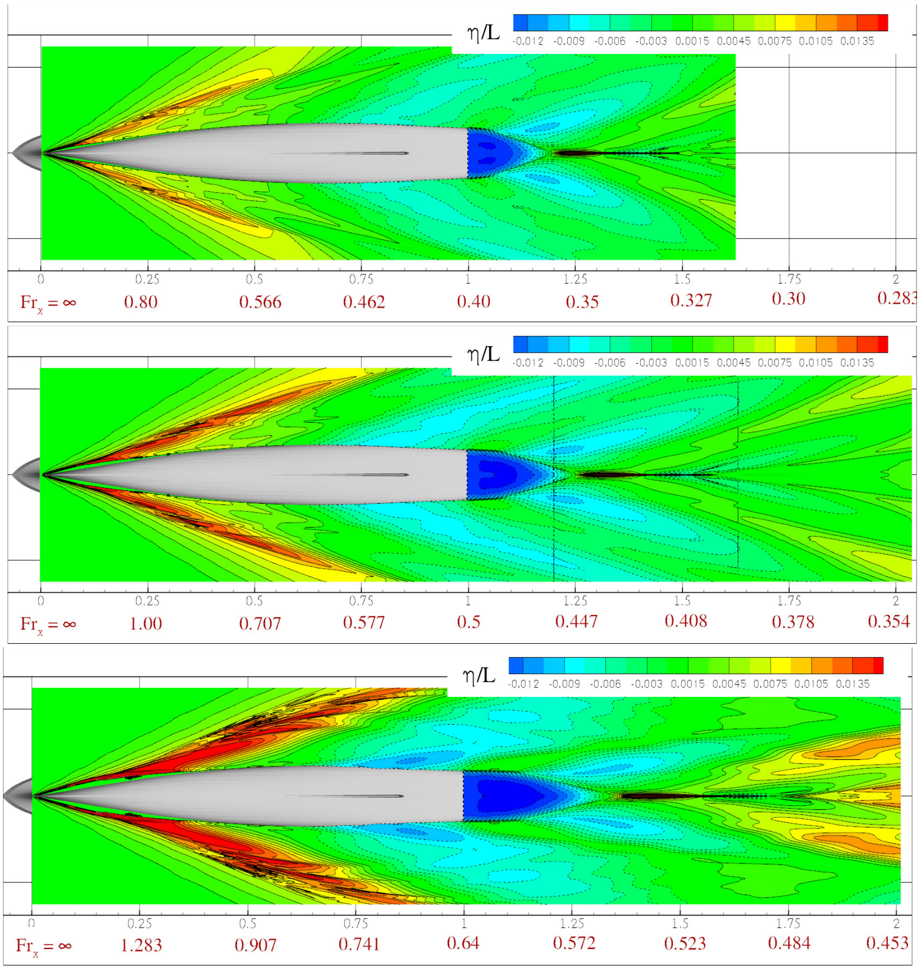

Figure 10.18.: The wave pattern generated by the Athena vessel motion for different values of the Froude number. The value of the *local* Froude number Fr_x is reported along the ship hull.

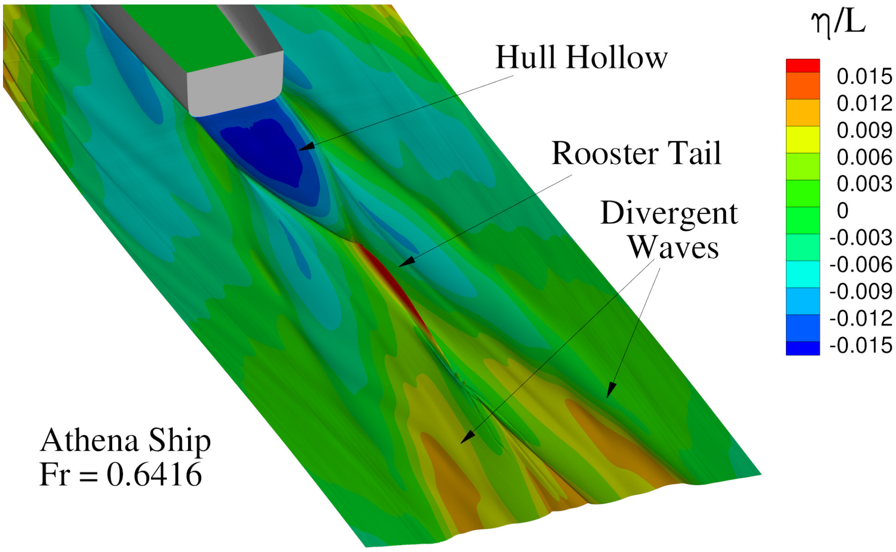

Figure 10.19.: Snapshot of the wave pattern in the transom zone.

10.1.4 Results for the Alliance ship

Here a brief discussion of the results for the NATO research vessel "Alliance" is provided. The ship length (L) is 82 m, the beam (B) at the waterline is 15.2 m, the draft (D) is equal to 5.2 m and the displacement is equal to 2920 tons. In figure 10.20 the ship body plan is displayed. Respect to the Athena hull the ratio D/L is larger while the ratio B/L is smaller. As a consequence, different bow breaking patterns are expected.

A rear view of wave pattern obtained is depicted in figures 10.21 and 10.22 respectively for $Fr = 0.33$ and $Fr = 0.44$. In this case the behaviour of the first plunging is rather different respect to the Athena ship. Indeed, the plunging jet is generally higher and more energetic for similar values of the Froude number. In particular for $Fr = 0.33$ one single vortical structure is observed while two structures are generated for $Fr = 0.44$. Moreover, the plunging jet occurs quite close to the ship hull as highlighted in figure 10.23. It is important to underline that the simulation at $Fr = 0.44$ does not represent a realistic case since the ship maximum velocity is 16 knots corresponding to $Fr \simeq 0.3$. Finally in table 10.2 the characteristics of the plunging jets are shown along with the spatial discretization adopted. Note that the resolution used for $Fr = 0.33$ is just sufficient to resolve the plunging jet.

Fr	$dx/L \times 10^4$	x_{plunge}/L	y_{plunge}/L	H_{pj}/D
0.33	3.6	0.121	0.045	0.11
0.44	3.6	0.181	0.083	0.32

Table 10.2.: Summary of the simulated Froude numbers for the Alliance ship together with the resolution needed and the main features of the plunging jet.

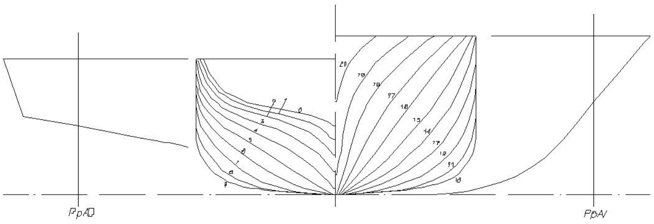

Figure 10.20.: Body plan of the Alliance vessel.

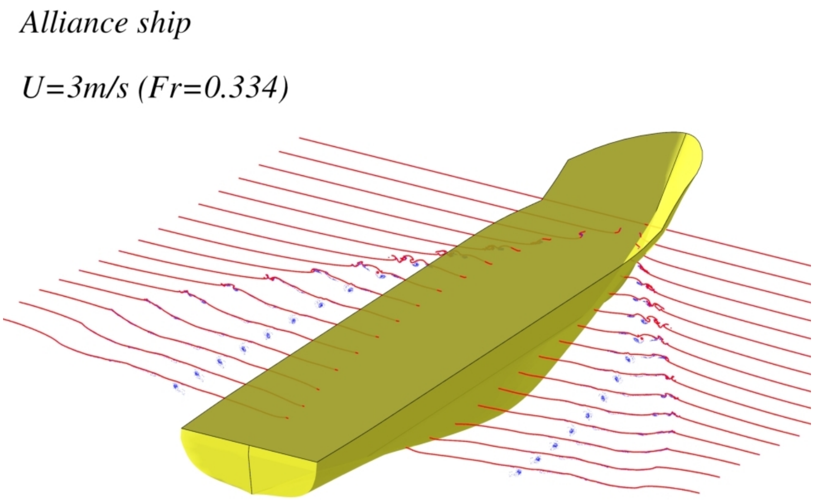

Figure 10.21.: The global wave pattern generated by the Alliance vessel motion for Froude number equal to 0.334

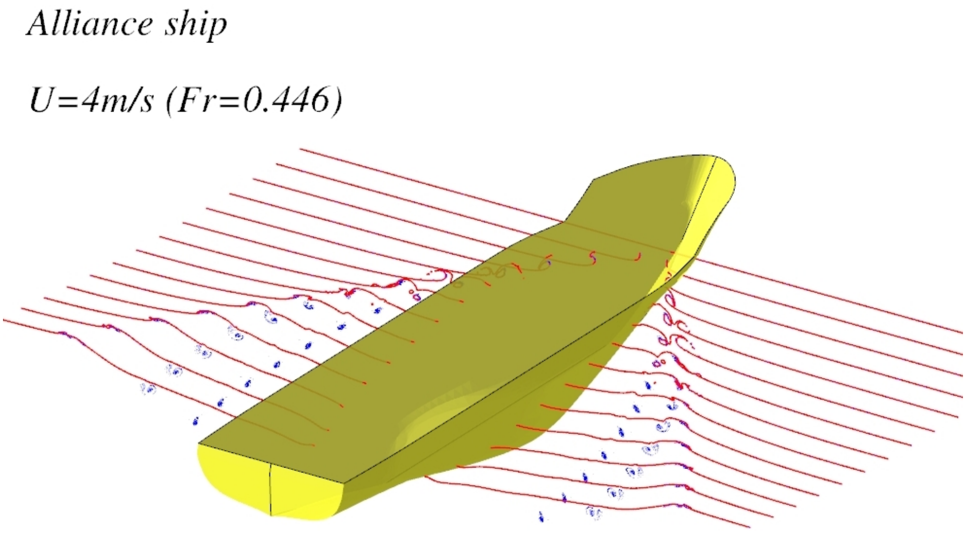

Figure 10.22.: Global wave pattern generated by the Alliance vessel motion for Froude number equal to 0.44.

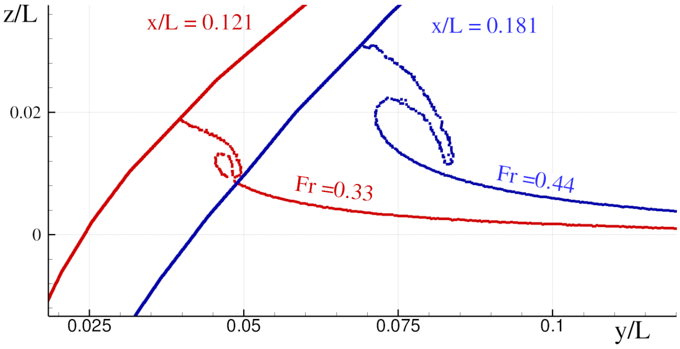

Figure 10.23.: Snapshots of bow breaking wave at the plunge point for the Alliance hull at Fr = 0.33 and Fr = 0.44

10.2 SIMULATION OF A FULLY 3D WAVE PATTERN

In the present section the 3D parallel SPH solver described in appendix A is used in order to carry on the 3D wave pattern computation and to perform the physical characterization of the bow wave. The activity is complex, in fact simulations with varying spatial discretization require a h-variable formulation (see Hernquist and Katz 1989; Nelson and Papaloizou 1994) that is not easy to be effectively implemented in a parallel code. Moreover, a h-variable scheme may be not enough robust in simulating phenomena where strong mixing of particles occur. Therefore, in the present study, only a h-constant variable resolution is adopted (see section 4.3 for further details) that allows achieving high efficiency in the parallel code at the cost of a greater number of particles in the domain.

A preliminary assessment of the capabilities of the 3D solver to perform wave breaking simulations is performed on a test case specifically conceived. From the analysis of such a test the minimum discretization necessary to describe the plunging jet is obtained and compared to previous results from the $2D + t$ analysis. The numerical effort to reach such a resolution in 3D is considerable because the fluid domain has to be large enough to simulate deep water behaviour and avoid wave reflections at the side boundaries. The number of particles needed for these simulations is of the order of 10^8 for which the hybrid MPI-OpenMP parallelization described in appendix A has been specifically developed. The obtained SPH results are then compared with experimental measurements and with simulations obtained by a RANS solver coupled with a Level Set algorithm.

10.2.1 Preliminary computations for simplified problem

In order to test the capacity of the 3D SPH code to simulate the breaking wave, a special test is devised. The computational-domain geometry is given in figure 10.24 and represents a channel with incident velocity. Inflow and outflow conditions are enforced at the open boundaries, respectively, and free-slip solid boundary conditions are enforced at the bottom and lateral walls. The left side wall (in the stream-wise direction) is straight while the other resembles a ship bow with a large flare (ruled surface/bent wall) so that the interaction with the incident velocity leads to a breaking wave similarly as at the bow of an advancing ship . The inflow velocity is uniform and constant while zero normal gradient for the velocity and pressure are enforced at the outflow boundary (i.e. free ouflow condition). The height of the water inflow is $H = 1m$. The non-dimensional velocity of the flow is $Fr_H = U_{flow}/\sqrt{gH}$. The ruled surface, say S, can be derived as a linear combination of the parametric representation of two lines $\alpha(t)$ and $\beta(t)$ as follows:

$$S(t,u) = u\,\alpha(t) + (1-u)\,\beta(t) \qquad u \in [0,1],\ t \in [0,5]$$

$$\alpha(t): \begin{cases} x = 5 \\ y = 0 \\ z = t \end{cases} \quad \beta(t): \begin{cases} x = 5 + L \\ y = \frac{\sqrt{2}}{2}t + \frac{L}{4} \\ z = \frac{\sqrt{2}}{2}t \end{cases} \tag{10.8}$$

The incoming flow interacting with the ruled surface causes a jet impacting on the liquid and leading to splash-up cycles. Two tests, hereafter called *Test1* and *Test2* with different spatial resolution are performed in order to verify the convergence of the numerical results. Table 10.3 provides the number of particles (Npart) and the discretization (dx) in the two cases, as well as, the height of the overturning jet recorded numerically. In figure 10.26, transversal cuts related to *Test1* and *Test2* are shown just before the closure of the plunging jet. It has to be noticed that the jet longitudinal position corresponding to the cavity closure is not exactly the same in the two cases. The spatial resolution of *Test1* is insufficient to reproduce the plunging jet.

In figure 10.25 the free-surface evolution for *Test2* is shown through the contour of the wave elevation. In particular, in the last two plots of the figure, clear scar-lines are visible on the free surface. Those are generated by vortical structures induced by the splash-up process, as discussed in Colagrossi et al. (2001). In figures 10.27 and 10.28 a 3D view is displayed at $t = 18(H/g)^{1/2}$, when the wave front reaches steady conditions. The first figure shows the free-surface coloured according to the modulus of the vorticity while figure 10.28 displays the entrapment in the vortical structures of the two layers of particles closest to free surface at the inflow boundary.

	H_{pj}/H	Npart$\times 10^6$	H_{pj}/dx	dx
Test1	0.5	4	12.5	0.04
Test2	0.5	32	25.0	0.02

Table 10.3.: Parameters of the preliminary simulations described in section 10.2.1

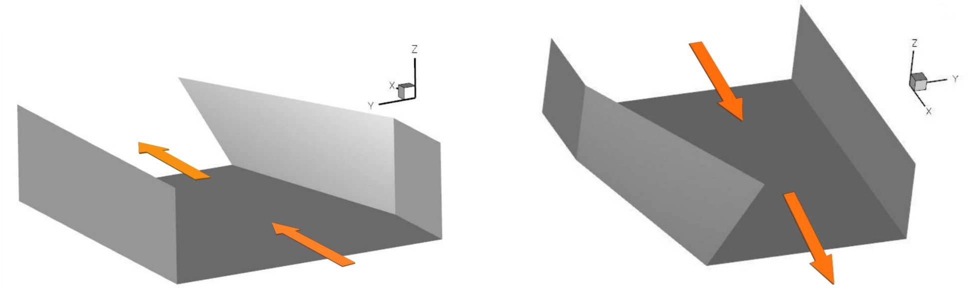

Figure 10.24.: Geometry of the channel with a bent wall used to generate an overturning wave. View from the inflow (left) and the outflow (right).

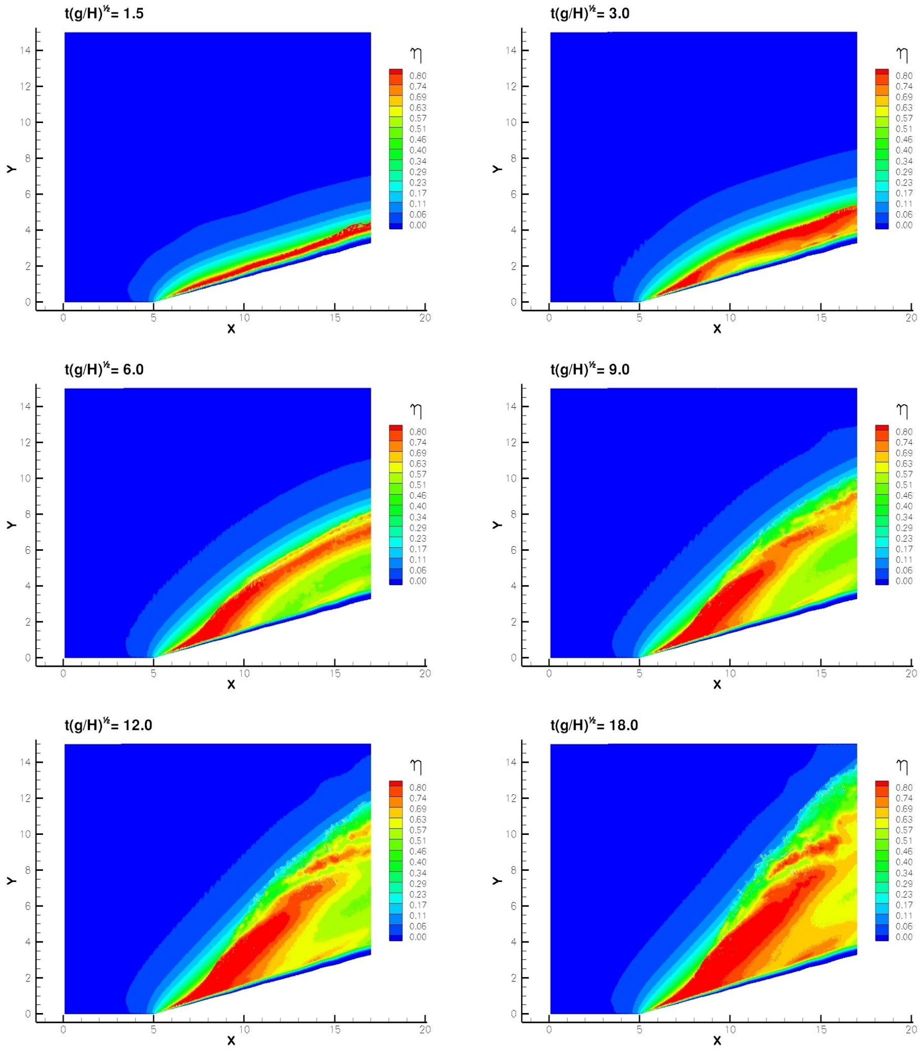

Figure 10.25.: Channel with a bent wall: evolution of the wave elevation during the breaking until the steady conditions are reached.

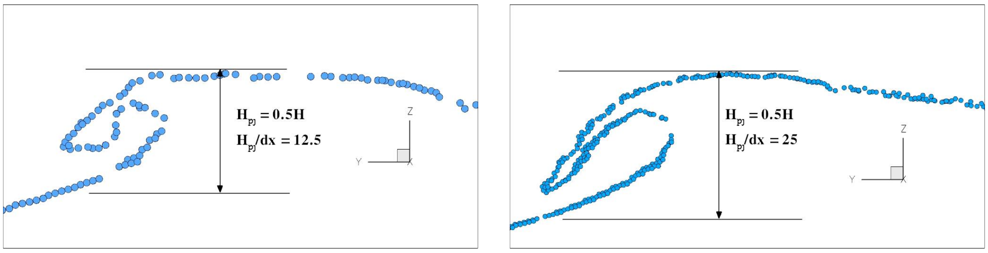

Figure 10.26.: Channel with a bent wall: transversal cut for *Test1* (left) and *Test2* (right).

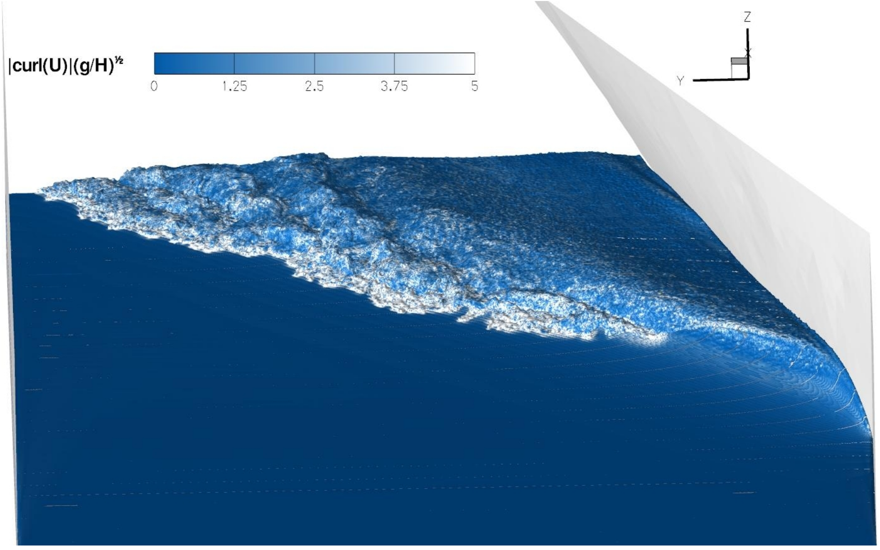

Figure 10.27.: Channel with a bent wall: contour of the modulus of the vorticity, $t = 18(H/g)^{1/2}$.

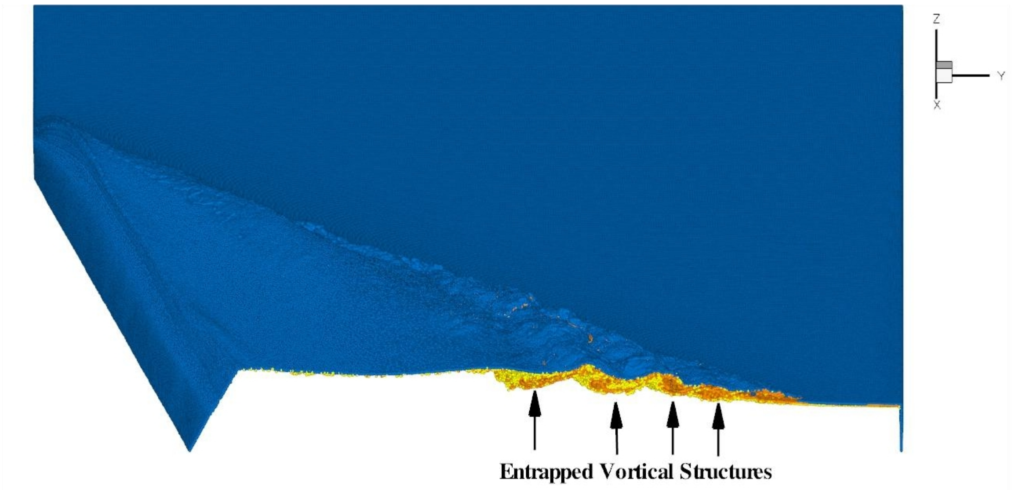

Figure 10.28.: Channel with a bent wall: 3D view of the overturning wave, steady conditions, $t = 18(H/g)^{1/2}$.

10.2.2 Simulation of a ship in steady forward motion

Description of the computational domain

Here the 3D solver is used to simulate the free surface flow around the hull of the Alliance ship in forward motion. The study is divided in two parts:

- the validation of the code in terms of global wave pattern;
- a detailed study on the evolution of the bow wave and breaking inception.

The simulations are carried on in the frame of reference of the ship, i.e. the problem of a fixed ship with a constant inflow velocity is studied. z is the vertical axis (pointing upwards), x the longitudinal axis of the hull (streamwise positive), and y the transversal axis of the model. A forced inflow is fixed at a certain distance from the bow, and a free outflow condition is given at the downstream boundary. For what concerns the lateral and bottom boundaries, solid walls are used [1]. The Froude number of the computation is set to $\mathrm{Fr} = 0.328$ (18.1 knots in full scale) in order to compare the numerical outcome with the experimental data by Perelman (2010). A sketch of the numerical domain is depicted in figure 10.29.

The numerical effort to reach a sufficient resolution is considerable in 3D because the fluid domain has to be sufficiently large to properly simulate a deep water behaviour and avoid wave reflections at the lateral boundaries. The resulting test condition is therefore necessarily a compromise.

	Full Scale	Numerical Simulation
Lenght Lpp (m)	82	1
g (m/s^2)	9.81	1
Breadth (B)	15.2	0.186
Draft (D)	5.2	0.063
Displacement Δ	2920 (t)	5.3 (m^3)

Table 10.4.: Alliance ship parameters.

Pre-processing of ship geometry

The body geometry is approximated by discretizing the body CAD surface using a triangle-mesh generator. Each triangle on the body is then substituted by a computational point placed at the centroid and associated with the normal vector to the triangle and its area. Because of the complexity of the ship

---

[1] Strictly speaking, to ensure open-water conditions, the lateral boundaries should be control surfaces allowing outgoing waves. No models of such conditions are reported in the SPH literature

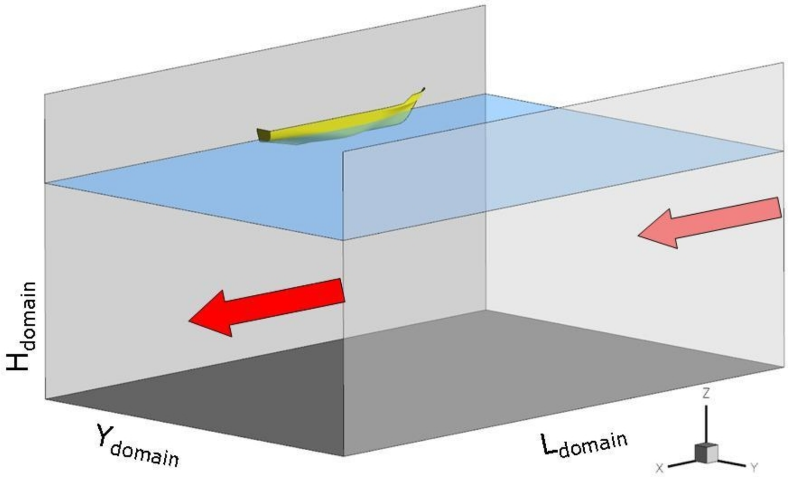

Figure 10.29.: Sketch of the problem

geometry, here the technique inspired to normal flux (see 7.1.2) is adopted to enforce solid boundary condition. This means that an accurate discretization of the ship geometry is needed to simulate adequately the body. The full-scale dimensions of the problem and the values used in the numerical simulation are displayed in table 10.4 while the ship body plan of the Alliance vessel is depicted in figure 10.20.

Remarks on breaking bow wave from the 2D+t analysis

The 2D+t SPH studies for the Alliance vessel at Fr= 0.33 in section 10.1 are used to identify an adequate discretization of the problem to capture correctly the generated plunging jet. This must be taken as a rough preliminary design of the numerical simulation of the plunging jet, because the examined Froude number is too small for a correct evaluation of the whole wave pattern through the $2D + t$ model (see e.g. Fontaine et al. 2000). Figure 10.30 shows a detail of the plunging jet obtained with the $2D + t$ SPH model. The characteristic height of the plunging jet is $H_{pj} = 0.08 Lpp$. This represents a small dimension and so quite challenging to capture in 3D simulations. As shown in Colagrossi et al. (2009*a*), a proper spatial discretization is needed to correctly reproduce the plunging jet. In particular the $2D + t$ results in section 10.1 suggests that the relation:

$$H_{pj}/dx > 20 \tag{10.9}$$

has to be verified. This relation in our case is equivalent to $D = 150dx$, where D is the ship draft. This result is very close to the one obtained in section 10.2.1 where a 3D breaking wave around a simplified ship bow is simulated.

10.2.3 Discussion of the results

In this section, the 3D SPH code is validated on the global wave pattern and on the breaking bow wave pattern generated by the Alliance vessel. The numerical simulations are compared with the experimental data from DGA-Hydrodynamics, see Perelman (2010). The origin is fixed at the intersection between the still water level and the first perpendicular of the ship. The x-axis points as the forward velocity.

In table 10.5 details of the SPH computations are given. *Test4* and *Test5* are performed with the same resolution but for two different sizes of the computational domain. *Test6* and *Test7* are obtained using the domain adopted in *Test4* but with a multi-resolution technique explained in section 10.2.3.

	L [Lpp]	W [Lpp]	D [Lpp]	Npart [$\times 10^6$]	D/dx [-]	t_f [$\sqrt{(g/L)}$]	dx [Lpp]	Multires ratio
Test4	1.25	0.8	0.26	17	25.2	5.0	0.0025	1
Test5	2.25	0.8	0.56	65	25.2	10.0	0.0025	1
Test6	1.25	0.8	0.26	22	38.0	4.0	0.0017	1.5
Test7	1.25	0.8	0.26	145	75.9	4.0	0.0008	1.5

Table 10.5.: Numerical parameters for the wave pattern computations.

Analysis of the global wave pattern

We start the analysis of the global wave pattern using the SPH results for the *Test5* of table 10.5. Top plot of figure 10.31 reports experimental measurements of the wave elevation. The middle plot shows the SPH wave contours while bottom panel shows the same field obtained by a RANS code (CNR-INSEAN Xnavis code by Di Mascio et al. 2007). The global agreement is fair,

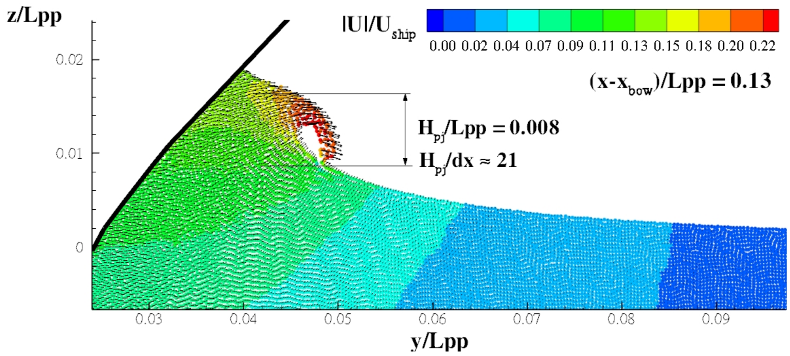

Figure 10.30.: 2D+t around the Alliance hull (section 10.1): snapshot of plunging jet of the bow wave for Fr = 0.33. Ship section (x/Lpp = 0.12).

the SPH result appears to be close to the RANS calculation and both of them well reproduce the bow wave measured in the experiment while they seem to underestimate the rear divergent waves. In order to validate the wave field in the region close to the hull a longitudinal wave cut has been extracted at $y/Lpp = 0.12$ where no experimental data are available. The result is displayed in figure 10.32. The comparison between the two solvers is satisfactory especially in the part beside the ship. In figure 10.33 a wave cut farther from the hull ($y/Lpp = 0.24$) is shown. In this case the SPH prediction is less accurate but can be qualitatively compared with the experimental data. As seen in the previous comparison, the SPH prediction is more accurate in the forward part of the wave field.

Note that from the experiment it seems that the breaking bow wave affects the wave pattern close to the bow region as well as the rear divergent wave. In particular, it is highlighted in figure 10.34 where a dashed line is drawn to track the breaking bow wave and so the region of influence on the rear wave pattern. This region is characterized by high curvature of the free-surface which is not resolved in both simulations. Indeed, the discretization adopted is not sufficient to capture the breaking wave phenomenon and its influence on the wave pattern.

Focus on the bow wave

To capture the physics of the breaking wave, the resolution has to be increased. On the other hand increasing resolution for the computational domain of *Test5* is not practically possible with the available resources. Then, a run with smaller domain is attempted in *Test4* (see table 10.5). The field is reduced in two directions, the water depth and the outflow position. Even if the smaller domain induces non-negligible effects of the bottom and downstream boundaries, it is observed that the main characteristics of the wave pattern are preserved until $t(g/L)^{1/2} = 4$.

In particular, the bow region is kept almost undisturbed despite the rear wave field is deformed by the outflow as shown in top plot of figure 10.35. In fact, comparing the results of *Test4* with the one obtained in *Test5*, one can observe the wave fields are similar up to $x = 0.5L$. Therefore, the main idea is to capture the breaking bow wave performing a simulation with a domain extension equal to *Test4* in a time interval equal to $t(g/L)^{1/2} \in [0, 4]$ with a spatial resolution as fine as possible.

To further increase the spatial discretization, a multi resolution technique keeping h constant has been adopted as in section 10.1. On a layer of thickness $0.25D$ close to the free surface, the ratio h/dx is set equal to 1.33 (266 neighbours). The thickness is given by the maximum depth reached by vortical structures as shown in 10.1. The ratio h/dx is reduced to 0.90 (80 neighbours) for the rest of the domain where small gradients of the flow field occur. In

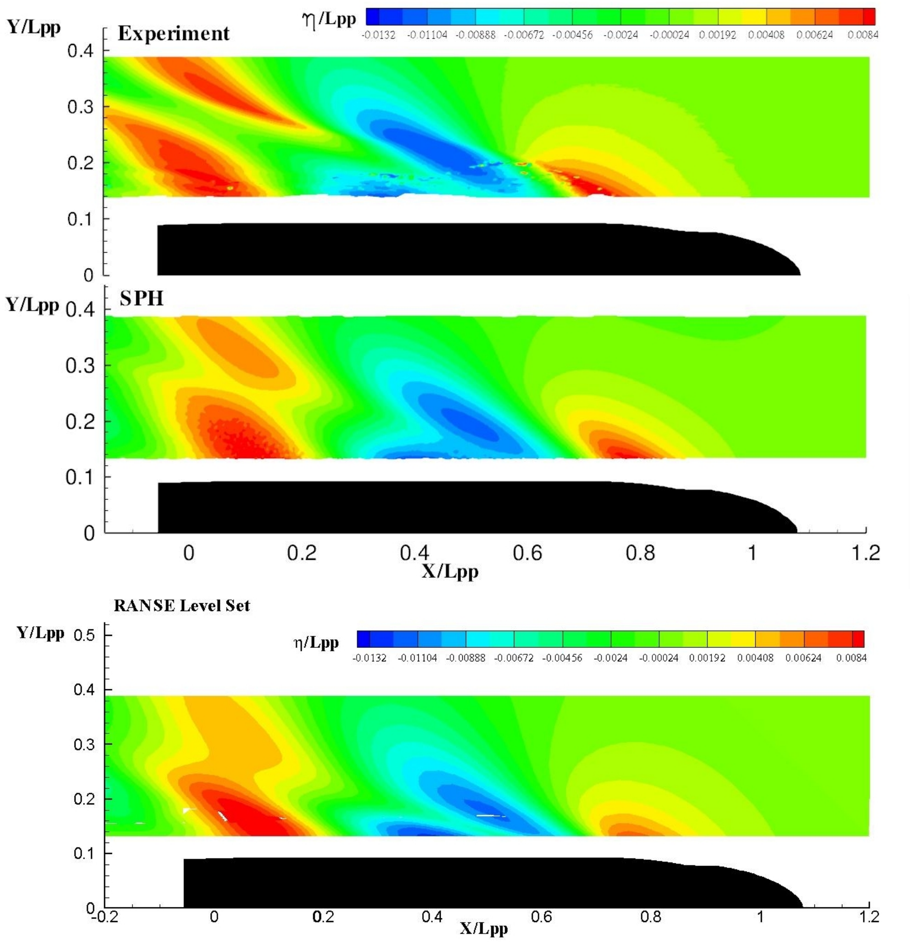

Figure 10.31.: Contours of the wave elevation for Fr $= 0.328$: top panel experimental results from DGA-Hydrodynamics; middle panel SPH results; bottom panel RANS results.

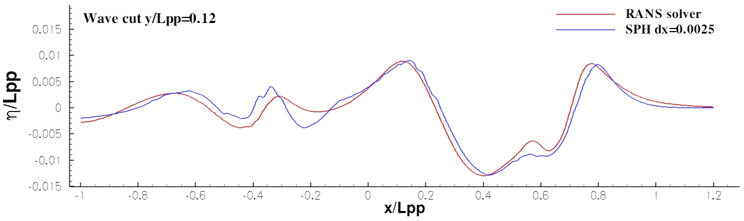

Figure 10.32.: Longitudinal wave cut at $y/\mathrm{Lpp} = 0.12$: RANS (red curve) and SPH (blue curve) solutions.

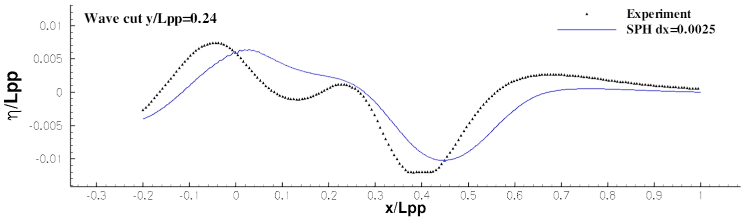

Figure 10.33.: Longitudinal wave cut a $y/Lpp = 0.24$: SPH solution (blue curve) and experimental mearurements (black triangles).

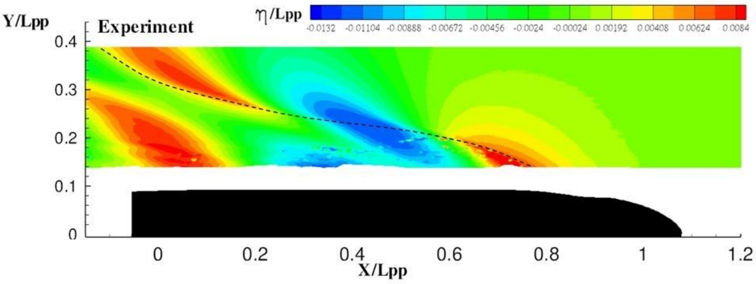

Figure 10.34.: Contours of the experimental wave elevation for $Fr = 0.328$ (results from DGA-Hydrodynamics). The dashed line represents the path of the breaking bow wave and so indicates the region of its influence on the rear wave pattern

this way the size of particles in the low-resolution zone is larger by a factor 1.5 (multi-resolution ratio in table 10.5). Another simulation (*Test6*) is performed in order to verify the robustness and the correctness of the solution with this technique. The size of the domain is the same as in *Test4* as well as the discretization of the low-resolution region. Bottom plot of figure 10.35 shows the wave pattern given by *Test6* matching the pattern from *Test4* in the region with the same discretization for the two simulations, demonstrating the validity of the proposed multi-resolution technique.

Finally, *Test7* is designed with a spatial resolution large enough to capture the breaking of the bow wave. From figure 10.36 it is possible to observe that the shape of the bow wave obtained in *Test7* is closer to the experimental results than the solution from *Test5*. To analyse more in detail the improvement in the numerical solution, a longitudinal wave cut at $y/Lpp = 0.18$ has been plotted in figure 10.37. The comparison with the experiment in terms of shape and height of the bow wave is very good representing a large improvement respect to the results with a coarser resolution (*Test5*). Note that the curve related to *Test7* has been shifted by a quantity equal to $\Delta x/Lpp = -0.003$ to better appreciate the agreement with the experimental data.This phase shift is probably due to the limited extension of the domain, that could slightly also influence the bow wave.

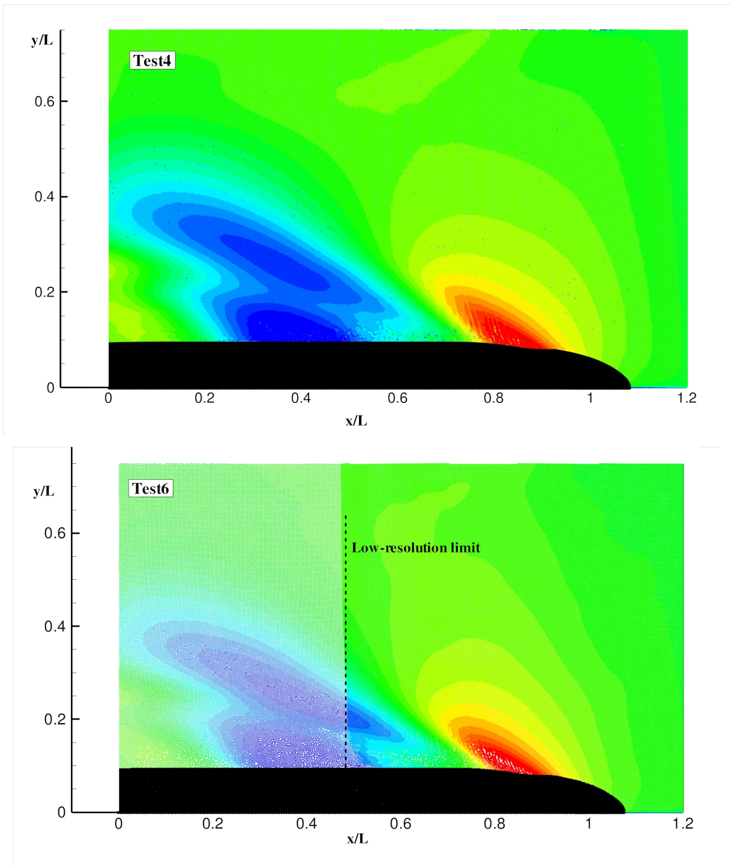

Figure 10.35.: Wave patterns for case *Test4* (top) and *Test6* (bottom)

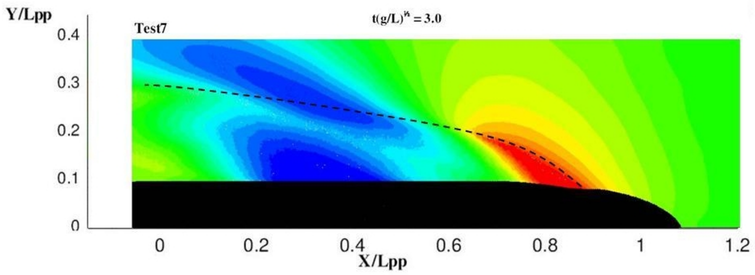

Figure 10.36.: Contours of wave elevation for SPH simulation Test7. The dashed line highlights the breaking wave front.

In the bottom plot of figure 10.39 a 3D view of the bow wave simulated in *Test7* is shown. A qualitative comparison with the top picture of figure 10.39 taken at DGA-Hydrodynamics indicates that the global behaviour of the phenomenon is retained. In figure 10.38 the top view of the bow wave is depicted. Comparing with figure 10.34 it is possible to notice that the extension and the shape of the breaking zone is well reproduced. However, the resolution is still slightly insufficient to fully resolve all the breaking features. The SPH solution

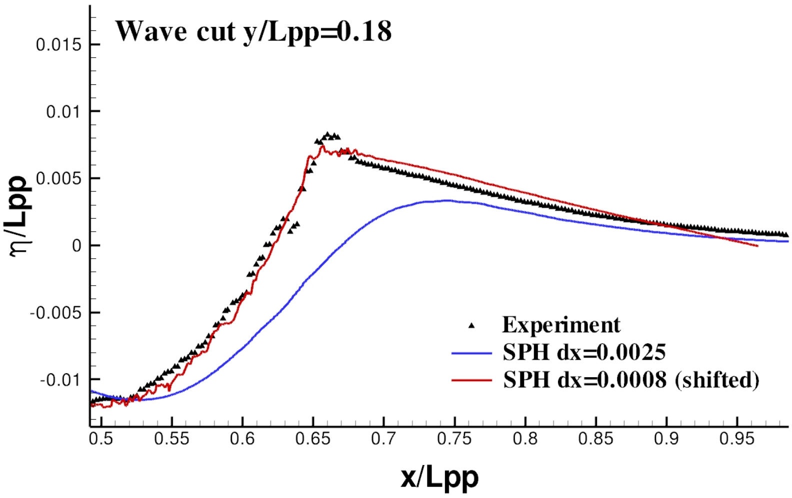

Figure 10.37.: Longitudinal wave cut at $y/Lpp = 0.18$. SPH solution from *Test5*(blue line) and *Test7*(red line), and experimental data (black triangles).

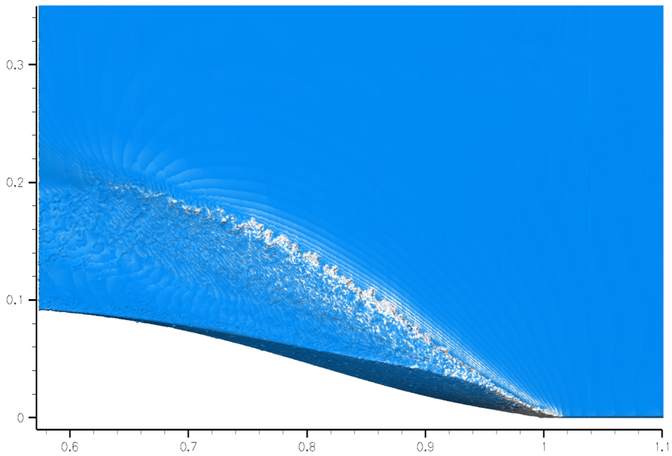

Figure 10.38.: Top view of the breaking bow waves in the SPH simulation, $Fr = 0.328$.

seems to predict a spilling breaking evolution while in figure 10.40 it is evident that energetic splash-up occurs. Unfortunately, it is not possible to compare with results from $2D + t$ since the Froude number is quite low and, therefore, the solution is valid only in a region very close to the bow. In this region, since the plunging is not fully solved in the 3D simulation it is not possible to recognize the breaking features highlighted by the $2D + t$ simulation.

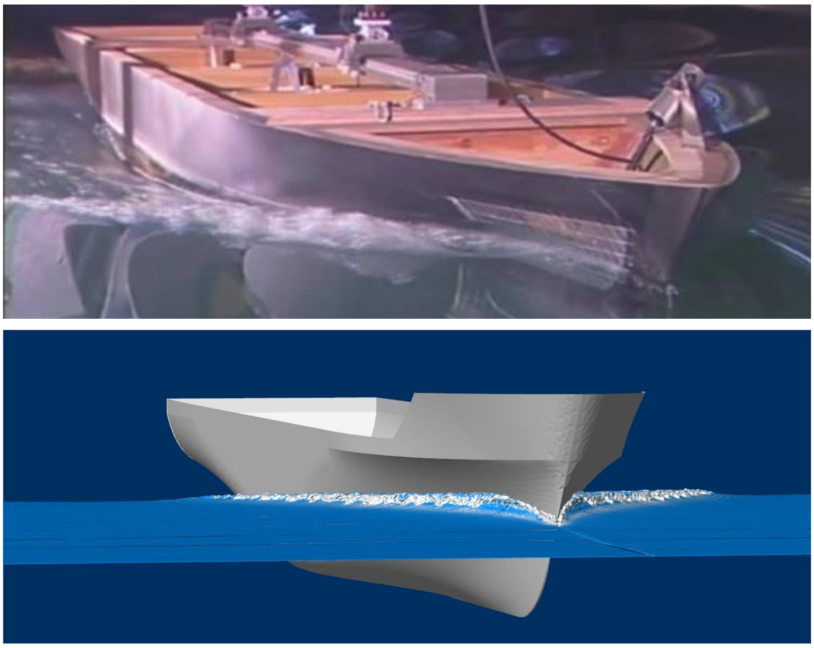

Figure 10.39.: Breaking bow wave during experiments at DGA- Hydrodynamics (top) and 3D view of the breaking bow wave in the SPH simulation (bottom plot), $Fr = 0.328$.

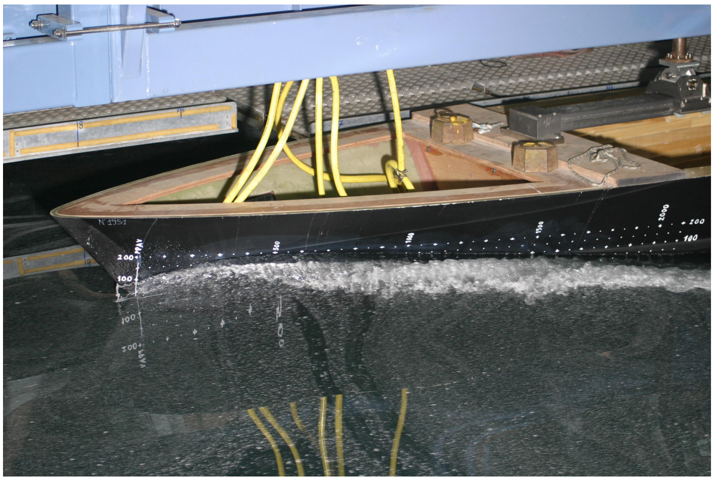

Figure 10.40.: Details of the breaking bow wave during experiments at DGA- Hydrodynamics, $Fr = 0.328$.

11 CONCLUSIONS AND PERSPECTIVES

A Smoothed Particle Hydrodynamics solver has been developed and specialized to study free-surface flows interacting with rigid structures. This kind of phenomena plays a key role in maritime and coastal engineering, their prediction being crucial in the design and the safety of marine structures. The choice of such a numerical model is motivated by the fact that it couples a Lagrangian approach with a meshless character. These features make this method particularly suitable for treating violent water impact problems.

The method was born about forty years ago in the astrophysics context however only in the two past decades it has been applied to free-surface flows. Recently the SPH has received increasing attention, becoming a more reliable and robust numerical support for the engineer. The growing number of researchers joining the SPH European Research Interest Community (SPHERIC) and the birth of European projects focused on SPH, e.g. the NEXTMUSE project of the Seventh Framework Programme, are an evidence of this trend. Nonetheless, there are still several weak points of the method that do not allow it to be widely applied as other more established numerical techniques.

Present contributions to the numerical model

In the present research activity some of the main drawbacks of the weakly-compressible SPH model have been tackled. The occurrence of spurious numerical noise in the pressure field is one of these. In the present work an enhanced SPH model, called δ-SPH is described. Within this model, numerical diffusive terms in the continuity equation are added in order to alleviate the pressure flickering. The model is applied and validated throughout the thesis in several cases ranging from the water impacts to the propagation of gravity waves. The enforcement of boundary conditions represents a more crucial point for the SPH method. Above all, solid boundary treatment still represents an open problem. Two different techniques have been described: the first is a generalization of the classical ghost particle technique in order to treat complex solid geometries; it has been called *fixed ghost particle technique*. An alternative formulation for the evaluation of forces acting on solid bodies has also been described. This formula takes advantage of the interactions between fluid particles and ghost ones, allowing the saving of computational resources. This boundary treatment has shown to be robust and accurate in evaluating local and global loads, though it is not easy to extend to generic 3D surfaces. In the latter case, another technique, developed in the Riemann SPH context and here adapted for the standard SPH model, has been used. Both techniques present pros and cons, and the best choice, that combines accuracy and flexibility, still has not been identified yet.

As for the free-surface boundary conditions, in the present work it has been extensively described how SPH intrinsically satisfies them, provided that the dynamic condition is of zero free-surface pressure. This avoids the need of knowing the exact configuration of the free surface. However, in some cases it can be useful to identify the particles belonging to the free-surface, for example to enforce peculiar free-surface conditions or to better analyse the numerical outcome. The latter is required, above all, when dealing with complex 3D flows for which the numerical results may be quite unclear if represented as a cloud of particles. For these purposes, a novel algorithm for the detection of free-surface particles has been proposed. The algorithm has been extensively validated and, further, an appropriate Level-Set function (i.e. a colour function representing the signed distance of the particles from the free surface) has been defined in order to interpolate particle data onto a regular grid.

Finally, an algorithm to correctly initialize the SPH simulation in generic solid-boundary configurations has been described. It causes a resettlement of the fluid particles to achieve a regular and uniform spacing even in complex geometries. This pre-processing procedure avoids the generation of spurious currents due to local defects in the particle distribution at the beginning of the simulation.

Application to fluid-structure interaction problems

The obtained solver has been applied and validated for several problems concerning fluid-structure interactions. Four different benchmarks have been preliminary used. Firstly, the capability of the solver in dealing with water impacts has been assessed for the problems of a jet impinging on a flat plate and a dam-break flow against a vertical wall. In these cases, the prediction of local loads and the smoothness of the pressure field have been the main focus. Then, the viscous flow around a cylinder, both in steady and unsteady problems, has been simulated, comparing the results with reference solutions. Finally, the solver has been tested in the generation and propagation of gravity waves. Several regimes of propagation have been examined and the results successfully compared against a fully non-linear potential solver.

The SPH model obtained has been applied to several cases of free-surface flows striking rigid structures and to the problem of the generation and evolution of ship generated waves. In the former, the robustness of the solver has been challenged in 2D and 3D water impacts against complex solid surfaces. The correctness of the prediction of the local loads and of the evolution of the free-surface has been verified through comparison with analytical solutions, experimental data and other numerical results. As for the ship generated waves, the problem has been firstly studied within the $2D + t$ theory, focusing the analysis on the occurrence and features of breaking bow waves. Then, a specific 3D SPH parallel solver has been developed to tackle the simulation of the entire ship moving in open sea. The simulation is quite demanding due to the complexities of the solid boundaries and computational resources required. Some problems arise from the approximations adopted for the open-boundary conditions (since there are no available techniques to properly enforce them within the SPH model) and their limitation has led to a further increase of the number of particles. In any case, the wave pattern obtained has been compared against experimental data and results from other numerical methods, showing in both cases a fair and encouraging agreement. It is important to highlight that, on the basis of the applications so far carried out by SPH state-of-the-art solvers, the simulation of the entire wave pattern around a ship represents, by itself, a remarkable result of the present research activity.

Regarding SPH and High Performance Computations (HPC), a simple but effective parallelization has been obtained through MPI/OpenMP hybridization. It still presents some limitations, such as the mono-directional domain decomposition, but the results are encouraging and confirm the suitability of SPH for massive computations. The next step for the development of the present solver will be the domain decomposition in all three directions.

Future developments

Many problems concerning SPH are still far from being addressed. Concerning the basics of the model, a technique to ensure uniform particle distribution during the simulation, without loosing the valuable conservative properties of the method, has not been found yet. This remains a key point to solve, since many recent works have shown that most of the problems related to the accuracy of the model are linked with the particle distribution. On the other hand, many techniques have been proposed in this sense, some relies on remeshing of particles, others on higher order interpolation formulae. However, in both cases, the intrinsic conservative properties of SPH are lost.

Another critical issue is the multi-resolution. Indeed, in SPH only schemes with smoothing length slightly variable are available. This means that particle size can vary with a very small size ratio and, nevertheless, larger particles and smaller ones should not mix together during the simulations. Moreover, variable-h schemes are more difficult to implement in SPH codes and make the parallelization significantly more complex. Therefore, if SPH is meant to be a competitive support for engineering, a more effective multi-resolution technique is needed.

The computational costs are the reason for which multiphase flows are not treated here. Even if reliable and robust models are available, the cost of introducing also the air phase is still large even in 2D. Therefore, when the SPH costs will be decreased, through the aforementioned parallelization and multi-resolution techniques, it will be possible to model both phases and to resolve breaking flows with larger accuracy.

Incidentally, it is appropriate to mention that in the present work the turbulence sub-scales are not modelled. In fact, the Euler version of the SPH equations is adopted when high Reynolds number flows are solved, while the Navier-Stokes SPH solver is used only for sufficiently low Reynolds numbers.

This is due to the fact that turbulence models in SPH still have not been fully validated. In the literature it some models from others numerical schemes have been directly applied to SPH but a comprehensive analysis of their behaviour in such a complex method has not been provided.

A PARALLELIZATION OF THE 3D SPH SOLVER

In order to perform 3D expensive computations (like the simulation of ship waves in section 10.2), it is necessary to develop a 3D parallel solver able to run efficiently on a cluster. The solver has been made targeting a simulation of hundreds of millions particles. Because of the Lagrangian nature of the SPH model, the parallelization of the code is non trivial and specific algorithms for this aim have to be designed and validated. Indeed, as opposed to mesh-based methods for which a fixed grid is employed, the SPH method relies on moving particles advected by the calculated fluid flow. Depending on the problem being treated, large particle displacements may occur. The parallel scheme should necessarily take this specificity into account.

This Lagrangian characteristic also implies a major disorder of the particles, and therefore of scattered data in memory. Note that for mesh-based methods, the connections are fixed during the calculation: the neighbourhood of a given cell of interest remains the same throughout the calculation. Thus, a recurrent pattern of interpolation can be used, simplifying the parallelization scheme. Unfortunately, such a simplification is not possible in the SPH formalism, the neighbourhoods of SPH particles constantly changing during the calculation. The parallelization is thereby affected, requiring a special procedure to update neighbourhoods. More precisely the core of the parallel algorithmic structure naturally revolves around a neighbour search procedure. Therefore, one has to care about the communication of neighbouring particles belonging to different processors and the update and trade-off of the processor working loads.

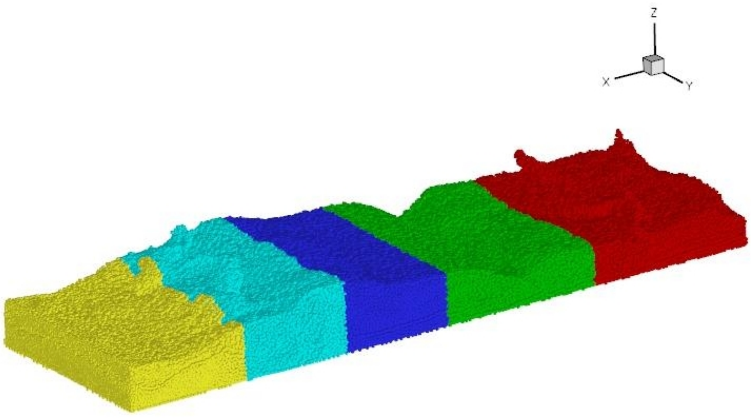

Figure A.1.: Example of division of the fluid domain over processors.

The parallelization strategy here adopted takes advantage of a MPI domain decomposition, realized in a very simple but effective manner, coupled with an OpenMP data decomposition in order to take advantage of the shared memory architectures. This choice is given by the increasing importance of multi-processors units in the supercomputing context that makes opportune the development of a hybrid parallelization.

In order to simplify the MPI parallelization procedure and make the code faster, some specific hypotheses have been assumed in the present problem. In simulating ship wave the fluid domain is characterized by a dominant length corresponding to the main flow direction. Therefore it is possible to divide the fluid domain into parallel slices along the main flow direction, say the x-axis, equally balancing the number of particles per processor (figure A.1). In this way there is just one direction of communication between adjacent nodes. It allows simplifying the parallelization algorithm: the more the simulated phenomenon has a principal direction of evolution, the more the parallelization will be efficient.

Generally in common SPH practice it is useful and fast for the neighbour search to create a regular grid overlapping the computational domain. Each cell of the grid is a cube with size equal to the kernel radius. In this way the neighbours of each particle are found in the cells surrounding the particle one (Cell Linked List algorithm, see e.g Allen and Tildesley 1999). At each time step the list of particles and their belonging cells are calculated. In order to further simplify the problem, the computational domain is separated into subdomains that rely on the grid used for particle neighbour search. The idea is to use this grid to speed up the operations between processors.

Since the list of the particles belonging to different cells is already calculated, it can be used to quickly update the list of particles belonging to different processors and to determine the buffer particles to be communicated to the adjacent processors. Considering a single processor, the buffer particles are virtual particles that are received from the two adjacent processors and are needed to complete the interpolation of particles placed in proximity of the processor boundaries. In other words the buffer particles give contributions to the equation of motion of the local particles but their physical quantities are not updated because they belongs to another processor.

According to the parallelization strategy adopted, each processor extends over a finite number of cells along the x-axis, overlapping for one cell the adjacent processors (see figure A.2), while it covers all the computational domain along the y-axis and z-axis. In this way, a single layer of cells is scanned looking for particles to be sent to adjacent processor as buffer particles. With this approach, it is also straightforward for each processor to update its belonging particles. As already mentioned, the particles cross naturally the processors boundaries. These particles are sent together with buffer particles and hence

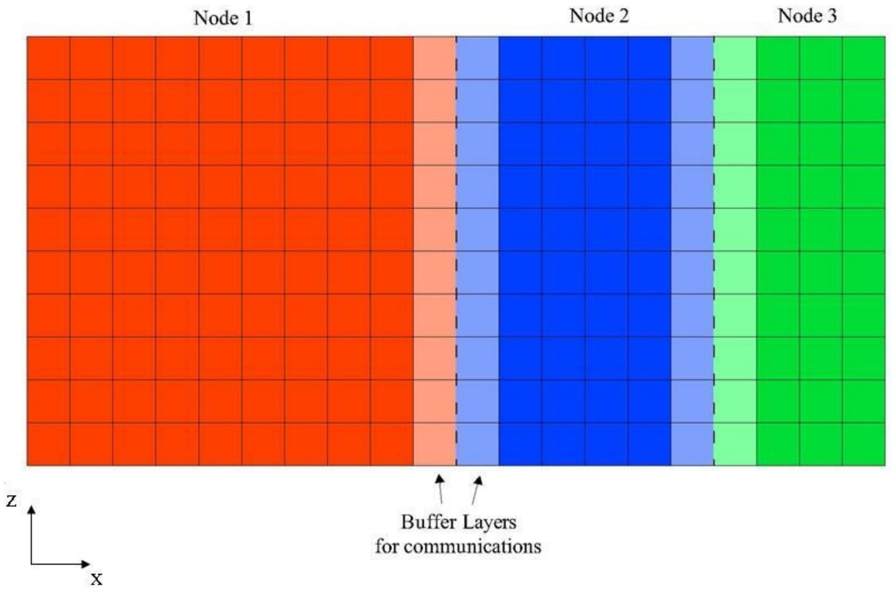

Figure A.2.: Sketch of the cell grid and processor sub-domains.

are assigned in the cells of the receiving processor. Then, each processor scans the cells of its own sub-domain to update the list of particles.

For what concerns the load balancing, it is necessary to pay attention to some constrains resulting from the parallelization strategy adopted. First, the sub-domain size of the processor can change just along the x-axis. Second, the length of the sub-domains has to be equal to a multiple of the cell size, meaning that each processor has to exchange at least the amount of particles contained in a cell plane parallel to the yz-plane. During the simulation, the balancing algorithm is called whenever the most loaded processor has a number of particles that exceeds the average number of particle per processor by specific threshold.

The procedure is designed to balance processors load through a diffusive-like process. Each processor compares its number of particles with the one of the adjacent processor. If it is greater, the cell planes (starting from the one nearest to the receiver) that contains a number of particles as close as possible to the half of the unbalance between the two processors are sent to the adjacent processor. In this way it is not necessary to use collective communications to balance CPU loads.

The balancing algorithm was tested on a dam-break problem. In figure A.3 is shown the initial domain decomposition with 4 processors together with the grid needed for neighbour search and domain decomposition . The total number of particles in the simulation is $400,000$. In figure A.4 is plotted the history of the workload per processor in terms of local number of particles over ideal number of particles per processor.

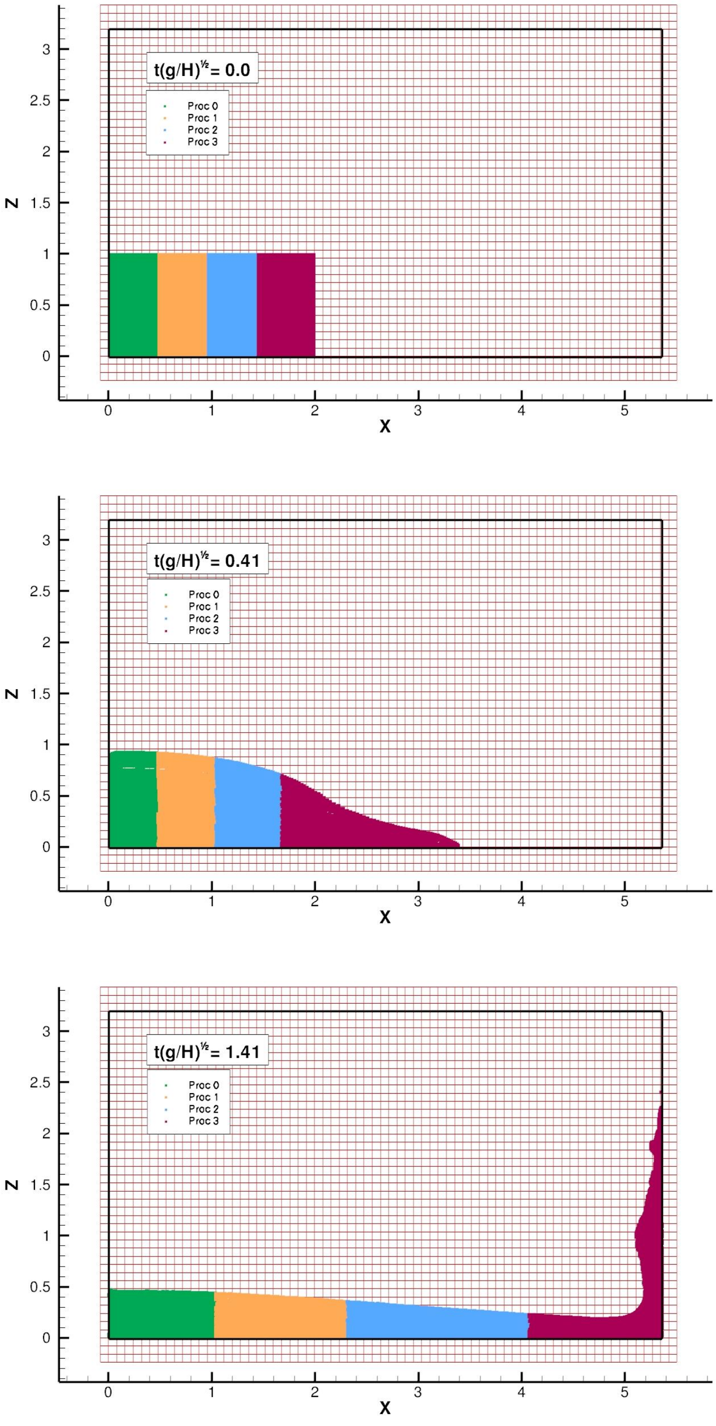

Figure A.3.: Three different time instants of the evolution of the dam-break test case run with 4 processors. Different colours refer to different processors. The underlying mesh represents the grid needed for the neighbour search algorithm.

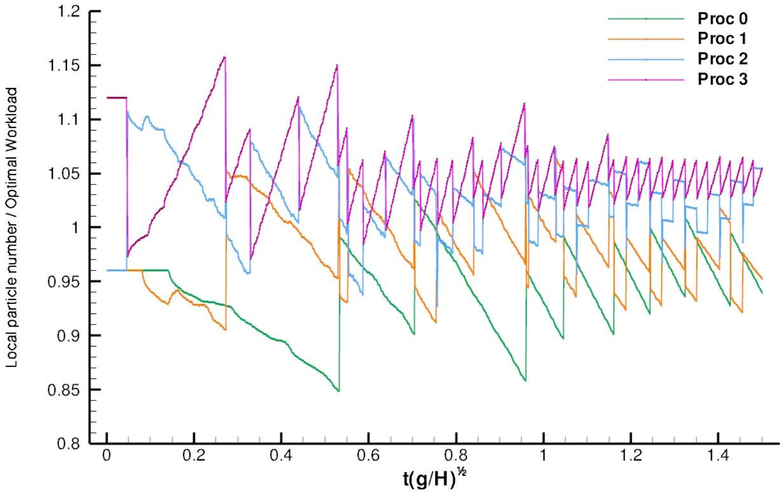

Figure A.4.: Time history of the workload per processor in terms of local number of particles over ideal number of particles per processor. The benchmark used is the dam-break test case.

At the beginning of the simulation the processor #3, that is the one owning the water front, increases its number of particles as consequence of the flow evolution. Consequently the balance algorithm transfers particles to the nearest processors (#2 and #1) enlarging their domains. As the flow starts to fill the tank (bottom plot of figure A.3) more cell planes can be exchanged and thus also the processor #0 get enlarged.

One can observe that the initial distribution of the dam-break problem is not favourable to an optimal balance since all the fluid domain is bounded in few cells along the x-axis and thus the workload per processor has an unbalance of about 10%. During the evolution of the dam-break the fluid domain expands over the x-axis and, thanks to the balance algorithm, processor workloads are balanced in a more acceptable range of ±5% respect to the ideal balance.

The limit of this algorithm is that if too many particles are contained in a single cell plane it is not possible to have a good balance because it is not possible to split a cell plane. To overcome this problem it was chosen to add the OpenMP parallelization (shared memory) for the interaction loops. In this way it is possible reduce the number of MPI process, enlarging each single subdomain and hence providing for a more effective balance procedure, without loosing efficiency. For example if 128 cores distributed on 16 dual quad-core racks are available, it is possible to run a simulation on 16 MPI nodes with 8 OpenMP processors per node instead of 128 MPI nodes that would result in a worse balance.

The OpenMP parallelization is obtained through a data decomposition performed on the loops over particles. An high efficiency is obtained in this case

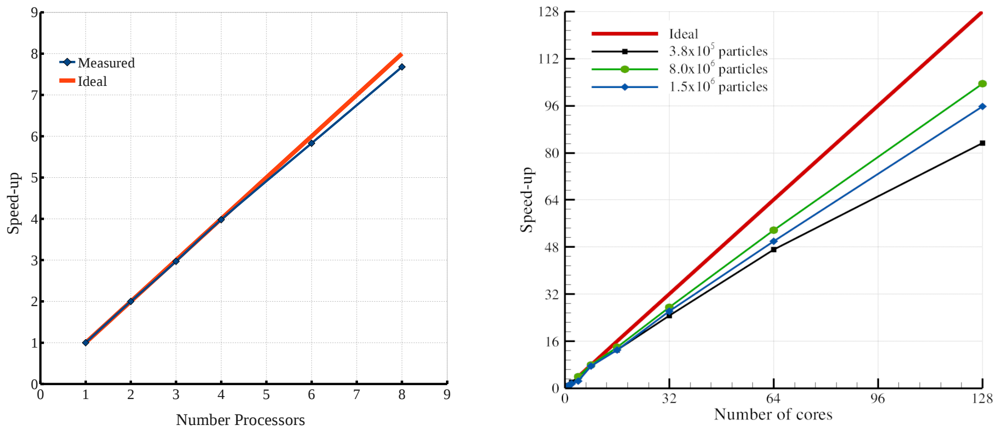

Figure A.5.: Speed-up obtained for the simulation of a fluid with hydrostatic pressure distribution in a tank. Left: Speed-up only for the OpenMP parallelization. Right:Overall speed-up of the combination of both MPI and OpenMP parallelization standards.

thanks to the removal of the sources of race conditions. For example the pair symmetry of particle interactions is not exploited leading to a slow down of the serial code but, on the other hand, allowing for an effective fork of the interaction loops. In left plot of figure A.5 the speed-up obtained using only OpenMP parallelization (i.e. no domain decomposition) is displayed considering the simulation of a tank filled with fluid at rest. In right plot of figure A.5 the overall speed-up is shown for different particle numbers. These curves are obtained firstly increasing the number of OpenMP threads used (from 1 up to 8) and then increasing the number of MPI nodes (from 1 up to 16). The result clearly proves the effectiveness of the parallelization strategy adopted. Indeed, simulations can be run up to 128 cores (8 threads per 16 nodes) with a fair scalability.

B

DEFINITION OF A LEVEL-SET FUNCTION

The interpolation of particle data onto a regular grid can be useful both for allowing an in-depth analysis of the flow features through adequate post-processing, or for remeshing the particles during free-surface flow simulations. In order to perform this procedure it is necessary to locate the free surface across the grid. In other words, one needs to separate nodes inside the fluid domain from those outside. This can be done from the knowledge of the free-surface particle subset $\mathbb{F}$. Let us consider a regular Cartesian grid of spatial resolution dx, and which encloses all the computational domain. For each node N close to free surface particles of subset $\mathbb{F}$, the nearest free-surface particle F_N is detected and the scalar quantity d_{NF_N} is evaluated through:

$$d_{NF_N} = (\mathbf{r}_{F_N} - \mathbf{r}_N) \cdot \mathbf{n}_{F_N} \tag{B.1}$$

where $\mathbf{n}_{F_N}$ is the normal to the free surface evaluated in F_N. For each node it is now possible to define a level-set function $\phi(\mathbf{x}_N)$:

$$\phi(\mathbf{r}_N) = \begin{cases} -1 & d_{NF_N} \leqslant -2h \\ d_{NF_N}/2h \quad -2h < & d_{NF_N} < 2h \\ 1 & d_{NF_N} \geqslant 2h \end{cases} \tag{B.2}$$

This function is positive inside the fluid, negative outside it and equal to 0 along the free surface where $d_{NF_N} = 0$. More precisely, under the assumption that the actual free-surface location is at a distance $dx/2$ from the center of mass of particles belonging to $\mathbb{F}$, the value of ϕ on the free surface has to be $\phi = -dx/4h$ and not zero any more.

At the computational level, the procedure to evaluate ϕ can be executed in a fast manner. At each node the particles present within a $2h$-distance are first identified. This subset of particles is denoted $\mathbb{N}_{2h}$ through which the function $\phi(\mathbf{r}_N)$ can be evaluated as:

$$\begin{array}{cl} -1 & \mathbb{N}_{2h} = \emptyset \\ 1 & \mathbb{N}_{2h} \neq \emptyset,\ \mathbb{N}_{2h} \cap \mathbb{F} = \emptyset \\ d_{NF_N}/2h & \mathbb{N}_{2h} \neq \emptyset,\ \mathbb{N}_{2h} \cap \mathbb{F} \neq \emptyset,\ \lambda_{F_N} \geqslant 0.1 \\ -|\mathbf{r}_N - \mathbf{r}_{F_N}|/2h & \mathbb{N}_{2h} \neq \emptyset,\ \mathbb{N}_{2h} \cap \mathbb{F} \neq \emptyset,\ \lambda_{F_N} < 0.1 \end{array} \tag{B.3}$$

where λ_{F_N} is the minimum eigenvalue of the matrix $\mathbf{B}^{-1}$ (see eq. 7.21) for the particle F_N. For $\lambda_{F_N} < 0.1$ the nearest free-surface particle for the node N is a solitary particle. In such a case the vector $\mathbf{n}_{F_N}$ is null (see eq. 7.23) and consequently the scalar product d_{NF_N} is meaningless. Therefore, the latter is directly substituted with the distance $|\mathbf{r}_N - \mathbf{r}_{F_N}|$. Further, to smooth out the function ϕ on the whole mesh, a Gaussian filter on the nodes is performed once ϕ is evaluated by equation (B.3).

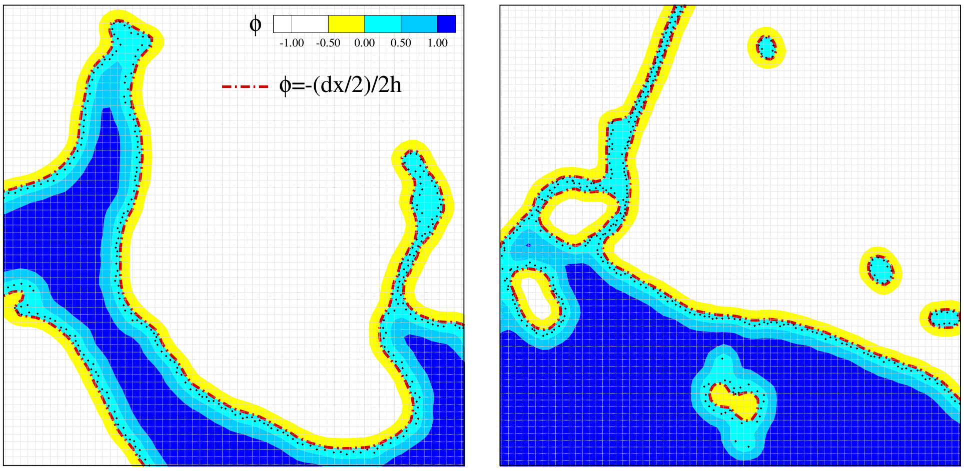

Figure B.1.: Contour plot of function ϕ for the particle distribution shown in figure 7.8. Free-surface particles (black dots) and free-surface contour level (red dash-dotted curve).

In figure B.1 the contour plots of function ϕ for the two time instants of figure 7.8 are shown. The free surface is represented by the red dash-dotted line which corresponds to the contour level $\phi = -dx/4h$, in close agreement with the free-surface particles positions if they were shifted by $dx/2$.

In 3D simulations the interpolation on a regular mesh clearly brings higher benefits. Indeed, the visualization and the flow analysis of a 3D SPH simulation is generally quite difficult. This is highlighted in figure B.2 where a spherical fluid domain with three concentric toroidal cavities and a small spherical cavity of 3h diameter is considered. Even though only the free-surface particles are shown (left panel), it is obvious how difficult it is to detect the geometry of the fluid domain. On the right side of the same figure, the iso-surface $\phi = -dx/4h$ representing the free surfaces conversely gives a clear representation of the fluid domain, thanks to transparency features which are a standard visualization tool on a regular mesh.

To illustrate the method capabilities on an actual complex 3D situation the results of the application of the algorithm on the water impact against a tall structure of section 9.1 In figure B.3 the whole particle distribution and the detected free-surface particles are shown for a time instant just after the impact. Anyway in these plots only a few flow features can be analysed. Therefore the Level-Set definition is used to improve the flow analysis. Some interpolation results are presented in the following. This operation has been carried out with

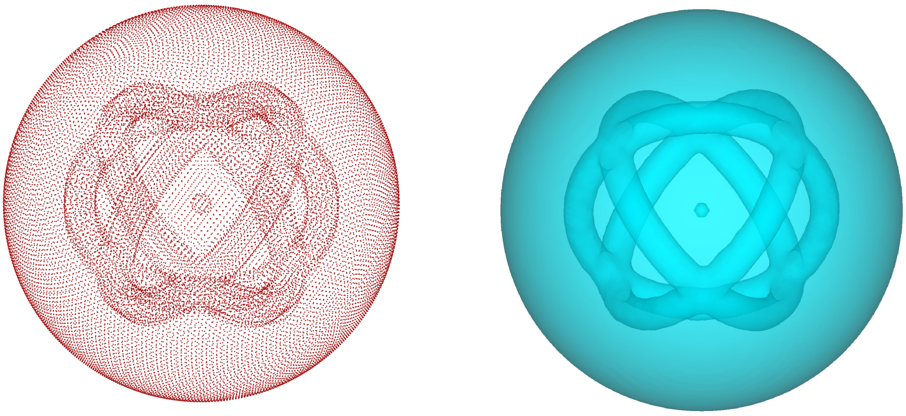

Figure B.2.: Spherical fluid domain with three toroidal cavities and a spherical cavity of 3h diameter. Left: free-surface particles. Right: iso-surface $\phi = -dx/4h$.

a Moving-Least Square (MLS) interpolator that exactly interpolates a linear field on a regular grid from scattered points. The representation of the free surface is given by the iso-contour $\phi = -dx/4h$ in figure B.4. In particular, the pressure distribution during the impact is evidenced through contours interpolated on a vertical plane inside the domain. Finally, the last plots of figure B.4 show how it is possible to analyse flow internal details through the reconstruction of the free surface as an iso-surface. In particular, entrapped bubbles and a large tube cavity due to a strong wave breaking are clearly identifiable.

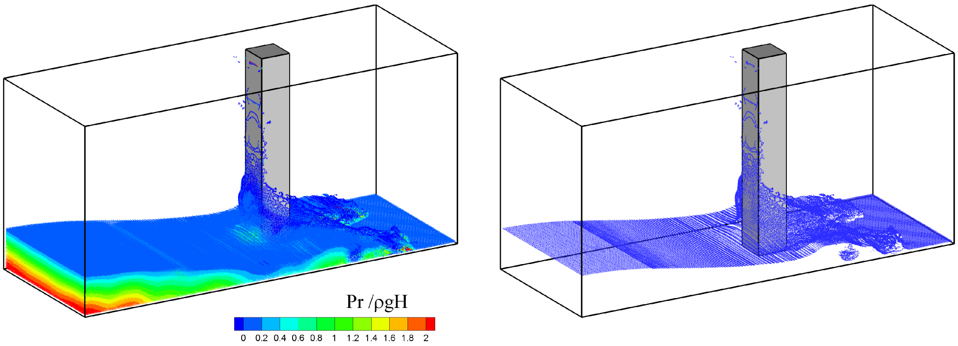

Figure B.3.: 3D impact against a tall structure after a dam-break described in section 9.1. Left: whole particle distribution over the fluid domain; the colors represent the pressure. Right: free-surface particles detected by the algorithm at same time instant.

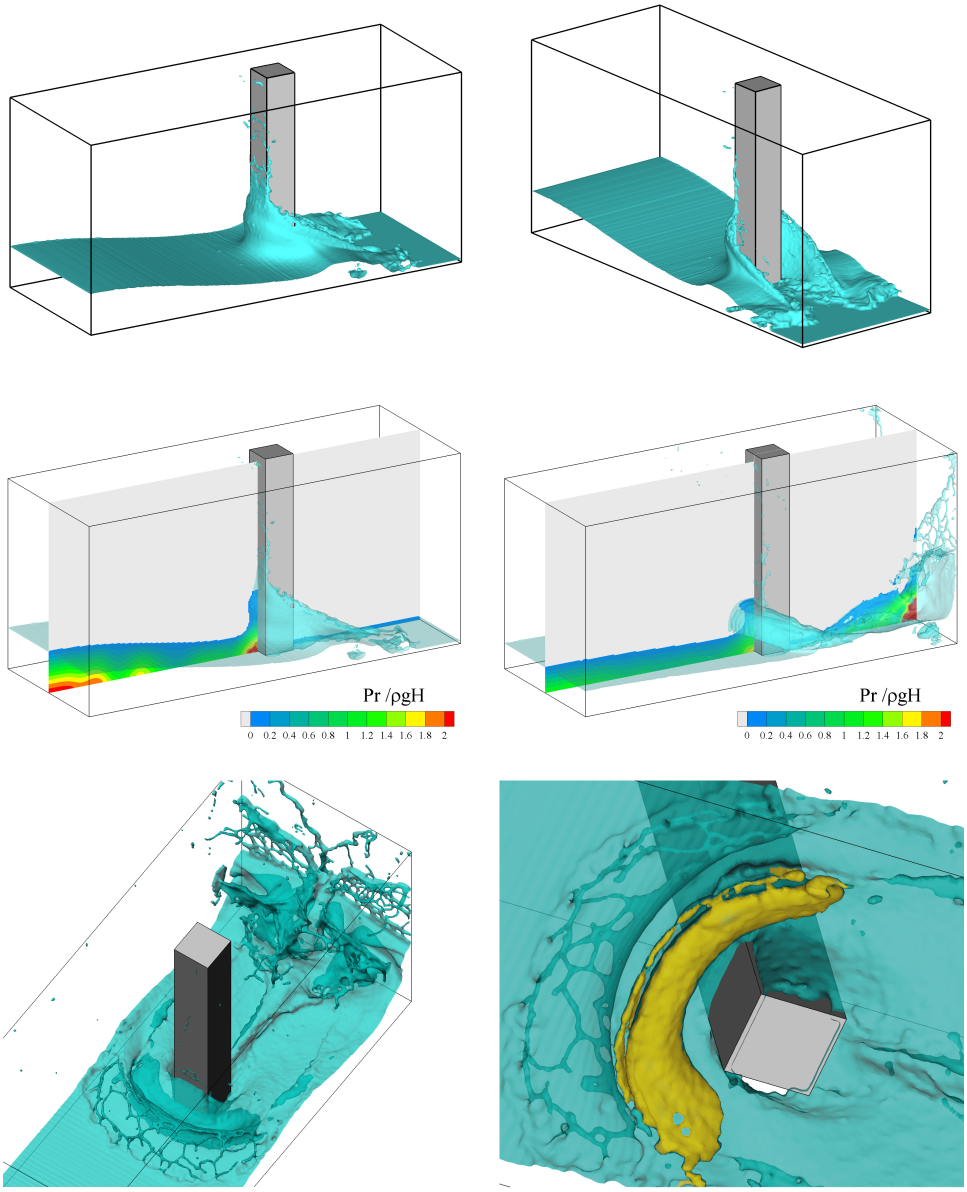

Figure B.4.: 3D Flow impact against a tall structure after a dam-break described in section 9.1. Top: two views of the free surface represented by iso-surface $\phi = -dx/4h$. Middle: free-surface and pressure contours interpolated on a vertical plane at two different time instants. Bottom: two views of the free-surface iso-surface at a later stage of the flow evolution; on the right plot a detail of the cavity generated in front of the column is given (seen from below).

C CONVERGENCE ANALYSIS: DETAILS OF COMPUTATIONS

In this brief section some details on the convergence analyses reported in this work are provided.

Let us consider the signal $f = f(s)$ with $s \in [s_0, s_f]$. Here, the symbol s represents the spatial or the time variable according to the case at hand. Then, the error between two signals f_1 and f_2 in the L^1 norm is:

$$\varepsilon_{21} = \int_{s_0}^{s_f} |\, f_1 - f_2 \,| \, ds \tag{C.1}$$

Now, let assume that f_2 is obtained by doubling the resolution of f_1 and, similarly, consider a signal f_3 that doubles the resolution of f_2. Then, the convergence rate C of the quantity f is given by:

$$C = \log\left(\frac{\varepsilon_{32}}{\varepsilon_{21}}\right) / \log(2)\,. \tag{C.2}$$

The relative error with respect to the reference solutions (for example BEM solution in section 8.3) is given by:

$$\varepsilon_{R1} = \left(\int_{s_0}^{s_f} |\, f_1 - f_R \,| \, ds\right) \left(\int_{s_0}^{s_f} |\, f_R \,| \, ds\right)^{-1}\,. \tag{C.3}$$

where the symbol f_R indicates the signal of the reference solution.

D BOTTOM EFFECTS ON $2D + t$ SHIP WAVE PATTERN PREDICTION

When simulating three dimensional wave patterns, the depth of the domain is usually chosen to be at least larger than three hull lengths. This condition ensures that the bottom effects on the wave pattern are negligible. In particular, the longitudinal components of the wave pattern are the most affected by the bottom because of their longer lengths. In the $2D + t$ framework only the divergent components are considered and, therefore, the bottom effects are strongly reduced. This is an advantage respect to the three dimensional simulations since the size of the domain can be considerably reduced. In the following, we consider three different simulations where the distance of the bottom from the undisturbed free surface increases from $2D$ to $4D$ and up to $8D$ (where D is the ship draft). The Froude number is set equal to 0.60 even though similar results have been found for the other Froude numbers presented in the paper. Figure D.1 shows the section where the plunging jet is hitting the underlying free surface. The three different plots of this figure refer to the three different depths adopted. It is possible to note that the differences between the three solutions are quite small. This proves that the depth adopted for the computations in the present work is adequate to study the breaking bow wave.

In any case, the bottom may influence the post-breaking evolution. Figures D.2 and D.2 show wave cuts for two other transversal sections abaft. Here local differences related to the bottom effects can be clearly noticed. However, these discrepancies do not modify the qualitative analysis of the global wave field proposed in the present work.

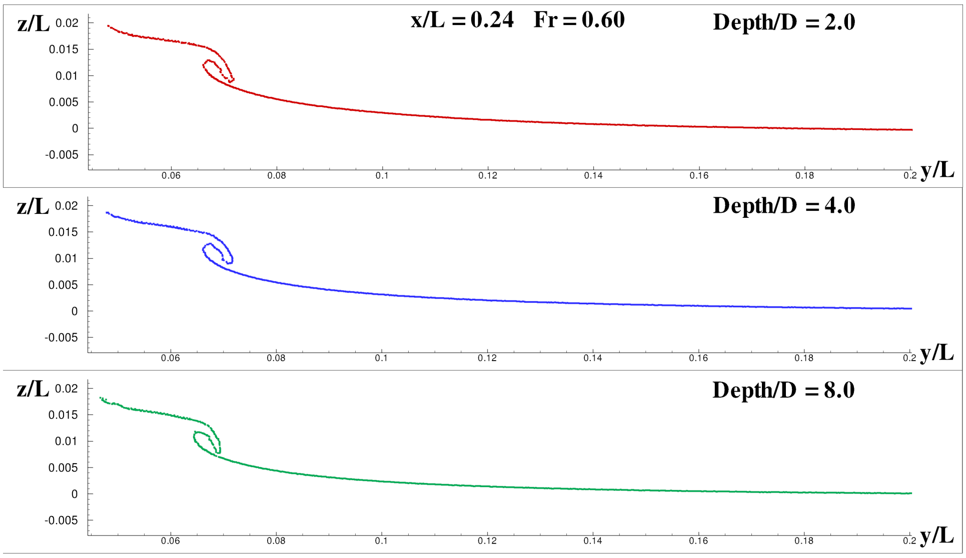

Figure D.1.: Comparison between simulations at three different depth of the fluid domain for Fr = 0.60. The snapshot is taken at x/L = 0.24.

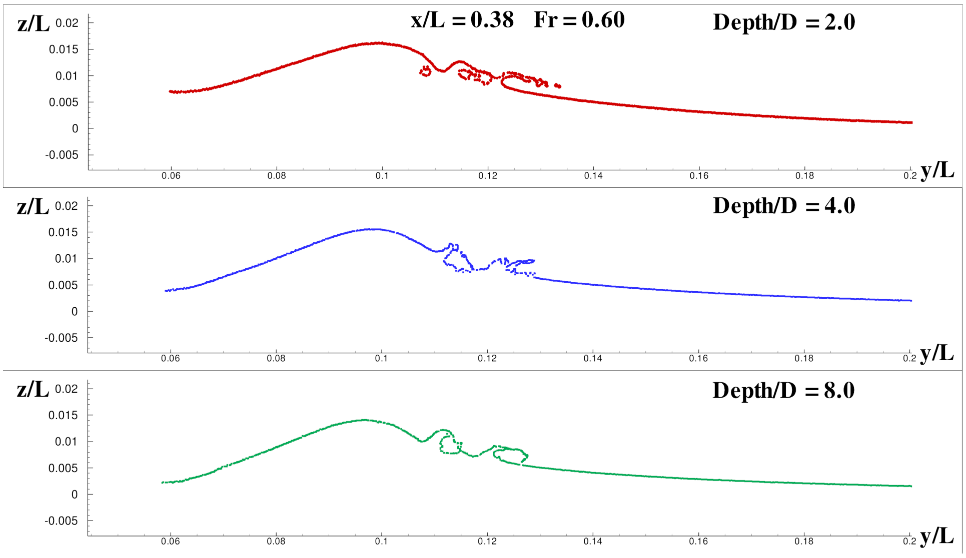

Figure D.2.: Comparison between simulations at three different depth of the fluid domain for Fr = 0.60. The snapshot is taken at x/L = 0.38.

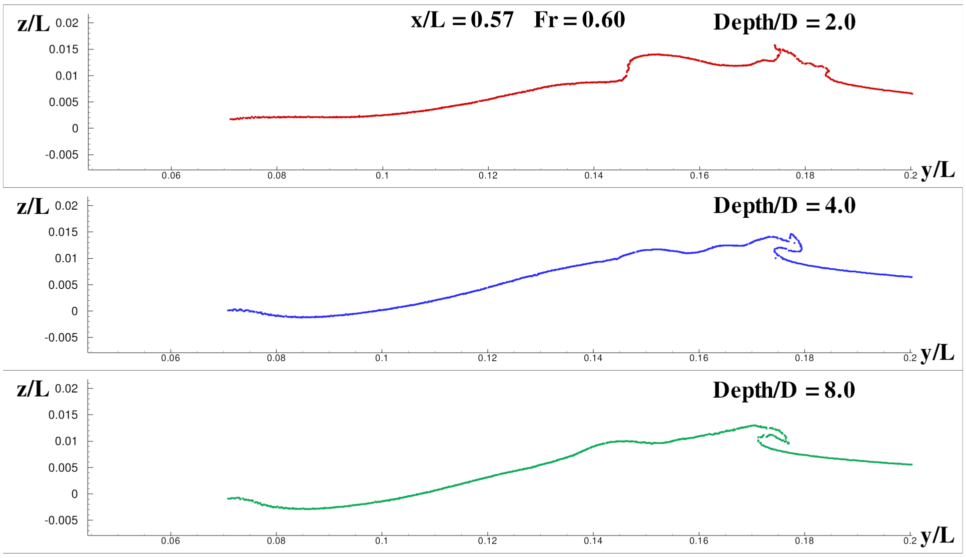

Figure D.3.: Comparison between simulations at three different depth of the fluid domain for $Fr = 0.60$. The snapshot is taken at $x/L = 0.57$.

BIBLIOGRAPHY

Allen, M.P. and D.J. Tildesley (1999). *Computer simulation of liquids*. Oxford University Press.

Amicarelli, A., J. Marongiu, F. Leboeuf, J. Leduc, M. Neuhauser, L. Fang, and J. Caro (2011*a*). "SPH truncation error in estimating a 3D derivative". In: *Int. J. Numer. Meth. Engn* 87, pp. 677–700.

Amicarelli, A., J. Marongiu, F. Leboeuf, J. Leduc, and J. Caro (2011*b*). "SPH truncation error in estimating a 3D function". In: *Comp. Fluids* 44, pp. 279–296.

Antuono, M., A. Colagrossi, S. Marrone, and D. Molteni (2010). "Free-surface flows solved by means of SPH schemes with numerical diffusive terms". In: *Comp. Phys. Comm.* 181, pp. 532–549.

Antuono, M., A. Colagrossi, S. Marrone, and C. Lugni (2011). "Propagation of gravity waves through an SPH scheme with numerical diffusive terms". In: *Comp. Phys. Comm.* 182, pp. 866–877.

Baba, E. (1969). *Study on separation of ship resistance components*. Tech. rep. 59. Mitsubishi Technical Bulletin.

Balsara, D.S. (1995). "von Neumann Stability Analysis of Smoothed Particle Hydrodynamics Suggestions for Optimal Algorithms". In: *J. Comp. Phys.* 121, pp. 357–372.

Basa, M., N.J. Quinlan, and M. Lastiwka (2008). "Robustness and accuracy of SPH formulations for viscous flow". In: *Int. J. Numer. Meth. Fluids*. DOI: http://dx.doi.org/10.1002/fld.1927.

Batchelor, George Keith (1967). *Introduction to Fluid Dynamics*. Cambridge University Press, New York.

Belytschko, T., Y. Krongauz, J. Dolbow, and C. Gerlach (1998). "On the completeness of meshfree particle methods". In: *Int. J. Numer. Meth. Engng* 43.5 (Nov. 1998), pp. 785–819.

Bicknell, G.V. (1991). "The Equations of Motion of Particles in Smoothed Particle Hydrodynamics". In: *SIAM J. Sci. Comput.* 12.5, pp. 1198–1206.

Bonet, J. and S. Kulasegaram (2001). "Remarks on tension instability of Eulerian and Lagrangian corrected smooth particle hydrpdynamics (CSPH) methods". In: *Int. J. Numer. Meth. Engng* 52, pp. 1203–2120.

Bonet, J. and T.S.L. Lok (1999). "Variational and momentum preservation aspects of Smoothed Particle Hydrodynamics formulations". In: *Comput. Methods Appl. Mech. Eng.* 180, pp. 97–115.

Bonet, J. and M.X. Rodriguez-Paz (2005). "Hamiltonian formulation of the variable-h SPH equations". In: *J. Comp. Phys.* 209, pp. 541–558.

Børve, S., M. Omang, and J. Trulsen (2005). “Regularized smoothed particle hydrodynamics with improved multi-resolution handling”. In: *J. Comp. Phys.* 208, pp. 345–367.

Braza, M., L. Martinelli, and A. Jameson (1986). “Numerical study and physical analysis of the pressure and velocity fields in the near wake of a circular cylinder”. In: *J. Fluid Mech.* 165, pp. 79–130.

Brookshaw, L. (1985). “A method of calculating radiative heat diffusion in particle simulations”. In: *Proc. Astron. Soc. Aust.* 6.2, pp. 207–210.

Buchner, B. (2002). “Green Water on Ship-type Offshore Structures”. PhD thesis. Delft University of Technology.

Calhoun, D. (2002). “A cartesian grid method for solving the two-dimensional streamfunction-vorticity equations in irregular regions”. In: *J. Comp. Phys.* 176.2, pp. 231–275.

Carrica, P.M., R.V. Wilson, and F. Stern (2005). “Free surface flows around ships: progress toward simulation of high-speed flows and motions”. In: *Mecanica Computacional* XXIV.

Chaniotis, A.K., D. Poulikakos, and P. Koumoutsakos (2002). “Remeshed smoothed particle hydrodynamics for the simulation of viscous and heat conducting flows”. In: *J. Comp. Phys.* 182, pp. 67–90.

Cleary, P. (1998). “Modelling confined multi-material heat and mass flows using SPH”. English. In: *Applied Mathematical Modelling* 22.12, pp. 981–993. ISSN: 0307-904X.

Cleary, P. and J.J. Monaghan (1993). “Boundary interactions and transition to turbulence for standard CFD problems using SPH”. In: *Proc. 6th International Computational Techniques and Applications Conference*. Canberra, pp. 157–165.

Colagrossi, A. (2005). “A meshless lagrangian method for free-surface and interface flows with fragmentation”. PhD thesis. Università di Roma La Sapienza.

Colagrossi, A. and M. Landrini (2003). “Numerical Simulation of Interfacial Flows by Smoothed Particle Hydrodynamics”. In: *J. Comp. Phys.* 191, pp. 448–475.

Colagrossi, A., M. Landrini, and M.P. Tulin (2001). “Numerical studies of wave breaking compared to experimental observations”. In: *Proc.* 4th *Numerical Towing Tank Symposium (NuTTS)*. Hamburg, Germany.

Colagrossi, A., M. Antuono, and S. Marrone (2009*a*). “A 2D+t SPH model with enhanced solid boundary treatment”. In: 4th *ERCOFTAC SPHERIC Workshop*. Nantes, France.

Colagrossi, A., M. Antuono, and D. Le Touzé (2009*b*). “Theoretical considerations on the free-surface role in the smoothed-particle-hydrodynamics model”. In: *Physical Review E* 79.

Colagrossi, A., G. Colicchio, C. Lugni, and M. Brocchini (2010*a*). "A study of violent sloshing wave impacts using an improved SPH method". In: *Journal of Hydraulic Research* 48, pp. 94–104.

Colagrossi, A., M. Antuono, A. Souto-Iglesias, P. Izaguirre-Alza, and D. Le Touzé (2010*b*). "Theoretical analysis of SPH in simulating free-surface viscous flows". In: 5th *ERCOFTAC SPHERIC Workshop*. Manchester, UK.

Colagrossi, A., M. Antuono, A. Souto-Iglesias, and D. Le Touzé (2011). "Theoretical analysis and numerical verification of the consistency ov viscous SPH formulations in simulating free-surface flows". In: *Physical Review E*. accepted for pubblication.

Colicchio, G. (2004). "Violent disturbance and fragmentation of free surfaces". PhD thesis. University of Southampton.

Colicchio, G., M. Greco, and O.M. Faltinsen (2006). "Fluid-body interaction on a Cartesian grid: dedicated studies for a CFD validation". In: 21st *International Workshop on Water Waves and Floating Bodies*. Loughborough, UK.

— (2010). "Domain-decomposition strategy for marine applications with cavity entrapments". In: *Journal of Fluids and Structures* 27, pp. 567–585.

Cummins, S.J. and M. Rudman (1999). "An SPH projection method". In: *J. Comp. Phys.* 152.2, pp. 584–607.

Dalrymple, R.A. and B. Rogers (2006). "Numerical modeling of water waves with the SPH method". In: *Coastal Engineering* 53 (2-3), pp. 141–147.

De Leffe, M., D. Le Touzé, and B. Alessandrini (2009). "Normal flux method at the boundary for SPH". In: 4th *ERCOFTAC SPHERIC Workshop*. Nantes, France.

— (2011). "A modified no-slip condition in weakly-compressible SPH". In: 6th *ERCOFTAC SPHERIC Workshop*. Hamburg, Germany.

Di Lisio, R., E. Grenier, and M. Pulvirenti (1997). "On the Regularization of the Pressure Field in Compressible Euler Equations". In: *Annali della Scuola Normale Superiore di Pisa, Classe Scienze 4 série* 24.2, pp. 227–238. URL: http://www.numdam.org/item?id=ASNSP_1997_4_24_2_227_0.

— (1998). "The convergence of the SPH method". In: *Comp. Math. Appl.* 35.1–2, pp. 95–102.

Di Mascio, A., R. Broglia, and R. Muscari (2007). "On the application of the single-phase level set method to naval hydrodynamic flows". In: *Computers & Fluids* 36, pp. 868–886.

Di Monaco, A., S. Manenti, M Gallati, S. Sibilla, G. Agate, R. Guendalini, and A. Maffio (2009). "A semi-analytic approach for SPH modeling of solid boundaries". In: 4th *ERCOFTAC SPHERIC Workshop*. Nantes, France.

Dilts, G.A. (1999). "Moving-Least-Squares-Particle Hydrodynamics—I. Consistency and Stability". In: *Int. J. Numer. Meth. Engng* 44, pp. 1115–1155.

— (2000). "Moving-least-squares-particle hydrodynamics - II. Conservation and boundaries". In: *Int. J. Numer. Meth. Engn* 48, pp. 1503–1524.

Dommermuth, D.G., D.K.P. Yue, W.M. Lin, R.J. Rapp, E.S. Chan, and W.K. Melville (1988). "Deep-water plunging breakers, a comparison between potential theory and experiments". In: *J. Fluid Mech.* 189, pp. 423–442.

Doring, M. (2005). "Dèveloppement d'une mèthode SPH pour les e e applications à surface libre en hydrodynamique". PhD thesis. Ecole Centrale de Nantes.

Dyka, C.T. and R.P. Ingel (1995). "An approach for tension instability in Smoothed Particle Hydrodynamics (SPH)". In: *Comp. Struct.* 57.4, pp. 573–580.

Ellero, M., M. Serrano, and P. Español (2007). "Incompressible smoothed particle hydrodynamics". In: *J. Comp. Phys.* 226, pp. 1731–1752.

Español, P. and M. Revenga (2003). "Smoothed dissipative particle dynamics". In: *Physical Review E* 67.

Faltinsen, O.M. (2000). *Sea loads on High Speed Marine Vehicles*. Trondheim, Norway: NTNU.

— (2006). *Hydrodynamics of High-Speed Marine Vehicles*. Cambridge University Press.

Faltinsen, O.M. and R. Zhao (1991). "Numerical predictions of ship motions at high forward speed". In: *Philosophical Transactions of the Royal Society of London A* 334, pp. 241–252.

Federico, I. (2010). "Simulating Open-Channel Flows and Advective Diffusion Phenomena through SPH Model". PhD thesis. Università della Calabria.

Feldman, J. and J. Bonet (2007). "Dynamic refinement and boundary contact forces in SPH with applications in fluid flow problems". In: *Int. J. Numer. Meth. Engng* 72, pp. 295–324.

Ferrand, M., D. Laurence, B. Rogers, and D. Violeau (2010). "Improved time scheme integration approach for dealing with semi analytical boundary conditions in SPARTACUS2D". In: 5th *ERCOFTAC SPHERIC Workshop*. Manchester, UK.

Ferrari, A., M. Dumbser, E. F. Toro, and A. Armanini (2009). "A new 3D parallel SPH scheme for free surface flows". In: *Comp. Fluids* 38, pp. 1203–1217.

Ferrari, A., L. Fraccarollo, M. Dumbser, E. F. Toro, and A. Armanini (2010). "Three-dimensional flow evolution after a dam break". In: *J. Fluid Mech.* 663, pp. 456–477.

Fey, M. and R. Jeltsch (1999). "Hyperbolic Problems: Theory, Numerics, Applications". In: *Int. Ser. Numer. Math.* 130, pp. 897–898.

Fontaine, E. and M.P. Tulin (1998). "On the prediction of free-surface flows past slender hulls using the 2D+t theory: the evolution of an idea". In: *Proceedings of the Symposium NATO/RTO/AVT Fluid dynamics problems of vehicules operating near or in the air-sea interface*. Amsterdam, Netherlands.

Fontaine, E., O.M. Faltinsen, and R. Cointe (2000). "New insight into the generation of ship bow waves". In: *Journal of Fluid Mechanics* 421, pp. 15–38.

Fries, T.P. and H.M. Matthies (2004). *Classification and Overview of Meshfree Methods*. Tech. rep. 2003-03. Brunswick, Germany: Institute of Scientific Computing, Technical University Braunschweig.

Ghidaglia, J. and F. Pascal (2005). "The normal flux method at the boundary for multidimensional finite volume approximations in CFD". In: *Europ. J. Mech. B/Fluids* 24, pp. 1–17.

Gingold, R.A. and J.J. Monaghan (1977). "Smoothed Particle Hydrodynamics: theory and application to non-spherical stars". In: *Mon. Not. R. Astron. Soc.* 181, pp. 375–389.

— (1982). "Kernel estimates as a basis for general particle methods in hydrodynamics". In: *J. Comp. Phys.* 46, pp. 429–453.

Glowinski, R. and P. Le Tallec (1989). *Augmented Lagrangian and operator-splitting methods in nonlinear mechanics*. SIAM ed.

Gray, J.P., J.J. Monaghan, and Swift R.P. (2001). "SPH elastic dynamics". In: *Comput. Methods Appl. Mech. Engrg.* 190, pp. 6641–6662.

Greco, M. (2001). "A Two-dimensional Study of Green-Water Loading". PhD thesis. University of Trondheim, Norway.

Greco, M., G. Colicchio, and O.M. Faltinsen (2007). "Shipping of water on a two-dimensional structure. Part 2". In: *J. Fluid Mech.* 581, pp. 371–399.

Grenier, N., M. Antuono, A. Colagrossi, D. Le Touzé, and B. Alessandrini (2009). "An Hamiltonian interface SPH formulation for multi-fluid and free surface flows". In: *J. Comp. Phys.* 228, pp. 8380–8383.

Guilcher, P.M. (2008). "Contribution au développement d'une méthode SPH pour la simulation numérique des interactions houle-structure". PhD thesis. Ecole Centrale de Nantes.

Haque, A. and G.A. Dilts (2007). "Three-dimensional boundary detection for particle methods". In: *J. Comp. Phys.* 226, pp. 1710–1730.

Hernquist, L. and N. Katz (1989). "TreeSPH: A Unification of SPH with the Hierarchical Tree Method". In: *Astrophysical Journal Supplement* 70, pp. 419–446.

Hieber, S.E. and P. Koumoutsakos (2008). "An immersed boundary method for smoothed particle hydrodynamics of self-propelled swimmers". In: *J. Comp. Phys.* 227, pp. 8636–8654.

Hirsch, C. (1990). *Numerical computation of internal and external flows. Vol. 2 - Computational methods for inviscid and viscous flows*. Ed. by Ltd. John Wiley & Sons.

Hongbin, J. and D. Xin (2005). "On criterions for Smoothed Particle Hydrodynamics kernels in stable field". In: *J. Comp. Phys.* 202, pp. 699–709.

Hu, X.Y. and N.A. Adams (2006*a*). "A multi-phase SPH method for macroscopic and mesoscopic flows". In: *J. Comp. Phys.* 213 (2), pp. 844–861.

— (2006*b*). "Angular-momentum conservative smoothed particle hydrodynacmis for incompressible viscous flows". In: *Phys. of Fluids* 18 (2 2006), pp. 702–706.

Inui, T. (1981). "From bulbous bow to free-surface shock wave – Trends of 20 years' research on ship waves at the Tokyo University Tank". In: *Journal of Ship Research* 25.3, pp. 147–180.

Johnson, G.R. and S.R. Beissel (1996). "Normalized smothing functions for SPH impact calculations". In: *Int. J. Numer. Meth. Engn* 39.16, pp. 2725–2741.

Kleefsman, K.M.T, G. Fekken, A.E.P. Veldman, B. Iwanowski, and B. Buchner (2005). "A Volume-of-Fluid based simulation method for wave impact". In: *J. Comp. Phys.* 206.

Koshizuka, S. and Y. Oka (1996). "Moving-particle semi-implicit method for fragmentation of incompressible fluid". In: *Nuclear Sci. Eng.* 123.3, pp. 421–434.

Koumoutsakos, P. (2005). "Multiscale flow simulations using particles". In: *Annual Review of Fluid Mechanics* 37, pp. 457–487.

Kulasegaram, S., J. Bonet, R.W. Lewis, and M. Profit (2004). "A variational formulation based contact algorithm for rigid boundaries in two-dimensional SPH applications". In: *Comp. Mech.* 33, pp. 315–325.

Landrini, M., A. Colagrossi, and M.P. Tulin (2001). "Breaking Bow and Stern Waves: Numerical Simulations". In: 16th *International Workshop on Water Waves and Floating Bodies*. Hiroshima, Japan.

Landrini, M., A. Colagrossi, and O.M. Faltinsen (2003). "Sloshing in 2D Flows by the SPH Method". In: *8th Int. Conf. on Num. Ship Hydrodynamics. Busan. Korea*.

Landrini, M., A. Colagrossi, M. Greco, and M.P. Tulin (2007). "Gridless simulations of splashing proces and near-shore bore propagation". In: *J. Fluid Mech.* 591, pp. 183–213.

Lecointe, Y. and J. Piquet (1984). "On the use of several compact methods for the study of unsteady incompressible viscous flow around a circular cylinder". In: *Comp. Fluids* 12.4, pp. 336–280.

Libersky, L.D., A.G. Petschek, T.C. Carney, J.R. Hipp, and F.A. Allahdadi (1993). "High strain Lagrangian hydrodynamics a three-dimensional SPH code for dynamic material response". In: *J. Comp. Phys.* 109.1, pp. 67–75.

Lucy, L.B. (1977). "A numerical approach to the testing of the fission hypothesis". In: *Astronomical Journal* 82, pp. 1013–1024.

Lugni, C. (1999). "'A study about the free-surface waves and the freely floating structure interactions". in italian. PhD thesis. Università di Roma La Sapienza.

Lugni, C., A. Colagrossi, Landrini M., and O.M. Faltinsen (2004). "Experimental and Numerical Study of Semi-displacement Mono-hull and Catamaran in calm water and incident waves". In: *Proceedings of* 25th *Symposium on Naval Hydrodynamics*. St. John's, Canada.

Macià, F., M. Antuono, L. M. González, and A. Colagrossi (2011). "Theoretical analysis of the no-slip boundary condition enforcement in SPH methods". In: *Progr. Theor. Phys.* accepted for pubblication.

Madsen, P.A. and H.A. Shäffer (2006). "A discussion of artificial compressibility". In: *Coastal Engineering* 53, pp. 93–98.

Marongiu, J. (2007). "Méthode numérique lagrangienne pour la simulation d'écoulements à surface libre - Application aux turbines Pelton". PhD thesis. Ecole Centrale de Lyon.

Marongiu, J., F. Leboeuf, and E. Parkinson (2008). "Riemann solvers and efficient boundary treatments: an hybrid SPH-finite volume numerical method". In: 3^{rd} *ERCOFTAC SPHERIC Workshop*. Lausanne, Switzerland.

Marrone, S., A. Colagrossi, D. Le Touzé, and G. Graziani (2010). "Fast free-surface detection and level-set function definition in SPH solvers". In: *J. Comp. Phys.* 229, pp. 3652–3663.

Marrone, S., M. Antuono, A. Colagrossi, G. Colicchio, D. Le Touzé, and G. Graziani (2011). "δ-SPH model for simulating violent impact flows". In: *Comput. Methods Appl. Mech. Engrg.* 200, pp. 1526–1542.

Marsden, J.E. and T.J.R. Hughes (1994). *Mathematical foundations of elasticity*. Dover ed.

Marsh, A.P., M. Prakash, S.E. Semercigil, and Ö.F. Turan (2010). "A shallow-depth sloshing absorber for structural control". In: *J. Fluid. Struct.* 26, pp. 780–792.

Marsh, A.P., G. Oger, D. Le Touzé, and G. Guibert (2011). "Validation of a conservative variable-resolution SPH scheme including grad(h) terms". In: 6^{th} *ERCOFTAC SPHERIC Workshop*. Hamburg, Germany, pp. 86–93.

Maruo, H. (1989). "Evolution of the theory of slender Ships". In: *Ship Technology Research* 36, pp. 107–133.

Maruo, H. and W. Song (1994). "Nonlinear Analysis of Bow Wave Breaking and Deck Wetness of a High-Speed Ship by the Parabolic Approximation". In: *Symposium on Naval Hydrodynamics*20^{th}. University of California, Santa Barbara.

Mas-Gallic, S. and P.A. Raviart (1987). "A Particle Method for First-order Symmetric Systems". In: *Numer. Math.* 51, pp. 323–352.

Maxeiner, E.A., M. Shakeri, and J.H. Duncan (2008). "A Parametric Investigation of Breaking Bow Waves using a 2D+t Wave Maker". In: *Proceedings of* 61^{st} *Annual Meeting of the American Physical Society: Division of Fluid Dynamics*, San Antonio, Texas, USA.

Mei, C.C. (1983). *The applied dynamics of ocean surface waves*. Vol. 1. Advance Series on Ocean Engineering. Singapore: World Scientific.

Michell, J.H. (1890). "On the Theory of Free Stream Lines". In: *Philosophical Transactions of the Royal Society of London. A* 181, pp. 389–431.

Milne-Thomson, L.M. (1968). *Theoretical Hydrodynamics*. Vol. Fifth. The MacMillan Press Ltd.

Molteni, D. and A. Colagrossi (2009). "A simple procedure to improve the pressure evaluation in hydrodynamic context using the SPH". In: *Comp. Phys. Comm.* 180, pp. 861–872.

Molteni, D., A. Colagrossi, and G. Colicchio (2007). “On the use of an alternative water state equation in SPH”. In: 4^{th} *ERCOFTAC SPHERIC Workshop*. Madrid, Spain.

Monaghan, J.J. (1988). “An introduction to SPH”. In: *Comp. Phys. Comm.* Pp. 89–96.

— (1989). “On the problem of penetration in particle methods”. In: *J. Comp. Phys.* 82.

— (1992). “Smoothed Particle Hydrodynamics”. In: *Annual Review of Astronomy and astrophysics* 30, pp. 543–574.

— (1994). “Simulating Free Surface Flows with SPH”. In: *J. Comp. Phys.* 110.2, pp. 39–406.

— (2000). “SPH without a tensile instability”. In: *J. Comp. Phys.* 159.2, pp. 290–311.

— (2005*a*). “Smoothed particle hydrodynamic simulations of shear flow”. In: *Mon. Not. R. Astron. Soc.* 365, pp. 199–213. DOI: 10.1111/j.1365-2966.2005.09783.x. URL: http://dx.doi.org/10.1111/j.1365-2966.2005.09783.x.

— (2005*b*). “Smoothed particle hydrodynamics”. In: *Reports on Progress in Physics* 68, pp. 1703–1759.

— (2009). “An SPH Turbulence Model”. In: 4^{th} *ERCOFTAC SPHERIC Workshop*. Nantes, France, pp. 188–192.

Monaghan, J.J. and R.A. Gingold (1983). “Shock Simulation by the Particle Method SPH”. In: *J. Comp. Phys.* 52, pp. 374–389.

Monaghan, J.J. and J.B. Kajtar (2009). “SPH particle boundary forces for arbitrary boundaries”. In: *Comp. Phys. Comm.* 180, pp. 1811–1820.

Monaghan, J.J. and A. Kos (1999). “Solitary waves on a Cretan Beach”. In: *J. Waterway, Port, Coastal, and Ocean Eng.* 125.3, p. 145.

— (2000). “Scott Russell’s Wave Generator”. In: *Phys. of Fluids* 12.3, p. 622.

Monaghan, J.J., A. Kos, and N. Issa (2003). “Fluid motion generated by impact”. In: *University of Monash* 129.6, pp. 250–259.

Morris, J.P. (1996*a*). “A Study of Stability Properties of Smooth Particle Hydrodynamics”. In: *Publ. Astron. Soc. Aust.* 13, pp. 97–102.

— (1996*b*). “Analysis of SPH with applications”. PhD thesis. Melbourne, Australia: Monash University.

Morris, J.P., P.J. Fox, and Y. Zhu (1997). “Modeling Low Reynolds Number Incompressible Flows Using SPH”. In: *J. Comp. Phys.* 136, pp. 214–226. DOI: http://dx.doi.org/10.1006/jcph.1997.5776.

Moussa, B.B. (2006). “On the convergence of SPH method for scalar conservation laws with boundary conditions”. In: *Method Appl. Anal.* 13, pp. 29–62.

Moussa, B.B., N. Lanson, and J.P. Vila (1999). “Convergence of meshless methods for conservations laws: applications to Euler equations”. In: *Int. Ser. Numer. Math.* 129, pp. 31–40.

Nelson, R.P. and J.C.B. Papaloizou (1994). “Variable smoothing lengths and energy conservation in SPH”. In: *Mon. Not. R. Astronom. Soc.* 270, pp. 1–20.

Ng, Y.T., M. Chohong, and F. Gibou (2009). "An efficient fluid–solid coupling algorithm for single-phase flows". In: *J. Comp. Phys.* 228, pp. 8807–8829.

Oelschläger, K. (1991). "On the Connection Between Hamiltonian Many-Particle Systems and the Hydrodynamical Equations". In: *Arch. Rational Mech. Anal.* 115, pp. 297–310.

Oger, G., M. Doring, B. Alessandrini, and P. Ferrant (2006). "Two-dimensional SPH simulations of wedge water entries". In: *J. Comp. Phys.* 213 (2), pp. 803–822.

Oger, G., C. Leroy, E. Jacquin, D. Le Touzé, and B. Alessandrini (2009). "Specific pre/post treatments for 3-D SPH applications through massive HPC simulations". In: 4th *ERCOFTAC SPHERIC Workshop*. Nantes, France.

Oguz, H.N. and A. Prosperetti (1991). "Numerical calculation of the underwater noise of rain". In: *Journal of Fluid Mechanics* 228, pp. 417–442.

Peregrine, D.H (2003). "Water-wave impact on walls". In: *Annu. Rev. Fluid Mech.* 35, pp. 23–43.

Perelman, O. (2010). *Minutes of towing tank test, Task E6.BE2*. Tech. rep. DGA-Hydrodynamics.

Quinlan, N.J., M. Basa, and M. Lastiwka (2006). "Truncation error in mesh-free particle methods". In: *Int. J. Numer. Meth. Engn* 66, pp. 2064–2085.

Randles, P.W. and L.D. Libersky (1996). "Smoothed Particle Hydrodynamics: some recent improvements and applications". In: *Comput. Methods Appl. Mech. Eng.* 39, pp. 375–408.

— (2000). "Normalized SPH with stress points". In: *Int. J. Numer. Meth. Engn* 48.10, pp. 1445–1462.

Rasio, F.A. (2000). "Particle Methods in Astrophysical Fluid Dynamics". In: *Progr. Theor. Phys. Suppl.* 138, pp. 609–621.

Read, J.I., T. Hayfield, and O. Agertz (2010). "Resolving mixing in smoothed particle hydrodynamics". In: *Mon. Not. R. Astron. Soc.* 405, pp. 1513–1530.

Reed, A.M. and J.H. Milgram (2002). "Ship wakes and their radar images". In: *Annual Review of Fluid Mechanics* 34, pp. 469–502.

Shadloo, M.S., A. Zainali, A. Sadek, and S.M. Yildiz and (2010). "Improved Solid Boundary Treatment Method for the Solution of Flow over an Airfoil and Square Obstacle by SPH Method". In: 5th *ERCOFTAC SPHERIC Workshop*. Manchester, UK.

Shakeri, M., M. Tavakolinejad, M. Mayer, P. Kang, and J.H. Duncan (2006). "On the Geometrical Characteristics of Jets Produced in Plunging Breaking Bow Waves". In: *Proceedings of* 59th *Annual Meeting of the American Physical Society: Division of Fluid Dynamics*. Tampa Bay, Florida, USA.

Shao, S. and Y.M.L. Edmond (2003). "Incompressible SPH method for simulating Newtonian and non-Newtonian flows with a free surface". In: *Adv. Water Res.* 26, pp. 787–800.

Shimada, K. (1993). "Physically-based mesh generation; automated triangularization of surface and volumes via Bubble packing". PhD thesis. Massachusetts Institute of Technology.

Souto-Iglesias, A., L. Pérez Rojas, and R. Zamora-Rodríguez (2004). "Simulation of anti-roll tanks and sloshing type problems with smoothed particle hydrodynamics". In: *Ocean Engineering* 31, pp. 1169–1192.

Springel, V. (2010). "Smoothed Particle Hydrodynamics in Astrophysics". In: *Ann. Rev. Astron. Astrophys.* 48, pp. 391–430.

Swegle, J.W., D.L. Hicks, and S.W. Attaway (1995). "Smoothed Particle Hydrodynamics Stability Analysis". In: *J. Comp. Phys.* 116, pp. 123–134.

Takeda, H., S. M. Miyama, and M. Sekiya (1994). "Numerical Simulation of Viscous flow by Smoothed Particle Hydrodynamics". In: *Progr. Theor. Phys.* 92.5.

Taylor, G. (1966). "Oblique Impact of a Jet on a Plane Surface". In: *Math. Phys. Sci.* 260.1110, pp. 96–100.

Trivellato, F., E. Bertolazzi, and A. Colagrossi (2006). "Flow solvers for liquid–liquid impacts". In: *Vorticity and Turbulence Effects in Fluid Structure Interactions*. Southampton: WIT Press. Chap. 11, pp. 261–287. ISBN: 1-84564-052-7.

Tulin, M.P. and M. Landrini (2000). "Breaking waves in the Ocean and around Ships". In: *23rd Symp on Naval Hydrodynamics*. Val de Reuil, France.

Tulin, M.P. and M. Wu (1996). "Divergent bow waves". In: *21th ONR Symposium on Naval Hydrodynamics*. Trondheim, Norway.

Vila, J.P. (1999). "On particle weighted methods and Smooth Particle Hydrodynamics". In: *Mathematical Models & Methods in Applied Sciences* 9.2, pp. 161–209.

Wagner, H. (1932). "Uber stoss- und gleitvorgange an der oberflache von flussigkeiten". In: *Z. Angew. Math. und Mech.* 12.4, pp. 192–235.

Watkins, S.J., A.S. Bhattal, J.A. Francis, J.A. Turner, and A.P. Whitworth (1996). "A new prescription for viscosity in Smoothed Particle Hydrodynamics". In: *Astron. Astrophys. Suppl. Ser.* 119, pp. 177–187.

Williamson, C.H.K. (1996). "Vortex dynamics in the cylinder wave". In: *Annu. Rev. Fluid Mech.* 28, pp. 79–130.

Wu, M., M.P. Tulin, and E. Fontaine (2003). "On the Simulation of Amplified Bow Waves Induced by Motion in Head Seas". In: *Journal of Ship Research* 44.4, pp. 290–299.

Yildiz, M., R.A. Rook, and A. Suleman (2009). "SPH with the multiple boundary tangent method". In: *Int. J. Numer. Meth. Engng* 77, pp. 1416–1438.

Zhang, S., D.K.P. Yue, and K. Tanizawa (1996). "Simulation of plunging wave impact on a vertical wall". In: *J. Fluid Mech.* 327, pp. 221–254.

ASSOCIATED PUBLICATIONS

PAPERS ON INTERNATIONAL JOURNALS

- Marrone S., Colagrossi A., Le Touzé D., Graziani G., "Fast free-surface detection and level-set function definition in SPH solvers", *Journal of Computational Physics*, **229**, 3652–3663, (2010)
- Antuono M., Colagrossi A., Marrone S., Molteni D., "Free-surface flows solved by means of SPH schemes with numerical diffusive terms", *Computer Physics Communications*, **181(3)**, 532-549, (2010)
- Antuono M., Colagrossi A., Marrone S., Lugni C., "Propagation of gravity waves through a SPH scheme with numerical diffusive terms" *Computer Physics Communications***182(4)**, 866-877, (2011)
- Marrone S., Antuono M., Colagrossi A., Colicchio G., Le Touzé D., Graziani G., "δ-SPH model for simulating violent impact flows", *Computer Methods in Applied Mechanics and Engineering*, **200**, 1526-1542, (2011)
- Marrone S., Colagrossi A., Antuono M., Lugni C., Tulin M.P., "A 2D+t SPH model to study the breaking wave pattern generated by fast ships", *Journal of Fluids and Structures*, **27**,1199-1215, (2011)
- Marrone S., Bouscasse B., Colagrossi A., Antuono M., "Challenges in the numerical simulations of ship breaking wave patterns through a 3D parallel SPH code", *Submitted to Computer & Fluids*
- Federico I., Marrone S., Colagrossi A., Aristodemo F., Veltri P., "Simulating 2D open-channel flows through SPH model", *Submitted to European Journal of Mechanics–B/Fluids*
- Colagrossi A., Bouscasse B., Antuono M., Marrone S., "Particle packing algorithm for SPH schemes", *Submitted to Computer Physics Communications*

PAPERS IN PROCEEDINGS OF NATIONAL AND INTERNATIONAL CONFERENCES

- Marrone S., Colagrossi A., Le Touzé D., Graziani G., "A fast algorithm for free-surface particle detection in 2D and 3D SPH methods", *Proc. fourth Int. SPHERIC Workshop*, Nantes, France, May 27–29, 2009

– Colagrossi A., Antuono M., Marrone S., "A 2D+t SPH model with enhanced solid boundary treatment", *Proc. fourth Int. SPHERIC Workshop*, Nantes, France, May 27–29, (2009)

– Marrone S., Antuono M., Colagrossi A., Colicchio G., Graziani G., "Enhanced Boundary Treatment in 2D Smoothed Particle Hydrodynamics Models", *XIX Cong. Naz. AIMETA*, Ancona (2009)

– Colagrossi A., Marrone S., Antuono M. and Tulin M.P., "A numerical study of breaking bow waves for different ship hulls", *XII Numerical Towing Tank Symposium* (Ed. V. Bertram), Cortona, 2009

– Antuono M., Marrone S., Colagrossi A., Lugni C., "Gravity wave propagation solved through an enhanced SPH method", *Proc. 1st European IAHR Congress*, Edinburgh, UK, (2010)

– Marrone S., Antuono M., Colagrossi A., Colicchio G., Le Touzé D., Graziani G., "Violent fluid-structure impacts solved through a delta-SPH model", *Proc. 5th Int. SPHERIC Workshop*, Manchester UK, June 23–25, (2010)

– Federico I., Marrone S., Colagrossi A., Aristodemo F., Veltri P., "Simulating free-surface channel flows through SPH", *Proc. 5th Int. SPHERIC Workshop*, Manchester UK, June 23–25, (2010)

– Antuono M., Marrone S., Colagrossi A., Lugni C., "Propagation of gravity wave-packets through a δ-SPH method", *Proc. 5th Int. SPHERIC Workshop*, Manchester UK, June 23–25, (2010)

– Federico I., Marrone S., Colagrossi A., Aristodemo F., Veltri P., "Simulations of hydraulic jump through SPH model", *Proc. XXXII IDRA Italian Conference of Hydraulics and Hydraulic Construction*, Palermo (2010)

– Bouscasse B., Antuono M., Marrone S., Colagrossi A., "Particle initialization through a novel packing algorithm", *6th International SPHERIC Workshop*, Hamburg, Germany, 8–10 June (2011)

– Marrone S., Bouscasse B., Colagrossi A., "Simulating ship wave patterns through a 3D parallel SPH code" *6th International SPHERIC Workshop*, Hamburg, Germany, 8–10 June 2011

– Federico I., Marrone S., Aristodemo F., Colagrossi A., Veltri P., "SPH simulations of buoyant and non-buoyant jets into open-channel flows", *6th International SPHERIC Workshop*, Hamburg, Germany, 8–10 June 2011

– Federico I., Marrone S., Aristodemo F., Colagrossi A., Veltri P., "Modelling of shallow water jets using smoothed particle hydrodynamics method", *IV Convegno Nazionale di Idraulica Urbana - Acqua e Città 2011*, Venezia, 21-24 June 2011

- Marrone S., Colagrossi A., Antuono M., Graziani G., “SPH modeling of Laminar flows through a novel ghost-fluid technique”, *XX Convegno AIMETA, Bologna, Italy, 12–15 September 2011*